The Anion Chemistry of Transition Metal Oxides and Oxychlorides

A thesis submitted to the
Board of the Faculty of Physical Sciences
in partial fulfilment of the requirements
for the degree of Doctor of Philosophy

by

Edward Dixon

New College

Trinity Term 2011

The Anion Chemistry of Transition Metal Oxides and Oxychlorides

Edward Dixon, New College, University of Oxford
Submitted for the degree of Doctor of Philosophy, Trinity Term 2011

Abstract

This investigation is based on the topotactic reduction reactions of 3 sets of phases: $La_{1-x}Sr_xMnO_3$ ($0.6 \leq x \leq 1$), $La_{1-x}Ca_xMnO_3$ ($0.6 \leq x \leq 1$) and $Sr_3Fe_{2-x}Co_xO_5Cl_2$ ($0 \leq x \leq 1$).

The topotactic reduction reactions of $La_{1-x}Sr_xMnO_3$ ($0.6 \leq x \leq 1$) perovskite phases using NaH as a solid state reducing agent result in the formation of reduced phases which contain manganese centres with a constant average oxidation state of +2.5, thus leading to an empirical composition of $La_{1-x}Sr_xMnO_{3-(0.5+x)/2}$. The structures of the reduced phases contain a 6-layer OOTOOT' stacking sequence of the octahedral (O) and tetrahedral (T) sheets and so are closely related to the 4-layer OTOT'-stacked brownmillerite structure. Close inspection reveals that the structures of the $La_{1-x}Sr_xMnO_{3-y}$ (x = 0.67, 0.7 and 0.75) reduced phases contain an intralayer ordered arrangement of twisted tetrahedral chains, and are the first instances of refined 6-layer structures containing such an arrangement. The driving force dictating the arrangement of the twisted tetrahedral chains in these 6-layer structures are shown to be the size of the tetrahedral chain dipole moment and the coupling between neighbouring tetrahedral layers in a similar manner to the brownmillerite structure. This logic has been applied to rationalise the ordering arrangement of the twisted tetrahedral chains in other structures containing tetrahedral layers. Variable temperature neutron diffraction data reveal that the $La_{1-x}Sr_xMnO_{3-y}$ ($0.67 \leq x \leq 0.83$) reduced phases adopt magnetically ordered structures incommensurate with the nuclear structures below T_N.

In contrast, the structures adopted by reduced phases formed by topotactic reduction reactions of $La_{1-x}Ca_xMnO_3$ ($0.6 \leq x \leq 1$) perovskite phases using NaH are split into 2 groups as a function of the La:Ca ratio: The reduction of perovskite phases in the range ($0.6 \leq x \leq 0.8$) result in the formation of reduced phases with an empirical composition of $La_{1-x}Ca_xMnO_2$ which adopt structures containing a disordered arrangement of layers of edge-sharing MnO_6 octahedra and layers of vertex-sharing MnO_4 tetrahedra. In contrast, reduction of the perovskite phases in the range ($0.9 \leq x \leq 1$) result in the formation of reduced phases with an empirical composition of $(La_{1-x}Ca_x)_{0.5}Mn_{0.5}O$ which adopt the rock salt structure with a disordered arrangement of the cations. The ($x < 1$) reduced phases are the first reported examples of extended oxides which contain manganese centres with an average oxidation state of below 2. Variable temperature neutron diffraction data reveal that the $La_{1-x}Ca_xMnO_{3-y}$ (x= 0.6, 0.67 and 0.7) reduced phases adopt G-type antiferromagnetically ordered magnetic structures below approximately $T_N \sim 220$ K.

The structure of $Sr_3Fe_2O_5Cl_2$ is closely related to that of the $A_3B_2O_7$ n = 2 Ruddlesden-Popper structure. The topotactic reduction reaction of $Sr_3Fe_2O_5Cl_2$ with LiH results in the formation of the Fe(II) phase $Sr_3Fe_2O_4Cl_2$. Neutron powder diffraction data show that $Sr_3Fe_2O_4Cl_2$ adopts a body-centred tetragonal crystal structure with anion vacancies located within the central SrO layer of the phase. The structure of $Sr_3Fe_2O_4Cl_2$ is therefore a rare example of a structure consisting of infinite sheets of corner-sharing $Fe(II)O_4$ square planes. In addition, the effect of cobalt-doping on the magnetic properties of the isostructural $Sr_3Fe_{2-x}Co_xO_4Cl_2$ ($0 \leq x \leq 1$) series of reduced phases was investigated. Cobalt-doping was found to frustrate the antiferromagnetic order initially leading to a decrease in the magnetic ordering temperature but ultimately leading to spin glass behaviour.

Declaration

The work described in this thesis was carried out at the Inorganic Chemistry Laboratory at the University of Oxford between October 2007 and May 2011 under the supervision of Dr. M. A. Hayward. All the work is my own, except where I have either acknowledged help from a named person or given a reference to a published source, and has not been submitted by the author for any other degree at this, or any other university.

Edward Dixon

August 2011

Dedicated to Mum and Dad

Acknowledgements

First and foremost I would like to thank my supervisor, Dr. Mike Hayward. His passion for solid state chemistry has made my time in his group incredibly rewarding. In addition his knowledge (or willingness to argue his point) about almost everything else has made it all rather fun! This project has taken me off the straight and narrow a bit (too much!) and so I owe an immense debt of gratitude to everyone I have collaborated with. Firstly, Prof. Dr. Joke Hadermann collected invaluable electron diffraction data, without which many of the structures in this work would never have been solved. Secondly, Dr. Andrew Goodwin spent countless hours working on RMC simulations for the structural models detailed in Chapter 7. Finally, I would like to thank all of the beam scientists and technicians at ISIS, Diamond and the ILL who have helped me; especially Dr. Ron Smith, Dr. Silvia Ramos and Dr. Emma Suard.

My DPhil would have been infinitely less enjoyable without all members of the Hayward Group past and present (‘*planto Hayward dum sol solis fulsi*’). Drs. Adkin, Parsons, Saratovsky put up with my endless questions at the start of my research and really ignited my interest in solid state chemistry. All the Part IIs in the group have always provided me with just the right amount of distraction when I have needed it. Special memories include: Stick Sports (‘06), Jeeves and IMFC (‘07), Tom Brady (‘08), the Goddess of Spontaneity (‘09) and educating Kun about British culture (‘10). In addition, my thanks go to all members of Team SJC (especially DRP) who have kept me company over the long and lonely summers.

My thanks also go to Team 93Fa and Team Weston XVI for keeping me sane through the medium of various manly activities; Tuesdays will never be as good again! Finally, my ultimate thanks have to go to my family (especially Hamish) for, well, everything!

Contents

Chapter 1: Introduction *1*

1.1. Perovskite structure **1**

1.2. Topotactic reduction **2**

1.3. Brownmillerite structure **3**

1.4. Brownmillerite structural variants **4**

1.4.1. Tetrahedral chain twisting 4

1.4.2. Possible structural variants 5

1.4.3. Explanation of the ordering of the twisted tetrahedral chains 7

1.4.3.1. Introduction 7

1.4.3.2. Dipole cancellation 8

1.4.3.3. Rationalisation of tetrahedral chain ordering scheme 8

1.4.3.4. 'Structure map' 9

1.5. Selectivity **11**

Chapter 2: Experimental Techniques *13*

2.1. Ceramic synthesis **13**

2.2. Hydride reductions **13**

2.2.1. General information 13

2.2.2. 'Pressure bomb' 15

2.2.3. Pressure-venting apparatus 16

2.2.4. Removal of unwanted by-products 17

2.3. Powder diffraction **17**

2.3.1. X-ray diffraction 18

2.3.1.1. Philips PW1710 diffractometer 19

2.3.1.2. PANalytical X'pert PRO diffractometer 20

2.3.2. Neutron diffraction 21

2.3.2.1. Institut Laue Langevin (ILL) 22

2.3.2.1.1. D2b 23

2.3.2.1.2. D1a 23

2.3.2.1.3. D1b 24

2.3.2.2. POLARIS at ISIS 25

2.3.3. Transmission Electron Microscopy (TEM) 26

2.3.3.1. General introduction 26

2.3.3.2. Introduction to TEM 26

2.3.3.3. Electron diffraction 26

2.3.3.4. HAADF-STEM 27

2.4. Structural analysis **28**

2.4.1. The Rietveld method 28

2.4.2. Peak shapes 29

2.4.2.1. Profile function 2 (constant wavelength data) 30

2.4.2.2. Profile function 3 (time-of-flight data) 31

2.5. Reverse Monte Carlo simulation **31**

2.5.1. Introduction 31

2.5.2. Pair Distribution Function (PDF) 32

2.5.3. Fitting the PDF 32

2.6. Bond valence sums **33**

2.7. DC SQUID magnetometry **34**

2.7.1. Curie-Weiss law 36

2.8. Thermogravimetric analysis (TGA) **36**

2.9. Iodometric titrations **37**

2.10. X-ray Absorption Near Edge Structure (XANES) spectroscopy 38
Chapter 3: Topotactic Reduction of $La_{0.33}Sr_{0.67}MnO_3$ 40
3.1. Introduction 40
3.2. Experimental 41
3.2.1. Synthesis of perovskite starting material 41
3.2.2. Low temperature reduction with metal hydrides 42
3.3. Results 42
3.3.1. X-ray diffraction data 42
3.3.2. Thermogravimetric analysis 44
3.3.3. Electron diffraction data 45
3.3.4. Neutron diffraction data 47
3.3.5. Disorder in electron diffraction data 51
3.3.6. Disorder in neutron diffraction data 52
3.3.7. Structural data 55
3.4. Discussion 57
3.4.1. Ambiguity in the empirical composition 58
3.4.2. Models accounting for observed partial disorder 59
3.4.1. Possible adoption of brownmillerite structure 61
3.4.2. Comparison to *RE*$Sr_2Cu_2GaO_7$ 63
3.5. Conclusion 63
Appendix 3 64
A. 3.1. (3+1)D crystallography 64
A. 3.1.1 Introduction 64
A. 3.1.2 Brownmillerite phases 64
A. 3.1.3 6-layer phases 67
Chapter 4: Reduction of $La_{1-x}Sr_xMnO_3$ ($0.6 \leq x \leq 0.75$) 69
4.1. Introduction 69
4.2. Experimental 70
4.2.1. Synthesis of perovskite starting materials 70
4.2.2. Low temperature reduction with metal hydrides 70
4.2.3. Annealing 71
4.3. Results 71
4.3.1. Thermogravimetric analysis ($0.6 \leq x \leq 1$) 71
4.3.2. X-ray diffraction data 72
4.3.3. Electron diffraction data ($0.6 \leq x \leq 0.83$) 73
4.3.4. Neutron diffraction data (x= 0.7 and 0.75) 74
4.3.5. Disorder in neutron diffraction data (x = 0.7 and 0.75) 76
4.4. Discussion 79
4.4.1. Introduction to ordering of the twisted tetrahedral chains 79
4.4.2. Rationalisation of ordering of the twisted tetrahedral chains 80
4.4.3. Disorder 82
4.4.4. Comparison to other anion vacancy ordered structures 83
4.4.4.1. Other m = 3 structures ($(La_{1/3}Ca_{2/3})_3Fe_3O_8$) 83
4.4.4.2. Comparison to m > 3 structures 84
4.4.4.3. Overall ordering scheme 86
4.4.5. 'Cooperative twist' theory 88
4.4.5.1. Introduction 88
4.4.5.2. Exceptions to 'cooperative twist' theory 91
4.4.5.3. Coordination sphere of the A-cation 93
4.4.5.4. Other perovskite-based structures 94
4.5. Structural conclusion 95
4.6. Magnetic properties of the '6-layer manganate' phases 96

4.6.1. Results ... 96
4.6.1.1. Magnetisation data ... 96
4.6.1.2. 5 K neutron diffraction data ... 98
4.6.1.3. Variable temperature neutron diffraction data ... 100
4.7. Discussion ... 102
4.7.1. Comparison to $La_{0.5}Sr_{0.5}MnO_{2.5}$ ... 102
4.7.2. Magnetic structure of the hypothetical Mn(III) '6-layer manganate' phase ... 104
4.7.3. Magnetic structure of '6-layer manganates' ... 105
4.7.3.1. Mixed valence ... 105
4.7.3.2. Twisted tetrahedral chains ... 106
4.7.3.3. Magnetic structure ... 107
4.7.3.4. Effect of Sr^{2+}-content on magnetic behaviour ... 108
4.8. Magnetic conclusion ... 108
Appendix 4 ... 109
Chapter 5: Characterisation of $La_{1-x}Sr_xMnO_{3-(0.5+x)/2}$ (x = 0.83, 0.9 and 1) ... 119
5.1. Introduction ... 119
5.2. Results ... 119
5.2.1. X-ray diffraction data ... 119
5.2.2. Neutron diffraction data ... 121
5.2.3. Structural refinement ... 122
5.2.3.1. $La_{0.17}Sr_{0.83}MnO_{2.33}$ ... 122
5.2.3.2. $La_{0.1}Sr_{0.9}MnO_{2.3}$ and $SrMnO_{2.25}$ ... 125
5.2.4. Imaging ... 126
5.2.4.1. Introduction ... 126
5.2.4.2. [102] direction ... 126
5.2.4.2.1. $La_{0.25}Sr_{0.75}MnO_{2.38}$ ... 126
5.2.4.2.2. Sr^{2+}-rich phases ... 127
5.2.4.3. Other directions ... 130
5.3. Discussion ... 130
5.3.1. Proposed Model ... 130
5.3.2. Explanation of Figure 5.10 ... 132
5.3.3. Explanation of Figure 5.12 ... 135
5.3.4. Proposed presence of twinning ... 136
5.3.5. Effect of Sr^{2+}-content on the structure ... 138
5.4. Conclusion ... 140
Appendix 5 ... 141
Chapter 6: $La_{0.4}Sr_{0.6}MnO_{3-y}$ and Conclusions Regarding the '6-layer Manganates' ... 143
6.1. Introduction ... 143
6.2. Results ... 143
6.2.1. Neutron diffraction data ... 143
6.2.2. Structural refinement ... 144
6.2.3. Electron diffraction data ... 146
6.3. Conclusions regarding '6-layer manganate' structure ... 149
6.3.1. Level of reduction ... 149
6.3.2. Structure of $La_{0.5}Sr_{0.5}MnO_{2.5}$ ... 151
Appendix 6 ... 152
Chapter 7: Reduction of $La_{1-x}Ca_xMnO_3$ ($0.6 \leq x \leq 1$) phases ... 153
7.1. Introduction ... 153
7.2. Experimental ... 154
7.2.1. Synthesis of perovskite starting materials ... 154
7.2.2. Low temperature reduction with metal hydrides ... 155

7.3. Results 155
7.3.1. X-ray diffraction data 155
7.3.2. Electron diffraction data 158
7.3.3. Neutron diffraction data 159
7.3.4. Structural Refinement (x = 0.6, 0.67 and 0.7) 160
7.3.5. Iodometric titrimitry 165
7.3.6. Thermogravimetric analysis 165
7.3.7. XANES spectroscopy 166
7.3.7.1. Experimental 166
7.3.7.2. Results 167
7.3.8. Local structure determination 168
7.3.8.1. Introduction 168
7.3.8.2. Pair Distribution Function 168
7.3.8.3. Reverse Monte Carlo Simulation 169
7.3.8.4. Results 171
7.3.8.5. Bond Lengths 174
7.3.9. Structure of $La_{0.2}Ca_{0.8}MnO_2$ 175
7.4. Discussion 177
7.4.1. Comparison to infinite-layer structure 178
7.4.2. '$Sr_{0.5}Mn_{0.5}O$' 179
7.4.3. Oxidation state 181
7.4.4. Structural conclusion 181
7.5. Magnetic properties of $La_{1-x}Ca_xMnO_2$ ($0.6 \leq x \leq 0.7$) 182
7.5.1. Introduction 182
7.5.2. Results 182
7.5.2.1. Magnetic susceptibility data 182
7.5.2.2. Neutron Diffraction Data 183
7.5.3. Discussion 185
Chapter 8: Topotactic Reduction of $Sr_3Fe_2O_5Cl_2$ 189
8.1. Introduction 189
8.2. Experimental 190
8.2.1. Synthesis of $Sr_3Fe_2O_5Cl_2$ 190
8.2.2. Low temperature reduction with metal hydrides 191
8.3. Results 192
8.3.1. Reactivity of $Sr_3Fe_2O_5Cl_2$ 192
8.3.2. Structural characterisation 193
8.3.2.1. X-ray diffraction data 193
8.3.2.2. Electron diffraction data 194
8.3.2.3. Neutron diffraction data 195
8.3.2.4. Iodometric titrimetry 198
8.3.3. Magnetic characterisation 198
8.4. Discussion 199
8.4.1. Magnetic behaviour 201
8.4.2. Structural selectivity 204
8.4.2.1. Selective removal of O(1) 204
8.4.2.2. Barrier to further reaction 206
8.4.2.3. Chemical selectivity 207
8.4.2.3.1. Strength of the Sr-Cl contacts 208
8.4.2.3.2. Lattice energy of the by-product 209
8.4.3. Sr_2FeO_3Cl formation 209
8.4.3.1. Possible reaction routes 210
8.4.3.2. Driving force 211
8.4.3.3. Relative stabilities of the oxychlorides 211

8.5. Conclusion **212**
Appendix 8 ..... **213**
Chapter 9: Topotactic Reduction of $Sr_3Fe_{2-x}Co_xO_5Cl_2$ ***214***
9.1. Introduction **214**
9.2. Experimental **217**
9.2.1. Preparation of $Sr_3Fe_{2-x}Co_xO_5Cl_2$ phases 217
9.2.2. Reduction of $Sr_3Fe_{2-x}Co_xO_5Cl_2$ phases 217
9.3. Results **218**
9.3.1. Reactivity of $Sr_3Fe_{2-x}Co_xO_5Cl_2$ 218
9.3.2. Structural refinement 219
9.3.2.1. Neutron diffraction data 219
9.3.2.2. Room temperature neutron diffraction data 219
9.3.3. Magnetic characterisation 222
9.4. Discussion **226**
9.4.1. Structural discussion 226
9.4.2. Magnetic discussion 228
9.4.2.1. Paramagnetic susceptibility data 229
9.4.2.2. Magnetic interactions 229
9.4.3. Comparison to $SrFe_{1-x}Co_xO_2$ ($x \leq 0.3$) 230
9.4.4. Comparison to high pressure $SrFeO_2$ and $Sr_3Fe_2O_5$ phases 231
9.5. Conclusion **233**
Appendix 9 ..... **233**
Chapter 10: Summary of Findings ***240***
10.1. Introduction **240**
10.2. Reduction of $La_{1-x}A_xMnO_3$ (A = Ca^{2+} and Sr^{2+}) Phases **240**
10.3. Selectivity **242**
Chapter 11: Bibliography ***244***

Chapter 1: Introduction

1.1. Perovskite structure

Complex transition metal oxides are an important class of material due to the wide range of electronic, magnetic, dielectric and transport properties they exhibit.[1, 2] Many of these interesting and useful properties are the result of strong electron-electron and electron-lattice correlations and couplings. These properties allow application of certain transition metal oxides in a wide range of technologies such as catalysis,[3] fuel cells,[4] and information process and storage technologies.[5, 6]

There has been great interest in transition metal oxides which adopt the perovskite structure with the general formula ABO_3 (where A = Group I, Group II metal or lanthanide and B = transition metal). The perfect cubic perovskite structure (shown in Figure 1.1) contains 12-coordinate A-cations and a 3D network of vertex-sharing BO_6 octahedra. $CaTiO_3$ crystallises in the eponymous perovskite structure but contains slight cooperative tilting of the TiO_6 octahedra which leads to a subtle distortion away from the perfect cubic perovskite structure (see Figure 1.1).

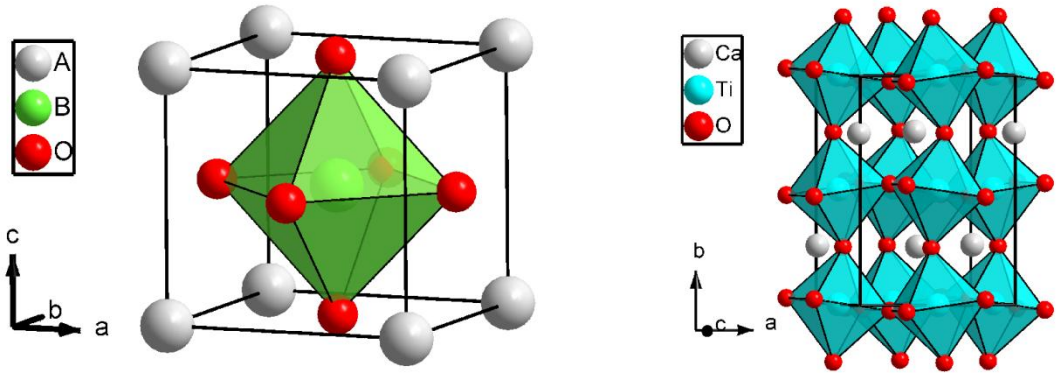


Figure 1.1: Perfect cubic perovskite structure (left) and structure of $CaTiO_3$ (right).

This cooperative distortion occurs to compensate for the mismatch in size of the constituent cations which can be quantified using the Goldschmidt tolerance factor:[7]

where and are the A-O and B-O bond lengths. When $t = 1$, in $SrTiO_3$ for example, the structure adopts the perfect cubic perovskite structure in which all the B-O-B bonds have a bond angle of 180°.[7] If $t > 1$, the material crystallises in a hexagonal arrangement, whereas, if $t < 1$, distorted cubic perovskite structures result in which cooperative distortions lower the B-O-B angle to less than 180°.[8]

One particular area of interest has been the formation of materials that adopt anion-deficient perovskite structures. The low anion content in these phases necessarily leads to a reduction of the transition metal centres compared to stoichiometric phases, which, when combined with the disruption in the metal-oxygen-metal framework caused by the anion vacancies, can lead to drastic changes in the magnetic and electronic properties of materials.[9] For instance, the superconducting temperature (T_c) of $YBa_2Cu_3O_{7-\delta}$ can be increased from 0 K to 90 K depending on the concentration and location of these anion vacancies.[6]

1.2. Topotactic reduction

Typical synthetic techniques used to form complex transition metal oxides, including anion-deficient phases, employ high temperatures to overcome the large energetic barriers which limit the diffusion of ions in the solid state. Inevitably, this results in the formation of thermodynamically stable materials in which the ions adopt positions so as to minimise the free-energy of the system. This results in only a limited set of oxidation states and coordination environments being available for study. However, by utilising kinetically controlled reactions, a wide range of metastable anion-deficient phases can be formed which cannot be synthesised using reactions under thermodynamic control.

Kinetically controlled reactions take advantage of differing reactivities within a system, of which there are many that can be exploited. However one of the most useful reactivities, with respect to the formation of anion-deficient phases, is the greater mobility of the anion sub-

lattice compared to that of the cation sub-lattice. This difference in mobility allows the anion sublattice to be manipulated at temperatures below the point at which the cation sublattice becomes mobile. By the use of a suitable topotactic reducing agent, oxide anions can be removed from the structure while leaving the cation framework intact (topotactic reduction), resulting in the formation of metastable anion-deficient phases.

1.3. Brownmillerite structure

The flexibility in the ABO_3 perovskite structure described in section 1.1 makes it remarkably tolerant to oxide vacancies. It is therefore unsurprising that a large number of anion-deficient perovskite phases can be prepared.[10] The majority of ABO_{3-y} anion-vacancy ordered phases can be constructed by the stacking of distinct layers of BO_n polyhedra. This segregation into distinct polyhedral layers is favoured due to the mismatch in bond lengths in different BO_n polyhedra. One of the most common anion-deficient perovskite structures is that adopted by the mineral Brownmillerite (Ca_2AlFeO_5).[11]

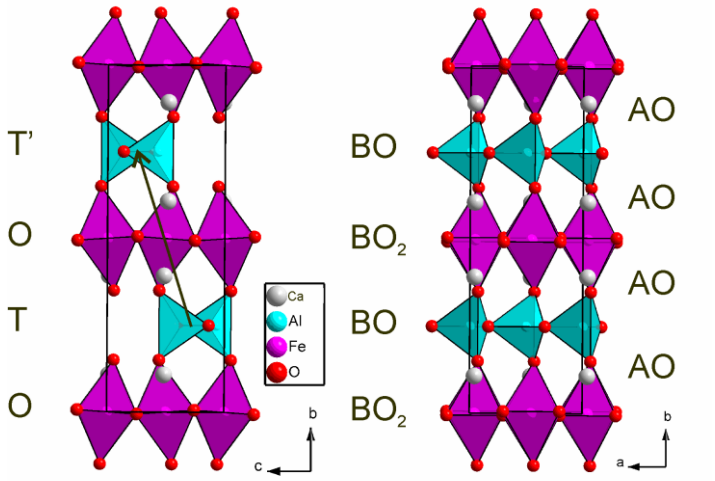


Figure 1.2: 2 views of the brownmillerite structure of Ca_2AlFeO_5. The arrow represents the ½[111] shift vector relating the chains of tetrahedra in different layers.

As shown in Figure 1.2, the brownmillerite structure consists of layers of BO_6 octahedra (O) and BO_4 tetrahedra (T) stacked in an OTOT' sequence. The prime denotes the fact that the tetrahedral layers are stacked in a staggered manner up the *b*-axis, i.e. the tetrahedral chains are related by a ½[111] shift vector.

The brownmillerite structure is related to the fully anion-stoichiometric ABO_3 cubic perovskite structure by the removal of half the anions from alternate BO_2 layers to form an -AO-BO_2-AO-BO- stacking sequence up the *b*-axis (see Figure 1.2). The anion vacancies are arranged within the BO layer in an ordered manner to form chains parallel to the $[101]_p$ direction of the simple cubic perovskite unit cell. The resulting layers consist of chains of apex-linked tetrahedra running parallel to the $[101]_p$ direction (see Figure 1.3).

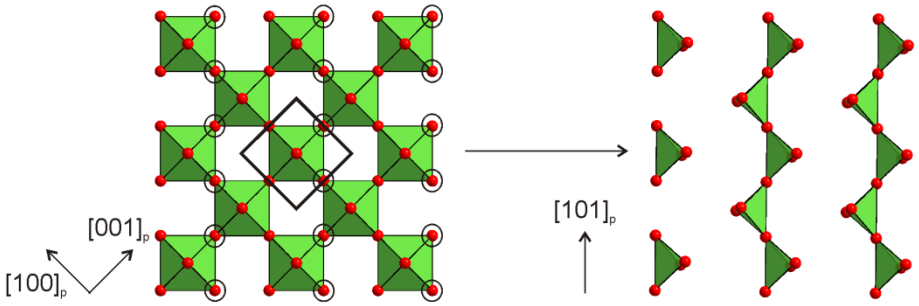


Figure 1.3: Formation of tetrahedral chains from the perfect cubic perovskite structure. The unit cell of the simple cubic perovskite unit cell is shown on the structure on the left.

1.4. Brownmillerite structural variants

1.4.1. Tetrahedral chain twisting

As shown in Figure 1.2, the BO_4 tetrahedra and BO_6 octahedra in the brownmillerite structure are distorted away from those found in the ideal cubic perovskite structure. The structural distortions can be attributed to the mismatch in the bonding requirements of the A- and B-cations. This mismatch results in the tilting of the BO_6 octahedra and twisting of the chains of BO_4 tetrahedra in the brownmillerite structure.

The cooperative twisting of the tetrahedral chains in the brownmillerite structure can occur in either a clockwise or an anti-clockwise sense. This leads to the formation of 2 types of twisted tetrahedral chains (arbitrarily labelled R and L - Figure 1.4)[12-15] which are related by 180^o rotation symmetry:

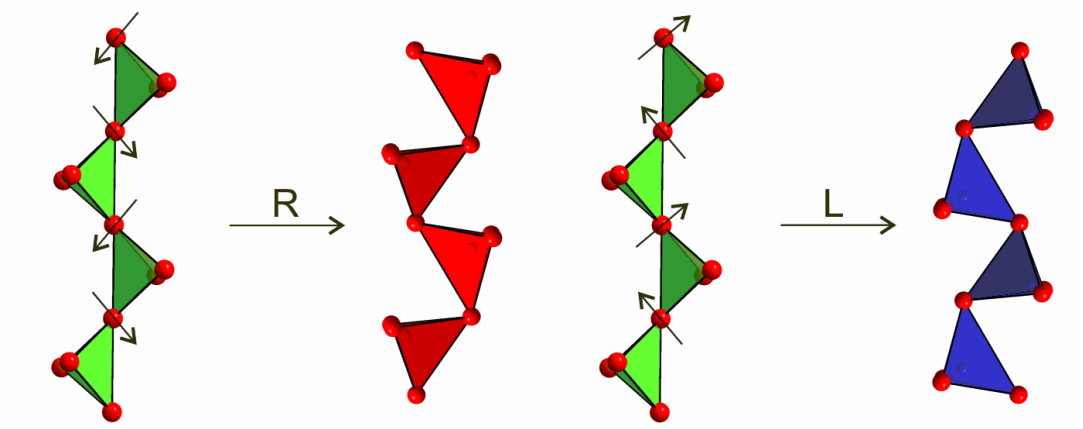


Figure 1.4: Formation of R and L twisted tetrahedral chains

1.4.2. Possible structural variants

The 3D arrangement of the twisted tetrahedral chains within the brownmillerite structure gives rise to a large number of distinct structural variants, the simplest 5 of which are shown in Figure 1.5 and briefly described in the following paragraphs.

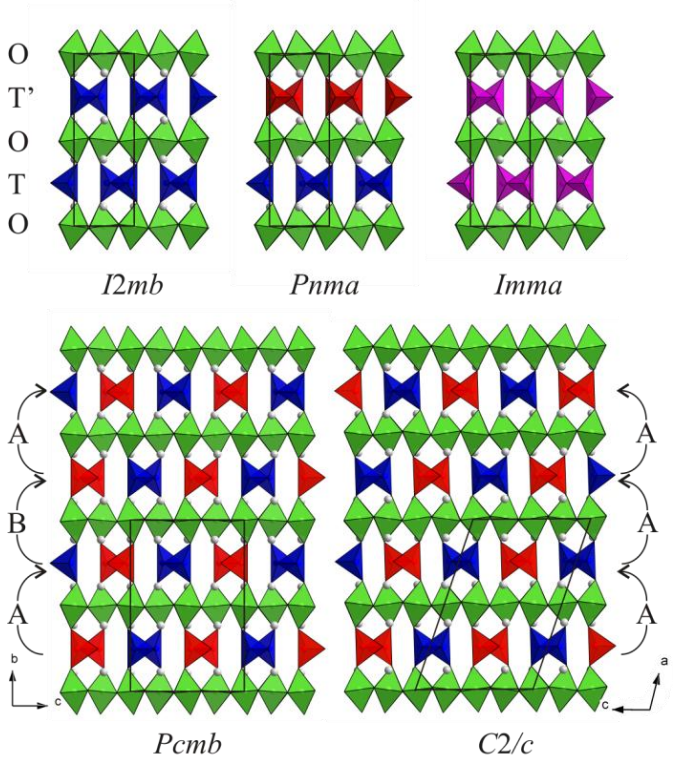


Figure 1.5: The 5 simplest arrangements of the twisted tetrahedral chains in the brownmillerite structure and their respective space groups. The red and the blue chains denote the R and L twisted chains respectively. A and B represent the vectors used to describe the relationship between tetrahedral chains with the same twisting direction in the intralayer ordered variants: A = ½[111] and B = ½[11$\bar{1}$].

All of the tetrahedral chains are twisted in the same manner (i.e. all L or all R) in the model described with *I2mb* symmetry (defined as intralayer non-ordered in this

investigation). The model described with *Pnma* symmetry has all the tetrahedral chains in the same layer twisted in the same direction, however, the twist direction changes between alternate layers (interlayer order).

The L and R chains can also order in a 1:1 alternating arrangement within each tetrahedral layer (i.e. -L-R-L-R-). As shown in Figure 1.5, these so-called intralayer ordered layers can then be stacked in one of two ways: either with a stacking vector of ½[111] which displaces the entire tetrahedral layer to the left of the original layer (type A stacking), or with a stacking vector of ½[11$\bar{1}$] which displaces the entire tetrahedral layer to the right of the original layer (type B stacking).[16, 17] As shown in Figure 1.5, the simplest methods for stacking these layers are in an ABAB fashion (as in the model described with *Pcmb* symmetry) or in an AAAA fashion (as in the model described with *C*2/*c* symmetry). However, additional variants exist with more complex stacking arrangements of the -L-R-L-R- ordered layers (e.g. AABA, etc.).[16]

In addition, there can be a disordered arrangement of L and R chains. This variant can be described using the *Imma* space group and a $\sqrt{2}a_p$ x $4a_p$ x $\sqrt{2}a_p$ expanded unit cell. To account for the disorder in the arrangement of the L and R chains, the tetrahedral transition metal and tetrahedral equatorial oxide ion sites are split to generate the superposition of both types of twisted tetrahedral chains, as shown in Figure 1.6.

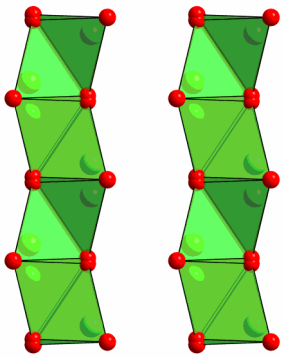


Figure 1.6: The atomic positions in the tetrahedral layers of the *Imma* brownmillerite structural variant

1.4.3. Explanation of the ordering of the twisted tetrahedral chains

1.4.3.1. Introduction

A large amount of research has focussed on understanding why different ordering schemes of the twisted chains of tetrahedra within the brownmillerite structure are adopted by different phases.[13, 14, 17] Abakumov *et al.* proposed a model based on the stabilisation of the dipole moments generated by the twisting of the tetrahedral chains.[12] As shown in Figure 1.7, each B-O bond in the BO_4 tetrahedra possesses a dipole moment (represented by the black arrows in Figure 1.7) due to the difference in electronegativity between the 2 elements. In an undistorted tetrahedral chain (green chain in Figure 1.7), the dipoles from neighbouring tetrahedra cancel and there is no net dipole moment along the chain. However, the twisting of the tetrahedral chains (red and blue chains in Figure 1.7) leads to imperfect cancellation of the B-O dipole moments, leading to a net dipole moment parallel to the tetrahedral chain propagation direction. The R and L twisted tetrahedral chains contain net dipole moments that are anti-parallel but equal in magnitude.

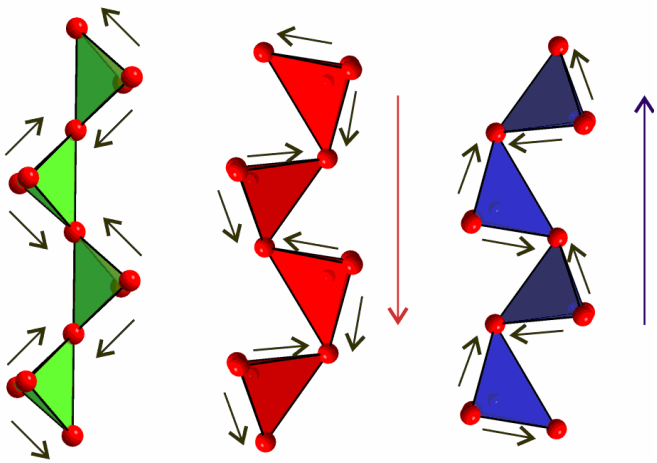


Figure 1.7: The dipole moments of the Mn-O bonds (black arrows) in the MnO layer, shown in the undistorted tetrahedral chains (left) and the R (middle) and L (right) twisted chains. The blue and the red arrows represent the direction of the net dipole moment in the twisted tetrahedral chains.

More recently, Parsons *et al.* published a modified and extended rationalisation based on similar logic.[17] A brief summary of the aspects of this combined research relevant to this project is presented in the following sections.

1.4.3.2. Dipole cancellation

Each arrangement of the twisted tetrahedral chains uses a different dipole cancellation mechanism to stabilise the structure:

1. Polar microdomain formation. The *I*2*mb* variant of the brownmillerite structure has all the tetrahedral chains twisted in the same direction, and is thus polar. These materials are predicted to crystallise with small polar domains aligned with anti-parallel polarization vectors in neighbouring domains to allow macroscopic dipole cancellation.[13]
2. 'Interlayer' cancelation. In the *Pnma* structural variant, all the tetrahedral chains in a particular tetrahedral layer are twisted in the same direction, with the twist direction inverting between adjacent layers. Therefore dipoles are cancelled between neighbouring layers.[18]
3. 'Intralayer' cancellation. In the *Pcmb* and *C*2/*c* variants the chains within each tetrahedral layer adopt an alternating -L-R-L-R- arrangement, allowing dipole cancellation within each layer.[17]

1.4.3.3. Rationalisation of tetrahedral chain ordering scheme

The adoption of the different tetrahedral ordering schemes in the $A_2B_2O_5$ brownmillerite phases has been justified on the basis of 2 competing factors: the efficiency of the dipole cancellation mechanism and the structural disruption associated with the adoption of each tetrahedral chain ordering scheme.[17] The efficiency of the dipole cancellation mechanisms associated with the tetrahedral chain ordering schemes in the $A_2B_2O_5$ brownmillerite phases follows the order: intralayer ordered (*Pcmb* or *C*2/*c* variants) > interlayer ordered (*Pnma* variant) > 'non-ordered' (*I*2*mb* variant).[17] In addition, the degree of structural disruption associated with the adoption of each ordering arrangement is thought to follow the same

order.[17] Thus, the adoption of the tetrahedral chain ordering scheme depends on the interplay of these 2 factors.

1.4.3.4. 'Structure map'

Two specific structural parameters can be used to rationalise the trends in the ordering of the twisted tetrahedral chains:[14, 17]

1. The degree of twisting in the tetrahedral chains which can be quantified using the departure of the O-O-O angle in the BO layer away from 180^{o} (see Figure 1.8 (a)). This angle is proportional to tetrahedral chain dipole moment.
2. The separation between neighbouring tetrahedral layers (see Figure 1.8(b)).

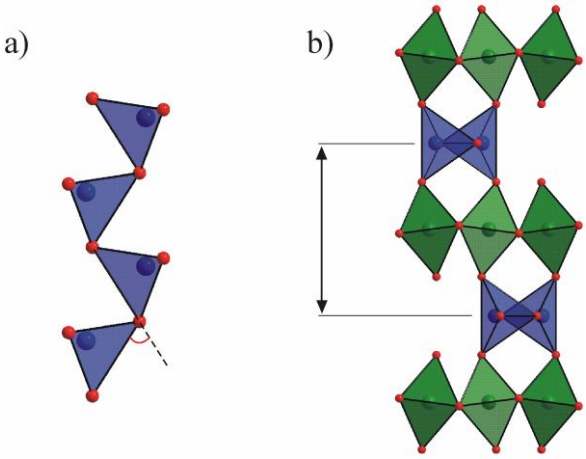


Figure 1.8: a) Tetrahedral twist angle and b) tetrahedral layer separation in the brownmillerite structure.[17]

Parsons *et al.* published a 'structure map' of the different brownmillerite structural variants by plotting the tetrahedral layer separation against the distortion angle in the tetrahedral chains of a large number of known brownmillerite phases (see Figure 1.9).[17]

As shown in Figure 1.9, the brownmillerite phases containing tetrahedral chains with a small distortion angle, and correspondingly small dipole moments, adopt the *I*2*mb* structural variant in which all the tetrahedral chains are twisted in the same direction. These materials are stabilised by the formation of polar microdomains, which cancel the net dipole of the structure. As the distortion angle of the tetrahedral chains increases in the brownmillerite phases, the polar microdomain formation mechanism is insufficient to stabilise the larger

dipole moments. Therefore, the brownmillerite phases have to adopt variants which contain ordered arrangements of the twisted tetrahedral chains which allow more efficient dipole cancellation but also incur greater structural disruption (i.e. the ordered interlayer (*Pnma* variant) and the ordered intralayer (Pcmb and *C*2/*c* variants)).

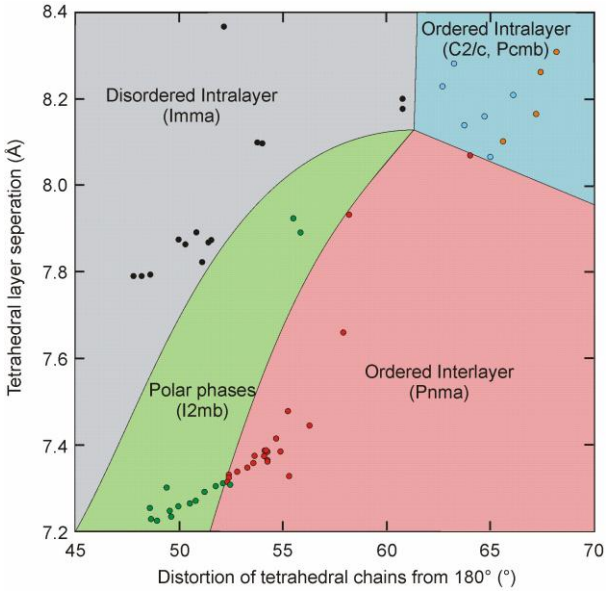


Figure 1.9: 'Structure map' of brownmillerite structural variants as a function of tetrahedral layer separation and tetrahedral chains twist angle.[17]

When the tetrahedral layer separation is relatively small (i.e. below 8 Å), the interlayer dipole mechanism can be used to stabilise the *Pnma* structural variant in which neighbouring tetrahedral layers contain oppositely twisted chains. However, when the distortion angle is large (i.e. above 62^{o}) and the tetrahedral layer separation is large (i.e. above 8 Å), only the intralayer arrangement (-L-R-L-R-) of the twisted tetrahedral chains provides an efficient enough mechanism to stabilise the structure. Therefore, despite the large structural disruption caused by the adoption of intralayer ordered arrangement of twisted tetrahedral chains, these brownmillerite phases adopt the *Pcmb* and *C*2/*c* structural variants.

Previous work has shown that the topotactic reduction reactions of phases in the compositional range $La_{1-x}A_xMnO_3$ ($0.2 \leq x \leq 0.5$; A = Ca^{2+}, Sr^{2+} or Ba^{2+}) results in the formation of series of reduced phases with empirical compositions of $La_{1-x}A_xMnO_{2.5}$ which adopt the $A_2B_2O_5$ brownmillerite structure (see Figure 1.2).[17, 19-21] These $La_{1-x}A_xMnO_{2.5}$

materials contain manganese centres with an average oxidation state of between +2.2 and +2.5. Neutron and electron diffraction studies reveal that a complex interplay between A-cation size and manganese oxidation state results in the selective adoption of the different tetrahedral chain ordering schemes detailed in section 1.4.2.[17] In addition, the magnetic properties exhibited by these $La_{1-x}A_xMnO_{2.5}$ brownmillerite phases are highly dependent on the average manganese oxidation state.[22]

Therefore, to allow comparison to the La^{3+}-rich brownmillerite phases, the topotactic reduction reactions of phases in the compositional ranges $La_{1-x}Sr_xMnO_3$ ($x \geq 0.5$ - see Chapters 3-6) and $La_{1-x}Ca_xMnO_3$ ($x > 0.5$ – see Chapter 7) were performed. These reactions are predicted to form brownmillerite phases containing manganese centres with average oxidation states above +2.5, thereby allowing further study of the effect of the average manganese oxidation state on the magnetic and electronic properties of the materials. In addition, these new phases may allow the extension of the 'structure map' of the brownmillerite structural variants published by Parsons *et al*.[17]

1.5. Selectivity

In order to reap the full benefit of topotactic reduction reactions and achieve a situation where the directed synthesis of target anion-deficient phases is possible, it is necessary to control which of the various anions in a substrate phase are removed and how the resulting anion vacancies order. One strategy to exert such control over topotactic reduction reactions utilizes the strong interaction between the anion and cation lattices in complex oxides to direct the progress and products of anion deintercalation reactions. For example, the reduction of the isostructural and isoelectronic A-cation ordered phases $YBaCo_2O_5$ and $LaBaCo_2O_5$ with NaH yields $YBaCo_2O_{4.5}$ and $LaBaCo_2O_{4.25}$, respectively.[9] These two reduced phases have different anion contents and anion vacancy ordering patterns, despite

starting from isostructural substrate phases, demonstrating the directing influence, based on size, of the yttrium and lanthanum cations.

Furthermore, the B-site composition of the substrate phase has been shown to have an effect on the selectivity of topotactic reduction reactions. For instance, the topotactic reduction reactions of the n = 2 Ruddlesden Popper $Sr_3Mn_2O_{7-\delta}$ and $Sr_3Fe_2O_{7-\delta}$ phases proceed with the removal of oxide anions from different sites to form $Sr_3Mn_2O_{6+\delta}$[23] and $Sr_3Fe_2O_6$,[24] respectively (see Figure 1.10). The formation of $Sr_3Mn_2O_{6+\delta}$ and $Sr_3Fe_2O_6$ proceed with the removal of oxide ions from the equatorial sites of the $MnO_{6-\delta}$ polyhedra and terminal axial sites of the $FeO_{6-\delta}$ polyhedra respectively.

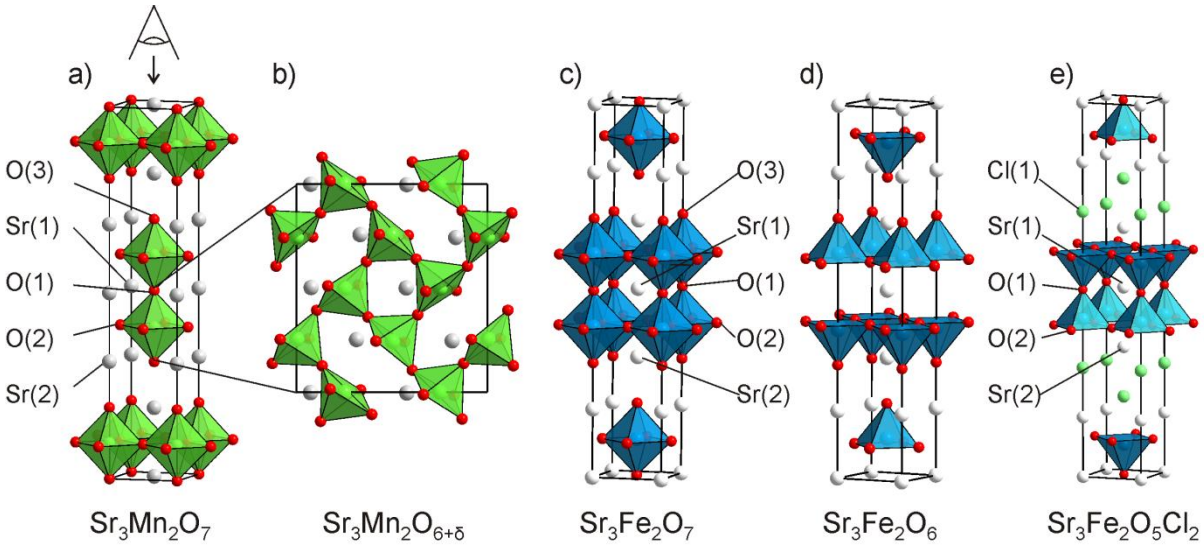


Figure 1.10: Structures of some n = 2 Ruddlesden Popper phases and their anion-deficient relatives. Reduction reactions of $Sr_3Mn_2O_{7-\delta}$ and $Sr_3Fe_2O_{7-\delta}$ proceed with the removal of the O(2) and O(1) anion respectively sites to form $Sr_3Mn_2O_{6+\delta}$ and $Sr_3Fe_2O_6$. Figure b) shows a single layer of the structure of $Sr_3Mn_2O_{6+\delta}$ which is rotated by 90° relative to that in $Sr_3Mn_2O_7$ (i.e. it is viewed down the direction highlighted by the 'eye' in a)).

In contrast, there has been relatively little study of the directing influences of heteroanions on the progress of topotactic reductions in mixed anion solids. As shown in Figure 1.10, $Sr_3Fe_2O_5Cl_2$ adopts an n = 2 Ruddlesden Popper structure based on $Sr_3Fe_2O_7$ but the terminal apical oxygen position (O(3)) of the repeat perovskite block has been replaced by a chloride ion (Cl(1)).[25] Therefore, to allow comparison to the topotactic reduction reaction of $Sr_3Fe_2O_7$, the reduction of $Sr_3Fe_2O_5Cl_2$ was performed.

Chapter 2: Experimental Techniques

2.1. Ceramic synthesis

During the course of this investigation, standard ceramic techniques were used to synthesise thermodynamically stable solids. Exact synthetic details for each phase are included in the appropriate chapter. However, the basic procedure involved thoroughly grinding together stoichiometric quantities of the appropriate starting materials (metal oxides, carbonates or chlorides) in an agate pestle and mortar to ensure good mixing of the materials. Then the samples were pressed into 2 g pellets (to minimise the required diffusion length within the solid) and heated to high temperatures (to overcome the large activation barrier to ionic diffusion within solids). After each firing, the samples were thoroughly reground (to ensure sample homogeneity) and re-pressed into pellets. When metal carbonates were used as starting materials, the samples were initially fired for 24 hours in an alumina crucible at 900 ^{o}C to decompose the starting materials, before being heated at the required reaction temperature. The reactions were considered complete when X-ray powder diffraction patterns collected from products after successive firings showed no change.

2.2. Hydride reductions

2.2.1. General information

Recent work has shown that binary metal hydrides (namely NaH, CaH_2 and LiH) can be used to extract oxide ions at relatively low temperatures (200 ^{o}C to 550 ^{o}C) from a wide range of materials to form metastable anion-deficient phases.[26-28] Reduction of a generic ABO_3 perovskite phase using NaH can be described as follows:

The ease with which the sodium-containing by-products can be removed from the sample (see section 2.2.4) and the lack of H_2 gas production during the reaction meant that NaH was used as the reducing agent whenever possible in this investigation.

However, the low decomposition temperature of NaH placed an upper limit on the possible reaction temperatures (~ 250 ^{o}C) and reactions involving several substrates were found to require higher temperatures to overcome the activation barrier for the reaction. When this is the case, CaH_2 can be used as a topotactic reducing agent at reaction temperatures up to 600 ^{o}C,[27] with the general equation shown below:

In addition, work by Adkin *et al*. has shown that LiH can also be used as a topotactic reducing agent at ~ 400 ^{o}C:[28]

The hydride reducing agents are kept in an argon-filled glovebox (O_2 and H_2O < 1 ppm) due to their air- and moisture-sensitive nature. In addition, any mixtures containing these reagents were kept under an inert atmosphere at all times. The substrate to be reduced was typically ground with 2 stoichiometric equivalents of the appropriate binary metal hydride reducing agent in an argon-filled glovebox and sealed under vacuum in a glass ampoule. The sample was then heated to the desired temperature at a ramp rate of 1 ^{o}C min^{-1} to ensure that the temperature of the furnace did not over-shoot the relatively low target temperature of the reactions. After the desired time period, typically 24 hours, the ampoules were opened in a glovebox and the sample reground. This procedure was repeated until the reaction was judged complete with the progress of the reaction monitored using X-ray powder diffraction.

The exothermic nature of the reduction reactions meant that, when preparing large-scale samples (e.g. samples suitable for characterisation by neutron powder diffraction), the samples were heated at 30 ^{o}C below the target temperature for the first heating cycle to prevent the sample temperature exceeding the target temperature.

Due to the hazards associated with the production of H_2 gas as a by-product when using LiH or CaH_2 as reducing agents,[27, 29] large-scale samples had to be prepared using alternative techniques which are detailed in the following sections.

2.2.2. 'Pressure bomb'

The 'pressure bomb' setup consists of a Parr Series 4740 Pressure Vessel (see Figure 2.1) which is capable of withstanding pressures up to 128 bar, far in excess of pressures generated in this investigation. Inside an argon-filled glovebox, the substrate was ground with the appropriate binary metal hydride reducing agent and then transferred into an alumina finger and fitted with a loose glass lid to prevent sample contamination.

This set-up was then placed in a steel vessel and the vessel fitted with a screw cap housing 6 bolts which compress a gasket containing a graphite O-ring. The screw cap was then connected to a gauge block assembly using a coned pressure fitting. The combination of the graphite O-ring and the coned pressure fitting allow the formation of an air-tight seal. The system was then closed to the atmosphere using the valve on the gauge block assembly.

Outside of the glovebox, the compression blots were tightened with a torque of 13.5 Nm in a criss-cross pattern (to ensure an even pressure on the graphite seal) and then a torque of 20.3 Nm. Next the system was connected to a 3-way tap which is connected to a vacuum pump and an argon supply.

The system was then evacuated, purged with argon and then evacuated once more. Next the valve on the gauge block assembly was opened and the sample environment held under vacuum for 10 minutes. Finally, the valve on the gauge block was sealed, thus holding the sample under a 'static' vacuum, and the entire vessel heated to the target reaction temperature. These experimental conditions replicate those used to synthesise small scale samples, i.e. sealed silica ampoules.

After the desired time period, the vessel was disconnected from the 3-way tap and passed into the glovebox where the sample could be retrieved.

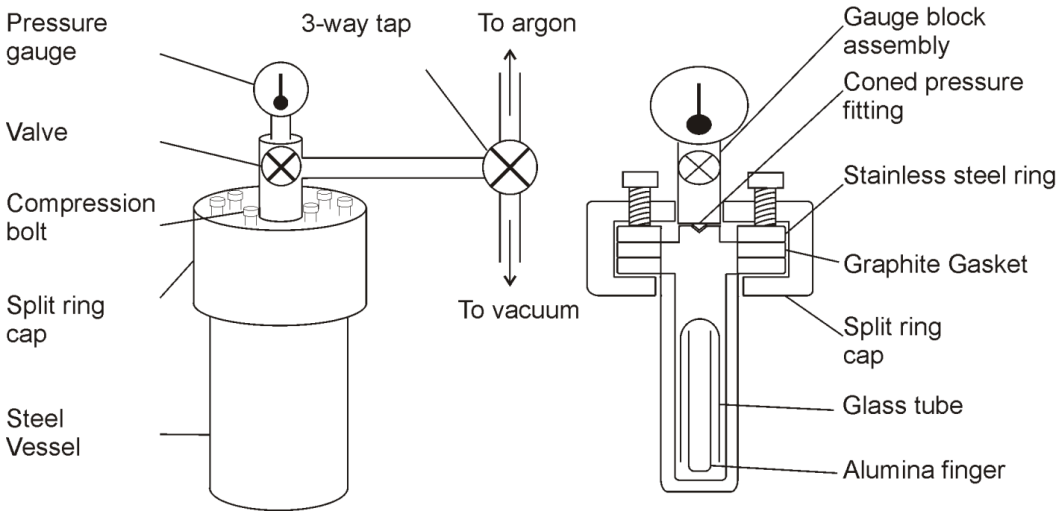


Figure 2.1: 'Pressure bomb' (left) and slice through 'pressure bomb' (right).

2.2.3. Pressure-venting apparatus

As described above, the starting material and hydride were ground together in a glovebox before being placed in an alumina boat. The boat was then placed inside a large silica tube and closed with a steel endcap by the use of a rubber O-ring. The tube and end-cap are then connected to the pressure venting apparatus as shown in Figure 2.2.

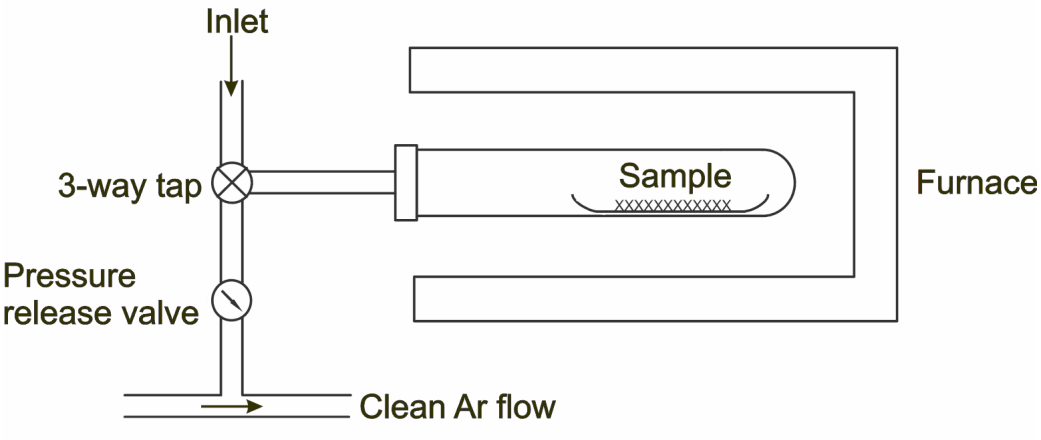


Figure 2.2: 'Pressure-venting' system

The glass tube was heated to the desired reaction temperature. After the desired time period, the apparatus was cooled and the 3-way tap closed. The tube could then be evacuated and passed into the glovebox.

2.2.4. Removal of unwanted by-products

The reduction reactions were considered complete when X-ray powder diffraction patterns collected from products after successive heating cycles showed no change. Once this was the case, the products were washed using a suitable solvent to remove unwanted materials (i.e. NaOH, Li_2O or CaO by-products or unreacted metal hydrides). When using NaH or LiH as the reducing agent, the unwanted materials were removed by washing with 4 x 100 mL of CH_3OH. However, CaO is insoluble in CH_3OH, therefore to remove the CaO, the reaction mixture was initially washed with 6 x 100 mL of 0.1 M solution of NH_4Cl in CH_3OH. The mixture was then washed with CH_3OH to remove any unwanted NH_4Cl.

The washing procedures were all carried out under nitrogen using standard Schlenk line techniques. Finally the sample was dried under vacuum before passing it into a glovebox.

2.3. Powder diffraction

Powder diffraction techniques are the most widespread structural characterisation method used in solid state chemistry. X-ray, neutron and electron diffraction data sets formed a key part of the elucidation of the structures detailed within this investigation. The theory of diffraction is well-studied but beyond the scope of this thesis, however a basic introduction will be covered in the following section.

Figure 2.3 demonstrates that when a beam of X-rays is directed towards a regular array of lattice planes (i.e. a crystalline solid), where the wavelength of the incident radiation is similar to the spacing between the lattice planes, diffraction occurs according to Bragg's law:

where λ is the wavelength of the incident beam, d_{hkl} is the interplanar distance and θ is the angle made by the incident beam to the appropriate lattice plane.

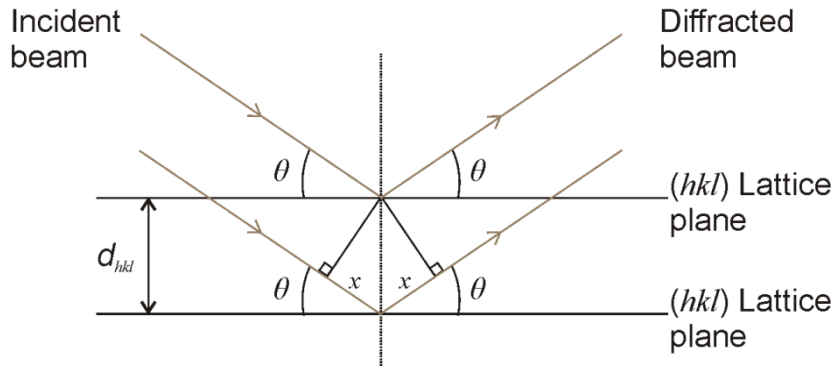


Figure 2.3: Cartoon showing Bragg's approach to diffraction

Whilst the unit cell dimensions define the *d*-spacing (d_{hkl}) of a given reflection, the intensity of said reflection (I_{hkl}) is given by the following relationship:

where L is the sample-independent Lorentz-polarisation function, m is the reflection multiplicity, A is the absorption factor and F_{hkl} is the structure factor.

The structure factor governs how the intensity of a given diffraction reflection depends on the arrangement of atoms in the unit cell:

where f_n is the atomic scattering factor and x_n, y_n and z_n are the fractional coordinates of the n^{th} atom in the unit cell. The exponential term including the atomic isotropic thermal factors (U_{iso_n}) determines the magnitude of the reduction in intensity as a function of scattering angle. It should be noted that at certain points in this investigation, anisotropic thermal factors were used.

2.3.1. X-ray diffraction

As stated above, powder diffraction techniques are of great utility to structural characterisation. In contrast to other widely used powder diffraction techniques, X-ray diffraction is routinely used to characterise structures due to the ready availability of sources of monochromatic X-rays. The atomic scattering factor (f_n) of an atom is related to its atomic

number (Z_n). For this reason, the diffracted intensity from a structure is relatively insensitive to changes in the fractional occupancy or positional coordinates of atomic sites filled with light elements in the presence of relatively heavy elements. Therefore complete elucidation of structures containing a combination of light and heavy elements (e.g. the majority of the complex transition metal oxides and oxychlorides detailed in this investigation) using X-ray powder diffraction data is not always possible.

2.3.1.1. Philips PW1710 diffractometer

Data collected using the Philips diffractometer were routinely used to monitor reaction progress. The diffractometer operates in Bragg-Brentano focussing geometry and uses both Cu $K\alpha_1$ and $K\alpha_2$ incident radiation. Data were collected from samples judged to be non-air-sensitive on an aluminium plate. The sample was loaded into a recess in the plate measuring 20 mm x 10 mm x 0.5 mm. As a result, additional diffraction reflections attributable to the aluminium sample holder were present in the patterns. Furthermore, diffraction data often showed intensity variation due to preferred orientation of the crystallites within the sample. When these features prevented structural characterisation, diffraction data were collected from samples placed on a glass slide coated with a small amount of Dow-Corning high vacuum grease. Measurements were taken over the range $3\ ^{o} < 2\theta < 70\ ^{o}$ with a continuous scan at a speed of $0.04\ ^{o}\ 2\theta\ s^{-1}$.

When X-ray powder diffraction patterns had to be collected from air-sensitive samples, the samples were loaded into air-tight sample holders (see Figure 2.4) in an argon-filled glovebox. The samples were loaded onto a glass slide coated with a small amount of Dow-Corning high vacuum grease, which was then placed in an aluminium holder which contained a thin Mylar window (see Figure 2.4) and sealed with a rubber O-ring and brass cap. The data were collected over the range $10\ ^{o} < 2\theta < 70\ ^{o}$ using a continuous scan at a speed of

0.02 ^{o} 2θ s^{-1}. The slower scan rate relative to that used to collect data from air-stable materials compensates for the loss of intensity due to absorption of X-rays by the Mylar window.

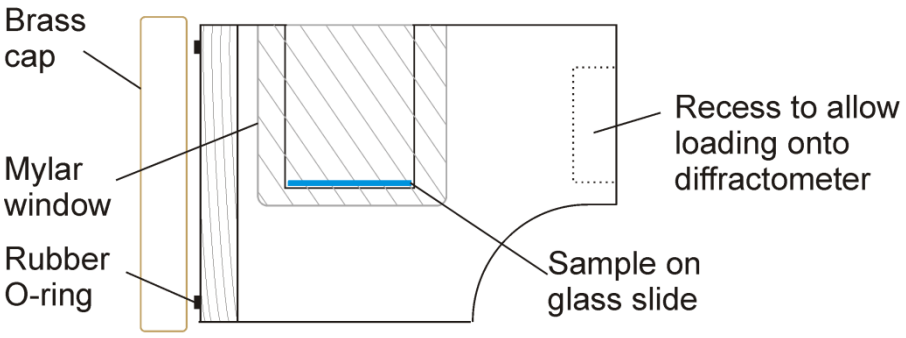


Figure 2.4: Sample holder for collecting X-ray powder diffraction patterns from air-sensitive samples.

2.3.1.2. PANalytical X'pert PRO diffractometer

The X'pert diffractometer was used to obtain high quality data sets suitable for structural refinement. The machine operates using Bragg-Brentano focussing geometry and utilises a crystal monochromator to exclusively select Cu Kα_1 radiation. In addition, 0.02 mm Soller slits were added into both the incident and diffracted beam paths to further collimate the beams. These 2 features combine to allow very high resolution diffraction patterns to be obtained.

Non-air-sensitive samples were loaded onto a silicon wafer coated with a thin layer of Dow-Corning high vacuum grease. This silicon wafer is cleaved along the [110] plane which is systematically absent with respect to diffraction, to ensure no reflections from the wafer are present in the diffraction pattern. The data were collected over the range 3 ^{o} < 2θ < 70 ^{o} with a continuous scan speed of 0.006 ^{o} 2θ s^{-1}. During the course of the measurement the silicon wafer was rotated at 30 rpm to minimise the effect of any non-uniformity in the sample distribution.

Data sets were collected from air-sensitive samples using the same sample holder as described in section 2.3.1.1. The data were collected from 10 ^{o} < 2θ < 70 ^{o} with a continuous scan at a speed of 0.006 ^{o} 2θ s^{-1}.

2.3.2. Neutron diffraction

Neutron powder diffraction is incredibly useful as a complementary technique to X-ray powder diffraction. Whereas X-rays are scattered by the periodic electron density of a crystalline solid, neutrons are scattered by an interaction with atomic nuclei. As a result, neutron diffraction differs from X-ray diffraction in a several ways:

- There is no linear relationship between the neutron scattering length of an atom and its atomic number.[30] Indeed, the neutron scattering lengths of all atoms are much more similar than the X-ray scattering lengths.[30] There is therefore typically (although notable exceptions do exist) a much more even contribution to the total scattering from the structure from its constituent elements. Consequently, neutron diffraction data can usually be used to locate light atoms in the presence of much heavier elements and atoms of similar atomic weights can typically be distinguished.
- Secondly, while the X-ray scattering form factor drops off rapidly as the angle at which scattering occurs increases, the neutron form factor can be regarded as independent of the scattering angle. Therefore, in contrast to X-ray diffraction data, there is no fall-off in the intensity of diffraction reflections with increasing angle.
- Thirdly, the neutron scattering interaction is relatively weak. Therefore, relatively large sample sizes are required for most neutron diffraction experiments (2 g – 4 g) whereas X-ray diffraction experiments require samples on the mg scale.
- Finally, neutrons are spin-1/2 particles which can interact with unpaired electrons. Scattering from an ordered array of electron spins gives rise to magnetic reflections in the diffraction pattern, thereby allowing the determination of magnetic structures in the material.

The magnetic scattering structure factor ( ), for an unpolarised neutron source, can be expressed as follows:

where $\boldsymbol{q}_j$ is the magnetic interaction vector, p_j the magnetic scattering length, $\boldsymbol{h}$ the magnetic scattering vector and $\boldsymbol{x}_j$ the position vector of magnetic atom within the unit cell. The observed intensity of a magnetic reflection ($I_{mag,hkl}$) is proportional to the square of the projection of the magnetic structure factor onto the scattering vector:

where α is the angle between the magnetic scattering structure vector and the relevant lattice plane.

For all neutron powder diffraction experiments, the samples were sealed in vanadium cans (as vanadium has a very low coherent neutron scattering length (-0.3824 fm))[30] under an argon atmosphere (due to the air-sensitive nature of all samples measured using neutron diffraction in this investigation). These cans were sealed with either indium washers for measurements in the range 5 < T (K) < 300 or copper gaskets for measurements above 300 K. Variable temperature measurements were collected using 'orange' cryostats in the range 5 ≤ T (K) < 300 or a vacuum furnace with a vanadium heating element for measurements above 300 K.

2.3.2.1. Institut Laue Langevin (ILL)

Neutron powder diffraction data were collected at 2 external facilities, the Institut Laue Langevin (ILL) and ISIS, during the course of this investigation. A brief overview of the latter will be covered in section 2.3.2.2.

At the ILL, neutron diffraction experiments are carried out using a beam of neutrons produced from a ^{235}U fission nuclear reactor. The 'fast' neutrons produced from this fission reaction have energies in the MeV range, whereas the cross-section for neutron induced fission of ^{235}U nuclei is highest for neutrons with energies in the meV range. Therefore, in

order to sustain the fission process, the energy of the neutrons produced is reduced using a moderator filled with D_2O. Fortuitously, these neutrons are then of suitable thermal energies to perform effective neutron diffraction experiments where the appropriate wavelength can be selected using a crystal monochromator. The instruments at the ILL which were used during this work are detailed below.

2.3.2.1.1. D2b

D2b is a high resolution two-axis diffractometer, see Figure 2.5, with a high take-angle (135^o) for the monochromator.[31] Scans were performed over the range $5^o < 2\theta < 160^o$ with several scans being summed to improve the statistics. D2b contains a germanium crystal monochromator and the wavelength can be selected by rotation within the (*hhl*) plane. For all work in this investigation a wavelength of 1.594 Å was used.

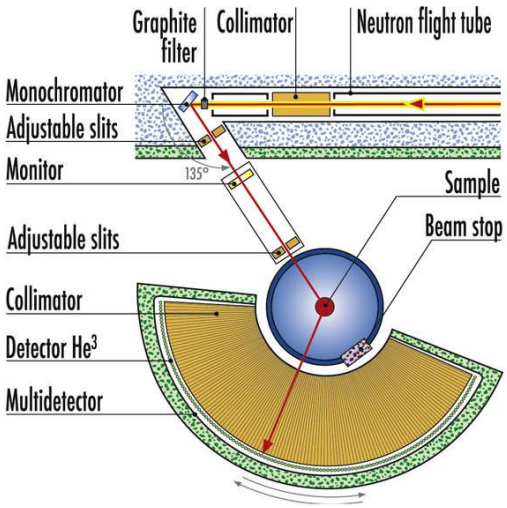


Figure 2.5: D2b instrument at the ILL facility.[32]

2.3.2.1.2. D1a

D1a was a relatively high-resolution powder diffractometer, see Figure 2.6, with a relatively high take-off angle of 122^o for the monochromator.[33] For all work in this investigation a wavelength of 1.911 Å was employed. Scans were performed between $0^o < 2\theta < 160^o$ with a step size of 0.05^o. D1a is no longer in operation at the ILL.

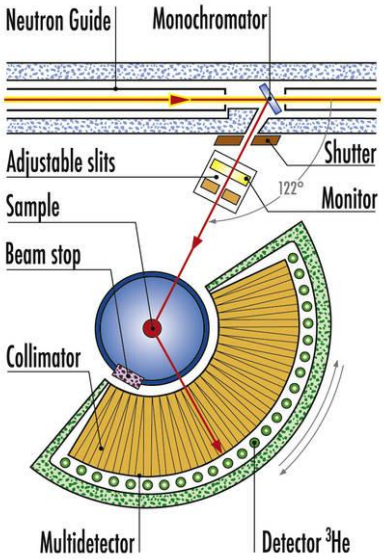


Figure 2.6: D1a instrument at the ILL facility.[34]

2.3.2.1.3. D1b

D1b is a two-axis high intensity neutron diffractometer, see Figure 2.7.[35] For all work in this investigation a wavelength of 2.52 Å was employed. D1b is optimised for the collection of data suitable for the elucidation of magnetic structures due to both the high spatial resolution at low angle and the very high neutron flux (thereby allowing for rapid data collection whilst scanning the temperature). Measurements were performed over the range 10 $^{o} < 2\theta < 90\ ^{o}$ with a step size of 0.2 ^{o}.

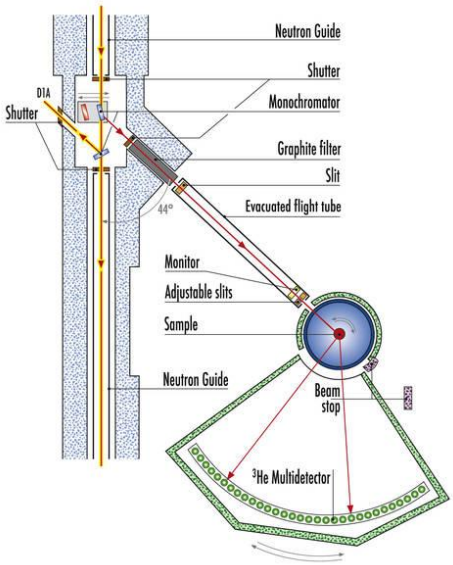


Figure 2.7: D1b instrument at the ILL facility.[36]

2.3.2.2. POLARIS at ISIS

The ISIS neutron facility at the Rutherford Appleton Laboratory uses a spallation neutron source.[37] Pulses of protons are accelerated to an energy of 800 MeV in a synchrotron and fired at a tantalum target. Bombardment of the target causes an intranuclear cascade, resulting in the formation of pulses of neutrons. The neutrons produced have very high thermal energies and must be slowed down using a hydrogenous moderator (H_2O in the case of the POLARIS instrument) so that they have suitable wavelengths for neutron scattering. This method of neutron generation produces pulses of neutrons with a continuous distribution of wavelengths which can be used for time-of-flight measurements.

Constant wavelength diffractometers (e.g. those used at the ILL) use incident radiation of a constant wavelength and measure diffraction patterns as a function of scattering angle. In contrast, time-of-flight diffractometers use a 'white' source of neutrons and use fixed angle detectors to measure diffraction patterns as a function of wavelength, which can be related to the velocity of the radiation using the De Broglie relationship:

where h is Planck's constant, m is the neutron mass and t is the time taken for the neutron to travel from the distance (L) from the moderator to the detector via the sample. The resolution, $\Delta d/d$, of a time-of-flight diffractometer is shown in the following relationship:



where Δt is the timing uncertainty, ΔL is the path length uncertainty and $\Delta\theta$ is the angular uncertainty. For a fixed detector $\Delta d/d$ effectively reduces to a constant, therefore, Δd decreases as the d-spacing decreases.

POLARIS in its pre-2011 incarnation was a medium resolution, high intensity diffractometer with a total of 434 ^{3}He and ZnS scintillator detectors arranged into four detector banks: the back scattering bank ($130^{o} \leq 2\theta \leq 160^{o}$), which provides the highest resolution given the dependence in the above relationship; the 90^{o} bank ($85^{o} \leq 2\theta \leq 95^{o}$); and the low angle banks ($13^{o} \leq 2\theta \leq 15^{o}$ and $28^{o} \leq 2\theta \leq 42^{o}$) which provide a wide *d*-spacing range. POLARIS is currently being rebuilt following a major upgrade.

2.3.3. Transmission Electron Microscopy (TEM)

2.3.3.1. General introduction

TEM is a powerful technique for structural investigation in solid state chemistry. A wide spectrum of information can be garnered using different operational modes of a transmission electron microscope.[38] The 2 modes used in this investigation were Selected Area Electron Diffraction (SAED) and High Angle Annular Dark Field Scanning Transmission Electron Microscopy (HAADF-STEM). The detailed practical functioning of, and underlying theories behind,[38] these techniques are beyond the scope of this investigation, however brief introductions to TEM, SAED and HAADF-STEM are detailed in the following sections.

2.3.3.2. Introduction to TEM

A Transmission Electron Microscope contains an electron gun and a series of condenser lenses to generate a nearly parallel beam of electrons. The beam of electrons then passes through an ultra-thin sample of the material of interest. Electrons are charged particles and so interact with the sample through columbic forces.

2.3.3.3. Electron diffraction

Electron diffraction holds 2 main advantages over neutron and X-ray powder diffraction due to the differing scattering mechanisms involved. The relatively strong coulombic interaction between the electron beam and the periodic potential within a crystal means that measurements can be performed on very small crystallites. Additionally, the shorter

wavelength of electrons affords the technique much higher resolution than X-ray or neutron diffraction, consequently, short-range order and cell expansions are readily observed.[39]

Electron diffraction measurements were performed using a JEOL JEM-2000FX Transmission Electron Microscope at the University of Oxford and, when required, additional measurements were performed by Prof. Dr. Joke Hadermann using a Philips CM20 microscope at the University of Antwerp. Samples were ground into fine particles in an argon-filled glovebox and then dispersed in CH_3OH or $CHCl_3$. A few drops of the suspension were pipetted onto a lacey-copper grid and placed in the microscope.

An electron diffraction pattern is a two-dimensional set of lattice points in reciprocal space. The *d*-spacing of a particular point is determined using the following formula:

—

where R is the distance from the origin to the point of interest, λ is the wavelength of the electron beam and L is the camera length, λL is a therefore a constant. By studying the systematic absences of the diffraction spots, the Bravais lattice and the presence of any screw axes and glide planes in the crystal structure can be determined.

2.3.3.4. HAADF-STEM

HAADF-STEM involves focussing the electron beam to a fine probe, with which the sample is 'scanned'. An objective aperture is inserted in the back focal plane to block out all electrons bar the high angle, incoherently scattered electrons. An annular (ring-like) detector is used and a dark field image (as the direct beam has been removed) is created. The intensity of the detected electrons is approximately proportional to the square of the scattering density, related to the atomic number (Z) of atoms present, at the focal point of the beam. By moving the focal point of the beam over the sample, a 'scattering map' of the sample can be built up

allowing an 'image' of the sample to be generated. This technique is especially useful for the 'imaging' of defects and domain structures within a sample.

All HAADF-STEM measurements were performed by Prof. Dr. Joke Hadermann using a JEOL 3000F microscope or a FEI TITAN 50-80 transmission electron microscope at the University of Antwerp. Prior to insertion into the microscope, the samples were plasma-cleaned in an argon-oxygen atmosphere for 30 seconds, then dispersed in ethanol and deposited onto a holey carbon grid.

2.4. Structural analysis

2.4.1. The Rietveld method

The Rietveld method of profile refinement was employed to analyse all neutron and X-ray diffraction data in this investigation using the GSAS suite of programs.[40, 41] The Rietveld method is a procedure used to extract structural information from powder diffraction data where peak overlap and d_{hkl} degeneracy prevent exact structure factors being calculated from the reflection intensities.

Using diffraction and structural parameters, a diffraction pattern can be generated and the calculated intensity of each point compared to the observed intensity in an experimental diffraction pattern using the following expression:

where w_i is the weighting factor, y_{io} is the observed intensity of the i^{th} point and y_{ic} is the calculated intensity of the i^{th} point. Diffraction and structural parameters can then be refined against the experimental data using a least squares optimisation technique to minimise *S*.

The quality of the fit to the data can be assessed using three 'goodness of fit' functions: the reduced χ^2, the residual function (R_p) and the weighted residual function (wR_p). These functions are defined using the following expressions:

where n_{obs} is the number of observations in all histograms and n_{var} is the number of variables in the least squares refinement.

2.4.2. Peak shapes

The accurate description of the experimentally observed peak shapes in diffraction patterns is fundamental to the success of Rietveld refinement. Peak widths in diffraction data are dependent on three main factors:

1. The Darwin width. Due to the uncertainty principle, exact knowledge of the position of a photon necessarily implies an intrinsic ambiguity about the momentum, and therefore wavelength, of said photon. This ambiguity leads to diffraction reflections of a finite width (Darwin width). However the broadening attributable to this effect is generally negligible compared to other experimental considerations.
2. Instrumental factors, e.g. imperfect measuring geometry (ambiguity in the sample height for instance), uncertainty in the wavelength of the incident radiation and optical effects (e.g. unwanted diffraction of the beam by the parts of the instrument rather than the sample).
3. The theory of diffraction from a material assumes that the material is an infinite perfect crystal. However deviations away from this hypothetical crystal lead to broadening of reflections in the diffraction pattern. This broadening can be measured to acquire certain information about the sample, e.g. particle size or strain within the lattice.

It was initially assumed in the development of the Rietveld method that the peak shapes could be accounted for using a Gaussian profile function, corrected for asymmetry.[42] While the Gaussian profile function models instrumental peak broadening well, the use of a Lorentzian profile function is required to model the peak broadening due to structural features. Thus, the overall profile function can be modelled as an integral of the Pseudo-Voigt function ($F(\Delta T)$)[41, 43] involving a linear combination of both the Gaussian and Lorentzian components:

where ΔT is defined as the deviation in position of a reflection from its calculated position, Γ is a function of the Full Width at Half Maximum (FWHM) and η is defined as the mixing parameter which is used to include the optimal contribution from each component function.[42] Depending on the measurement type, peak shapes in this study were modelled either using the constant wavelength profile function 2 or the time-of-flight profile function 3.

2.4.2.1. Profile function 2 (constant wavelength data)

In profile function 2 the peak width is corrected ($\Delta T'$) to take into account contributions from asymmetry. The FWHM of a particular reflection is a function of the Gaussian component, Γ_g, and the Lorentzian component, γ.[44] The Gaussian component can be expressed as follows:

where the U, V and W terms model the instrumental broadening. The final term was subsequently added to take into account the Scherrer broadening for the Gaussian component.[44] The Lorentzian component can be described as follows:

with the first set of terms used to describe the contributions from Scherrer broadening and the second set of terms the strain broadening contribution. Additional profile parameters can also be used to account for broadening associated with stacking faults or the anisotropy of the sample with respect to the sample size or strain.[42]

2.4.2.2. Profile function 3 (time-of-flight data)

With data collected from time-of-flight experiments, ΔT can be defined as the deviation in position in msec of a reflection from its calculated position. The overall profile function convolutes the pseudo-Voigt function described in section 2.4.2 with 2 additional exponential functions. The Gaussian variance, , and Lorentzian parameter, , for time-of-flight experiments are defined as follows:

where σ_0, σ_1 and σ_2 are the Gaussian parameters; γ_1 and γ_{1e} account for microstrain broadening and γ_2 and γ_{2e} account for Scherrer broadening,

2.5. Reverse Monte Carlo simulation

2.5.1. Introduction

Many samples of interest contain disorder (e.g. chemical, displacive, etc.) in which the local structure of the material differs from that of the average structure. In these instances, the arrangement of atoms can't be effectively described using periodic translational symmetry. Therefore, in order to fully describe the structure of these 'disordered' materials it is necessary to move away from a description based on long range translational symmetry and consider structures as being built up from a large number of pairwise interatomic distances.

Over the last decade that there has been a surge in interest in the application of Reverse Monte Carlo (RMC) simulations in the determination of local structures in 'disordered' materials. The detailed theory of RMC simulations [45] is beyond the scope of this

investigation, however a brief introduction to this technique and the calculation of the Pair Distribution Function for use as a guide in RMC simulations will be covered in the following sections.

2.5.2. Pair Distribution Function (PDF)

Keen has prepared a comprehensive review of the various "confusing" notation conventions used in the field of total scattering,[46] the parts of which most relevant to this investigation are detailed below:

After background subtraction and normalisation, a neutron powder diffraction pattern gives the total scattering structure factor ( ) of a material in reciprocal space. Fourier transformation of the diffraction data (i.e. the Bragg reflections and the diffuse scattering, thus the name 'total scattering') yields a function proportional to the PDF ( ).

where is the average number density. The PDF can be interpreted as a real space histogram, weighted by the scattering power of the various atom pairs, of the interatomic distances in the sample.[47-49] It is then common to use the differential correlation function ( ) as an alternative representation to , where is defined as follows:[45]

2.5.3. Fitting the PDF

Fitting PDF profiles has provided a major challenge to researchers as large scale models containing many thousands of atoms are needed to account for all the significant pairwise interactions required to fully describe a local structure. The sheer size of the models precludes the use of least-squares refinement methods (as used in Rietveld refinement for instance) as they would inevitably diverge given the large number of free parameters being refined

compared to the number of observations. Therefore, Reverse Monte Carlo (RMC) simulations are widely used to account for the data.

The basic premise of RMC simulations is to generate an ensemble containing many thousands of atoms. The atoms are then moved in a stochastic manner in which changes in the fit to experimental data collected from the phase of interest (the PDF profile and Bragg diffraction data in this investigation) provide the basis for accepting or rejecting the atom movement according to the Monte-Carlo algorithm.[48] It should be stressed that the RMC simulation does not generate a single structure in the conventional sense with lattice parameters and atomic positions but rather an atomic configuration that, when the average structure is calculated, agrees with the collected data.

All data handling and RMC simulations were carried out by Dr Andrew Goodwin at the University of Oxford. The RMC simulations were carried out using the RMCProfile program which allows simultaneous fitting to the PDF and bulk diffraction data. Fitting against the bulk diffraction data allows many structural parameters (e.g. dimensions of the unit cell) to be constrained to values consistent with the long-range structure.

2.6. Bond valence sums

Calculation of bond valence sums allows an estimation of the valence of an ion based on the bond lengths to, and identity of, the contacts within its coordination sphere.[50] The total valence of an ion, V_i, is defined as the sum of the valences of the individual bonds within the coordination sphere:

where the valence, v_{ij}, of a bond between two atoms i and j can be calculated using the following empirical relationship:

where b is an empirical constant, R_{ij} is the 'bond-valence parameter' and d_{ij} is the bond length. Work by Brown and Altermatt showed that b can be taken to be a 'universal' constant of 0.37 and so this value was used throughout.[51] All bond valence calculations in this project used the R_{ij} values published by Brese and O'Keeffe.[50]

Bond valence sums can be considered to be a comparison of the bond lengths in a given coordination sphere with bond lengths involving the same ions in reported structures in the literature. The majority of the reported bond lengths in the literature will be extracted from thermodynamic phases, therefore bond valence sums should only be applied with caution to metastable phases (e.g. the topotactically reduced phases in this investigation).

2.7. DC SQUID magnetometry

DC SQUID (Superconducting Quantum Interference Device) magnetometry is a technique used to measure the magnetic properties of a system associated with the spin and orbital momentum of the electrons. The incredibly high accuracy of this measurement type is attributable to the superconducting detection coils within the device shown in Figure 2.8.

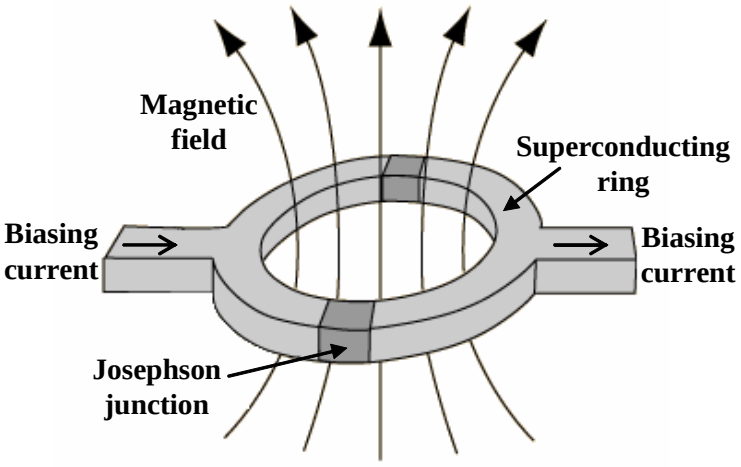


Figure 2.8: Schematic of SQUID (edited from a diagram extracted from 'Magnetism and the Chemical Bond')[52]

A measurement is performed by moving the sample through this superconducting detection coil which induces a current in the ring. The Josephson junctions act as a weak link in the superconducting ring forcing the current within the ring to become quantised. Variations in

the current within the superconducting ring produce equivalent variations in the output voltage of the SQUID which are proportional to the magnetic moment of the sample.

All magnetometry data in this investigation were collected using a Quantum Design MPMS XL SQUID Magnetometer. Approximately 50 mg of sample was weighed and then suspended in a drinking straw in a gelatin capsule with four empty gelatin capsules either side of the sample. The outermost capsules were covered in a layer of diamagnetic tape to hold the sample in place. Where the sample was believed to be highly air-sensitive, the sample was loaded into the straw in an argon-filled glovebox.

The SQUID magnetometer computes the magnetic moment of a sample in electromagnetic units (emu). The magnetisation (M in units of emu mol^{-1}) of the sample can be readily calculated by dividing the collected moment by the number of moles of sample measured. In a paramagnetic material, the molar magnetic susceptibility (χ_m in units of emu mol^{-1} Oe^{-1}) below saturation can then be calculated as follows:

—

where H is the applied field in units of Oersted (Oe). Three types of magnetic measurements were found to be of particular use during this investigation:

Firstly, the magnetic susceptibility of a sample was recorded as a function of increasing temperature (usually $5 \leq T$ (K) ≤ 300) at a constant applied field (usually 100 Oe). This measurement was carried out twice, first when the sample was cooled from 300 K in the absence of an applied magnetic field and subsequently when the sample was cooled in the measuring field. Secondly, the magnetisation of a sample was recorded as a function of applied field ($-50000 \leq H$ (Oe) ≤ 50000) at a constant temperature (usually 5 K and 300 K).

Finally, paramagnetic susceptibility data were collected from samples containing trace amounts of ferromagnetic impurities (e.g. elemental iron) using the "ferrosubtract method".[9]

The magnetisation of these ferromagnetic impurities was observed to saturate in applied magnetic fields of at least 3.5 T. Thus the paramagnetic susceptibility of a bulk sample can be measured in the presence of these ferromagnetic impurities by measuring the gradient of magnetisation-field isotherms in applied fields larger than 3.5 T. To this end the magnetisation of samples was measured in a series of 7 fields between 3.5 T and 5 T. The magnetisation-field isotherms were fitted to a linear function, with data points with large errors excluded. All fits had at least 5 data points. This procedure was repeated at 5 K intervals between 5 K and 300 K to measure the temperature dependent susceptibility of samples.

2.7.1. Curie-Weiss law

When appropriate, the magnetic susceptibility can be modelled using the Curie-Weiss law:

$$\chi = \frac{C}{T - \theta}$$

where the Weiss constant (θ) is a measure of the strength of the magnetic interactions present and the Curie constant (C) can be defined as:

$$C = \frac{N_A \mu_B^2 g^2 S(S+1)}{3 k_B} = \frac{N_A \mu_{eff}^2}{3 k_B}$$

where N_A is Avogadro's constant, μ_B is the Bohr magneton, g is the Landé factor, S is the spin quantum number of the magnetic ion, k_B is Boltzmann's constant and μ_{eff} is the effective magnetic moment. The Curie-Weiss law can be modified to take into account of the effect of temperature independent paramagnetism by the inclusion of a further constant (K):

$$\chi = \frac{C}{T - \theta} + K$$

2.8. Thermogravimetric analysis (TGA)

Thermogravimetry measures the mass of a sample as a function of temperature in order to ascertain chemical information about the sample. Thermogravimetric reoxidation data (i.e.

measurement of the mass change upon heating under flowing oxygen) were particularly useful during this investigation as it allowed the level of anion deficiency in the reduced phases to be measured directly. From knowledge of the mass of the initial sample and the molar mass of the final sample, the molar mass of the initial sample can be calculated.

Reoxidative thermogravimetric measurements were performed by heating approximately 50 mg of powered sample on a Netzsch STA 409 PC balance under flowing O_2. It should be noted that the inverse relationship between the temperature and density of the gas in the sample chamber induces a systematic error into the thermogravimetric measurements. Therefore, the data were corrected according to a test measurement using a sample of known and temperature independent mass.

2.9. Iodometric titrations

The oxygen content of phases can also be determined using iodometric titrations. In general these titrations give a more accurate oxygen content than those calculated from thermogravimetric data. Determination of the amount of I_2 released by the oxidation of I^- ions (usually contained in a solution of KI) by transition metal cations allows the calculation of the oxidation state of said transition metal. The amount of I_2 liberated can be calculated by titration against a solution of $Na_2S_2O_3$, the concentration of which can be deduced by titration against a standard solution of KIO_3. In the case of manganese and iron cations, a reaction summary is shown below:

Due to the air sensitive nature of the materials within this investigation, preparations of samples for titration were carried out in an argon filled glovebox. Roughly 40 mg of powdered sample was loaded into a 3-necked, round bottom flask and then sealed with suba-seals. The titrations were carried out under an argon atmosphere to prevent partial oxidation of the iodide solution by air. The flask was removed from the glovebox and flushed with argon.

Under a positive pressure of argon, 10 mL of 1:5 concentrated HCl and distilled H_2O was added to the flask followed by roughly 0.2 g (an excess) of KI. The solution was stirred using a magnetic stirrer plate and the liberated I_2 was titrated against the $Na_2S_2O_3$ solution. As the solution became a pale-straw colour, a few drops of starch were added to highlight the endpoint. In order to ensure the accuracy, at least 3 titrations were performed for each sample.

2.10. X-ray Absorption Near Edge Structure (XANES) spectroscopy

X-rays of sufficient energies can be used to ionise core electrons from an atom. The X-ray absorption spectrum of an atom of interest can thus be collected by recording the variation in the absorption of X-rays as a function of the energy of the incident radiation. The energy at which the absorption of the incident photons increases dramatically is defined as an absorption edge. Each absorption edge occurs when the energy of the incident photons is just sufficient to cause ionisation of core electrons from the absorbing atom (see Figure 2.9).

The energy of the absorption edge is characteristic of the element ionised and the oxidation state. Information regarding the oxidation state of an atom can therefore be gained from comparison of the energy of its absorption edge to those of the same atom in standard samples. XANES spectroscopy probes the region of the X-ray absorption spectrum within approximately 50 eV of the absorption edge. In addition to the ionisation of core electrons, excitation of core electrons to higher energy shells, e.g. $1s \rightarrow 5p$, gives near-edge fine structure.

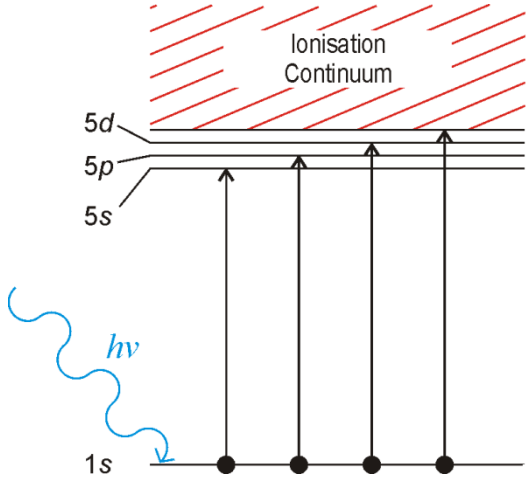


Figure 2.9: Cartoon depicting the excitation of a core electron

Chapter 3: Topotactic Reduction of $La_{0.33}Sr_{0.67}MnO_3$

3.1. Introduction

Anion-deficient phases of the form $La_{1-x}Sr_xMnO_{3-y}$ have received particular attention due to their potential application as mixed ionic/electronic conductors in solid oxide fuel cell (SOFC) cathodes and other devices.[53] It is useful to divide the $La_{1-x}Sr_xMnO_{3-y}$ series into 2 groups: those with $x \leq 0.5$ and those with $x > 0.5$. Considering the La^{3+}-rich group first, topotactic reduction reactions of the $La_{1-x}Sr_xMnO_3$ ($0.2 \leq x \leq 0.5$) phases result in the formation of reduced phases with an empirical composition of $La_{1-x}Sr_xMnO_{2.5}$ which adopt the $A_2B_2O_5$ brownmillerite structure (see Figure 1.2).[17, 19, 20] These reduced phases contain manganese centres with an average oxidation state of between +2.2 and +2.5.

In contrast to the La^{3+}-rich phases, previously reported topotactic reduction reactions of the Sr^{2+}-rich phases result in the formation of reduced phases which contain manganese centres with significantly higher average oxidation states (+2.84 to +3.4) and structures consisting of MnO_5 square-based pyramids and MnO_6 octahedra.[54-57] For example, the reduction chemistry of the x = 1 member, $SrMnO_3$, results in a wide array of anion-vacancy ordered structures (see Figure 3.1). These structures contain rigorous charge ordering of the Mn^{3+} and Mn^{4+} cations with all the Mn^{3+} cations exclusively located on sites with square based pyramidal coordination. In order to determine if the observed higher oxidation states and lower anion deficiency of Sr^{2+}-rich $La_{1-x}Sr_xMnO_{3-y}$ phases relative to the $La_{1-x}Sr_xMnO_{2.5}$ ($0.2 \leq x \leq 0.5$) brownmillerite phases indicates a stability boundary, or only that a more powerful chemical agent is required to reduce these phases, the topotactic reduction reactions of the $La_{1-x}Sr_xMnO_3$ ($x > 0.5$) substrates with NaH, previously reported to be a powerful solid-state reducing agent,[26] were attempted. This chapter focuses on the topotactic reduction chemistry of $La_{0.33}Sr_{0.67}MnO_3$.

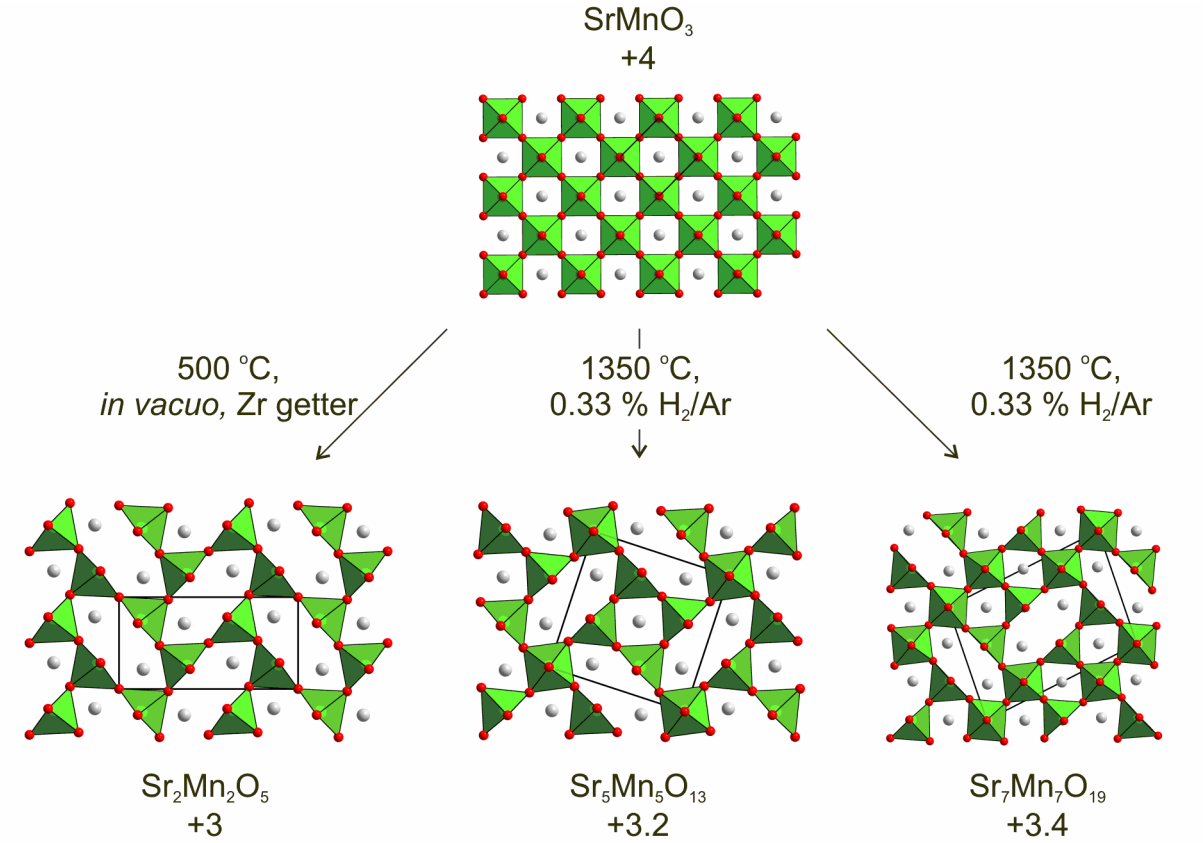


Figure 3.1: Structures of the reduced phases formed by topotactic reduction reactions of $SrMnO_3$.[54-56]

3.2. Experimental

3.2.1. Synthesis of perovskite starting material

A 5 g sample of $La_{0.33}Sr_{0.67}MnO_3$ was prepared using the standard ceramic synthesis method.[58] The formation of the target cubic perovskite phase competes with the formation of the more thermodynamically stable hexagonal perovskite phase $SrMnO_3$.[58, 59] Therefore, in an attempt to inhibit the formation of $SrMnO_3$, all heating occurred under reducing conditions. This use of these conditions can be rationalised using the Goldschmidt tolerance factor (see section 1.1).[7] As $SrMnO_3$ is reduced and the B-O bond length increases, the tolerance factor decreases. This destabilises this hexagonal perovskite structure with respect to the cubic perovskite structure and suppresses the formation of $SrMnO_3$ as an impurity phase.

The appropriate stoichiometric ratios of La_2O_3 (99.999 %, dried at 900 ^oC), $SrCO_3$ (99.99 %) and MnO_2 (99.999 %) were ground in an agate mortar and then heated at 900 ^oC in

an alumina boat under flowing argon to decompose the carbonate. The resulting powder was reground and pressed into 2-3 g, 13 mm pellets. The sample was then heated at 1350 ^{o}C for 3 periods of 48 hours under flowing argon. After each heating period, the material was reground and pressed into pellets as before. Finally, to ensure the material was oxide stoichiometric rather than anion deficient, the sample was annealed at 500 ^{o}C in air for 12 hours, before slow cooling to room temperature. After a further regrinding, X-ray powder diffraction data confirmed that a phase-pure sample had been obtained with lattice parameters consistent with those previously reported for the $La_{1-x}Sr_xMnO_3$ series (a = 3.8394(1) Å).[58]

3.2.2. Low temperature reduction with metal hydrides

The reduction of $La_{0.33}Sr_{0.67}MnO_3$ was performed using NaH as a solid state reducing agent (Aldrich > 95 %), as described in section 3.2.2. $La_{0.33}Sr_{0.67}MnO_3$ was ground thoroughly with 2 mole equivalents of NaH in an argon-filled glovebox and then sealed under vacuum in a Pyrex ampoule. The mixture was heated at 180 ^{o}C for 12 hours and then 210 ^{o}C for 4 periods of 48 hours with the mixture being ground in an argon-filled glovebox after each heating cycle. The sample was then washed with 4 x 100 ml aliquots of CH_3OH under nitrogen to remove sodium-containing phases (NaOH and NaH) before being dried under vacuum.

3.3. Results

3.3.1. X-ray diffraction data

The bottom diffraction pattern shown in Figure 3.2 was collected from the washed products of the reaction detailed above.

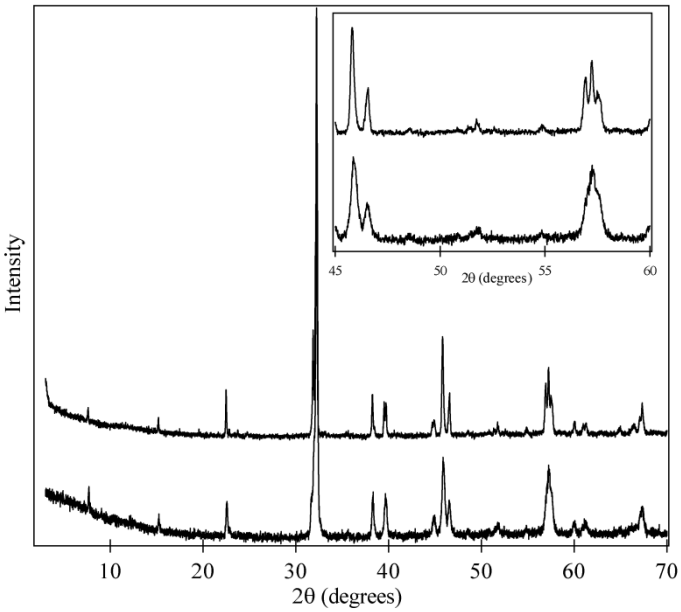


Figure 3.2: X-ray powder diffraction patterns collected from the washed products of the reaction between $La_{0.33}Sr_{0.67}MnO_3$ and NaH (bottom) and from the same sample heated at 400 ^oC in a sealed silica ampoule, i.e. annealed, (top).

The diffraction reflections can be indexed using an orthorhombic unit cell related to that of a simple cubic perovskite structure by means of a $\sqrt{2}a_p$ x na_p x $\sqrt{2}a_p$ (where n = 3 or 6) expansion, suggesting a topotactic reduction reaction had occurred. However, the reflections in the X-ray powder diffraction data are broad and poorly resolved, especially at high angle. This broadness is attributable to slight disorder within the anion sublattice, which can be encouraged to order by annealing. Various annealing experiments were therefore performed. Heating at 400 ^oC in a sealed evacuated silica ampoule was found to be the optimum regime. Below this temperature, there was no improvement in the crystallinity of the sample and above this temperature, mild decomposition to the substituent binary oxides occurred. The top diffraction pattern in Figure 3.2 was collected from the sample annealed at 400 ^oC. It is clear that the annealing has resulted in an improvement in the crystallinity of the sample.

Considering the observed lattice expansion, the 2 most likely anion vacancy ordered structural models consistent with the $La_{0.33}Sr_{0.67}MnO_{3-y}$ unit cell are those of $(La_{1/3}Ca_{2/3})_3Fe_3O_8$ (n = 3) and $RESr_2GaCu_2O_7$ (n = 6).[60, 61] As shown in Figure 3.3, the 3-layer structure of $(La_{1/3}Ca_{2/3})_3Fe_3O_8$ and 6-layer structure of $RESr_2GaCu_2O_7$ are closely

related but contain 2 slight differences: Firstly, the structure of *RE*$Sr_2GaCu_2O_7$ contains a 'staggered' arrangement of tetrahedral chains up the *b*-axis (SSTSST' stacking, where S denotes CuO_5 square based pyramidal layers). In contrast, the structure of $(La_{1/3}Ca_{2/3})_3Fe_3O_8$ contains an 'eclipsed' arrangement of tetrahedral chains up the *b*-axis (OOTOOT stacking). Secondly, the structure of *RE*$Sr_2GaCu_2O_7$ contains an anion vacant A-cation layer between the 2 CuO_2 layers in the perovskite-type block (labelled P' in Figure 3.3) whereas $(La_{1/3}Ca_{2/3})_3Fe_3O_8$ contains an AO layer between the 2 FeO_2 layers in the perovskite-type block (labelled P in Figure 3.3).

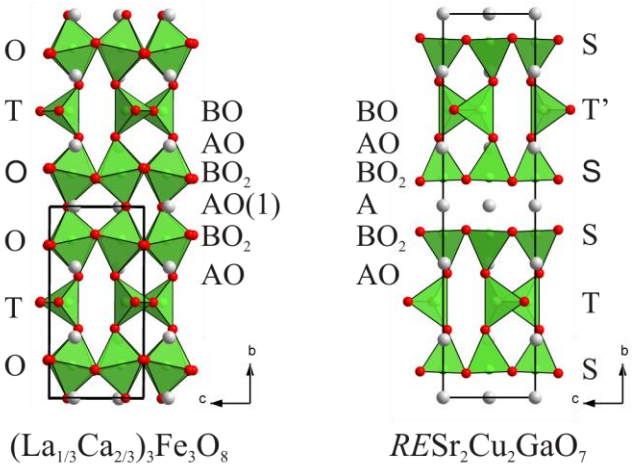


Figure 3.3: Possible structural models for $La_{0.33}Sr_{0.67}MnO_{3-y}$

Unfortunately, the relatively low scattering power of the oxide anions in comparison to the heavier cations means it is not possible to reliably differentiate between these 2 potential structural models on the basis of X-ray powder diffraction data. Therefore, electron and neutron powder diffraction data were collected from this phase. In addition, reoxidative thermogravimetric data were collected from $La_{0.33}Sr_{0.67}MnO_{3-y}$ in an attempt to calculate the empirical stoichiometry of the reduced phase.

3.3.2. Thermogravimetric analysis

$La_{0.33}Sr_{0.67}MnO_{3-y}$ shows a mass gain of 4.68(3) % upon reoxidation consistent with an empirical stoichiometry of $La_{0.33}Sr_{0.67}MnO_{2.42(3)}$ or '$(La_{0.33}Sr_{0.67})_3Mn_3O_{7.26}$' and an average

manganese oxidation state of +2.5. It should be noted that the empirical stoichiometry is intermediate in between those of *RE*$Sr_2GaCu_2O_7$ and $(La_{1/3}Ca_{2/3})_3Fe_3O_8$.

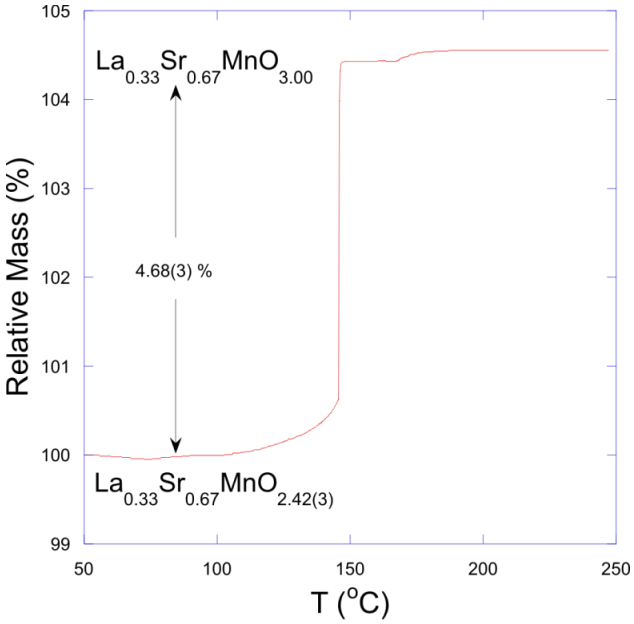


Figure 3.4: Reoxidative thermogravimetric data collected on heating $La_{0.33}Sr_{0.67}MnO_{3-y}$ under flowing oxygen

3.3.3. Electron diffraction data

Electron diffraction data collected from $La_{0.33}Sr_{0.67}MnO_{2.42}$ could be indexed using a unit cell related to that of a simple cubic perovskite structure with a $\sqrt{2}a_p$ x $6a_p$ x $\sqrt{2}a_p$ expansion. The 6-fold expansion along the *b*-axis provides evidence for the fact that $La_{0.33}Sr_{0.67}MnO_{2.42}$ adopts a structure based on that of *RE*$Sr_2GaCu_2O_7$ rather than that of $(La_{1/3}Ca_{2/3})_3Fe_3O_8$.

As demonstrated in Figure 1.5, the space groups of the 4-layer brownmillerite and 6-layer *RE*$Sr_2GaCu_2O_7$ type structures are intrinsically related to the arrangement of the twisted tetrahedral chain in these phases. In previous structural studies of brownmillerite phases, the electron diffraction data have been indexed using unit cells consistent with (3+1)D structural models based on the brownmillerite structure of $Sr_2Fe_2O_5$.[16] An introduction to (3+1)D crystallography is detailed in Appendix 3. Due to the structural similarities of the 4-layer brownmillerite phases and *RE*$Sr_2GaCu_2O_7$, a similar procedure was used to index the electron diffraction data collected from $La_{0.33}Sr_{0.67}MnO_{2.42}$.

Electron diffraction data collected from $La_{0.33}Sr_{0.67}MnO_{2.42}$ are consistent with a (3+1)D model with an *Imma*(00γ)*s*00 superspace group where $\gamma = ½$. According to Table 4 in a recent publication by D'Hondt *et al*.,[16] this indexation is consistent with a 3D model with *Pcmb*, *Pcma* or $Pcm2_1$ symmetry and a $\sqrt{2}a_p$ x $6a_p$ x $2\sqrt{2}a_p$ expanded unit cell.

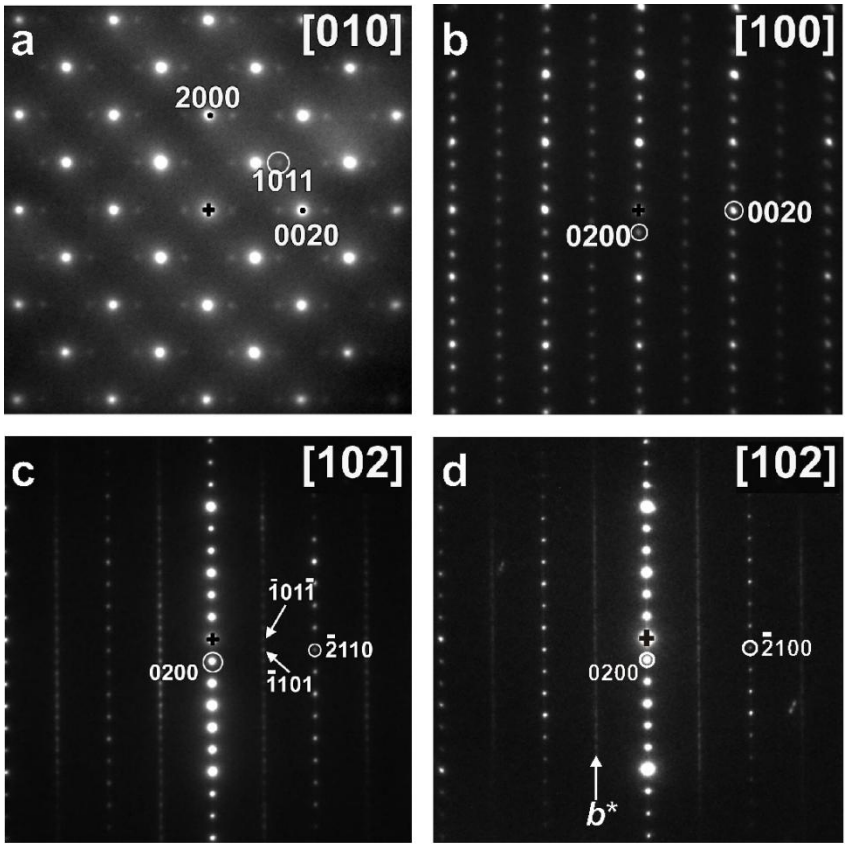


Figure 3.5: Electron diffraction data collected from the (a) [010], (b) [100] and (c) [102] zone axes of $La_{0.33}Sr_{0.67}MnO_{2.42}$. Figure (d) shows data collected from the [102] zone axis of $La_{0.33}Sr_{0.67}MnO_{2.42}$ exhibiting streaking parallel to the *b direction. The data were collected by Prof. Dr. Joke Hadermann.**

Both the set of space groups and the doubling of the *c*-lattice parameter suggest that the structure contains a 1:1 alternation of the 2 oppositely twisted tetrahedral chains within each tetrahedral layer (intralayer order). As a comparison, in the study of the $La_{1-x}A_xMnO_{2.5}$ brownmillerite structures, $La_{0.35}Sr_{0.65}MnO_{2.5}$ and $La_{0.4}Sr_{0.6}MnO_{2.5}$ could also be described using models with *Pcmb* symmetry and $\sqrt{2}a_p$ x $4a_p$ x $2\sqrt{2}a_p$ unit cells which contain intralayer order of the twisted tetrahedral chains.[17]

The *Pcmb* space group was chosen to describe the 6-layer $La_{0.33}Sr_{0.67}MnO_{2.42}$ structure as this is the highest symmetry space group which allows for a realistic intralayer ordering

scheme of the twisted tetrahedral chains. Some of the patterns (e.g. Figure 3.5 (d)) show streaking in some reflections. A more detailed description of this feature is included in section 3.3.5.

3.3.4. Neutron diffraction data

Neutron powder diffraction data were collected from $La_{0.33}Sr_{0.67}MnO_{2.42}$ at room temperature using the D2b instrument (see section 2.3.2.1.1) in order to determine the extent of the intralayer ordering of the twisted tetrahedral chains throughout the bulk structure. To confirm that $La_{0.33}Sr_{0.67}MnO_{2.42}$ adopts a long range anion vacancy ordered structure based on the 6-layer $RESr_2GaCu_2O_7$ structure rather than the 3-layer $(La_{1/3}Ca_{2/3})_3Fe_3O_8$ structure, as determined from the electron diffraction data, models based on these 2 structures were constructed and refined against the neutron powder diffraction data. As a slight complication, close inspection of the data revealed a weak set of additional diffraction reflections consistent with the presence of MnO. Therefore, a structural description of MnO was added to the refinements. The $20\ ^{o} \leq 2\theta \leq 40\ ^{o}$ sections of the fits to the neutron powder diffraction data using the 2 different structural models are shown in Figure 3.6 along with their goodness of fit statistics.

Both the goodness of fit statistics and the observable fit to the data are improved using the 6-layer $RESr_2GaCu_2O_7$ structural model over the 3-layer $(La_{1/3}Ca_{2/3})_3Fe_3O_8$ model. Furthermore, close inspection indicates that several weak reflections (marked with asterisks in Plot A and with the relevant lattice plane in Plot B) are consistent with the 6-layer model but not the 3-layer model. In conclusion, both electron and neutron powder diffraction data are consisent with $La_{0.33}Sr_{0.67}MnO_{2.42}$ adopting a 6-layer structure.

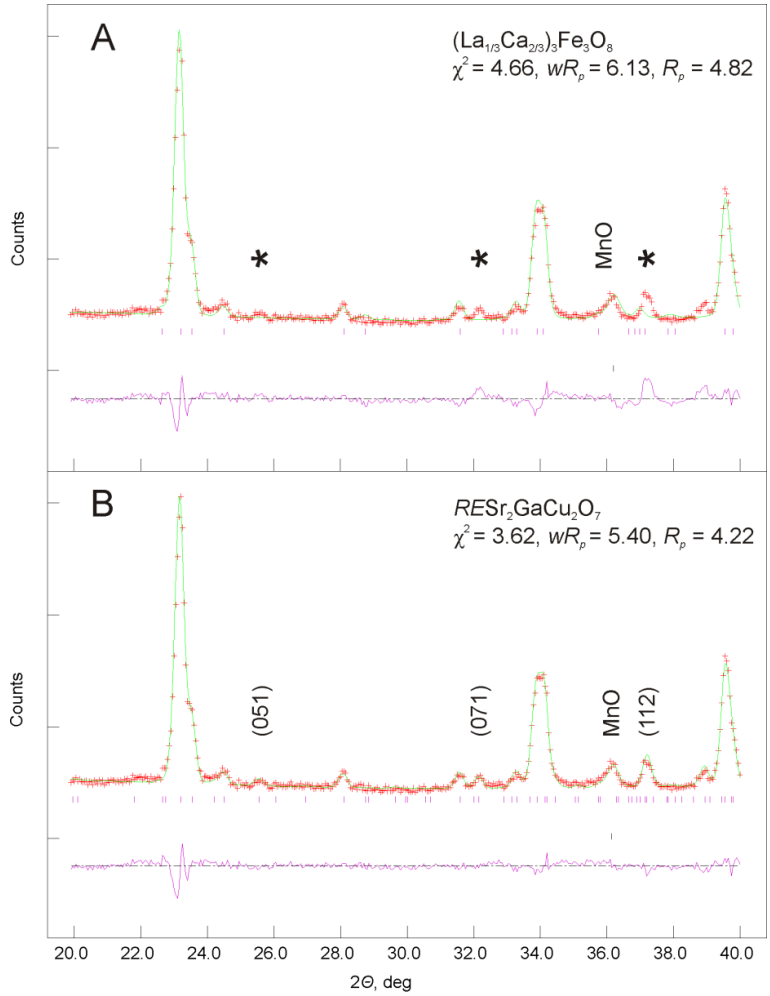


Figure 3.6: Observed, calculated and difference plots of refinements of structural models based on $(La_{1/3}Ca_{2/3})_3Fe_3O_8$ (A) and *RE*$Sr_2GaCu_2O_7$ (B) against neutron powder diffraction data collected from $La_{0.33}Sr_{0.67}MnO_{2.42}$. The bottom set of tick marks in each refinement relate to the presence of MnO.

In order to establish the exact anion vacancy ordering arrangement and polyhedral twisting patterns present in the structure of $La_{0.33}Sr_{0.67}MnO_{2.42}$, a series of structural models were constructed containing a 2:1 alternating sequence of MnO_6 octahedral and MnO_4 tetrahedral layers. Models were constructed in the *Pcmb* space group, determined from the electron diffraction data, and the 4 other space groups (*I*2*mb*, *Pnma*, *Imma* and *C*2/*c*) in which brownmillerite phases have been observed to crystallise (see section 1.4.2). These 5 structural models for $La_{0.33}Sr_{0.67}MnO_{2.42}$ were then refined against the room temperature neutron powder diffraction data.

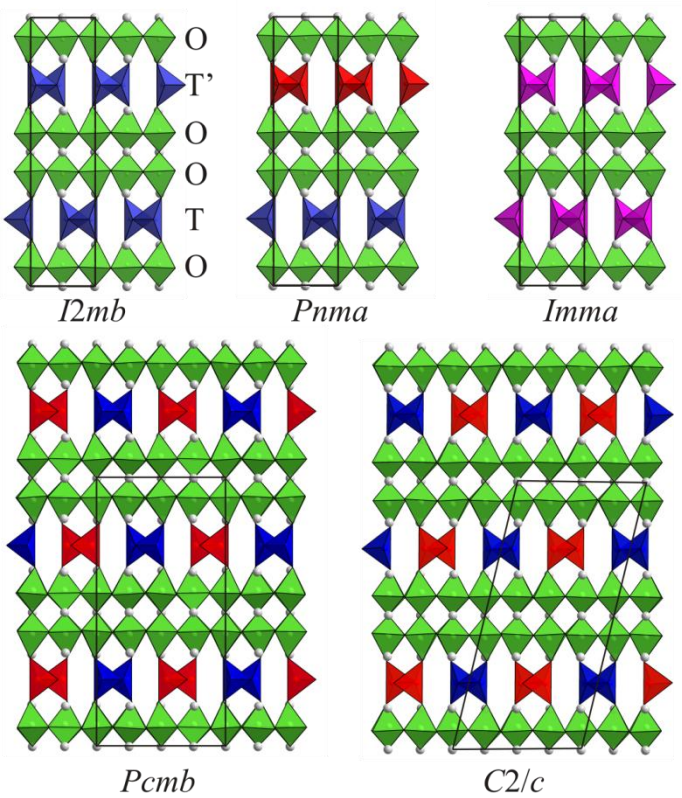


Figure 3.7: The five different 6-layer $A_3Mn_3O_8$ structural models refined against neutron diffraction data. The models incorporate the five common tetrahedral twist orderings observed in brownmillerite phases (see section 1.4.2).

In the latter stages of the refinements, all atomic positional and thermal parameters were allowed to vary. To account for the oxide nonstoichiometry of the reduced phase (i.e. reduction past the $A_3B_3O_8$ level consistent with a 2:1 alternating arrangement of MnO_6 octahedra and MnO_4 tetrahedra), the fractional occupancies of all the anion sites were also allowed to vary. While the majority of the anion sites remained fully occupied within error, the occupancy of 'bridging' anion site (labelled O(1) and O(8) in Figure 3.8) rapidly declined to approximately 0.07 in all 5 models with an associated improvement in the fit to the data in each case. This fractional occupancy distribution would lead to a refined empirical composition of $La_{0.33}Sr_{0.67}MnO_{2.35}$ clearly inconsistent with the stoichiometry of $La_{0.33}Sr_{0.67}MnO_{2.42}$ extracted from the thermogravimetric data. Therefore, the fractional occupancy of this 'bridging' anion site was constrained to 0.25 to fix the composition at a level consistent with the thermogravimetric data. In the final stages of the refinement, the

fractional occupancies of all of the atomic sites were allowed to vary, but all other atomic positions remained fully occupied within error. The goodness of fit statistics for each refinement are shown in Table 3.1.

Space group	χ^2	***wRp***	***Rp***	***Structural Parameters***	***Global Parameters***
I2mb	3.519	5.31 %	4.17 %	26	30
Imma	2.967	4.88 %	3.87 %	26	30
Pnma	3.394	5.22 %	4.12 %	26	30
C2/c	2.916	4.83 %	3.81 %	45	30
Pcmb	2.862	4.81 %	3.80 %	44	30

Table 3.1:Fitting statistics for the refinement of 6-layer models against neutron powder diffraction data collected from $La_{0.33}Sr_{0.67}MnO_{2.42}$ (2879 observations)

In accordance with the electron diffraction data, the model based on *Pcmb* symmetry most effectively accounts for the neutron diffraction data collected from $La_{0.33}Sr_{0.67}MnO_{2.42}$. However, it is clear that the fitting statistics for the refinement against neutron powder diffraction data are clearly not well separated enough to unequivocally determine the space group. Analysis of the different structural variants indicates that the L and R twisted tetrahedral chains differ by only small atomic displacements with these subtle alterations in structure only manifesting themselves in small changes in some neutron powder diffraction reflections. Therefore unequivocal determination of the ordering scheme of the twisted tetrahedral chains, and corresponding structural variant, cannot be reliably performed without recourse to the electron diffraction data.

The final fit to the neutron powder data using the 6-layer structural model based on *Pcmb* symmetry and the refined structure are shown in Figure 3.8. The final refined structural model for $La_{0.33}Sr_{0.67}MnO_{2.42}$ contains partially occupied 'bridging' anion sites (labelled O(1) and O(8) in Figure 3.8) between the 2 MnO_2 layers in the perovskite block. This results in the formation of layers comprising both MnO_5 square based pyramids and MnO_6 octahedra in the perovskite-type block. However, there is no evidence for an ordered arrangement of these different polyhedra in the *ac*-plane. For clarity, these mixed polyhedral layers are henceforth

described as comprising of ‘octahedra’, while the stacking sequence is still described as OOTOOT’.

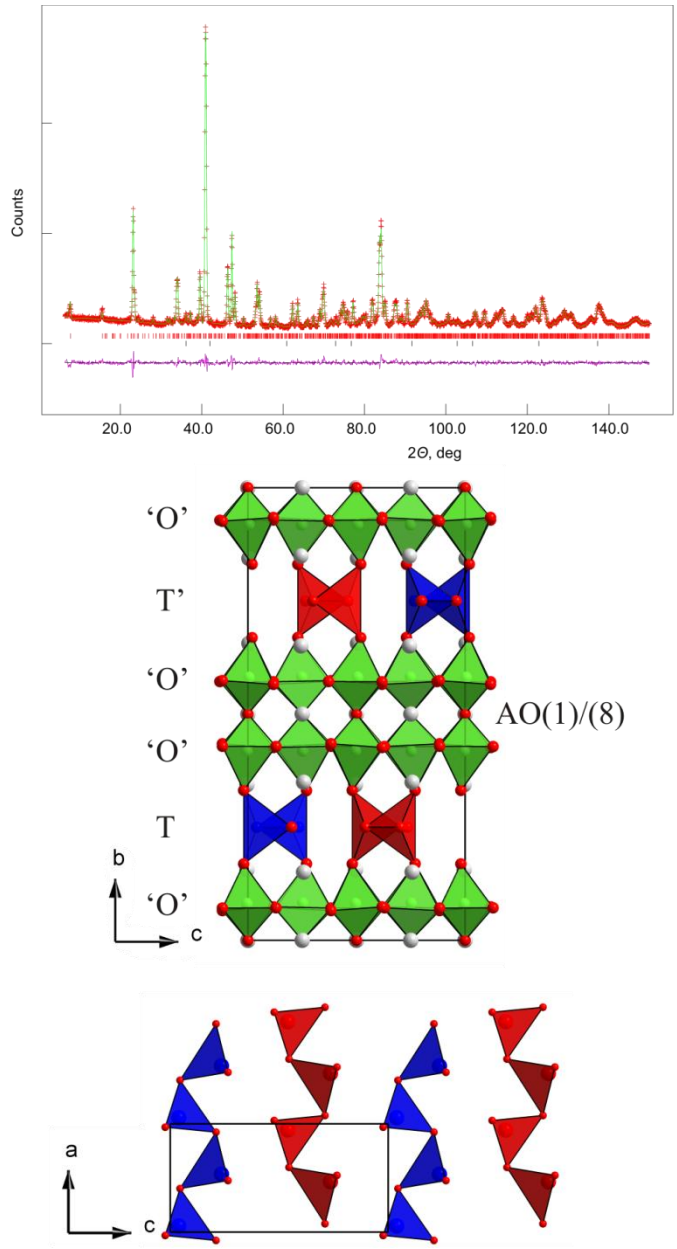


Figure 3.8: Top - observed calculated and difference plots from the structural refinement of $La_{0.33}Sr_{0.67}MnO_{2.42}$. Upper tick marks indicate peak positions from the majority phase, lower tick marks from a small quantity (1.5 wt. %) of MnO present in the sample. Middle - the refined structure of $La_{0.33}Sr_{0.67}MnO_{2.42}$. Anion sites O(1) and O(8) are 25% occupied. Bottom - a view down the *b*-axis of an -L-R-L-R- ordered tetrahedral layer. The slight disorder present in these sheets is omitted for clarity.

3.3.5. Disorder in electron diffraction data

Some electron diffraction patterns collected from $La_{0.33}Sr_{0.67}MnO_{2.42}$ crystallites exhibit slight streaking in the b^* direction (see Figure 3.5 d)). This observation is consistent with mild disorder parallel to this crystallographic direction, suggestive of a disordered stacking

along the *b*-axis of rigorously ordered *ac*-layers (no streaking along *a** or *c** directions). However, not all crystallites displayed this feature when viewed down an appropriate direction. This indicates that this disorder is not present across the entire sample with rigorous 3D order of the twisted tetrahedral chains present in the majority of the crystallites.

3.3.6. Disorder in neutron diffraction data

The proposed disorder in the arrangement of the twisted tetrahedral chains in the structure of $La_{0.33}Sr_{0.67}MnO_{2.42}$ can be in 2 forms: Firstly, there could be deviation of the rigorous 'staggering' of the tetrahedral chains between adjacent layers. This would mean that rather than the ordered SSTSST' 6-layer stacking sequence of the *RE*$Sr_2GaCu_2O_7$ structure,[61] there could be intergrowths of 3-layer OOT stacking. Alternatively the observed disorder could arise from 'faults' in the ordered array of twisted tetrahedral chains brought about by deviations from the rigorous ABAB stacking of the intralayer ordered (-L-R-L-R-) tetrahedral sheets, defined by the *Pcmb* space group, by the inclusion of some AA stacking typical of the *C2/c* structural type variant (see Figure 1.5 and Figure 3.9).

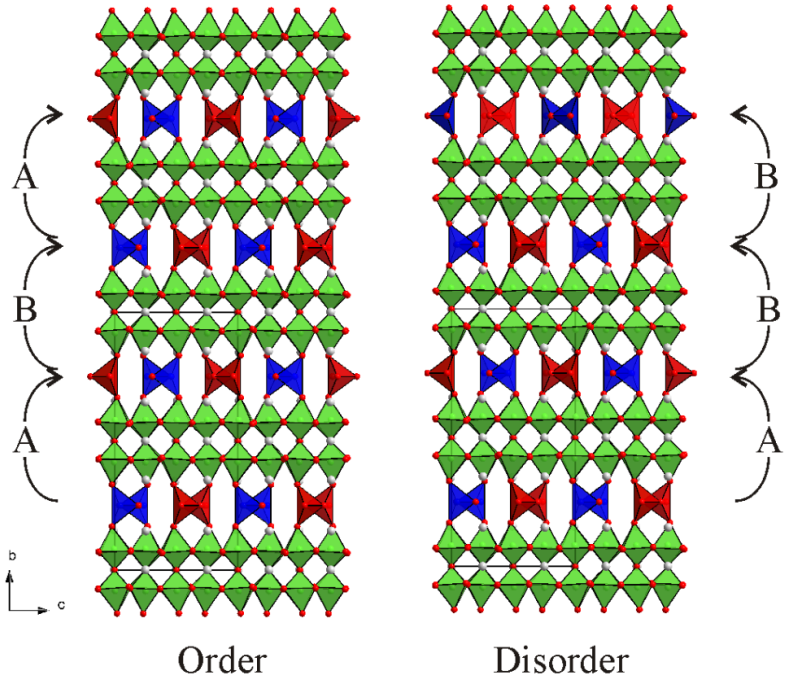


Figure 3.9: Left – *Pcmb* structural variant with regular ABA stacking of the intralayer ordered tetrahedral sheets. Right – Possible structure with deviations from ABA stacking

To determine if either of these stacking defects were present in the structure of $La_{0.33}Sr_{0.67}MnO_{2.42}$, models were constructed based on modifications to the ordered *Pcmb* model. To account for the first form of disorder described above (i.e. OOT stacking instead of OOTOOT' stacking), additional oxide ions were inserted into the tetrahedral layers of the model to represent the positions of oxide ions in 'eclipsed' tetrahedral chains (such disorder has been observed in the structure of $(La_{1/3}Sr_{2/3})_3Fe_3O_8$)).[62] Constraints were then applied to make all tetrahedral chains symmetrically equivalent.

The second form of disorder described above (i.e. regions with AA stacking instead of AB stacking) can best be described with structural models containing additional oxide ions present within the tetrahedral layers of the model to represent the positions of oxide ions in tetrahedral chains with the opposite twist to those of the ordered *Pcmb* model (i.e. an L twisted chain is superimposed on top of an R twisted chain, and vice versa). Constraints were then applied to make all the tetrahedral chains symmetrically equivalent and the fractional occupancies of both the 'correct' and 'incorrect' chains equal. This model is henceforth

described as the '*Pcmb* disorder' model. This arrangement of twisted tetrahedral chains is directly analogous to that in the *Imma* brownmillerite structural variant (see section 1.4.2).

The actual degree of disorder within the arrangement of the twisted tetrahedral chains can then be crudely quantified by allowing the fractional occupancy of the 'correct' and 'incorrect' tetrahedral chains in the '*Pcmb* disorder' model to refine. This structural model is henceforth labelled as the '*Pcmb* disorder varying *f*(Td)' model.

A second model ('*I*2*mb* anisotropic') can also be used to account for this disorder in the arrangement of the twisted tetrahedral chains. The '*I*2*mb* anisotropic' model is based on the 6-layer *I*2*mb* structural variant in which all the tetrahedral chains have the same twist direction (see Figure 3.7). However, the displacement ellipsoids of the oxide anions within the MnO layers are allowed to be highly anisotropic within the *ac*-plane in an attempt to model the scattering by oxide ions from both sets of twisted tetrahedral chains simultaneously (see Figure 3.10).

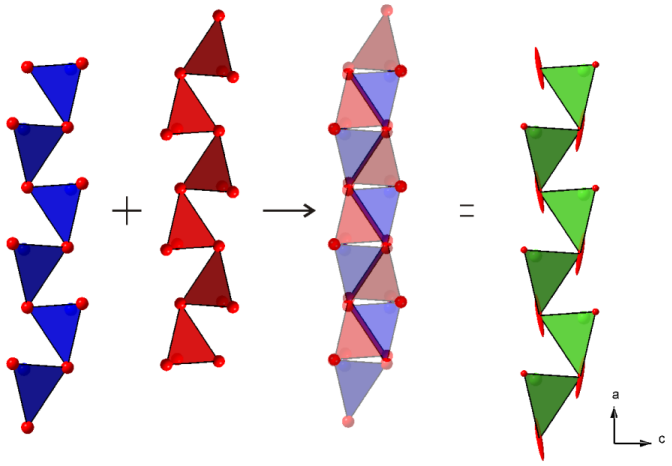


Figure 3.10: Right – tetrahedral chains in '*I*2*mb* aniso' model with anisotropic thermal ellipsoids used to account for the disorder in the arrangement of the L and R twisted tetrahedral chains.

All 3 disordered models were then refined against neutron powder diffraction data. The refinement of the disordered model describing the staggered/eclipsed disordering process was found to be highly unstable, with the occupancies of the defect sites rapidly declining to zero

when refined. This model was therefore discarded. The refinement statistics for the other disordered models are shown in Table 3.2:

Space group	χ^2	*wRp*	*Rp*
Pcmb	2.862	4.81 %	3.80 %
I2mb anisotropic	3.153	5.04 %	3.97 %
Pcmb disorder	2.918	4.85 %	3.83 %
Pcmb disorder varying *f*(Td)	2.715	4.65 %	3.68 %

Table 3.2: Fitting statistics for the refinement of 6-layer models against neutron powder diffraction data collected from $La_{0.33}Sr_{0.67}MnO_{2.42}$

Table 3.2 clearly shows that the *Pcmb* structural variant accounts for the neutron powder diffraction data more effectively that the '*Pcmb* disorder' model. This indicates that the ordering of the twisted tetrahedral chains is required to efficiently account for the neutron diffraction data. However, it is clear that the partially disordered structure with the refined fractional occupancies of the tetrahedral chains (i.e. *Pcmb* disorder varying *f*(Td)) is the most effective description of the structure. It was found that the fractional occupancy of the 'correct' tetrahedral chain converged to 0.76(2), consistent with approximately 24 % of the tetrahedral chains having the opposite twisting direction to that generated by the *Pcmb* symmetry.

3.3.7. Structural data

The refined structural parameters for $La_{0.33}Sr_{0.67}MnO_{2.42}$ using the '*Pcmb* disorder varying *f*(Td)' model with refined fractional occupancies of the tetrahedral chains are shown in Table 3.3. From inspection of Table 3.3 it is clear that the thermal parameter and fractional occupancy of the 'bridging' oxide anions (O(1) and O(8)) are ill defined given the data.

Atom	Wyckoff position	*x*	*y*	*z*	Occupancy	U_{iso} (Å^2)
La/Sr(1)	4*a*	½	0	0	0.33/0.67	0.002(1)
La/Sr(2)	4*c*	0.996(3)	0	¼	0.33/0.67	0.002(1)
La/Sr(3)	8*e*	0.499(2)	0.155(1)	0.992(1)	0.33/0.67	0.002(1)
La/Sr(4)	8*e*	0.998(2)	0.151(1)	0.254(1)	0.33/0.67	0.002(1)
Mn(1)	8*e*	0.002(5)	0.081(1)	0.997(2)	1	0.001(1)
Mn(2)	4*d*	0.535(5)	¾	0.265(2)	0.76(2)	0.001(1)
Mn(3)	4*d*	0.057(4)	¼	0.039(1)	0.76(2)	0.001(1)
Mn(4)	8*e*	0.504(3)	0.081(1)	0.250(2)	1	0.001(1)
Mn(5)	4*d*	0.464(5)	¾	0.265(2)	0.24(2)	0.001(1)
Mn(6)	4*d*	0.942(4)	¼	0.039(1)	0.24(2)	0.001(1)
O(1)	4*a*	0	0	0	0.25	0.41(5)*
O(2)	8*e*	0.969(2)	0.168(1)	0.977(1)	1	0.006(1)
O(3)	4*d*	0.923(4)	¼	0.210(1)	0.76(2)	0.006(1)
O(4)	4*d*	0.402(4)	¼	0.045(2)	0.76(2)	0.006(1)
O(5)	8*e*	0.750(4)	0.064(1)	0.374(1)	1	0.006(1)
O(6)	8*e*	0.244(3)	0.072(1)	0.363(1)	1	0.006(1)
O(7)	8*e*	0.476(2)	0.169(1)	0.265(1)	1	0.006(1)
O(8)	4*c*	½	0	¼	0.25	0.41(5)*
O(9)	8*e*	0.254(4)	0.072(1)	0.126(1)	1	0.006(1)
O(10)	8*e*	0.745(4)	0.074(1)	0.122(1)	1	0.006(1)
O(11)	4*d*	0.076(4)	¼	0.210(1)	0.24(2)	0.006(1)
O(12)	4*d*	0.597(4)	¼	0.045(2)	0.24(2)	0.006(1)
$La_{0.33}Sr_{0.67}MnO_{2.42}$: space group *Pcmb*, *a* = 5.5804(1) Å, *b* = 23.4104(7) Å, *c* = 11.2441(3) Å, cell volume = 1468.9(1) Å^3						
MnO: space group *Fm m*, *a* = 4.447(1) Å; wt. frac. = 1.5(1) %						
χ^2 = 2.715, wR_p = 4.65 %, R_p = 3.68 %						

Table 3.3: Structural parameters refined against neutron powder diffraction data collected from $La_{0.33}Sr_{0.67}MnO_{2.42}$. *The origin of the large refined displacement ellipsoids for the O(1) and O(8) ions is discussed in section 3.4.1.

Selected structural data extracted from the refined model are shown in Table 3.4 with the atomic positions labelled in Figure 3.11 and Figure 3.12.

Atom	Contact	Length (Å)	Contact	Length (Å)
Mn octahedral	Mn(1) - O(1)	1.897(23)	Mn(4) - O(5)	1.997(27)
	Mn(1) - O(2)	2.057(33)	Mn(4) - O(6)	1.940(24)
	Mn(1) - O(5)	1.997(31)	Mn(4) - O(7)	2.073(33)
	Mn(1) - O(6)	2.049(29)	Mn(4) - O(8)	1.896(23)
	Mn(1) - O(9)	2.031(31)	Mn(4) - O(9)	1.984(27)
	Mn(1) - O(10)	2.015(31)	Mn(4) - O(10)	1.977(27)
Mn tetrahedral	Mn(2) - O(3)	2.183(36)	Mn(3) - O(3)	2.063(19)
	Mn(2) - O(4)	2.262(32)	Mn(3) - O(4)	1.926(32)
	Mn(2) - O(7) x 2	1.954(24)	Mn(3) - O(2) x 2	2.101(23)
Tetrahedral twist	O(3) - O(4) - (3)	112.69(80)^o		

Table 3.4: Selected bond lengths and angle from the structural refinement of $La_{0.33}Sr_{0.67}MnO_{2.42}$.

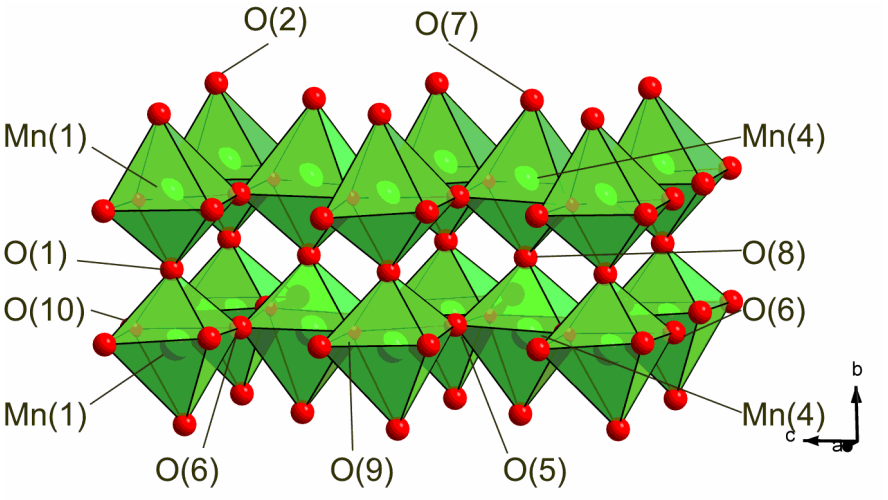


Figure 3.11: Double octahedral layer in structure of $La_{0.33}Sr_{0.67}MnO_{2.42}$

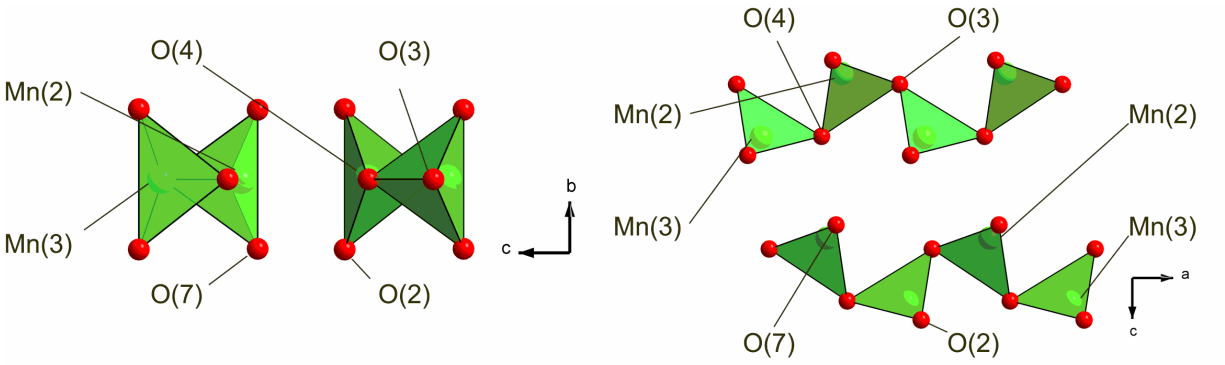


Figure 3.12: Tetrahedral layer in structure of $La_{0.33}Sr_{0.67}MnO_{2.42}$

3.4. Discussion

The reduction of $La_{0.33}Sr_{0.67}MnO_3$ to form $La_{0.33}Sr_{0.67}MnO_{2.42}$ was achieved using NaH as a solid state reducing agent. Through a combination of techniques, it was found that $La_{0.33}Sr_{0.67}MnO_{2.42}$ adopts a 6-layer structure comprising of perovskite-type blocks, containing a mixture of MnO_6 octahedra and MnO_5 square based pyramids, separated by MnO_4 tetrahedral layers. The structure contains an intralayer ordered arrangement of the twisted tetrahedral chains. However, both electron and neutron powder diffraction data collected from $La_{0.33}Sr_{0.67}MnO_{2.42}$ are consistent with slight disorder within the arrangement of the twisted tetrahedral chains. This disorder is manifested in the arrangement as the breakdown of the interlayer arrangement of the twisted tetrahedral chains with the intralayer order remaining intact.

The structure of $La_{0.33}Sr_{0.67}MnO_{2.42}$ is novel in 2 respects: Firstly, this structure is the first example of a *refined* 6-layer structure containing an intralayer ordered arrangement of the twisted tetrahedral chains. Previously refined examples of such intralayer ordered structures have been limited to some 4-layer brownmillerite structures.[12, 17, 19, 63] Secondly, the structure of $La_{0.33}Sr_{0.67}MnO_{2.42}$ is the first example of a 6-layer structure with partially filled 'bridging' anion sites (labelled O(1) and O(8) in Figure 3.8). Previously published 6-layer structures have been limited to those containing purely CuO_5 square based pyramids and BO_4 tetrahedra (e.g. *RE*$Sr_2Cu_2GaO_7$).[61] Some key features of the 6-layer structure of $La_{0.33}Sr_{0.67}MnO_{2.42}$ are discussed in the following sections.

3.4.1. Ambiguity in the empirical composition

As stated in section 3.3.4, the composition of $La_{0.33}Sr_{0.67}MnO_{3-y}$ extracted from refinement against neutron powder diffraction data differs from that obtained from reoxidative thermogravimetric data. However, the accuracy of this 'refined' composition is dependent on the ability to fully describe the scattering power of all the atomic sites. When a poorly occupied site contains a degree of positional disorder, the determination of the scattering density area for this particular site is intrinsically inaccurate. This in turn will limit the accuracy of the 'refined' composition.

The refinement of the structural model of $La_{0.33}Sr_{0.67}MnO_{2.42}$ against neutron powder diffraction data poorly accounts for the scattering power of the 'bridging' anion site (labelled O(1) and O(8) in Figure 3.8). This site has both a low fractional occupancy and slight positional disorder due to the apparently random in-plane arrangement of the MnO_6 and MnO_5 polyhedra in the structure.

Consequently, extracting the bulk fractional occupancy of this site from refinement against neutron powder diffraction data is inaccurate. As a result, the fractional occupancy of these

'bridging' oxide ion sites were constrained to values consistent with the thermogravimetric data (i.e. 25 % full in $La_{0.33}Sr_{0.67}MnO_{2.42}$) in the final structural refinement.

3.4.2. Models accounting for observed partial disorder

As shown in Figure 3.5 d), there is slight streaking of reflections involving *b** in the electron diffraction patterns collected from $La_{0.33}Sr_{0.67}MnO_{2.42}$. This streaking is evidence for slight disorder within the structure, most likely to arise from incomplete interlayer order of the twisted tetrahedral chains throughout the structure with the rigorous intralayer order remaining intact.

This disorder can be accounted for using a number of structural models: the *Imma* structural variant and the '*I*2*mb* aniso' and '*Pcmb* disorder' models. As shown in Figure 3.13, all of these models contain the superposition of a tetrahedral chain of opposing twist (an 'incorrect' chain) on top of each twisted tetrahedral chain already within the structural model (the 'correct' chains). To emphasise the differences between the model, Figure 3.13 also shows how the *Imma* structural variant and the '*I*2*mb* aniso' and '*Pcmb* disorder' models account for the scattering of one particular oxide anion in the MnO layer of both twisted chains (labelled with a black circle in Figure 3.13 a)). It should be noted that in this figure, the size of the oxide anions is proportional to the fractional occupancies of the respective anion sites.

The model based on *Imma* symmetry contains a mirror plane bisecting the tetrahedral chains which generates necessarily equal amounts of the 'correct' oxide ion and 'incorrect' oxide ion sites. This model should therefore only be applied when there is complete disorder within the arrangement of the twisted tetrahedral chains.

The '*I*2*mb* aniso' model contains a single oxide ion site located at the weighted average position of the 'correct' and 'incorrect' sites. In an attempt to model the scattering power at

both oxide sites simultaneously, the scattering density is modelled using a large prolate displacement ellipsoid.

The '*Pcmb* disorder' model contains exactly equal amounts of 'correct' and 'incorrect' sites. As stated already, this description of the tetrahedral chains is directly analogous to that in the model based on *Imma* symmetry. Finally, by allowing the fractional occupancy of both sites in the '*Pcmb* disorder' model to refine, a more accurate distribution of the scattering power of this anion can be achieved ('*Pcmb* disorder varying *f*(Td)').

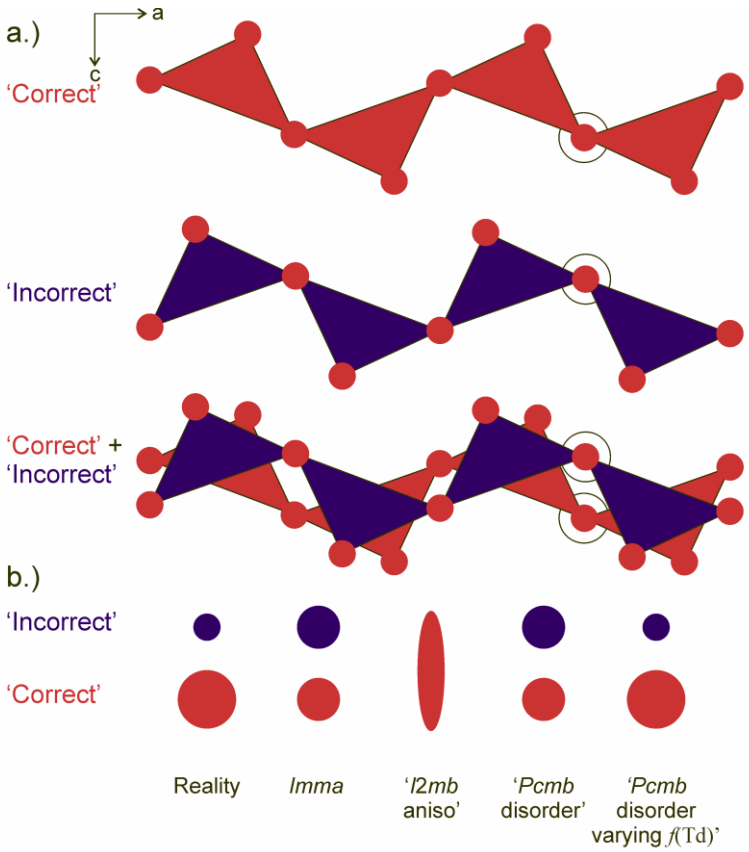


Figure 3.13: Figure depicting how several structural models account for the disorder in the arrangement of the twisted tetrahedral chains in the structure of $La_{0.33}Sr_{0.67}MnO_{2.42}$. Figure b.) shows how the oxide ions circles in Figure a.) are accounted for with the size proportional to the fractional occupancy of the site.

Comparison of the goodness of fit statistics shows that the '*Pcmb* disorder' and '*Pcmb* disorder varying *f*(Td)' models agree with neutron powder diffraction data more comprehensively than the '*I2mb* aniso' model. This observation can be rationalised in 2 ways: Firstly, the *Pcmb* symmetry in the former pair of models accounts for the tilting within

the ‘octahedral’ layers in a more effective manner. Secondly, the ‘*I2mb* anisotropic’ model predicts a maximum in the scattering density at the weighted average position of the oxide ion in the 2 opposing twist directions. In reality, no oxide ions are actually located at this average position. In contrast, the ‘*Pcmb* disorder’ and ‘*Pcmb* disorder varying *f*(Td)’ models locate the oxide ions at their correct positions with negligible scattering density at the average position.

3.4.1. Possible adoption of brownmillerite structure

Given the near ubiquity of phases adopting brownmillerite structures and the observation that the reduction of phases in the compositional range $La_{1-x}Sr_xMnO_3$ ($0.2 \leq x \leq 0.5$) results in the formation of reduced materials which adopt 4-layer $A_2B_2O_5$ brownmillerite structures,[17, 20] it is pertinent to ask: why does the reduction of $La_{0.33}Sr_{0.67}MnO_3$ not result in the formation of the hypothetical brownmillerite type phase ‘$La_{0.33}Sr_{0.67}MnO_{2.5}$’?

Some light can be shed on this issue by considering the structures of the $La_{1-x}Sr_xMnO_{2.5}$ ($0.2 \leq x \leq 0.5$) brownmillerite phases in detail. Bond valence sum calculations indicate that the tetrahedral manganese coordination sites within these $La_{1-x}Sr_xMnO_{2.5}$ ($0.2 \leq x \leq 0.5$) brownmillerite phases are occupied exclusively by Mn^{2+} centres,[17, 20] with the remaining octahedral sites occupied by a mixture of Mn^{2+} and Mn^{3+} centres in a proportion defined by the La:Sr ratio. Therefore, as shown in Figure 3.14, the octahedral sites in the most Sr^{2+}-rich brownmillerite phase, $La_{0.5}Sr_{0.5}MnO_{2.5}$, are exclusively occupied by Mn^{3+} centres.

The manganese centres in the hypothetical phase ‘$La_{0.33}Sr_{0.67}MnO_{2.5}$’ would have an average oxidation state of Mn+2.67 and as a consequence, if this phase were to adopt a brownmillerite type structure, would require some Mn^{3+} cations to be located within tetrahedral sites. This situation is highly unfavourable on CFSE and electrostatic grounds as demonstrated by the adoption of the ‘normal’ spinel structure by Mn_3O_4 and the disproportionation of Mn^{3+} to Mn^{2+} and Mn^{4+} within the spinel $NiMn_2O_4$.[64, 65]

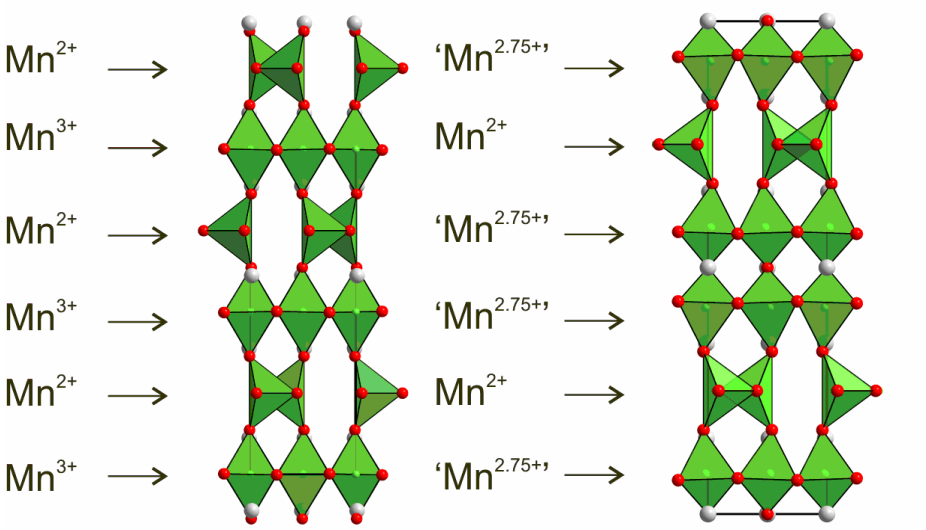


Figure 3.14: Oxidation states of the manganese centres in 4-layer brownmillerite $La_{0.5}Sr_{0.5}MnO_{2.5}$ (left) and 6-layer $La_{0.33}Sr_{0.67}MnO_{2.42}$ (right) phases.

Therefore, it was hypothesised that in contrast to the behaviour of the La^{3+}-rich $La_{1-x}Sr_xMnO_3$ phases, reduction of $La_{0.33}Sr_{0.67}MnO_3$ does not lead to the formation of a brownmillerite type phase so as to avoid the formation of tetrahedral Mn^{3+} sites. Instead a 6-layer structure is adopted in which the inclusion of an additional 'octahedral' layer into the stacking sequence removes the need to locate Mn^{3+} centres on tetrahedral sites, as shown in Figure 3.14.. Indeed, as shown in Table 3.5, bond valence sum calculations are consistent with the tetrahedral manganese sites in $La_{0.33}Sr_{0.67}MnO_3$ having an oxidation state of +2. Based on this argument, it is expected that brownmillerite phases will not be formed as products of the reduction of $La_{1-x}Sr_xMnO_3$ phases where $x > 0.5$.

Mn-site	Anion-site	Length (Å)	Contacts	BVS per contact	BVS	Total per cation
Mn3	O2	2.10	2	0.43	0.87	
	O4	1.92	1	0.70	0.70	
	O3	2.06	1	0.48	0.48	2.05
Mn2	O7	1.95	2	0.65	1.30	
	O3	2.26	1	0.28	0.28	
	O4	2.18	1	0.35	0.35	1.92

Table 3.5: Bond valence calculations for tetrahedral manganese sites in $La_{0.33}Sr_{0.67}MnO_{2.42}$

3.4.2. Comparison to *RE*$Sr_2Cu_2GaO_7$

There are clear similarities between the 6-layer structures of $La_{0.33}Sr_{0.67}MnO_{2.42}$ and *RE*$Sr_2Cu_2GaO_7$. Both structures contain double layers of BO_6 octahedra or BO_5 square based pyramids separated by layers containing chains of tetrahedra running down the $[101]_p$ direction of the simple perovskite unit cell.

As described previously, Roth *et al.* described the structure of *RE*$Sr_2Cu_2GaO_7$ as containing an ordered array of twisted tetrahedral chains with each tetrahedral chain having the same twisting direction (i.e. all L or all R, i.e. equivalent to the *I*2*mb* 6-layer structural variant).[61] However more recent structural reinvestigations of a number of 6-layer anion-deficient phases, most notably *RE*$Sr_2Cu_2GaO_7$ (*RE* = Y^{3+}),[63] based on electron diffraction data have been conducted.[61] It was found that the 6-layer structure of $YSr_2Cu_2GaO_7$ also contained an intralayer ordered arrangement of the twisted tetrahedral chains but again with significant disorder in the arrangement.[63] However, a full structural refinement of this proposed model of $YSr_2Cu_2GaO_7$ against neutron diffraction data was not carried out.

3.5. Conclusion

The formation of $La_{0.33}Sr_{0.67}MnO_{2.42}$ via the reduction of $La_{0.33}Sr_{0.67}MnO_3$, clearly demonstrates that highly reduced phases can be prepared by the reduction of $La_{1-x}Sr_xMnO_3$ ($x > 0.5$) substrates if sufficiently powerful reducing agents are used. The novel 6-layer anion-vacancy ordered structure adopted by $La_{0.33}Sr_{0.67}MnO_{2.42}$ has an apparently flexible anion content (via the partial occupation of the anion sites which link neighbouring 'octahedral' layers) suggesting it will be formed over a wide range of La:Sr ratios. Furthermore the adoption of this 6-layer structure in preference to the more common 4-layer brownmillerite structure - a preference proposed to be driven by the aversion to the formation of tetrahedral Mn^{3+} centres - reaffirms the importance of electronic/lattice coupling in

directing and determining the structure and anion mobility of anion deficient manganese perovskites. The research and findings in this chapter have been recently been published.[66]

Appendix 3

A. 3.1. (3+1)D crystallography

A. 3.1.1 Introduction

During the course of this investigation a number of phases with 6-layer structures containing tetrahedral layers analogous to those in the 4-layer brownmillerite structure were synthesised (see Chapter 3-6). These 6-layer structures contain OOTOOT' stacking of the octahedral (O) and tetrahedral (T) layers rather than the 4-layer OTOT' stacking present in the brownmillerite structure. A recent structural reinvestigation of the brownmillerite phase $Sr_2Fe_2O_5$ has shown the effectiveness of using electron diffraction data to differentiate between the different structural variants described above.[16]

The structural similarities of the $La_{1-x}A_xMnO_{2.5}$ brownmillerite phases to these 6-layer OOTOOT' materials means the symmetry analysis used to describe the twisted tetrahedral chain ordering scheme in the brownmillerite structures is directly applicable to the description of twisted tetrahedral chain ordering schemes of the 6-layer structures prepared in this study. A brief review of the use of (3+1)D crystallography to describe the structure of $Sr_2Fe_2O_5$ and its applicability to the 6-layer materials synthesised in this investigation is detailed below.

A. 3.1.2 Brownmillerite phases

The main reflections in the electron diffraction data sets collected from $Sr_2Fe_2O_5$ can be indexed using lattice parameters consistent with a brownmillerite structure.[16] However, satellite reflections, generally of lower intensity, indicate that a more complex description of the structure is required. All reflections, both strong and weak, could be indexed using a unit cell consistent with a (3+1)D structure.[16]

Whereas the atomic positions in a commensurate structures can be described using a lattice described by 3 vectors (*h*, *k* and *l*), materials described as incommensurate have their periodic

structures more effectively described using more than 3 vectors. These extra vectors are used to describe a periodic deformation of this basic 3D structure propagating throughout the lattice.

D'Hondt *et al.*, modelled the ordering of the tetrahedral chains as a modulation of the basic underlying 3D brownmillerite structure.[16] This formalisation results in the description of the overall structure with a (3+1)D structure, where 3 vectors (*h*, *k* and *l*) are used to describe the 3D structure and a 4th vector (*m*) is used to describe the modulation of this lattice caused by the ordering of the tetrahedral chains.

By using an incommensurate lattice based on a (3+1)D unit cell, all electron diffraction reflections can be indexed using 4 indices, *h*, *k*, *l* and *m*, in which the diffraction vector (**g**) is defined as $\mathbf{g} = h\mathbf{a^*} + k\mathbf{b^*} + l\mathbf{c^*} + m\mathbf{q^*}$, where **q**, the modulation vector, is defined as $\mathbf{q} = \beta\mathbf{b^*} + \gamma\mathbf{c^*}$. The values of β and γ can be determined by the reflection conditions in the electron diffraction data and so the superspace group (space groups describing this (3+1)D structure) can be restricted to 1 of 2 possibilities:[16, 67] For the general case when $\beta = 0$, the orthorhombic *Imma*(00γ)*s*00 (where $\mathbf{q} = \gamma\mathbf{c^*}$) superspace group can be used. For the case when $0 < \beta \leq ½$, the monoclinic *I*2/*m*(0$\beta\gamma$)0*s* (where $\mathbf{q} = \beta\mathbf{b^*} + \gamma\mathbf{c^*}$) superspace group, a subgroup of *Imma*(00γ)*s*00, can be used.

Superspace groups can be broken up into 3 parts: the basic space group of the unmodulated structure (i.e. *Imma* or *I*2/*m*), the symmetry of the modulation ((*s*00) or (0*s*)) and the direction and periodicity of the modulation ((00γ) or (0$\beta\gamma$)) where β is associated with the ordering of the tetrahedral chains along the stacking vector. For example, 2 of the simplest ordering arrangements of the twisted tetrahedral chains in brownmillerite and related phases are those with *Pcmb* and *C*2/*c* symmetry. These arrangements can be described using 2 example stacking vectors, ½[111] and ½[11], as shown in Figure 3.15:

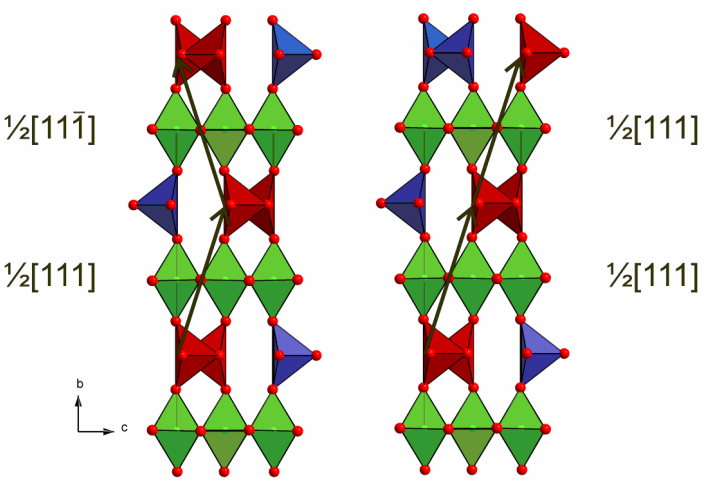


Figure 3.15: Figure shows the *Pcmb* (left) and *C*2/*c* (right) brownmillerite structural variants with 2 simple brownmillerite stacking vectors. The red and blue chains designate the L and R twisted tetrahedral chains. This figure is adapted from work by D'Hondt *et al.*[16]

If β and γ are simple fractions, the incommensurate structure can be described using a simple 3D structure with only a small geometric expansion relative to the underlying 3D lattice. The superspace groups and values for β and γ for the 5 simplest brownmillerite models described in section 1.4.2 are shown in Table 3.6. In addition Table 3.6 contains the lattice parameters for the 3D structures compared to those of a simple cubic perovskite structure. However, it should be noted that other more complicated ordering patterns are, in principle, possible.[67]

Superspace group	β	γ	Space group	Lattice parameters for 3D structure*
Imma(00γ)*s*00		0	*I*2*mb*	$\sqrt{2}a_p$ x $4a_p$ x $\sqrt{2}a_p$
Imma(00γ)*s*00		0	*Imma*	$\sqrt{2}a_p$ x $4a_p$ x $\sqrt{2}a_p$
Imma(00γ)*s*00		1	*Pnma*	$\sqrt{2}a_p$ x $4a_p$ x $\sqrt{2}a_p$
Imma(00γ)*s*00		½	*Pcmb*	$\sqrt{2}a_p$ x $4a_p$ x $2\sqrt{2}a_p$
*I*2/*m*(0$\beta\gamma$)0*s*	½	½	*C*2/*c*	

Table 3.6: Pertinent parameters for the (3+1)D superspace groups of the 5 simplest twisted tetrahedral chain ordering schemes in the brownmillerite structure. *The *C*/2*c* structural variant is based on an expanded unit cell which can't easily be related to that of a simple cubic perovskite.

This method for indexation of electron diffraction patterns was successfully used by Parsons *et al.* to determine the space groups of, and therefore twisted tetrahedral chain ordering schemes in, the structures of the $La_{1-x}A_xMnO_{2.5}$ ($x \leq 0.5$, A = Ca^{2+}, Sr^{2+} and Ba^{2+}) brownmillerite phases.[17] However, the authors noted the existence of an added complication

to the indexation of the electron diffraction patterns collected from these phases. On descending from a (3+1)D superspace group to a 3D space group, certain symmetry relations present in the superspace group are lost. Therefore, extra reflection conditions on top of those inherent in the 3D space group are observed. This implies that the actual structure of these brownmillerite phases contains translational symmetry elements over and above those described by the 3D space group.

A. 3.1.3 6-layer phases

The ordering of the twisted tetrahedral chains in the 6-layer structures in this investigation can be described in a directly analogous fashion to the brownmillerite phases. For example, 2 of the simplest ordering arrangements of the twisted tetrahedral chains in the 6-layer structures are those with *Pcmb* and *C*2/*c* symmetry. These arrangements can be described using the same example stacking vectors, ½[111] and ½[11] used to describe analogous arrangements in the brownmillerite phases.

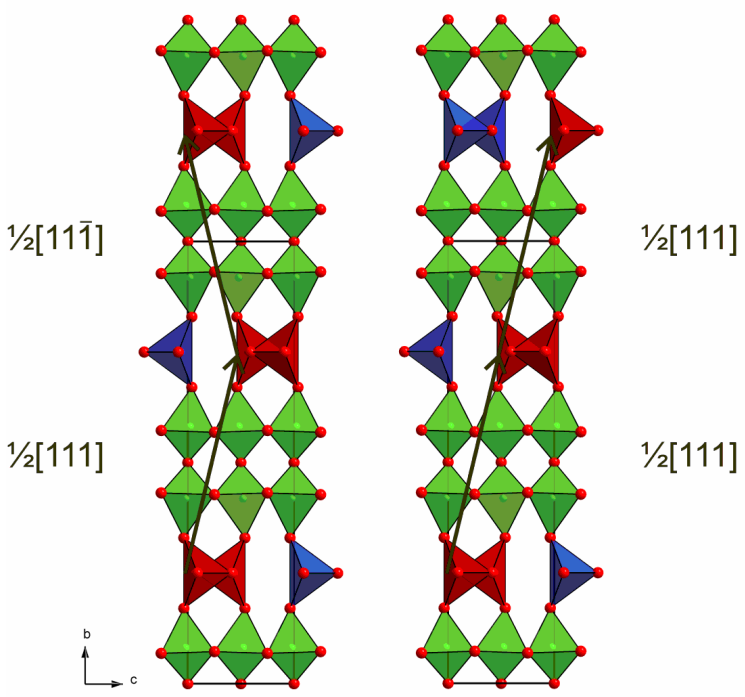


Figure 3.16: Figure shows the *Pcmb* (left) and *C*2/*c* (right) 6-layer structural variants with 2 simple stacking vectors.

As above, the simple 6-layer models in section 3.3.4 can be described with the following superspace groups and simple values of β and γ, as shown in Table 3.7. Again, more complicated ordering patterns of the twisted tetrahedral chains are possible.

Superspace group	$\boldsymbol{\beta}$	$\boldsymbol{\gamma}$	**Space group**	**Lattice parameters for 3D structure**
Imma(00γ)*s*00		0	*I*2*mb*	$\sqrt{2}a_p$ x $6a_p$ x $\sqrt{2}a_p$
Imma(00γ)*s*00		0	*Imma*	$\sqrt{2}a_p$ x $6a_p$ x $\sqrt{2}a_p$
Imma(00γ)*s*00		1	*Pnma*	$\sqrt{2}a_p$ x $6a_p$ x $\sqrt{2}a_p$
Imma(00γ)*s*00		½	*Pcmb*	$\sqrt{2}a_p$ x $6a_p$ x $2\sqrt{2}a_p$
*I*2/*m*(0$\beta\gamma$)0*s*	½	½	*C*2/*c*	

Table 3.7: Pertinent parameters for the (3+1)D superspace groups of the 5 simplest twisted tetrahedral chain ordering schemes in the 6-layer analogue of the brownmillerite structure.

Chapter 4: Reduction of $La_{1-x}Sr_xMnO_3$ ($0.6 \leq x \leq 0.75$)

4.1. Introduction

The topotactic reduction of $La_{0.33}Sr_{0.67}MnO_3$ yields $La_{0.33}Sr_{0.67}MnO_{2.42}$ which adopts a novel anion vacancy ordered structure with OOTOOT' stacking of the 'octahedral' (O) and tetrahedral (T) layers. This structure of $La_{0.33}Sr_{0.67}MnO_{2.42}$ forms part of a family of anion-deficient materials which accommodate anion vacancies in layers containing BO_4 tetrahedra stacked with other layers. Other members of this structural family include brownmillerite phases (OTOT' stacking), the 6-layer *RE*$Sr_2GaCu_2O_7$ phase (SSTSST' stacking) and the 3-layer $(La_{1/3}Ca_{2/3})_3Fe_3O_8$ phase (OOT stacking).

However, unlike other members of this structural family, the structure of $La_{0.33}Sr_{0.67}MnO_{2.42}$ contains some partially occupied anion sites (see Figure 3.6). The 'well-defined' oxygen contents of the other phases in this structural family, *RE*$Sr_2GaCu_2O_7$ and $(La_{1/3}Ca_{2/3})_3Fe_3O_8$ for example, are an obvious mechanism for controlling the structures of these materials.[60, 61] In contrast, the oxide anion content in $La_{0.33}Sr_{0.67}MnO_{2.42}$ appears somewhat arbitrary. The partial occupancy of the 'bridging' anion sites suggests that the level of reduction of $La_{0.33}Sr_{0.67}MnO_3$ is controlled to some degree by some additional factor, possibly electronic in origin. Further examples of this '6-layer manganate' structure are required to establish if there are any similarities in the empirical compositions and to evaluate the nature of this proposed electronically controlled end-point for reduction.

In addition, the structure of $La_{0.33}Sr_{0.67}MnO_{2.42}$ contains intralayer ordering of the twisted tetrahedral chains. As a direct analogy to the structurally related brownmillerite phases, a number of other possible 6-layer structural variants could exist with arrangements of the twisted tetrahedral chains (see section 1.4.2). Further examples of the '6-layer manganate' structure are required to ascertain whether any of these other possible 6-layer structural

variants are adopted Therefore, the topotactic reduction chemistries of phases in the range $La_{1-x}Sr_xMnO_3$ ($0.5 \leq x \leq 1$) were investigated.

4.2. Experimental

4.2.1. Synthesis of perovskite starting materials

5 g samples of $La_{1-x}Sr_xMnO_3$ (x = 0.5, 0.6, 0.7, 0.75, 0.83, 0.9 and 1) were prepared using the same synthetic procedure as that described for the synthesis of $La_{0.33}Sr_{0.67}MnO_3$ outlined in section 3.2.1.[58] The appropriate stoichiometric ratios of La_2O_3 (99.999 %, dried at 900 ^oC), $SrCO_3$ (99.99 %) and MnO_2 (99.999 %) were ground with an agate pestle and mortar and then heated at 900 ^oC in air. The resulting powders were reground, pressed into 2-3 g, 13 mm pellets and heated at 1350 ^oC for 3 x 48 hours under flowing argon. After each heating cycle the materials were reground and pressed into pellets as before. Finally, the samples were annealed at 500 ^oC in air for 12 hours, before slow cooling to room temperature. X-ray powder diffraction patterns confirmed that phase-pure samples of all the target materials had been obtained with lattice parameters in good agreement with published values (see Table 4.7 in Appendix 4).[58]

4.2.2. Low temperature reduction with metal hydrides

Low temperature reactions of phases in the compositional range $La_{1-x}Sr_xMnO_3$ ($x \geq 0.5$) with NaH were carried out using the same method used for the reduction of $La_{0.33}Sr_{0.67}MnO_3$ (see section 3.2.2). 5 g samples of $La_{1-x}Sr_xMnO_3$ were ground thoroughly with 2 mole equivalents of NaH in an argon-filled glovebox and then sealed under vacuum in a Pyrex ampoule. The mixtures were then heated at 180 ^oC for 12 hours and then 210 ^oC for 4 x 48 hours with the mixture being ground in an argon-filled glovebox after each heating cycle. The samples were then washed with 4 x 100 ml of CH_3OH under nitrogen to remove sodium-containing phases (NaOH and NaH) before being dried under vacuum.

4.2.3. Annealing

It was found that annealing $La_{0.33}Sr_{0.67}MnO_{2.42}$ resulted in an improvement in crystallinity (see section 3.3.1). Therefore, annealing experiments were conducted for the washed products of the reactions detailed above, the results of which are shown in Table 4.1.

<table>
<tr><th rowspan="2">$La_{1-x}Sr_xMnO_3$</th><th colspan="5">Annealing Temperature (^oC)</th></tr>
<tr><th>300</th><th>350</th><th>400</th><th>450</th><th>500</th></tr>
<tr><td>0.5</td><td rowspan="8" colspan="2">No improvement in crystallinity</td><td colspan="2" rowspan="2">Decomposition</td><td rowspan="8">Decomposition</td></tr>
<tr><td>0.6</td></tr>
<tr><td>0.67</td><td colspan="2" rowspan="3">Improvement in crystallinity</td></tr>
<tr><td>0.7</td></tr>
<tr><td>0.75</td></tr>
<tr><td>0.83</td><td colspan="2" rowspan="3">Decomposition</td></tr>
<tr><td>0.9</td></tr>
<tr><td>1.0</td></tr>
</table>

Table 4.1: Results from annealing washed products of reactions involving $La_{1-x}Sr_xMnO_3$ substrate phases and NaH

Subsequent measurements were therefore performed on annealed products (400 ^oC for 48 hours) of the reactions involving $La_{0.3}Sr_{0.7}MnO_3$ and $La_{0.25}Sr_{0.75}MnO_3$. However, subsequent measurements were performed on 'unannealed' samples of the other $La_{1-x}Sr_xMnO_3$ ($x \geq 0.5$) substrate phases.

4.3. Results

4.3.1. Thermogravimetric analysis ($0.6 \leq x \leq 1$)

Thermogravimetric data collected during the reoxidation of the washed products of the reaction between $La_{1-x}Sr_xMnO_3$ ($x \geq 0.6$) and NaH are shown in Figure 4.22 in Appendix 4, with the relevant details shown in Table 4.2.

$La_{1-x}Sr_xMnO_{3-(0.5+x)/2}$	Mass gain (%)	Empirical stoichiometry	Manganese oxidation state
0.6	4.41(4)	$La_{0.4}Sr_{0.6}MnO_{2.44(5)}$	+2.4(1)
0.7	4.82(5)	$La_{0.3}Sr_{0.7}MnO_{2.41(5)}$	+2.5(1)
0.75	5.14(3)	$La_{0.25}Sr_{0.75}MnO_{2.38(3)}$	+2.51(6)
0.83	5.42(4)	$La_{0.17}Sr_{0.83}MnO_{2.36(5)}$	+2.5(1)
0.9	5.88(3)	$La_{0.1}Sr_{0.9}MnO_{2.32(4)}$	+2.54(8)
1	6.97(3)	$SrMnO_{2.22(3)}$	+2.44(6)

Table 4.2: Relevant data from thermogravimetric analysis of $La_{1-x}Sr_xMnO_{3-y}$ ($x \geq 0.6$) phases

X-ray powder diffraction data collected from the products of the oxidation reactions are consistent with phase-pure samples of the $La_{1-x}Sr_xMnO_3$ starting materials, suggesting that topotactic reduction reactions had occurred. As shown in Table 4.2, the reoxidative thermogravimetric data are consistent with all $La_{1-x}Sr_xMnO_{3-(0.5+x)/2}$ ($0.6 \leq x \leq 0.83$) reduced phases containing manganese centres with an average oxidation state of +2.5 within error. The empirical stoichiometries of the reduced phases follow the general relationship: $La_{1-x}Sr_xMnO_{3-(0.5+x)/2}$.

4.3.2. X-ray diffraction data

Inspection of X-ray powder diffraction data collected from the washed products of the reaction between NaH and the $La_{1-x}Sr_xMnO_3$ substrate phases revealed that the products fall into 3 general classes as a function of the La:Sr ratio:

1. $x = 0.5$. The data are consistent with this reduced phase adopting the brownmillerite structure previously reported for $La_{0.5}Sr_{0.5}MnO_{2.5}$ (see Figure 4.23 in Appendix 4 for fit to data).[20] The difference in the topotactic reduction chemistries of $La_{0.5}Sr_{0.5}MnO_3$ and $La_{0.33}Sr_{0.67}MnO_3$ will be discussed in section 6.3.2.
2. $0.6 \leq x \leq 0.83$. All reflections could be indexed using unit cells based on that of $La_{0.33}Sr_{0.67}MnO_{2.42}$ (i.e. a $\sqrt{2}a_p$ x $6a_p$ x $2\sqrt{2}a_p$ expansion (see section 3.3.3)).
3. $x = 0.9$ and 1. The patterns could be partially indexed using unit cells based on that of $La_{0.33}Sr_{0.67}MnO_{2.42}$ but also contained several additional weak reflections inconsistent with this structural model.

Refinements of structural models based on the 6-layer structure of $La_{0.33}Sr_{0.67}MnO_{2.42}$ against X-ray powder diffraction data collected from phases in the range $La_{1-x}Sr_xMnO_{3-(0.5+x)/2}$ ($0.6 \leq x \leq 0.83$) resulted in satisfactory fits. Observed, calculated and difference plots for the refinements are shown in Figure 4.24 - Figure 4.27 in Appendix 4. Fuller structural

investigation of these 6-layer phases based on electron and neutron diffraction data is detailed in this chapter.

In contrast, refinements of structural models based on the 6-layer structure of $La_{0.33}Sr_{0.67}MnO_{2.42}$ against X-ray powder diffraction data collected from $La_{0.1}Sr_{0.9}MnO_{2.3}$ and $SrMnO_{2.25}$ gave only acceptable fits (see Figure 5.16 and Figure 5.17 in Appendix 5). This suggests that these Sr^{2+}-rich compositions adopt 6-layer structures closely related, but not identical, to that of $La_{0.33}Sr_{0.67}MnO_{2.42}$. A fuller description of the 6-layer structures of the Sr^{2+}-rich phases is covered in Chapter 5.

4.3.3. Electron diffraction data ($0.6 \leq x \leq 0.83$)

Electron diffraction data were collected from the phases in the range $La_{1-x}Sr_xMnO_{3-(0.5+x)/2}$ ($0.6 \leq x \leq 0.83$) to confirm the size and symmetry of the unit cells. Examination of the electron diffraction data sets revealed that the reduced phases fall into 3 general classes as a function of the La:Sr ratio:

1. x = 0.6. Data collected from $La_{0.4}Sr_{0.6}MnO_{2.45}$ are consistent with this phase adopting a 6-layer structure highly similar to that of $La_{0.33}Sr_{0.67}MnO_{2.42}$ but with a greatly expanded unit cell. A fuller structural investigation of $La_{0.4}Sr_{0.6}MnO_{2.45}$ is described in Chapter 6.
2. x = 0.75 (see Figure 4.1 a) and b)). The majority of the data can be indexed using a unit cell based on a $\sqrt{2}a_p$ x $6a_p$ x $\sqrt{2}a_p$ expansion with *I*2*mb* or *Imma* symmetry (i.e. the *c*-axis is halved relative to that of the structure of $La_{0.33}Sr_{0.67}MnO_{2.42}$). However, some of the data sets contain weak additional reflections (e.g. the reflection in Figure 4.1 c)) that require a doubling of the *c*-axis (i.e. a $\sqrt{2}a_p$ x $6a_p$ x $2\sqrt{2}a_p$ expansion). The doubling of the *c*-axis to a length of $2\sqrt{2}a_p$ is consistent with 3D intralayer order of the twisted tetrahedral chains in some crystallites of $La_{0.25}Sr_{0.75}MnO_{2.38}$.

3. x = 0.83. Electron diffraction data are consistent with this material adopting a 6-layer structure analogous to that of $La_{0.33}Sr_{0.67}MnO_{2.42}$. However, HAADF-STEM data collected from this phase are consistent with stacking defects in the OOTOOT' ordering sequence (see Figure 5.7). A fuller structural investigation of the structure of $La_{0.17}Sr_{0.83}MnO_{2.33}$ will be covered in Chapter 5.

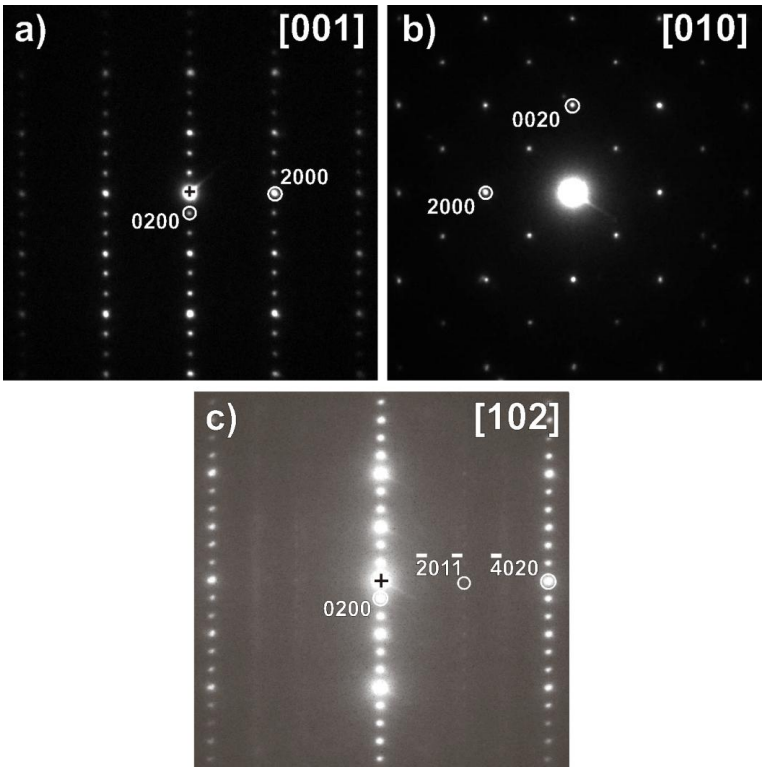


Figure 4.1: Electron diffraction data collected from the (a) [001], (b) [010] and (c) [102] zone axes of $La_{0.25}Sr_{0.75}MnO_{2.38}$ by Prof. Dr. Joke Hadermann.

A full investigation of the structures of $La_{0.3}Sr_{0.7}MnO_{2.4}$ and $La_{0.25}Sr_{0.75}MnO_{2.38}$ is detailed in the following sections.

4.3.4. Neutron diffraction data (x= 0.7 and 0.75)

Neutron powder diffraction data were collected from $La_{0.3}Sr_{0.7}MnO_{2.4}$ and $La_{0.25}Sr_{0.75}MnO_{2.38}$ using the D1a instrument (see section 2.3.2.1.2) to determine their structures. As discussed in section 3.3.4, the 3D arrangement of the twisted tetrahedral chains in the 6-layer OOTOOT'-stacked structure can yield a number of distinct structural variants. Models of the 5 simplest variants, i.e. those with *I*2*mb*, *Imma*, *Pnma*, *C*2/*c* and *Pcmb*

symmetry, were constructed for $La_{0.3}Sr_{0.7}MnO_{2.4}$ and $La_{0.25}Sr_{0.75}MnO_{2.38}$ and refined against neutron powder diffraction data.

During the refinements the fractional occupancies of all the anion sites were allowed to vary to account for the oxide non-stoichiometry of the reduced phases. In each refinement, the majority of the anion sites remained fully occupied within error with the exception of the 'bridging' anion site linking the neighbouring 'octahedral' layers (labelled O(1) and O(8) in Figure 3.6). The fractional occupancies of the 'bridging' anion sites refined to levels consistent with more anion-deficient empirical stoichiometries than suggested by reoxidative thermogravimetric data (see Table 4.2). Thus for consistency the fractional occupancies of these 'bridging' anion sites were constrained to levels consistent with the thermogravimetric data in each refinement (i.e. 0.2 for $La_{0.3}Sr_{0.7}MnO_{2.4}$ and 0.14 for $La_{0.25}Sr_{0.75}MnO_{2.38}$). The goodness of fit statistics for each refinement against neutron powder diffraction data are shown in Table 4.3.

Phase	**Space group**	χ^2	***wRp***	***Rp***
$La_{0.3}Sr_{0.7}MnO_{2.4}$	*I2mb*	3.735	6.05 %	4.61 %
	Imma	2.955	5.39 %	4.11 %
	Pnma	3.492	5.85 %	4.48 %
	C2/c	3.421	5.79 %	4.41 %
	Pcmb	2.425	4.86 %	3.81 %
$La_{0.25}Sr_{0.75}MnO_{2.38}$	*I2mb*	3.280	5.76 %	4.41 %
	Imma	2.964	5.46 %	4.24 %
	Pnma	3.306	5.76 %	4.44 %
	C2/c	2.806	5.31 %	4.13 %
	Pcmb	1.946	4.44 %	3.51 %

Table 4.3: Fitting statistics for the refinement of 6-layer models against neutron powder diffraction data collected from $La_{0.3}Sr_{0.7}MnO_{2.4}$ and $La_{0.25}Sr_{0.75}MnO_{2.38}$

In an analogous fashion to $La_{0.33}Sr_{0.67}MnO_{2.42}$, the models based on *Pcmb* symmetry which contain intralayer order of the twisted tetrahedral chains give the best fit to the neutron powder diffraction data collected from both $La_{0.3}Sr_{0.7}MnO_{2.4}$ and $La_{0.25}Sr_{0.75}MnO_{2.38}$.

As discussed in section 3.3.4, there is a certain amount of disorder in the arrangement of the twisted tetrahedral chains in the structure of $La_{0.33}Sr_{0.67}MnO_{2.42}$. While there is rigorous

intralayer order of the chains in the structure of $La_{0.33}Sr_{0.67}MnO_{2.42}$, there is incomplete interlayer order (i.e. faults in the ABA stacking arrangement of the tetrahedral layers). Some electron diffraction patterns collected from $La_{0.25}Sr_{0.75}MnO_{2.38}$ (i.e. those that can only be indexed using a *c*-axis with a length of $2\sqrt{2}a_p$ - see Figure 4.1 c)) are consistent with intralayer order of the twisted tetrahedral chains in the structure. However, the majority of the patterns do not require such a structural feature.

Given that some, but not all, of the electron diffraction patterns require a *c*-axis of length $2\sqrt{2}a_p$, it is logical to propose that the structure of $La_{0.25}Sr_{0.75}MnO_{2.38}$, in an analogous fashion to the structure of $La_{0.33}Sr_{0.67}MnO_{2.42}$, contains rigorous intralayer order of the twisted tetrahedral chains but incomplete interlayer order. The lack of full 3D order in the arrangement of the twisted tetrahedral chains prevents this proposed intralayer ordered arrangement of the twisted tetrahedral chains being experimentally observed in all the electron diffraction data sets.

Given that the La:Sr ratio in $La_{0.3}Sr_{0.7}MnO_{2.4}$ falls between those in $La_{0.33}Sr_{0.67}MnO_{2.42}$ and $La_{0.25}Sr_{0.75}MnO_{2.38}$, it is highly likely that $La_{0.3}Sr_{0.7}MnO_{2.4}$ also adopts a similar structure containing intralayer order of the twisted tetrahedral chains, yet incomplete interlayer order.

4.3.5. Disorder in neutron diffraction data (x = 0.7 and 0.75)

In order to characterise the proposed disorder in the structures of $La_{0.3}Sr_{0.7}MnO_{2.4}$ and $La_{0.25}Sr_{0.75}MnO_{2.38}$ a series of structural models, directly analogous to those utilised to analyse the disorder in the structure of $La_{0.33}Sr_{0.67}MnO_{2.42}$ (see section 3.3.6) were constructed and refined against neutron powder diffraction data. In common with the refinement against the data collected from $La_{0.33}Sr_{0.67}MnO_{2.42}$, refinement of models describing the possible staggered/eclipsed disordering of the tetrahedral chains were highly unstable when refined against neutron powder diffraction data collected from $La_{0.3}Sr_{0.7}MnO_{2.4}$ and $La_{0.25}Sr_{0.75}MnO_{2.38}$. These models were therefore discarded.

In contrast, refinement of the '*I2mb* anisotropic', '*Pcmb* disorder' and '*Pcmb* disorder varying *f*(Td)' models (see section 3.3.6) against neutron powder diffraction data collected from $La_{0.3}Sr_{0.7}MnO_{2.4}$ and $La_{0.25}Sr_{0.75}MnO_{2.38}$ resulted in stable minimisations. The goodness of fit statistics for the refinements of these disordered models and the rigorously intralayer ordered *Pcmb* variants for each composition are shown in Table 4.4.

Phase	Space group	χ^2	*wRp*	*Rp*
$La_{0.3}Sr_{0.7}MnO_{2.4}$	*Pcmb*	2.677	4.64 %	3.70 %
	I2mb anisotropic	3.153	5.04 %	3.97 %
	Pcmb disorder	2.698	4.66 %	3.69 %
	Pcmb disorder varying *f*(Td)	2.339	4.80 %	3.73 %
$La_{0.25}Sr_{0.75}MnO_{2.38}$	*Pcmb*	1.946	4.44 %	3.51 %
	I2mb anisotropic	2.146	4.66 %	3.68 %
	Pcmb disorder	1.901	4.35 %	3.44 %
	Pcmb disorder varying *f*(Td)	1.687	4.11 %	3.27 %

Table 4.4: Fitting statistics for the refinement of 6-layer models against neutron powder diffraction data collected from $La_{0.3}Sr_{0.7}MnO_{2.4}$ and $La_{0.25}Sr_{0.75}MnO_{2.38}$

It is clear from inspection of Table 4.4 that, in an analogous manner to $La_{0.33}Sr_{0.67}MnO_{2.42}$, the '*Pcmb* disorder varying *f*(Td)' models most effectively account for the neutron powder diffraction data collected from $La_{0.3}Sr_{0.7}MnO_{2.4}$ and $La_{0.25}Sr_{0.75}MnO_{2.38}$. Observed, calculated and difference plots for these refinements are shown in Figure 4.2 and Figure 4.3.

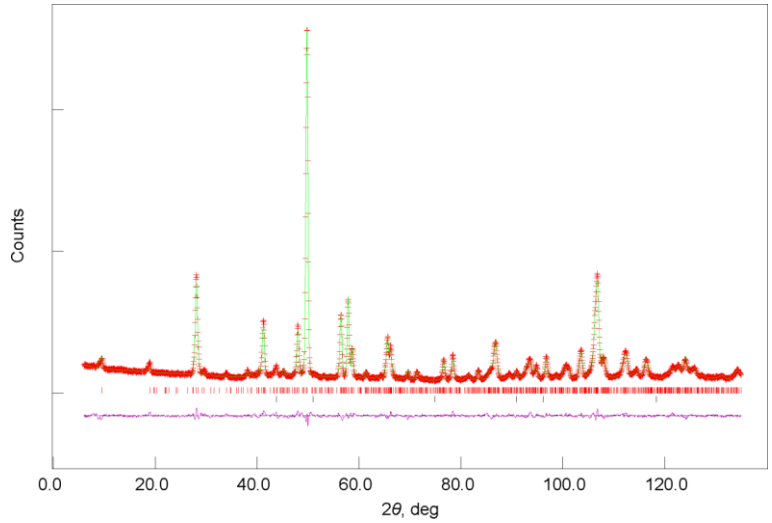


Figure 4.2: Plots for refinement against neutron powder diffraction data collected from $La_{0.3}Sr_{0.7}MnO_{2.4}$

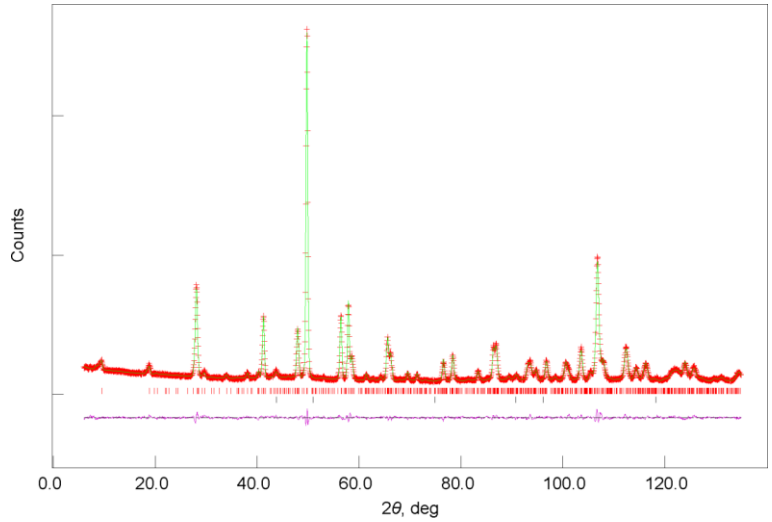


Figure 4.3: Plots for refinement against neutron powder diffraction data collected from $La_{0.25}Sr_{0.75}MnO_{2.38}$

Full structural data for these refinements of the '*Pcmb* disorder varying *f*(Td)' structural models and selected bond lengths are shown in Table 4.8 - Table 4.11 in Appendix 4. However, the most relevant structural parameters for the $La_{1-x}Sr_xMnO_{3-(0.5+x)/2}$ (x = 0.67, 0.7 and 0.75) phases are shown in Table 4.5.

Phase	O(3)-O(4)-O(3) (°)	Tetrahedral Separation (Å)	*f*(O(1)/(8))	*f(Td)*
$La_{0.33}Sr_{0.37}MnO_{2.42}$	112.7(8)	11.71	0.242	0.76(2)
$La_{0.3}Sr_{0.7}MnO_{2.4}$	112.2(2)	11.74	0.2	0.67(3)
$La_{0.25}Sr_{0.75}MnO_{2.38}$	111.2(2)	11.74	0.125	0.62(2)

Table 4.5:Relevant parameters from refined structural models for $La_{1-x}Sr_xMnO_{3-(0.5+x)/2}$ (x = 0.67, 0.7 and 0.75)

Inspection of Table 4.5 reveals that the tetrahedral chain distortion angle and tetrahedral layer separation remain relatively constant across the series. While the oxygen contents of the reduced phases extracted from thermogravimetric data are close once errors have been taken into account, the fractional occupancy of the 'bridging' anion site (O(1)/(8)) appears to decrease with increasing Sr^{2+}-content. In addition, the fractional occupancy of the tetrahedral chain with the twist direction generated by the *Pcmb* symmetry (*f*(Td) – see section 3.3.6) clearly decreases with increasing Sr^{2+}-content, consistent with decreasing order in the arrangement of the twisted tetrahedral chains. It should be noted that the separation between the tetrahedral layers in the 6-layer $La_{1-x}Sr_xMnO_{3-(0.5+x)/2}$ (x = 0.67, 0.7 and 0.75) phases is

much greater than in the structurally related $A_2B_2O_5$ brownmillerite phases, e.g. 8.38 Å in $La_{0.5}Sr_{0.5}MnO_{2.5}$.[20]

4.4. Discussion

The topotactic reduction of $La_{0.3}Sr_{0.7}MnO_3$ and $La_{0.25}Sr_{0.75}MnO_3$ using NaH results in the formation of reduced phases which adopt 6-layer structures analogous to that of $La_{0.33}Sr_{0.67}MnO_{2.42}$. These '6-layer manganate' structures all contain OOTOOT' stacking of the octahedral (O) and tetrahedral (T) layers and a -L-R-L-R- arrangement of the twisted tetrahedral chains within each tetrahedral layer (intralayer order). However, the structures of all 3 '6-layer manganate' phases are proposed to contain incomplete interlayer order of the twisted tetrahedral chains.

Quite unexpectedly, the '6-layer manganate' phases adopt an empirical composition of $La_{1-x}Sr_xMnO_{3-(0.5+x)/2}$ (x = 0.67, 0.7 and 0.75) with a common average manganese oxidation state of +2.5 across the series. The fact that the anion content varies across the topotactically reduced $La_{1-x}Sr_xMnO_{3-(0.5+x)/2}$ (x = 0.67, 0.7 and 0.75) materials in this way is highly unusual. More typical behaviour is exhibited by the topotactic reduction reactions of phases in the range $La_{1-x}Sr_xMnO_3$ ($0.2 \leq x \leq 0.5$) which result in the formation of products which adopt the brownmillerite structure with a constant empirical composition of $La_{1-x}Sr_xMnO_{2.5}$.

The apparent flexibility in the anion content of the $La_{1-x}Sr_xMnO_{3-(0.5+x)/2}$ (x = 0.67, 0.7 and 0.75) phases suggests that the level of reduction is not directly controlled by structural factors but, at least to some degree, by electronic factors. A fuller discussion of this topic is included in Chapter 6.

4.4.1. Introduction to ordering of the twisted tetrahedral chains

It seems reasonable to suggest that the phases which adopt the '6-layer manganate' structure refined for $La_{1-x}Sr_xMnO_{3-(0.5+x)/2}$ (x = 0.67, 0.7 and 0.75) can exhibit the same variety of twisted tetrahedral chain ordering schemes (structural variants) as observed for the

structurally related $A_2B_2O_5$ brownmillerite phases (see Figure 1.5). It also seems reasonable to suggest that these same factors based on dipole cancellation are also highly likely to influence which twisted tetrahedral chain ordering scheme is adopted by the '6-layer manganate' phases. Therefore, by analogy to the $A_2B_2O_5$ brownmillerite structures, it is logical to predict that there are 3 ordering arrangements of the twisted tetrahedral chains, and thus dipole cancellation mechanisms, in the 6-layer $La_{1-x}Sr_xMnO_{3-(0.5+x)/2}$ (x = 0.67, 0.7 and 0.75) phases:

1. When the tetrahedral twist angle (O(3)-O(4)-O(3)) is low, all the tetrahedral chains will be twisted in the same direction. This will yield a polar structure in space group *I*2*mb* (e.g. the structural model first proposed for *RE*$Sr_2Cu_2GaO_7$).[61] These materials are predicted to crystallise with small polar domains aligned with anti-parallel polarisation vectors in neighbouring domains to allow macroscopic dipole cancellation.
2. All the tetrahedral chains in a particular tetrahedral layer are twisted in the same direction, with the twist direction inverting between adjacent layers, in the *Pnma* structural variant. This variant is stabilised by an 'interlayer' dipole cancellation mechanism.
3. The chains within each tetrahedral layer could adopt an alternating -L-R-L-R- arrangement, which would exhibit an 'intralayer' dipole cancellation mechanism. This arrangement is adopted in the refined structures of $La_{1-x}Sr_xMnO_{3-(0.5+x)/2}$ (x = 0.67, 0.7 and 0.75) with *Pcmb* symmetry, and, in principle, the 6-layer *C*2/*c* variant analogous to that observed for the brownmillerite phase $La_{0.75}Sr_{0.25}MnO_{2.5}$.[17]

4.4.2. Rationalisation of ordering of the twisted tetrahedral chains

As discussed in section 1.4.3, the adoption of the different tetrahedral ordering schemes in the $A_2B_2O_5$ brownmillerite phases has been justified on the basis of 2 competing factors: the

efficiency of the dipole cancellation mechanism and the structural disruption associated with the adoption of each tetrahedral chain ordering scheme.[17] The efficiency of the dipole cancellation mechanisms associated with the tetrahedral chain ordering schemes in the $A_2B_2O_5$ brownmillerite phases follows the order: intralayer ordered (*Pcmb* or *C*2/*c*) > interlayer ordered (*Pnma*) > 'non-ordered' (*I*2*mb*).[17] However, the degree of structural disruption associated with the adoption of each ordering arrangement is thought to follow the same order.[17] Thus, the adoption of the tetrahedral chain ordering scheme depends on the interplay of these 2 factors.

Parsons *et al.* published a 'structure map' of the different brownmillerite structural variants by plotting the tetrahedral layer separation against the distortion angle in the tetrahedral chains (a measure of the magnitude of the dipole associated with the twisted tetrahedral chains – see Figure 1.8) of a large number of known brownmillerite phases.[17] It was observed that all reported intralayer ordered (*Pcmb* and *C*2/*c*) brownmillerite structures contained twisted tetrahedral chains with distortion angles greater than 62.5^{o} and tetrahedral layer separations greater than 8 Å.

On the basis of these observations it was argued that only phases with such highly twisted tetrahedral chains and such large tetrahedral layer separations could sustain an intralayer ordered arrangement of the twisted tetrahedral chains. This is because the resulting tetrahedral chain dipole moments and tetrahedral layer separations are too large for efficient dipole cancellation in the less structurally disrupted 'non-ordered' (*I*2*mb*) or interlayer ordered (*Pnma*) variants.

Inspection of Table 4.5 shows that all 6-layer $La_{1-x}Sr_xMnO_{3-(0.5+x)/2}$ (x = 0.67, 0.7 and 0.75) phases contain highly twisted tetrahedral chains and large tetrahedral layer separations, consistent with these phases adopting an intralayer ordered arrangement of the twisted tetrahedral chains (*Pcmb* or *C*2/*c* variant). As in the brownmillerite phases with intralayer

order of the twisted tetrahedral chains, the dipole cancellation mechanisms associated with the other tetrahedral chain ordering schemes (*I*2*mb* or *Pnma* variants) are clearly too inefficient to stabilise the relatively large dipole moments.

4.4.3. Disorder

The electron and neutron powder diffraction data collected from $La_{1-x}Sr_xMnO_{3-(0.5+x)/2}$ (x = 0.67, 0.7 and 0.75) are consistent with these phases adopting structures with rigorous -L-R-L-R- order within the tetrahedral layers but with faults in the ABA stacking arrangement of the tetrahedral layers defined by the *Pcmb* symmetry (see section 1.4.2).

Given the large distortion angle of the tetrahedral chains in the structures of the $La_{1-x}Sr_xMnO_{3-(0.5+x)/2}$ (x = 0.67, 0.7 and 0.75) phases, hypothetical structures containing a fully disordered arrangement of the twisted tetrahedral chains would be highly disfavoured due to the incomplete local cancellation of their relatively large chain dipole moments. Strong coupling between the tetrahedral chain dipole moments within each tetrahedral layer will strongly stabilise a rigorous -L-R-L-R- arrangement of the twisted tetrahedral chains (i.e. intralayer order) to maintain efficient local cancellation of the dipole moments. However, the faults in the stacking of the tetrahedral layers (i.e. interlayer disorder) indicate that the interactions between adjacent tetrahedral layers are relatively weak. This is unsurprising given the large spatial separation between the tetrahedral layers and the presence of a disordered anion deficient layer ('bridging' anion) between adjacent tetrahedral layers.

Inspection of Table 4.3 and Table 4.4 highlights 2 relevant trends in the structural parameters of the $La_{1-x}Sr_xMnO_{3-(0.5+x)/2}$ (x = 0.67, 0.7 and 0.75) phases with increasing Sr^{2+}-content: Firstly, the quality of the fit using the '*Pcmb* disorder varying *f*(Td)' model improves relative to that of the model based on *Pcmb* symmetry. Secondly, the fractional occupancies of the 2 superimposed twisted tetrahedral chains in the '*Pcmb* disorder varying *f*(Td)' structural model (see section 3.3.6) converge towards equal occupancy. Both trends are

clear indications of increasing disorder in the arrangement of the twisted tetrahedral chains with increasing Sr^{2+}-content.

As shown in Table 4.5, this increase in the disorder in the arrangement of the twisted tetrahedral chains coincides with a decrease of the fractional occupancy of the 'bridging' anion site. This positive correlation (see Table 4.5) suggests that the structural registry between adjacent tetrahedral layers is determined by the connectivity between neighbouring tetrahedral layers in the '6-layer manganate' phases (i.e. a 'through-bond' interaction) as opposed to the interlayer separation as in the case of the brownmillerite phases (i.e. a 'through-space' interaction).

4.4.4. Comparison to other anion vacancy ordered structures

Given the success of the rationalisation of the ordering arrangements of the twisted tetrahedral chains in the brownmillerite and '6-layer manganate' phases based on dipole cancellation, this logic can be applied to other related anion-deficient perovskite phases ($A_mB_mO_{3m-x}$)[10] containing analogous tetrahedral layers, e.g. $(La_{1/3}Ca_{2/3})_3Fe_3O_8$ (m = 3), $Ca_2MnAlO_{5.5}$ (m = 4) and $Ca_2Ba_2Nd_2Fe_6O_{15.6}$ (m = 6).[6, 60, 68]

4.4.4.1. Other m = 3 structures ($(La_{1/3}Ca_{2/3})_3Fe_3O_8$)

The structures of $(La_{1/3}Ca_{2/3})_3Fe_3O_8$ and the '6-layer manganate' phases are closely related. The former structure consists of double layers of FeO_6 octahedra separated by FeO_4 tetrahedral layers as shown in Figure 4.4.[60] However, the structure of $(La_{1/3}Ca_{2/3})_3Fe_3O_8$ contains an eclipsed arrangement of the tetrahedral chains up the b-axis, in contrast to the staggered arrangement observed in the structures of the '6-layer manganate' phases. In addition, the structure of $(La_{1/3}Ca_{2/3})_3Fe_3O_8$ contains a fully occupied 'bridging' anion site, while the '6-layer manganate' phases contain only partially occupied 'bridging' anion sites.

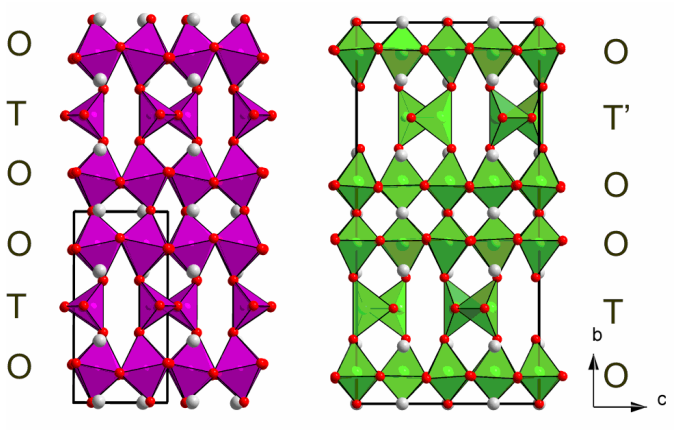


Figure 4.4: Structure of $(La_{1/3}Ca_{2/3})_3Fe_3O_8$ (left) and $La_{0.33}Sr_{0.67}MnO_{2.42}$ (right). O and T/T' denote the octahedral or 'octahedral' and tetrahedral layers.

Inspection of Figure 4.4 reveals that the tetrahedral layers in the 2 structures are similar allowing instructive comparisons between the 2 structures to be made. All the tetrahedral chains in the structure of $(La_{1/3}Ca_{2/3})_3Fe_3O_8$ are twisted in the same direction ('non-ordered'), as in the case for all other reported analogous 3-layer structures. As shown in Table 4.12 in Appendix 4, the distortion angles in the tetrahedral chains in $(La_{1/3}Ca_{2/3})_3Fe_3O_8$ and the other analogous 3-layer structures are relatively small. Therefore, given the lower dipole moments associated with the tetrahedral chains in the 3-layer structures, it can be hypothesised that sufficient dipole cancellation can be achieved in these 3-layer materials using the formation of polar micro-domains (see section 4.4.1). Thus, a more complex dipole cancellation mechanism (e.g. an intralayer mechanism), which would incur an additional structural penalty, is not adopted.

4.4.4.2. Comparison to $m > 3$ structures

This approach to structural rationalisation based on dipole cancellation can be further extended to some other $A_mB_mO_{3m-x}$ $m > 3$ anion-deficient structures which contain analogous tetrahedral layers, e.g. $Ca_2MnAlO_{5.5}$ ($m = 4$) and $Ca_2Ba_2Nd_2Fe_6O_{15.6}$ ($m = 5$). Both these phases are reported to contain a fully disordered arrangement of the twisted tetrahedral chains:[6, 68]

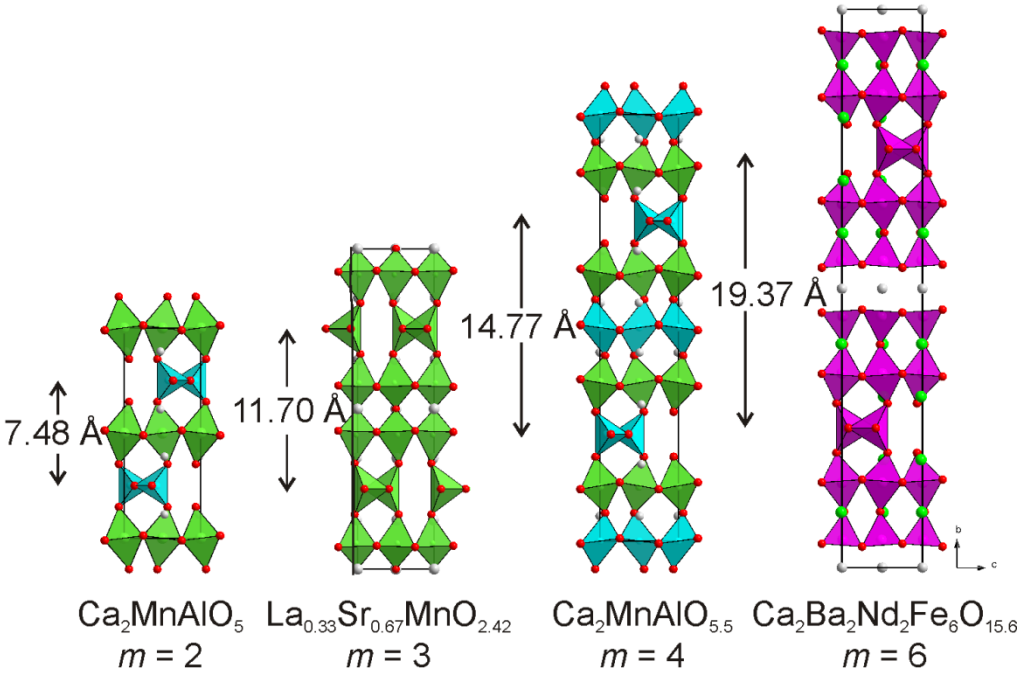


Figure 4.5: Structures and tetrahedral layer separations in some anion-deficient perovskite ($A_mB_mO_{3m-x}$) phases which contain tetrahedral layers.

Inspection of Figure 4.5 reveals that the tetrahedral layer separation in these phases scales with *m*. Consequently the interactions between adjacent tetrahedral layers in $Ca_2MnAlO_{5.5}$ (*m* = 4) and $Ca_2Ba_2Nd_2Fe_6O_{15.6}$ (*m* = 6) are likely to be severely limited due to the large separation. It is therefore unsurprising that the structures of both $Ca_2MnAlO_{5.5}$ and $Ca_2Ba_2Nd_2Fe_6O_{15.6}$ contain no interlayer ordering of the twisted tetrahedral chains.

A structural comparison between $Ca_2MnAlO_{5.5}$ and Ca_2MnAlO_5 provides an elegant demonstration of the link between the structural registry between tetrahedral layers and the interlayer order, or lack thereof, of the twisted tetrahedral chains.[68] Ca_2MnAlO_5 adopts the *I*2*mb* brownmillerite structural variant (*m* = 2) in which all the tetrahedral chains are twisted in the same direction.[69] $Ca_2MnAlO_{5.5}$ (*m* = 4), formed through the intercalation of oxide ions into every other tetrahedral layer of Ca_2MnAlO_5, adopts a disordered arrangement of the twisted tetrahedral chains.[68] It is clear that upon oxidation the interaction between neighbouring tetrahedral layers decreases as the tetrahedral separation increases, resulting in a loss of the interlayer order of the twisted tetrahedral chains.

The structures of $Ca_2Ba_2Nd_2Fe_6O_{15.6}$, $Ca_2MnAlO_{5.5}$ and $La_{0.33}Sr_{0.67}MnO_{2.42}$ all contain tetrahedral chains which are twisted to an approximately similar degree (111.18^o, 114.72^o and 112.69^o respectively) and thus have similar tetrahedral chain dipole moments. Given the relatively large tetrahedral chain dipole moments, a completely disordered arrangement of the twisted tetrahedral chains in these phases is likely to incur significantly unfavourable electrostatic interactions due to incomplete local dipole cancellation. Given the strong coupling between the dipole moments in neighbouring chains within each tetrahedral layer, it can be hypothesised that these phases adopt a -L-R-L-R- ordered arrangement of twisted tetrahedral chains within each tetrahedral layer to allow effective dipole cancellation. However, given the lack of interlayer order of the tetrahedral chains, this proposed intralayer ordered arrangement of the twisted tetrahedral chains is not experimentally observed by diffraction.

4.4.4.3. Overall ordering scheme

Drawing together comparisons made in the previous sections, Figure 4.6 summarises the effect of the registry between neighbouring tetrahedral layers and the degree of distortion in the tetrahedral chains on the ordering arrangements of the twisted tetrahedral chains in anion-deficient perovskite phases.

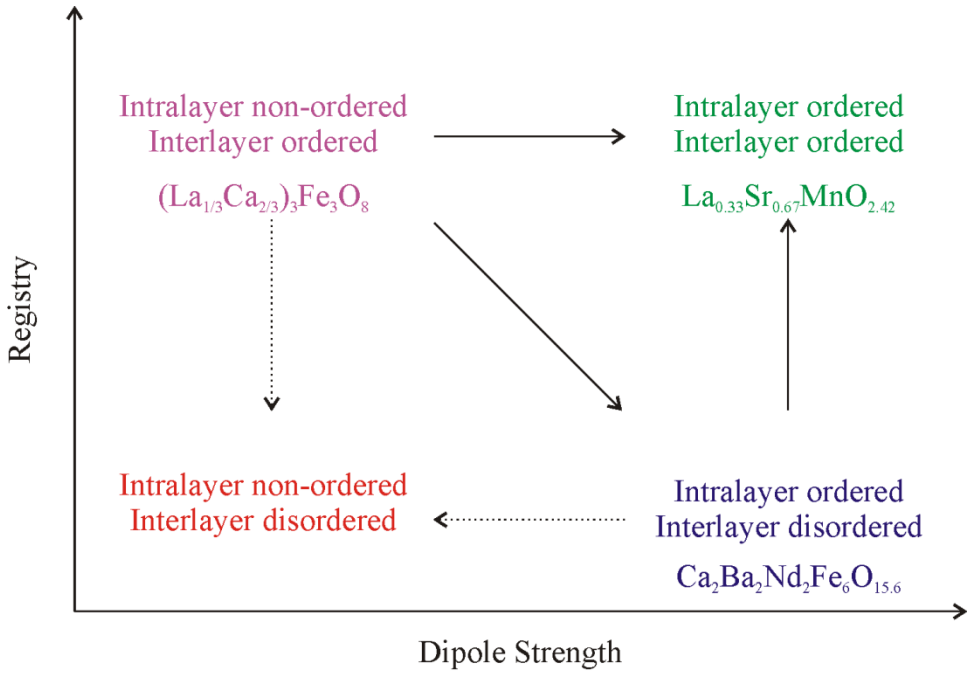


Figure 4.6: 'Structure map' of some anion-deficient perovskite phases which contain tetrahedral layers

Figure 4.6 shows that phases in which the tetrahedral dipole moment is small, and the coupling between the tetrahedral layers is strong, adopt structures in which all the tetrahedral chains are twisted in the same direction, e.g. $(La_{1/3}Ca_{2/3})_3Fe_3O_8$.

However, as the coupling between the neighbouring tetrahedral layers weakens, the interlayer order of the twisted tetrahedral chains is lost. Therefore, phases in which the tetrahedral dipole moment is small and the coupling between the tetrahedral layers is weak adopt structures in which all the tetrahedral chains are twisted in the same direction in each layer, but with no interlayer order. $(La_{1/3}Sr_{2/3})_3Fe_3O_8$ is reported to adopt such an arrangement, however the structure of this phase is further complicated by 'staggered/eclipsed' disordering of the tetrahedral layers and so an unequivocal determination of the tetrahedral chain ordering scheme is not possible.[62]

As the magnitude of the dipole moment associated with the tetrahedral chain increases, materials adopt structures with an -L-R-L-R- ordering arrangement of the twisted tetrahedral chains within each layer (intralayer order) to more efficiently cancel the increasing dipole moments, e.g. $Ca_2Ba_2Nd_2Fe_6O_{15.6}$ and $La_{0.33}Sr_{0.67}MnO_{2.42}$. The presence of interlayer ordering

of the tetrahedral chains, and so complete 3D order, is dependent on the coupling between neighbouring tetrahedral layers. Phases with only weak coupling between the tetrahedral layers adopt structures with an interlayer disordered arrangement of the twisted tetrahedral chains, e.g. $Ca_2Ba_2Nd_2Fe_6O_{15.6}$. However, as the strength of the coupling between tetrahedral layers increases, the degree of interlayer order of the twisted tetrahedral chains increases. $La_{0.33}Sr_{0.67}MnO_{2.42}$ adopts a structure with partial interlayer order of twisted tetrahedral chains.

4.4.5. 'Cooperative twist' theory

4.4.5.1. Introduction

As discussed in section 4.4.4.1, both $La_{0.33}Sr_{0.67}MnO_{2.42}$ and $(La_{1/3}Ca_{2/3})_3Fe_3O_8$ are m = 3 members of the $A_mB_mO_{3m-x}$ anion-deficient perovskite series.[10, 60] However, $La_{0.33}Sr_{0.67}MnO_{2.42}$ adopts a structure with a staggered arrangement of the tetrahedral layers up the *b*-axis (OOTOOT' stacking) whereas $(La_{1/3}Ca_{2/3})_3Fe_3O_8$ adopts an eclipsed arrangement (OOTOOT stacking). This contrast in the stacking will be rationalised in the following sections.

In the structural investigation of $Ca_2MnAlO_{5.5}$, Palmer *et al.* first proposed a model for the systematic structural behaviour of $A_mB_mO_{3m-x}$ systems containing only octahedral and tetrahedral layers.[68] As shown in Figure 4.7, phases containing an odd number of octahedral layers in the perovskite-type block between the tetrahedral layers adopt structures with a staggered arrangement of the tetrahedral layers up the *b*-axis, e.g. Ca_2MnAlO_5 (m = 2 – OTOT' stacking) and $Ca_2MnAlO_{5.5}$ (m = 4 – OOOTOOT' stacking). In contrast, phases containing an even number of octahedral layers adopt structures with an eclipsed arrangement of the tetrahedral layers up the *b*-axis, e.g. $(La_{1/3}Ca_{2/3})_3Fe_3O_8$ (m = 3 – OOTOOT stacking). It was proposed that this behaviour could be rationalised on the basis of the tilting within the rigid octahedral layers, henceforth labelled as the 'cooperative twist theory'.[68]

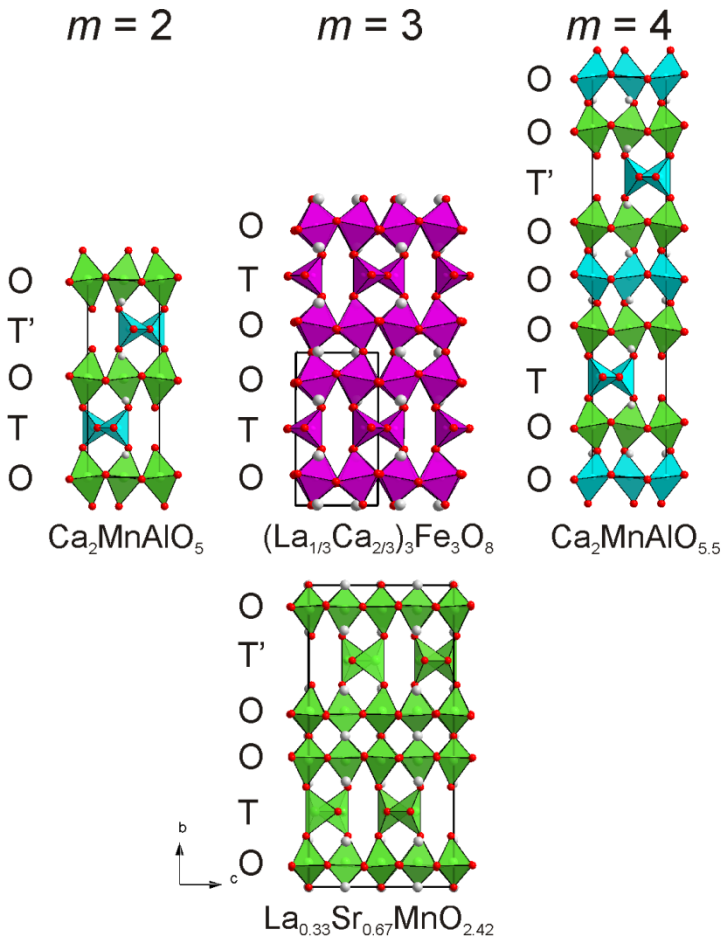


Figure 4.7: Anion deficient perovskite structures with stacking sequences which can be predicted by 'cooperative twist theory' (top) and the structure of $La_{0.33}Sr_{0.67}MnO_{2.42}$ (bottom).

Anion-deficient perovskite materials, $A_mB_mO_{3m-x}$, undergo a number of low energy distortions in an attempt to satisfy the bonding requirements of both the A- and B-cations simultaneously. In general, these distortions proceed with the retention of the BO_6 octahedral geometry at the expense of the deformation of the A-site coordination environment. In $A_mB_mO_{3m-x}$ structures containing octahedral and tetrahedral layers, these distortions are manifested by tilting within the octahedral layers and twisting within the tetrahedral layers.

Inspection of the Ca_2MnAlO_5 brownmillerite structure (see Figure 4.8(i))) shows that the MnO_6 octahedra undergo a cooperative $GdFeO_3$-type rotation within each octahedral layer.[70] The octahedral layers are then stacked in a staggered manner (with intervening tetrahedral layers) so as to produce an alternating arrangement of tilted MnO_6 octahedra up the *b*-axis.

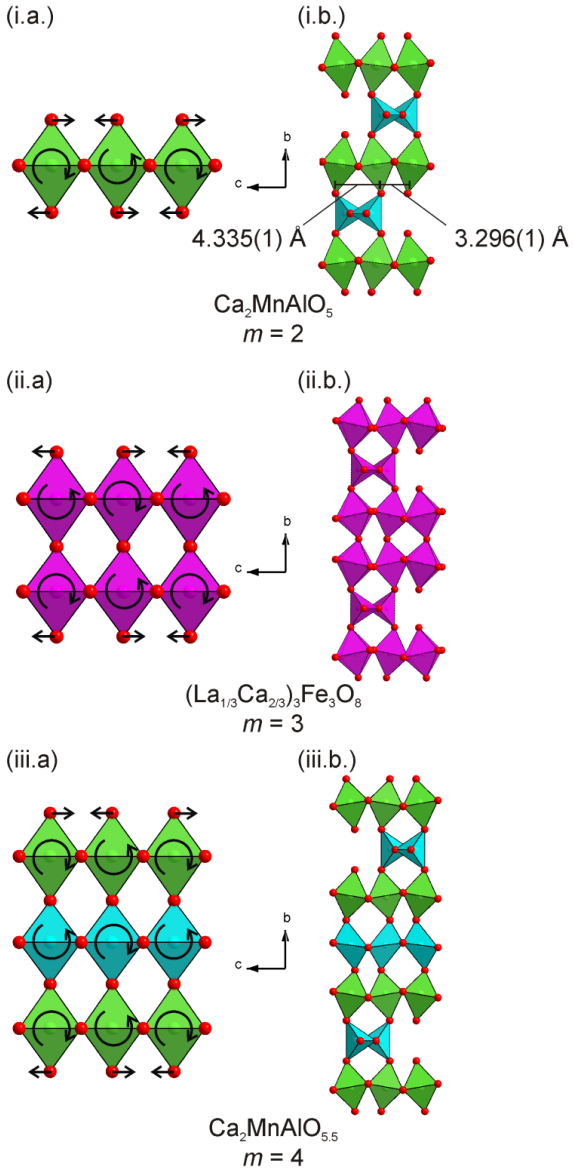


Figure 4.8: Cooperative twisting of octahedral layers in Ca_2MnAlO_5, $(La_{1/3}Ca_{2/3})_3Fe_3O_8$ and $Ca_2MnAlO_{5.5}$. Column (a) shows the cooperative twisting of the BO_6 octahedra. Column (b) shows the actual structures.

As shown in Figure 4.8 (i.a), the tilting of the octahedra creates 2 distinct sets of channels down the *a*-axis of Ca_2MnAlO_5. So as to minimise the equatorial compression of the AlO_4 tetrahedra, the tetrahedral chains run in the channels connected between the apical oxide ions with a large separation. As a result, Ca_2MnAlO_5 contains a staggered arrangement of tetrahedral layers up the *b*-axis.

As shown in Figure 4.8, this rationale can be extended to predict the stacking arrangements in other $A_mB_mO_{3m-x}$ structures based on only octahedral and tetrahedral layers, e.g. $(La_{1/3}Ca_{2/3})_3Fe_3O_8$ (m = 3) and $Ca_2MnAlO_{5.5}$ (m = 4).

4.4.5.2. Exceptions to ‘cooperative twist’ theory

The predictions of the stacking sequence using the ‘cooperative twist theory’ can break down when additional anion deficiency is incorporated into the system. The structures of both *RE*$Sr_2Cu_2GaO_7$ (SSTSST’ stacking) and $Ca_2Ba_2Nd_2Fe_6O_{15.6}$ (OSSOTOSSOT’ stacking) contain an even number of polyhedral layers between the tetrahedral layers. Therefore the ‘cooperative twist theory’ predicts that both materials should adopt structures with an eclipsed arrangement of tetrahedral chains up the *b*-axis rather than the observed staggered arrangement.

However, both *RE*$Sr_2Cu_2GaO_7$ and $Ca_2Ba_2Nd_2Fe_6O_{15.6}$ contain anion vacant A-cation layers. Therefore, as the shared oxide anion has been removed, neighbouring BO_5 square based pyramids are no longer forced to tilt in an opposing fashion across the anion vacant A-cation layers. Instead, the neighbouring BO_5 tilt in the same direction. By following the logic detailed above regarding the cooperative twisting of linked polyhedra, this tilting results in the formation of a staggered arrangement of the tetrahedral layers up the *b*-axis (see Figure 4.9).

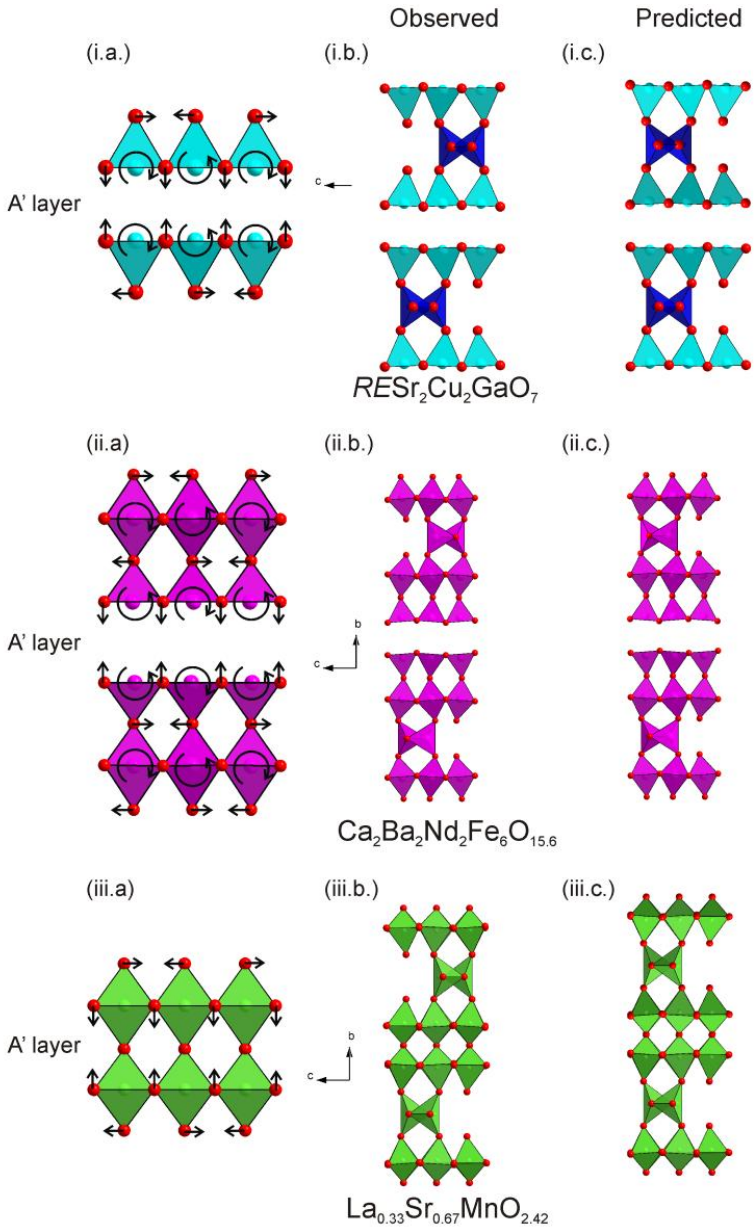


Figure 4.9: Structures which contravene the 'cooperative twist theory'. Column (a) shows the cooperative distortions in the BO_n polyhedra. Column (b) shows the actual structures. Column (c) shows the structures predicted on the basis of 'cooperative twist theory'.

The structures of the $La_{1-x}Sr_xMnO_{3-(0.5+x)/2}$ (x = 0.67, 0.7 and 0.75) phases contain only partially occupied 'bridging' anion sites (O(1)/(8)). This allows the 'octahedra' to tilt in the same direction across the anion-deficient AO(1)/(8)-layer, which thereby allows the tetrahedral layers to stack in a staggered manner up the *b*-axis.

It seems reasonable to suggest that $RESr_2Cu_2GaO_7$, $Ca_2Ba_2Nd_2Fe_6O_{15.6}$ and the $La_{1-x}Sr_xMnO_{3-(0.5+x)/2}$ ($x \geq 0.67$) series could all adopt structures with an eclipsed arrangement of the tetrahedral layers with the polyhedra tilting in an opposing fashion across the anion

deficient AO layer. The most plausible explanation for the relative stability of the observed structures compared to hypothetical variants with an eclipsed arrangement of the tetrahedral layers is based on the increased lattice energy associated with a more symmetric coordination environment of the A-cations in the anion deficient AO layers.

4.4.5.3. Coordination sphere of the A-cation

As discussed above, the common feature in the phases that violate the 'cooperative twist theory' (e.g. *RE*$Sr_2Cu_2GaO_7$, $Ca_2Ba_2Nd_2Fe_6O_{15.6}$ and the $La_{1-x}Sr_xMnO_{3-(0.5+x)/2}$ ($x \geq 0.67$) phases) is that the neighbouring BO_2 layers tilt in the same direction across the anion deficient AO layers. As shown in Figure 4.10, the coordination environments of the A-cations in the anion deficient AO layers in these structures are dependent on the tilting of the neighbouring BO_2 layers. In Figure 4.10 (a) the BO_2 layers tilt in an opposing fashion which is consistent with an hypothetical eclipsed arrangement of tetrahedral layers up the *b*-axis of the 6-layer structures of the $La_{1-x}Sr_xMnO_{3-(0.5+x)/2}$ ($x \geq 0.67$) phases. In Figure 4.10 (b) the BO_2 layers tilt in the same direction which is consistent with a staggered arrangement of tetrahedral layers up the *b*-axis in the observed 6-layer structures of the $La_{1-x}Sr_xMnO_{3-(0.5+x)/2}$ ($x \geq 0.67$) phases.

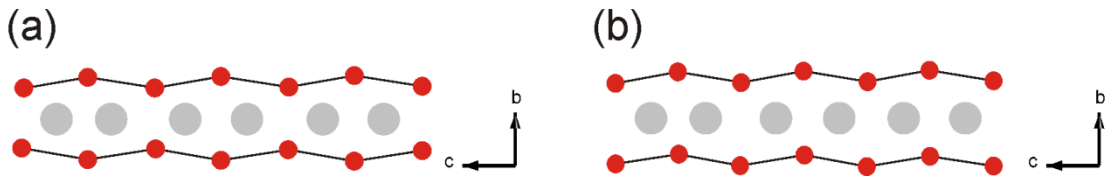


Figure 4.10: Potential coordination spheres of A-cations in anion-deficient AO layers

The A-cation coordination environment is more symmetric, and intuitively more stable, when the BO_2 layers tilt in the same direction (see Figure 4.10 (b)). Therefore, the variant with a staggered arrangement of tetrahedral layers is stabilised relative to the variant with an eclipsed arrangement.

4.4.5.4. Other perovskite-based structures

The apparent preference for the tilting of the neighbouring octahedral layers in the same direction, when freed from 'anchoring' oxide ions, is also demonstrated in other anion-deficient systems. $La_4Co_3O_9$ adopts an anion-deficient variant of an $n = 3$ Ruddlesden-Popper structure:[71]

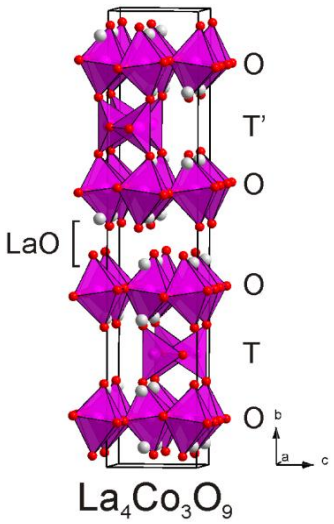


Figure 4.11: Structure of $La_4Co_3O_9$

The structure of $La_4Co_3O_9$ is best described by OTO-OT'O stacking, where the 'hyphen' denotes the presence of an LaO layer. An extension of the 'cooperative twist' theory to include Ruddlesden-Popper structures would predict that the neighbouring octahedra across the AO layer should tilt in an opposing fashion, thereby leading to an eclipsed arrangement of the tetrahedral layers up the *b*-axis (as in the case of the related $(La_{1/3}Ca_{2/3})_3Fe_3O_8$ perovskite-based structure).

However, the LaO layers act as 'spacer' layers between the CoO_6 octahedra in neighbouring perovskite-type blocks. In a similar fashion to the anion-deficient A-cation layers described above, the 'spacer' layers allow the CoO_6 octahedra to tilt in the same direction across the LaO layers. This tilting results in the formation of a staggered arrangement of the tetrahedral layers up the *b*-axis.

4.5. Structural conclusion

The topotactic reduction reaction of the $La_{1-x}Sr_xMnO_3$ (x = 0.7 and 0.75) phases results in the formation of reduced phases which adopt '6-layer manganate' structures (i.e. isostructural with $La_{0.33}Sr_{0.67}MnO_{2.42}$ – see Chapter 3). The '6-layer manganate' structure contains an intralayer ordered arrangement (i.e. -L-R-L-R-) of the twisted tetrahedral chains, albeit with slight disorder in the rigorous ABA stacking of the *Pcmb* structural variant. In an analogous fashion to the structurally related brownmillerite phases,[17] the adoption of this ordering arrangement can be justified on the basis of the cancellation of dipole moments within the material brought about by twisting of the tetrahedral chains.

Given the large distortion angle of the tetrahedral chains in the $La_{1-x}Sr_xMnO_{3-(0.5+x)/2}$ (x = 0.67, 0.7 and 0.75) phases, only the intralayer ordered arrangement of the twisted tetrahedral chains allows for an efficient enough dipole cancellation mechanism to stabilise the structure. This logic based on dipole cancellation can also be extended to rationalise the arrangement of the twisted tetrahedral chains in other anion-deficient perovskite structures containing tetrahedral layers (e.g. $(La_{1/3}Ca_{2/3})Fe_3O_8$ and $Ca_2MnAlO_{5.5}$).

Using Poeppelmeier's notation,[10] the '6-layer manganate structure' can be classed as an m = 3 member of the anion-deficient perovskite ($A_mB_mO_{3m-x}$) structural series. The '6-layer manganate' structure contains a staggered arrangement of the tetrahedral layers up the *b*-axis, while some other m = 3 members containing analogous tetrahedral layers, e.g. $(La_{1/3}Ca_{2/3})Fe_3O_8$, adopt an eclipsed arrangement. The relative arrangement of the tetrahedral layers in $(La_{1/3}Ca_{2/3})Fe_3O_8$ is governed by the cooperative tilting of the intervening BO_6 octahedra (labelled 'cooperative twist theory' in this investigation).[68]

In contrast to the full oxide ion site linking the BO_6 octahedra in the structures which 'obey' the 'cooperative twist theory', the oxide anion site between the MnO_6 octahedra is partially occupied in the '6-layer manganate' phases which frees the structure from this

restriction. This allows the '6-layer manganate' structure to contain a staggered arrangement of the tetrahedral layers up the *b*-axis. This staggered arrangement is proposed to be stabilised relative to the analogous eclipsed arrangement due to the formation of a more symmetric coordination environment for the A-cations between the 'octahedral' layers.

4.6. Magnetic properties of the '6-layer manganate' phases

4.6.1. Results

4.6.1.1. Magnetisation data

The magnetic behaviour of the '6-layer manganate' $La_{1-x}Sr_xMnO_{3-(0.5+x)/2}$ (x = 0.67, 0.7 and 0.75) phases will be described in this section. As discussed in Chapter 5, $La_{0.17}Sr_{0.83}MnO_{2.33}$ adopts a structure closely related to the '6-layer manganate' structure but has an entirely vacant 'bridging' anion site between the MnO_2 layers. Therefore the structure of $La_{0.17}Sr_{0.83}MnO_{2.33}$ is best described as SSTSST' stacking of the square-based pyramidal (S) and tetrahedral (T) layers rather than OOTOOT' stacking. Given the similarity in the structure and magnetic behaviour of $La_{0.17}Sr_{0.83}MnO_{2.33}$ to those of the '6-layer manganate' phases, the magnetic behaviour of $La_{0.17}Sr_{0.83}MnO_{2.33}$ will also be discussed in this section.

Figure 4.12 shows paramagnetic susceptibility data collected from $La_{0.33}Sr_{0.67}MnO_{2.42}$ using the 'ferromagnetic subtraction' technique described in section 2.7. This data set is typical of the paramagnetic susceptibility data collected from the $La_{1-x}Sr_xMnO_{3-(0.5+x)/2}$ (x = 0.7, 0.75 and 0.83) phases (see Figure 4.29 in Appendix 4). The common feature in the data collected from all the $La_{1-x}Sr_xMnO_{3-(0.5+x)/2}$ ($0.67 \leq x \leq 0.83$) phases is a slight upward curve in the paramagnetic susceptibility data (marked with an arrow) at approximately 60 K. However, unequivocal determination of the magnetic properties of the '6-layer manganate' materials is not possible on the basis of the paramagnetic susceptibility data.

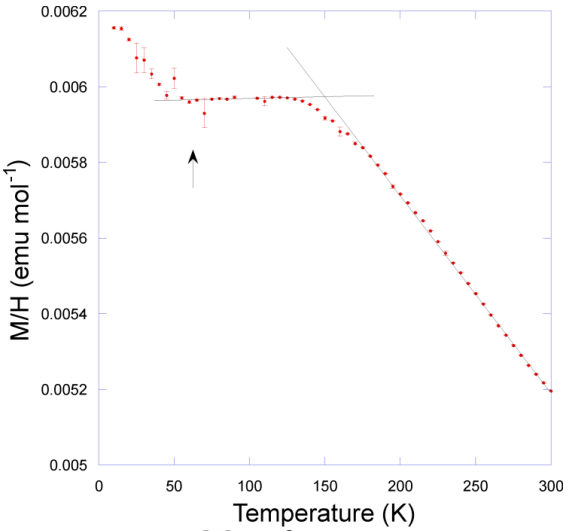


Figure 4.12: Plot of paramagnetic susceptibility of $La_{0.33}Sr_{0.67}MnO_{2.42}$ measured by 'ferromagnetic subtraction' method.

Magnetisation-field isotherms were collected from the $La_{1-x}Sr_xMnO_{3-(0.5+x)/2}$ ($0.67 \leq x \leq 0.83$) materials at 5 K and 300 K. The data collected from $La_{0.33}Sr_{0.67}MnO_{2.42}$ are shown in Figure 4.13, while data collected from the other '6-layer manganate' phases are shown in Figure 4.28 in Appendix 4.

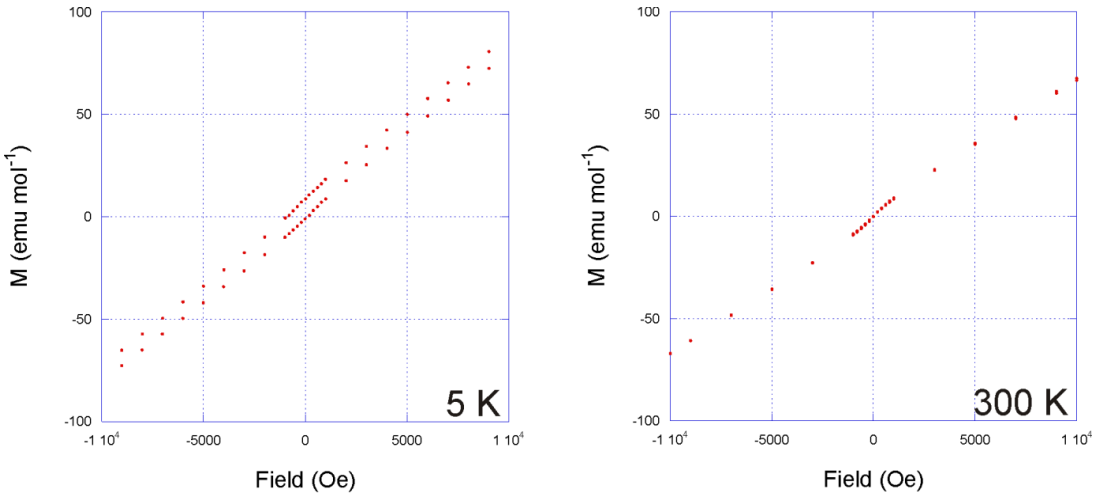


Figure 4.13: Magnetisation-field isotherms collected from $La_{0.33}Sr_{0.67}MnO_{2.42}$ at 5 K and 300 K.

The magnetisation-field loops collected at 300 K is consistent with the presence of a small amount of the corresponding ferromagnetic perovskite starting material. However, close inspection of the data collected at 5 K (see Figure 4.13 and Figure 4.28) from all the $La_{1-x}Sr_xMnO_{3-(0.5+x)/2}$ ($0.67 \leq x \leq 0.83$) materials reveal that the magnetisation-field loops are displaced to higher magnetisations in each case, consistent with spin-glass type behaviour.[72]

4.6.1.2. 5 K neutron diffraction data

Variable temperature neutron powder diffraction data were collected from samples of $La_{1-x}Sr_xMnO_{3-(0.5+x)/2}$ ($0.67 \leq x \leq 0.83$) using the D1b instrument (see section 2.3.2.1.3) to determine if long range magnetic order is present in these phases. Data collected from $La_{0.33}Sr_{0.67}MnO_{2.42}$ at 5 K (see Figure 4.14) reveal additional reflections at approximately 26° and 39° (labelled (a) and (b) respectively) and a further broad 'lump' between approximately 27.5° and 33° compared to the analogous data set collected at room temperature. The additional reflections ((a) and (b)) are consistent with the presence of long range magnetic order with the 'lump' suggesting the presence of further short range magnetic order.

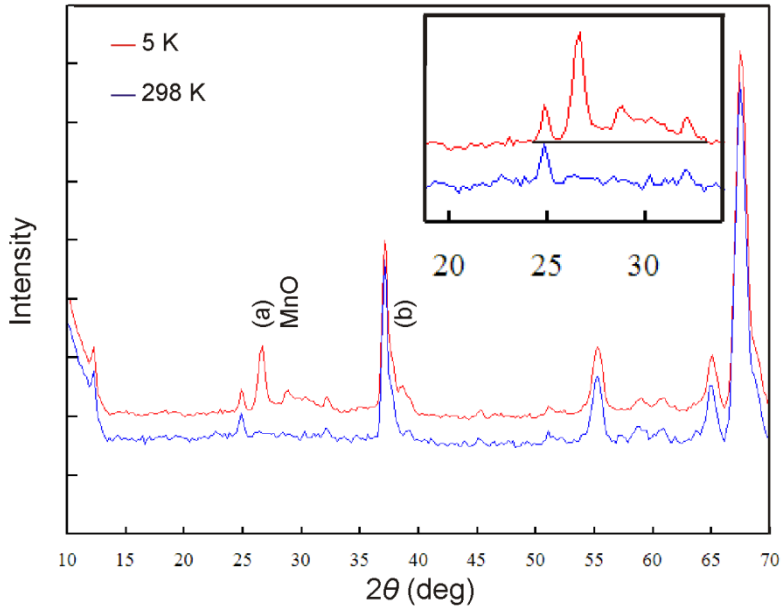


Figure 4.14: Neutron powder diffraction data collected from $La_{0.33}Sr_{0.67}MnO_{2.42}$ at 5 K (red) and 298 K (blue) using the D1b instrument. Inset highlights the 'lump' in the 5 K data set. The 5 K data set contains an additional reflection at approximately 29 ° consistent with the presence of antiferromagnetically ordered MnO (T_N = 116 K).[73]

As shown in Figure 4.15, data sets collected from the remaining $La_{1-x}Sr_xMnO_{3-(0.5+x)/2}$ ($0.7 \leq x \leq 0.83$) phases at 5 K also contain additional reflection(s) compared to the analogous data sets collected at room temperature. While the data sets collected from all $La_{1-x}Sr_xMnO_{3-(0.5+x)/2}$ ($0.7 \leq x \leq 0.83$) compositions contain reflections analogous to reflection (a), only the data set collected from $La_{0.3}Sr_{0.7}MnO_{2.4}$ contains an additional reflection analogous to reflection (b).

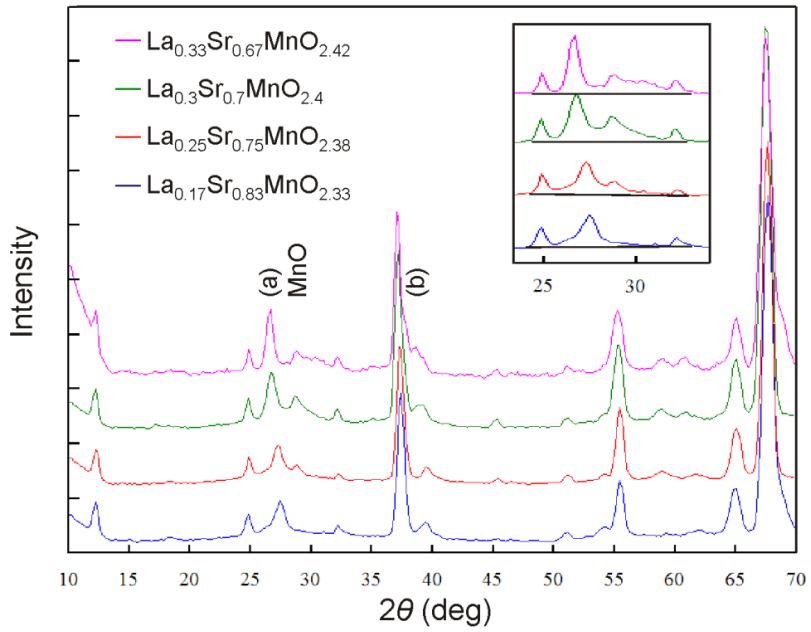


Figure 4.15: 5 K neutron powder diffraction data sets collected from $La_{1-x}Sr_xMnO_{3-(0.5+x)/2}$ ($0.67 \leq x \leq 0.83$). The 5 K data sets contain an additional reflection at approximately 29 ° consistent with the presence of antiferromagnetically ordered MnO (T_N = 116 K).[73]

Given the similarity in the positions and intensities of the magnetic reflections in the data sets, it is clear that the magnetic structures of all the '6-layer manganate' materials are similar. However, the presence of magnetic reflection (b) in the 5 K data set collected from $La_{0.33}Sr_{0.67}MnO_{2.42}$ and $La_{0.3}Sr_{0.7}MnO_{2.4}$, suggest that these phases adopt a slightly different magnetic ordering scheme to the more Sr^{2+}-rich phases, possibly due to the inclusion of an extra magnetic component. A further observation is that the additional 'lump' in the data between approximately 27.5° and 33° (see Figure 4.14) becomes less intense with increasing Sr^{2+}-content across the $La_{1-x}Sr_xMnO_{3-(0.5+x)/2}$ ($0.7 \leq x \leq 0.83$) series, consistent with the gradual removal of the additional short range magnetic order in the systems.

The magnetic reflection(s) observed in data collected from the $La_{1-x}Sr_xMnO_{3-(0.5+x)/2}$ ($0.67 \leq x \leq 0.83$) phases at 5 K could not be indexed using unit cells based on obvious expansions of the corresponding nuclear unit cells. Furthermore the positions of the observed magnetic reflections do not shift in a manner consistent with the shift in the crystallographic lattice as a function of the Sr^{2+}-content. For instance, the position of magnetic reflection (a) is very close to, but not coincident with, the position of the systematically absent (012) nuclear

reflection. However, as shown in Figure 4.16, the position of the magnetic reflection and the (012) nuclear reflection change to different extents as the Sr^{2+}-content increases.

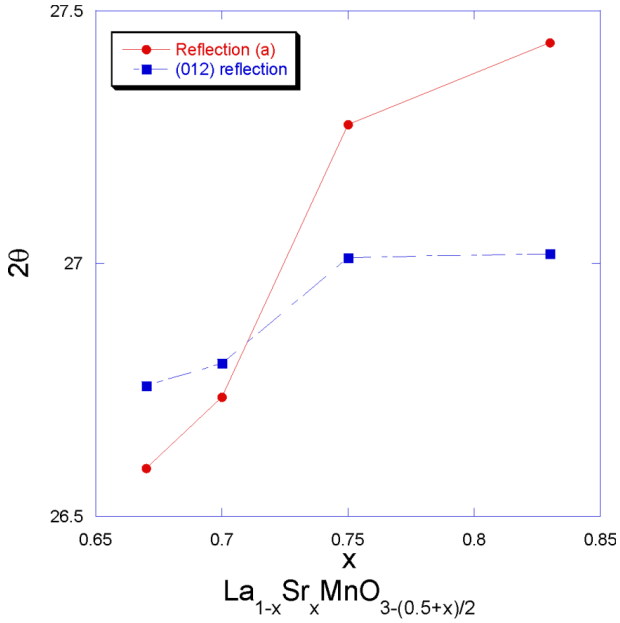


Figure 4.16: Position of magnetic reflection (a) and (012) systematically absent crystallographic reflection

Therefore, it was hypothesised that the magnetic unit cells of the $La_{1-x}Sr_xMnO_{3-(0.5+x)/2}$ ($0.67 \leq x \leq 0.83$) phases were incommensurate with respect to the nuclear unit cells. Given the low number of observed magnetic diffraction reflections and the incommensurate relationship between crystallographic and magnetic unit cells, it was not possible to deduce a magnetically ordered model.

4.6.1.3. Variable temperature neutron diffraction data

Variable temperature neutron diffraction data were collected from the $La_{1-x}Sr_xMnO_{3-(0.5+x)/2}$ ($0.67 \leq x \leq 0.83$) phases to determine the temperature dependence of the magnetic behaviour. Data collected from $La_{0.33}Sr_{0.67}MnO_{2.42}$ using the D1b instrument (see section 2.3.2.1.3) are shown in Figure 4.17.

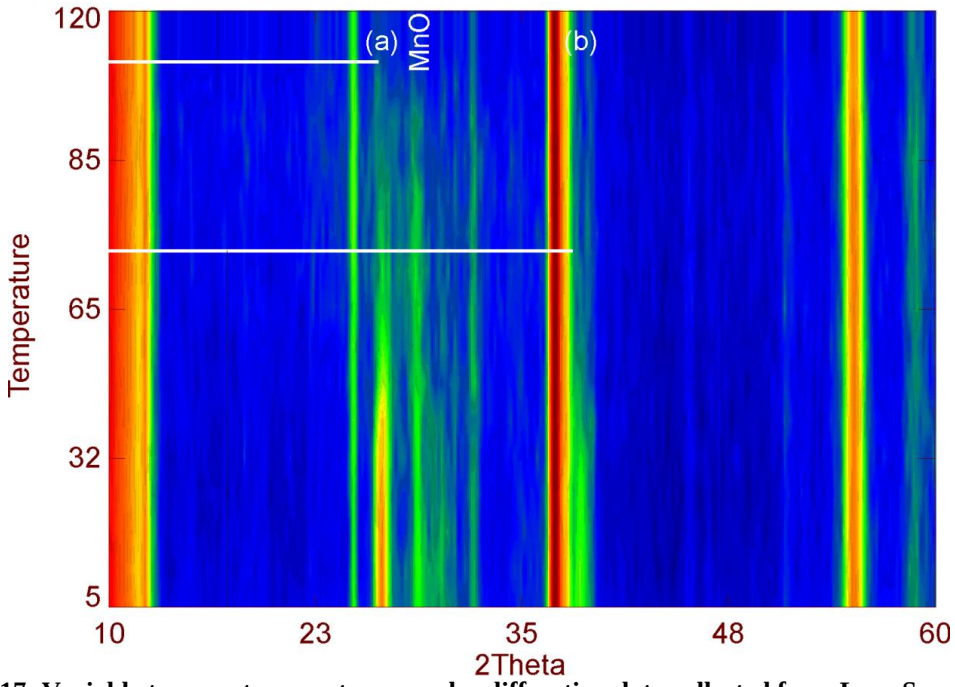


Figure 4.17: Variable temperature neutron powder diffraction data collected from $La_{0.33}Sr_{0.67}MnO_{2.42}$. The white lines mark the onset temperatures of the magnetic reflections.

It is clear that the onset of reflections (a) and (b) occur at different temperatures – a clear indication that there are multiple components to the magnetic ordering scheme of $La_{0.33}Sr_{0.67}MnO_{2.42}$. In addition, the additional 'lump' in the diffraction data ($27.5^o \leq 2\theta \leq 33^o$) starts to increase in intensity at a slightly lower temperature than the magnetic reflections. It is however not possible to match the features in the paramagnetic susceptibility data (see Figure 4.12) to the onset temperatures of the magnetic features in the diffraction data.

Analogous variable temperature data sets collected from $La_{1-x}Sr_xMnO_{3-(0.5+x)/2}$ ($0.75 \leq x \leq 0.83$) phases using the D1b instrument are shown in Figure 4.29 in Appendix 4. The onset temperatures for magnetic reflections (a) and (b) in these data sets are shown in Table 4.6.

$La_{1-x}Sr_xMnO_{3-(0.5+x)/2}$	Onset Temperature (K)	
	Reflection (a)	Reflection (b)
0.67	110(10)	75(10)
0.7	90(10)	50(10)
0.75	85(10)	N/A
0.83	75(10)	N/A

Table 4.6: Onset temperatures for magnetic reflections in neutron powder diffraction data collected from $La_{1-x}Sr_xMnO_{3-(0.5+x)/2}$ ($0.67 \leq x \leq 0.83$)

4.7. Discussion

The magnetic reflections ((a) and (b), when appropriate) in the neutron powder diffraction data sets collected at 5 K indicate that long range magnetic order is present in the $La_{1-x}Sr_xMnO_{3-(0.5+x)/2}$ ($0.67 \leq x \leq 0.83$) phases. The additional broad 'lumps' in the 5 K neutron powder diffraction data sets are consistent with further short range order in the magnetic structures of these phases.

In addition, the displacements of the 5 K magnetisation-field loops collected from 6-layer $La_{1-x}Sr_xMnO_{3-(0.5+x)/2}$ ($0.67 \leq x \leq 0.83$) to higher magnetisations are consistent with these phases displaying spin glass magnetic behaviour, indicative of magnetic frustration in the system. It is therefore clear that the magnetic systems of the '6-layer manganate' phases are highly complex and contain a number of different magnetic components.

4.7.1. Comparison to $La_{0.5}Sr_{0.5}MnO_{2.5}$

Some insight into the complex magnetic behaviour of the '6-layer manganate' phases can be gained from comparison to the magnetically ordered structure of the structurally related $La_{0.5}Sr_{0.5}MnO_{2.5}$ brownmillerite phase. The structure of $La_{0.5}Sr_{0.5}MnO_{2.5}$ shown in Figure 4.18 contains $Mn^{II}O_4$ tetrahedral centres (as in the '6-layer manganate' phases) and $Mn^{III}O_6$ octahedral centres. It adopts a simple G-type antiferromagnetically ordered arrangement below 140 K in which all the magnetic interactions are 'satisfied'.[21]

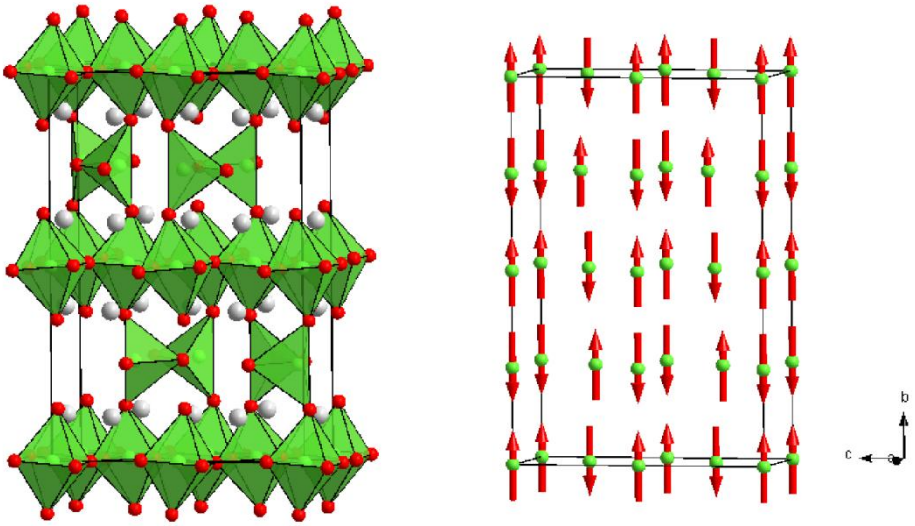


Figure 4.18: The nuclear (left) and magnetic (right) structure of the $La_{0.5}Sr_{0.5}MnO_{2.5}$ brownmillerite phase

Given the Jahn-Teller distortion, the octahedral Mn^{III} centres contain empty $3d_{x^2-y^2}$ orbitals. Considering the Goodenough-Kanamori rules,[52] the dominant superexchange magnetic interactions in $La_{0.5}Sr_{0.5}MnO_{2.5}$ shown in Figure 4.19 are predicted to be antiferromagnetic: The 180°, σ-type Mn^{III} $(d_{x^2-y^2})^0$ – O (2*p*) – Mn^{III} $(d_{x^2-y^2})^0$ superexchange interaction is predicted to bring about antiferromagnetic order within the *ac*-plane of the octahedral layers. In addition, the 180°, σ-type Mn^{III} $(d_{z^2})^1$ – O (2*p*) – Mn^{II} $(d_{z^2})^1$ superexchange interactions bring about antiferromagnetic order between the layers (i.e. parallel to the *b*-axis).

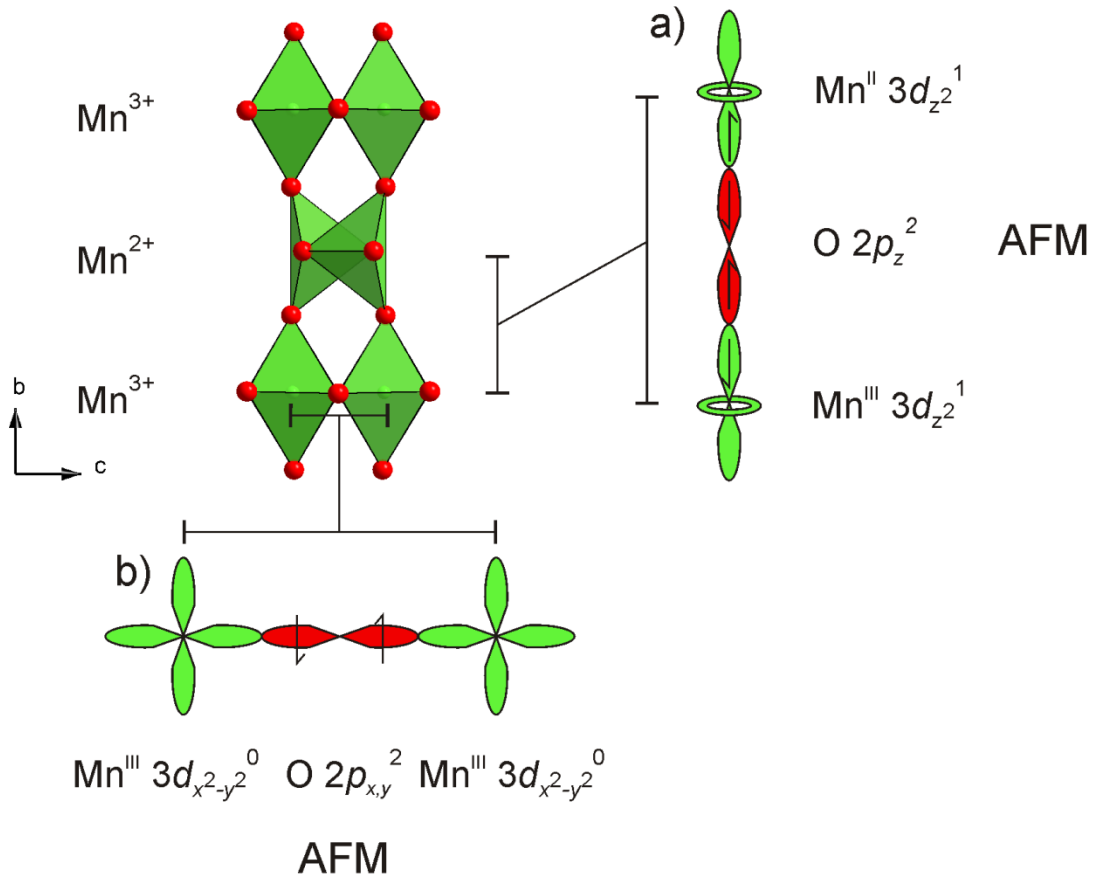


Figure 4.19: Predicted magnetic interactions in the brownmillerite $La_{0.5}Sr_{0.5}MnO_{2.5}$ phase

4.7.2. Magnetic structure of the hypothetical Mn(III) '6-layer manganate' phase

The same principles can be applied to the hypothetical 6-layer SSTSST'-stacked phase (i.e. isostructural with $La_{0.17}Sr_{0.83}MnO_{2.33}$) which contains an analogous 'charge ordering' scheme to that in $La_{0.5}Sr_{0.5}MnO_{2.5}$, i.e. $Mn^{II}O_4$ tetrahedral centres and $Mn^{III}O_5$ square-based pyramidal centres. In an analogous fashion to the $Mn^{III}O_6$ octahedra in $La_{0.5}Sr_{0.5}MnO_{2.5}$, the $Mn^{III}O_5$ square-based pyramidal centres in this hypothetical Mn^{III} 6-layer phase are predicted to contain empty $d_{x^2-y^2}$ orbitals.

As shown in Figure 4.20, the majority of the magnetic interactions in this hypothetical 6-layer phase are very similar to those in the 4-layer brownmillerite $La_{0.5}Sr_{0.5}MnO_{2.5}$ phase.[52] The 180°, σ-type in-plane Mn^{III} $(d_{x^2-y^2})^0$ – O $(2p)$ – Mn^{III} $(d_{x^2-y^2})^0$ superexchange interactions maintain antiferromagnetic order within each square-based pyramidal layer.

Whereas the 180°, σ-type Mn^{III} $(d_{z^2})^1$ – O (2*p*) – Mn^{II} $(d_{z^2})^1$ superexchange interactions maintain antiferromagnetic order parallel to the stacking direction in each STS-block. Full 3D magnetic order throughout the entire structure requires antiferromagnetic Mn^{III} $(d_{z^2})^1$ – Mn^{III} $(d_{z^2})^1$ direct exchange interactions between square-based pyramidal Mn^{III} centres in neighbouring layers.[52] Therefore, this hypothetical Mn^{III}-containing 6-layer SSTSST'-stacked phase is predicted to adopt a G-type antiferromagnetically ordered arrangement.

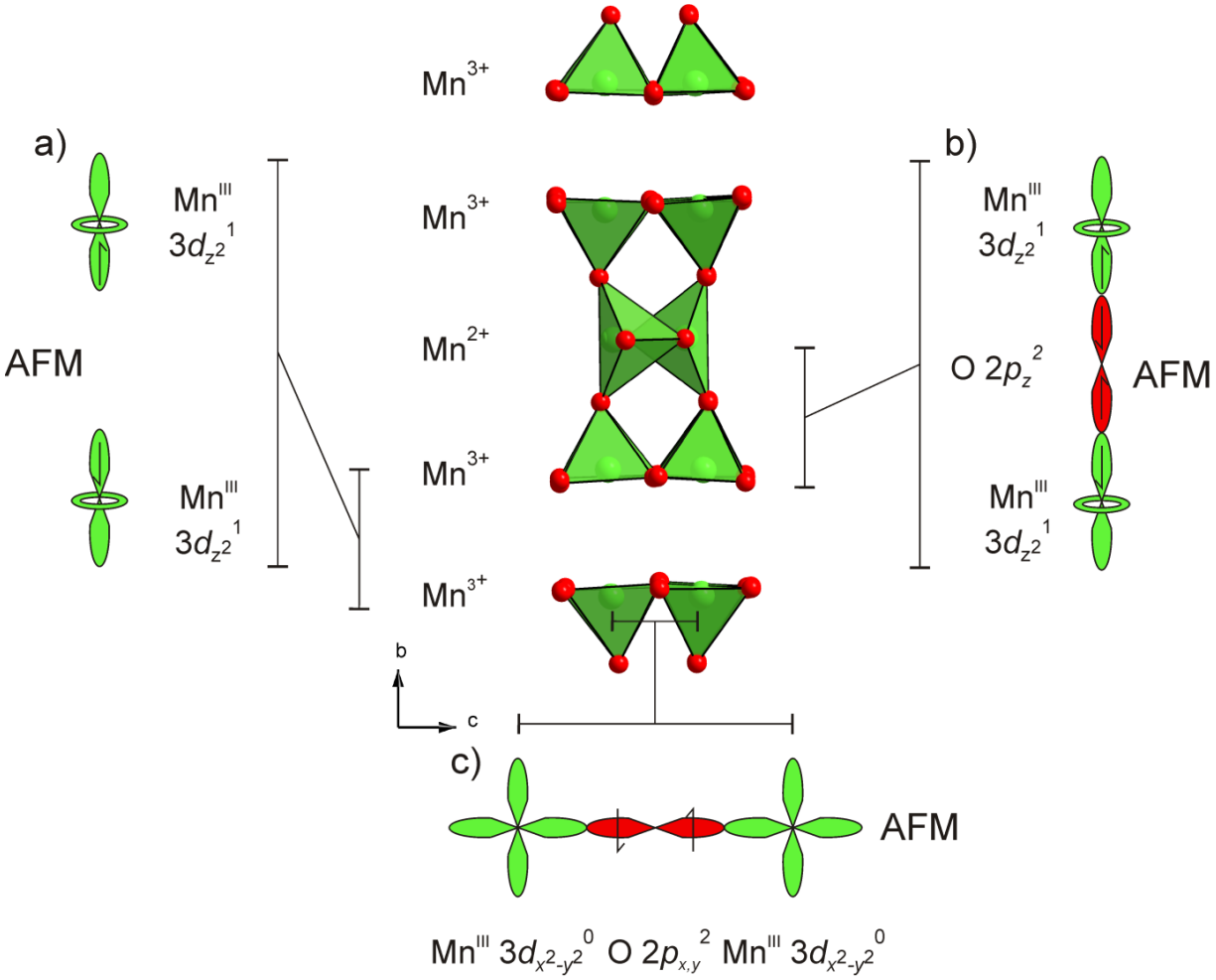


Figure 4.20: Predicted magnetic interactions in the hypothetical 6-layer phase containing $Mn^{II}O_4$ tetrahedral centres and $Mn^{III}O_6$ octahedral centres

4.7.3. Magnetic structure of '6-layer manganates'

4.7.3.1. Mixed valence

In an analogous fashion to the 4-layer brownmillerite $La_{0.5}Sr_{0.5}MnO_{2.5}$ phase and the hypothetical 6-layer SSTSST'-stacked phase discussed in the previous section, the '6-layer

manganate' $La_{1-x}Sr_xMnO_{3-(0.5+x)/2}$ (x = 0.67, 0.7 and 0.75) phases contain $Mn^{II}O_4$ tetrahedral centres. However, unlike the other phases, the 'octahedral' layers in the '6-layer manganate' structure contain manganese centres with an average oxidation state of +2.75. Within these 'octahedral' layers, the Mn(II) centres adopt high-spin d^5 configurations while the Mn(III) centres contain empty $d_{x^2-y^2}$ orbitals due to the Jahn-Teller-like distortion. The occupation of the d_{z^2} orbitals and, therefore, the magnetic interactions parallel to the *z*-direction are unaffected by the mixed valent nature of the 'octahedral' layers.

However, the mixed valence in the 'octahedral' layers of the '6-layer manganate' phases introduces the possibility of the strong σ-type, 180° Mn^{II} $(d_{x^2-y^2})^1$ – O (2*p*) – Mn^{III} $(d_{x^2-y^2})^0$ superexchange interactions. By consideration of the Goodenough-Kanamori rules,[52] this interaction is predicted to be ferromagnetic. This ferromagnetic interaction will compete with the antiferromagnetically coupled σ-exchange network and other in-plane σ-type couplings, such as Mn^{II} $(d_{x^2-y^2})^1$ – O (2*p*) – Mn^{II} $(d_{x^2-y^2})^1$ which are predicted to be antiferromagnetic.[52] It is highly likely that this competition between the ferromagnetic and antiferromagnetic interactions results in the formation of a frustrated magnetic system.

4.7.3.2. Twisted tetrahedral chains

In addition, as shown in Figure 4.21, the nature of the in-plane Mn^{II} $(d_{x^2-y^2})^1$ – O (2*p*) – Mn^{II} $(d_{x^2-y^2})^1$ superexchange interactions within the tetrahedral layers is dependent on the Mn-O-Mn in-plane angle.[52] This interaction is predicted to be antiferromagnetic when the link is 180° (see Figure 4.21 b)) but ferromagnetic when the link is 90° (see Figure 4.21 a)).[52] The in-plane Mn-O-Mn links within the tetrahedral chains in the structures of the $La_{1-x}Sr_xMnO_{3-(0.5+x)/2}$ (x = 0.67, 0.7 and 0.75) phases are highly distorted from 180°, e.g. 111.16° and 118.85° in the structure of $La_{0.33}Sr_{0.67}MnO_{2.42}$, and so may add an additional ferromagnetic component to the ordering scheme. This ferromagnetic component would then, as above,

compete with the underlying antiferromagnetic framework, thereby resulting in frustration in the magnetic system.

However, it should be noted that the brownmillerite structure of $La_{0.5}Sr_{0.5}MnO_{2.5}$ also contains highly distorted in-plane tetrahedral Mn-O-Mn links (110.91^{o}) but the manganese centres are in fact observed to couple antiferromagnetically in the brownmillerite phase.[20] Therefore, the in-plane Mn^{2+} – O – Mn^{2+} interaction can, but does not have to, add a ferromagnetic component to the magnetic ordering scheme.

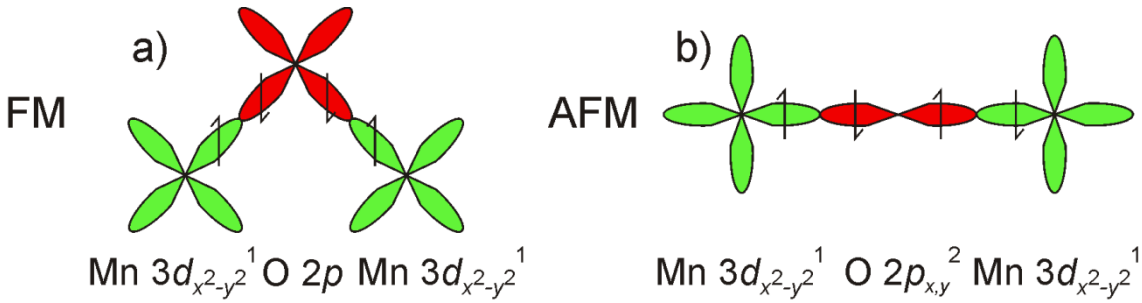


Figure 4.21: 2 competing magnetic interactions in the twisted tetrahedral chains

4.7.3.3. Magnetic structure

Given the number of competing magnetic interactions in the '6-layer manganate' phases, it is unsurprising that these phases adopt frustrated magnetic systems. Therefore, rather than adopting a 'simple' magnetic ordering structure like the $La_{0.5}Sr_{0.5}MnO_{2.5}$ brownmillerite phase, the '6-layer manganate' phases adopt magnetically ordered structures incommensurate with the nuclear structure to best satisfy the competing magnetic interactions.

As detailed above, all magnetic interactions parallel to the *b*-axis in the '6-layer manganate' phases are predicted to be antiferromagnetic. It is therefore logical to suggest that the magnetically ordered structure of the '6-layer manganate' phases is ordered in a manner commensurate with the nuclear structure parallel to the *b*-axis. However, there are in-plane ferromagnetic interactions which can compete with the underlying antiferromagnetic framework and thereby cause magnetic frustration.

4.7.3.4. Effect of Sr^{2+}-content on magnetic behaviour

The magnetic features in low temperature neutron diffraction data (see section 4.6.1.2) collected from the '6-layer manganate' phases are necessarily attributable to 3D magnetic order. As shown in Figure 4.20, the manganese centres within each OTO-block of the '6-layer manganate' structure are predicted to couple antiferromagnetically parallel to the stacking direction via strong 180°, σ-type superexchange interactions. However, for full 3D magnetic order to be present in the '6-layer manganate' phases, magnetic coupling between the manganese centres in the neighbouring 'octahedral' layers is required. Given the low fractional occupancy of the 'bridging' anion sites (f(O(1)/(8)($La_{0.33}Sr_{0.67}MnO_{2.42}$) = 25 %), magnetic coupling between neighbouring MnO_2 layers requires a mixture of σ-type Mn(d_{z^2})-O-Mn(d_{z^2}) superexchange and Mn(d_{z^2})-Mn(d_{z^2}) direct exchange interactions, both of which are predicted to be antiferromagnetic regardless of the formal charge on the manganese centres (see Table 4.13 in Appendix 4).[52]

As shown in Table 4.6, the onset temperatures for the magnetic reflections decrease with increasing Sr^{2+}-content. As the Sr^{2+}-content in the '6-layer manganate' phases increases, the fractional occupancy of the 'bridging' oxide anion sites decreases and, therefore, the number of strong 180°, σ-type Mn(d_{z^2})-O-Mn(d_{z^2}) superexchange interactions decreases. Instead, for 3D magnetic order to be maintained, these relatively strong superexchange interactions are replaced by weaker σ-type Mn(d_{z^2})-Mn(d_{z^2}) direct exchange interactions. It is therefore likely that the magnetic interactions between neighbouring 'octahedral' layers are the limiting factor in the formation of full 3D magnetic order

4.8. Magnetic conclusion

Analysis of the pairwise magnetic interactions in the $La_{1-x}Sr_xMnO_{3-(0.5+x)/2}$ ($0.67 \leq x \leq 0.83$) phases would predict the presence of magnetic frustration and no long range order. However, the $La_{1-x}Sr_xMnO_{3-(0.5+x)/2}$ ($0.67 \leq x \leq 0.83$) phases are magnetically ordered over the

long range, albeit in a manner incommensurate with the nuclear structure. Similar complex magnetic behaviour has been previously observed in the 4-layer $La_{1-x}A_xMnO_{2.5}$ ($0.2 \leq x \leq 0.5$; A = Ca^{2+}, Sr^{2+} and Ba^{2+}) brownmillerite phases.[22]

Appendix 4

$La_{1-x}Sr_xMnO_3$	Space group	Refined *a* (Å)	Refined *c* (Å)	Published *a* (Å)	Published *c* (Å)
0.5	*I*4/*mcm*	5.4423(3)	7.7538(5)	5.4446(1)	7.7595(1)
0.6	*I*4/*mcm*	5.4308(1)	7.7363(1)	5.4293(1)	7.7381(1)
0.7	*I*4/*mcm*	5.4281(1)	7.6692(1)	5.4301(1)	7.6704(2)
0.75	*Pm m*	3.8319(1)			
0.83	*Pm m*	3.8248(1)			
0.9	*Pm m*	3.8163(1)		3.8181(1)	
1	*Pm m*	3.8064(1)		3.8041(3)	

Table 4.7: Lattice parameters refined against X-ray powder diffraction data for $La_{1-x}Sr_xMnO_3$ starting materials

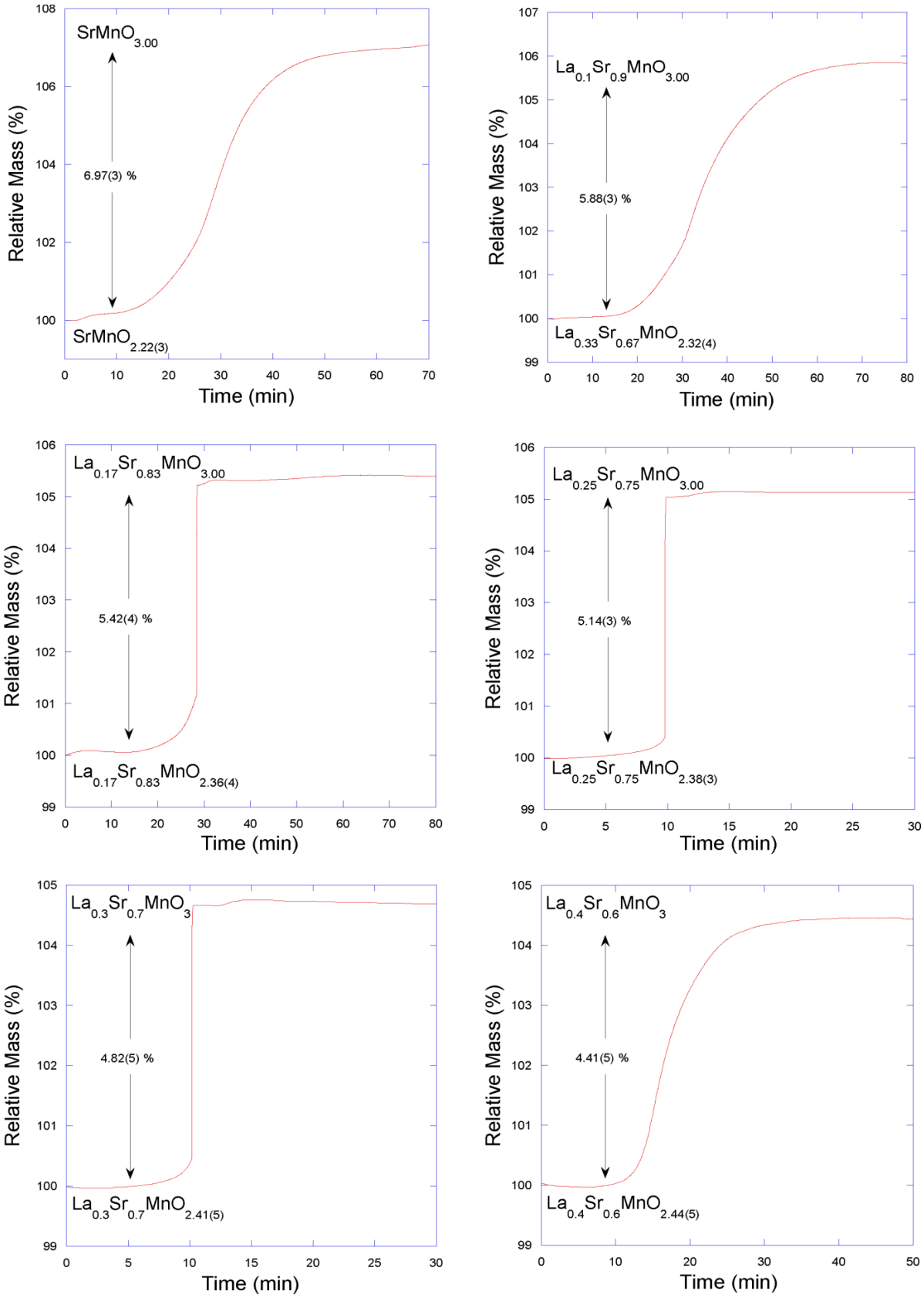


Figure 4.22: Reoxidative thermogravimetric data collected from $La_{1-x}Sr_xMnO_{3-(0.5+x)/2}$ phases

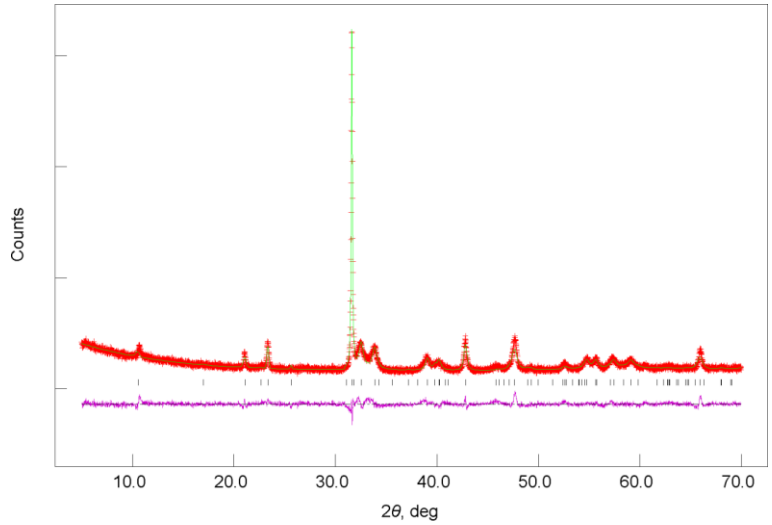


Figure 4.23: Plots for refinement against powder X-ray diffraction data collected from $La_{0.5}Sr_{0.5}MnO_{2.45}$, χ^2 = 1.152, *wRp* = 7.07 %, *Rp* = 8.44 %

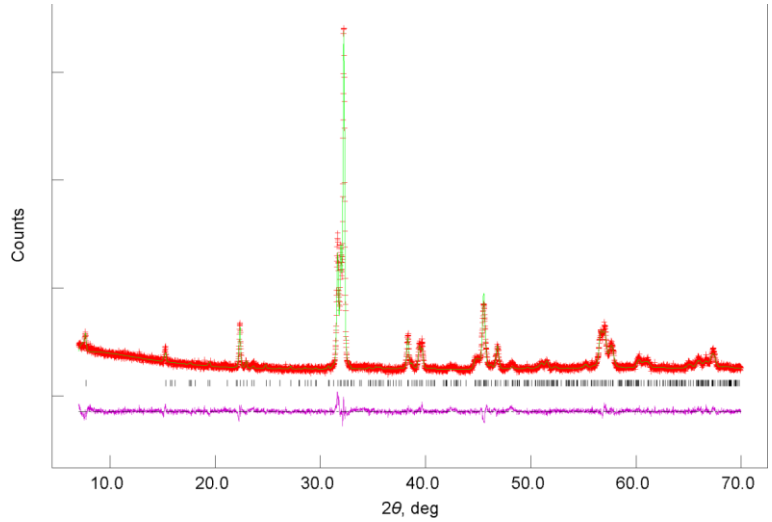


Figure 4.24: Plots for refinement against powder X-ray diffraction data collected from $La_{0.4}Sr_{0.6}MnO_{2.45}$, χ^2 = 1.104, *wRp* = 5.51 %, *Rp* = 6.07 %

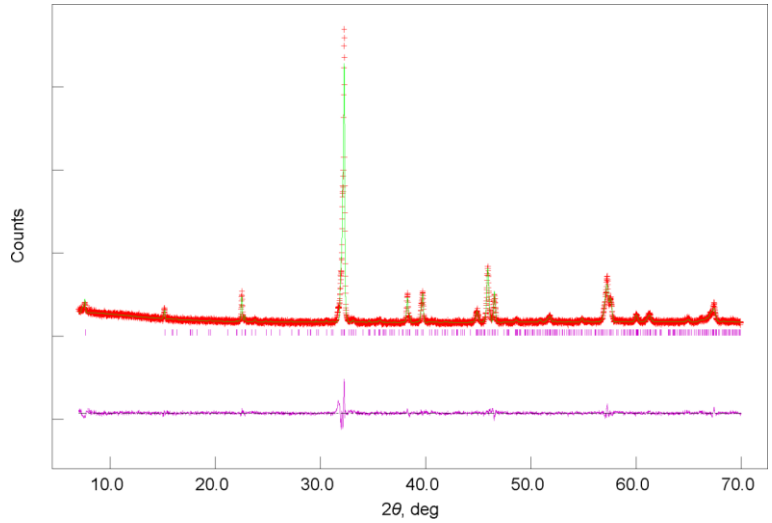


Figure 4.25: Plots for refinement against powder X-ray diffraction data collected from $La_{0.3}Sr_{0.7}MnO_{2.4}$, χ^2 = 1.139, *wRp* = 7.27 %, *Rp* = 5.43 %

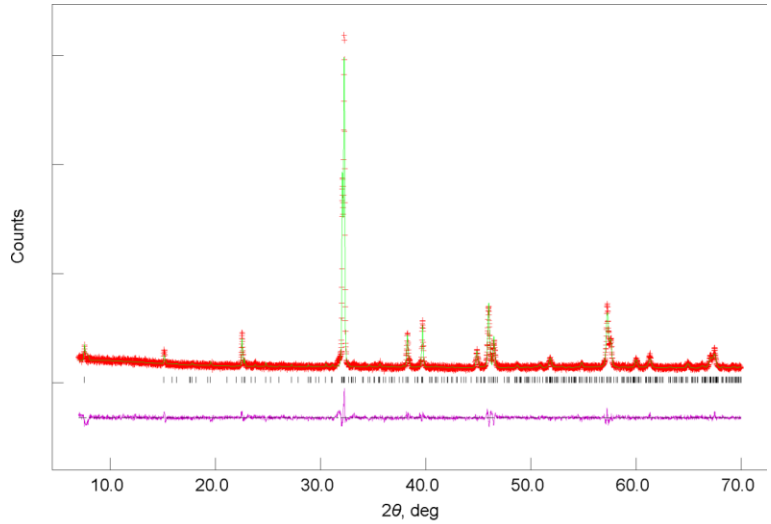


Figure 4.26: Plots for refinement against powder X-ray diffraction data collected from $La_{0.25}Sr_{0.75}MnO_{2.38}$, χ^2 = 1.052, *wRp* = 7.74 %, *Rp* = 5.97 %

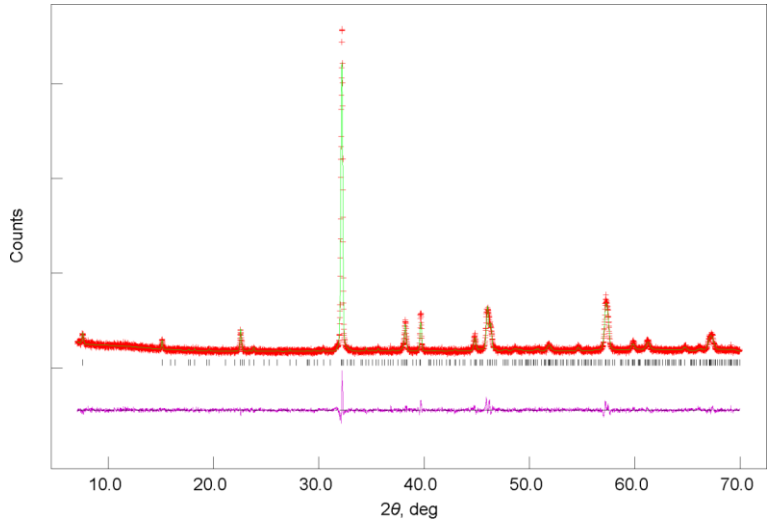


Figure 4.27: Plots for refinement against powder X-ray diffraction data collected from $La_{0.17}Sr_{0.83}MnO_{2.33}$, χ^2 = 1.104, *wRp* = 6.19 %, *Rp* = 4.82 %

Atom	Wyckoff position	*x*	*y*	*z*	Occupancy	U_{iso} (Å^3)
Sr/La(1)	4*a*	½	0	0	0.75/0.25	0.012(1)
Sr/La(2)	4*c*	0.004(3)	0	¼	0.75/0.25	0.012(1)
Sr/La(3)	8*e*	0.475(1)	0.156(1)	0.000(1)	0.75/0.25	0.012(1)
Sr/La(4)	8*e*	0.999(2)	0.148(1)	0.251(1)	0.75/0.25	0.012(1)
Mn(1)	8*e*	0.001(1)	0.082(1)	0.999(1)	1	0.004(1)
Mn(2)	4*d*	0.452(1)	¾	0.285(1)	0.56(2)	0.004(1)
Mn(2')	4*d*	0.548(1)	¾	0.285(2)	0.44(2)	0.004(1)
Mn(3)	4*d*	0.028(1)	¼	0.040(1)	0.56(2)	0.004(1)
Mn(3')	4*d*	0.972(1)	¼	0.040(1)	0.44(2)	0.004(1)
Mn(4)	8*e*	0.502(1)	0.082(1)	0.250(1)	1	0.004(1)
O(1)	4*a*	0	0	0	0.125	0.41(1)
O(2)	8*e*	0.994(3)	0.169(1)	0.982(1)	1	0.013(1)
O(3)	4*d*	0.914(1)	¼	0.220(1)	0.56(2)	0.013(1)
O(3')	4*d*	0.086(1)	¼	0.220(1)	0.44(2)	0.013(1)
O(4)	4*d*	0.414(1)	¼	0.049(1)	0.56(2)	0.013(1)
O(4')	4*d*	0.585(1)	¼	0.049(1)	0.44(2)	0.013(1)
O(5)	8*e*	0.752(3)	0.069(1)	0.375(2)	1	0.013(1)
O(6)	8*e*	0.251(1)	0.070(1)	0.373(1)	1	0.013(1)
O(7)	8*e*	0.502(2)	0.169(1)	0.235(1)	1	0.013(1)
O(8)	4*c*	½	0	¼	0.125	0.41(1)
O(9)	8*e*	0.252(2)	0.075(1)	0.124(2)	1	0.013(1)
O(10)	8*e*	0.743(2)	0.070(1)	0.128(1)	1	0.013(1)
$La_{0.3}Sr_{0.7}MnO_{2.4}$: space group *Pcmb*, *a* = 5.5902(3) Å, *b* = 23.4813(7) Å, *c* = 11.1795(7) Å, cell volume = 1467.48(13) Å^3						
MnO: space group *Fm m*, *a* = 4.447(1) Å; wt. frac. = 1.2(1) %						
χ^2 = 1.698, wR_p = 4.11 %, R_p = 3.23 %						

Table 4.8: Structural parameters refined against neutron powder diffraction data collected from $La_{0.25}Sr_{0.75}MnO_{2.38}$.

Atom	Wyckoff position	*x*	*y*	*z*	Occupancy	U_{iso} (Å^3)
Sr/La(1)	4*a*	½	0	0	0.7/0.3	0.010(1)
Sr/La(2)	4*c*	0.998(4)	0	¼	0.7/0.3	0.010(1)
Sr/La(3)	8*e*	0.497(3)	0.156(1)	0.996(1)	0.7/0.3	0.010(1)
Sr/La(4)	8*e*	0.999(3)	0.149(1)	0.257(1)	0.7/0.3	0.010(1)
Mn(1)	8*e*	0.004(1)	0.082(1)	0.001(2)	1	0.003(1)
Mn(2)	4*d*	0.480(1)	¾	0.275(2)	0.63(2)	0.003(1)
Mn(2')	4*d*	0.520(1)	¾	0.275(2)	0.37(2)	0.003(1)
Mn(3)	4*d*	0.050(1)	¼	0.025(1)	0.63(2)	0.003(1)
Mn(3')	4*d*	0.950(1)	¼	0.025(1)	0.37(2)	0.003(1)
Mn(4)	8*e*	0.494(1)	0.082(1)	0.252(2)	1	0.003(1)
O(1)	4*a*	0	0	0	0.2	0.41(1)
O(2)	8*e*	0.996(1)	0.167(1)	0.973(1)	1	0.011(1)
O(3)	4*d*	0.898(1)	¼	0.208(1)	0.63(2)	0.011(1)
O(3')	4*d*	0.102(1)	¼	0.208(1)	0.37(2)	0.011(1)
O(4)	4*d*	0.396(1)	¼	0.041(1)	0.63(2)	0.011(1)
O(4')	4*d*	0.604(1)	¼	0.041(1)	0.37(2)	0.011(1)
O(5)	8*e*	0.752(1)	0.069(1)	0.378(1)	1	0.011(1)
O(6)	8*e*	0.249(1)	0.067(1)	0.377(2)	1	0.011(1)
O(7)	8*e*	0.497(2)	0.169(1)	0.251(1)	1	0.011(1)
O(8)	4*c*	½	0	¼	0.2	0.41(1)
O(9)	8*e*	0.244(3)	0.076(1)	0.132(1)	1	0.011(1)
O(10)	8*e*	0.744(3)	0.070(1)	0.144(1)	1	0.011(1)
$La_{0.3}Sr_{0.7}MnO_{2.4}$: space group *Pcmb*, *a* = 5.5849(2) Å, *b* = 23.4734(9) Å, *c* = 11.2275(5) Å, cell volume = 1471.89(10) Å^3						
MnO: space group *Fm m*, *a* = 4.447(1) Å; wt. frac. = 1.0(1) %						
χ^2 = 2.286, wR_p = 4.71 %, R_p = 3.69 %						

Table 4.9: Structural parameters refined against neutron powder diffraction data collected from $La_{0.3}Sr_{0.7}MnO_{2.4}$.

Atom	Contact	Length (Å)	Contact	Length (Å)
Mn octahedral	Mn(1) - O(1)	1.93(2)	Mn(4) - O(5)	2.00(2)
	Mn(1) - O(2)	2.05(3)	Mn(4) - O(6)	1.99(1)
	Mn(1) - O(5)	1.98(2)	Mn(4) - O(7)	2.05(3)
	Mn(1) - O(6)	2.01(1)	Mn(4) - O(8)	1.93(2)
	Mn(1) - O(9)	1.99(2)	Mn(4) - O(9)	1.99(2)
	Mn(1) - O(10)	1.98(1)	Mn(4) - O(10)	2.02(1)
Mn tetrahedral	Mn(2) - O(3)	2.05(1)	Mn(3) - O(3)	2.11(1)
	Mn(2) - O(4)	2.00(1)	Mn(3) - O(4)	2.16(1)
	Mn(2) - O(7) x 2	1.94(1)	Mn(3) - O(2) x 2	2.02(2)
Tetrahedral twist	O(3) - O(4) - (3)	111.3(2)		

Table 4.10: Selected bond lengths and angle from the structural refinement of $La_{0.25}Sr_{0.75}MnO_{2.38}$

Atom	Contact	Length (Å)	Contact	Length (Å)
Mn octahedral	Mn(1) - O(1)	1.93(2)	Mn(4) - O(5)	2.04(1)
	Mn(1) - O(2)	2.02(3)	Mn(4) - O(6)	1.99(2)
	Mn(1) - O(5)	1.96(3)	Mn(4) - O(7)	2.04(3)
	Mn(1) - O(6)	2.02(3)	Mn(4) - O(8)	1.93(2)
	Mn(1) - O(9)	2.00(3)	Mn(4) - O(9)	1.95(2)
	Mn(1) - O(10)	1.95(3)	Mn(4) - O(10)	2.11(2)
Mn tetrahedral	Mn(2) - O(3)	2.12(8)	Mn(3) - O(3)	2.22(1)
	Mn(2) - O(4)	2.18(1)	Mn(3) - O(4)	1.941(8)
	Mn(2) - O(7) x 2	1.93(2)	Mn(3) - O(2) x 2	2.05(2)
Tetrahedral twist	O(3) - O(4) - (3)	112.2(2)		

Table 4.11: Selected bond lengths and angle from the structural refinement of $La_{0.3}Sr_{0.7}MnO_{2.4}$

Phase	Stacking of tetrahedral layers	*m* ($A_mB_mO_{3m-x}$)	Tetrahedral layer separation	In plane O-O-O angle in BO layer
$(La_{1/3}Sr_{2/3})_3Fe_3O_8$[62]	Eclipsed	3	11.88(1)	126.1(4)
$Ca_{2.5}Sr_{0.5}GaMn_2O_8$[74]	Eclipsed	3	11.38(1)	122.41(1)
$(Nd_{1/3}Ca_{2/3})_3Fe_3O_8$[60]	Eclipsed	3	11.35(1)	139.4(1)
$(La_{1/3}Ca_{2/3})_3Fe_3O8$[60]	Eclipsed	3	11.31(1)	137(1)
$Ca_3TiFe_2O_8$[75]	Eclipsed	3	11.20(1)	134.9(8)
$Ca_3Mn_{1.2}Fe_{1.8}O_8$[75]	Eclipsed	3	11.15(1)	118.7(6)
$CaMnAlO_{5.5}$[68]	Staggered	4	14.76(1)	130.4(1)
$Ca_2Ba_2Nd_2Fe_6O_{15.6}$[6]	Staggered	6	19.37(1)	111.2(3)
$Y_{0.65}Ca_{0.35}Sr_2Cu_2GaO_7$[76]	Staggered	3	11.40(1)	123.5(1)
$LaSr_2GaCu_2O_7$[61]	Staggered	3	11.57(1)	126.0(1)
$YSr_2GaCu_2O_7$[61]	Staggered	3	11.40(1)	121(1)

Table 4.12: Pertinent structural parameters from some anion-deficient perovskite phases ($A_mB_mO_{3m-x}$) containing tetrahedral layers

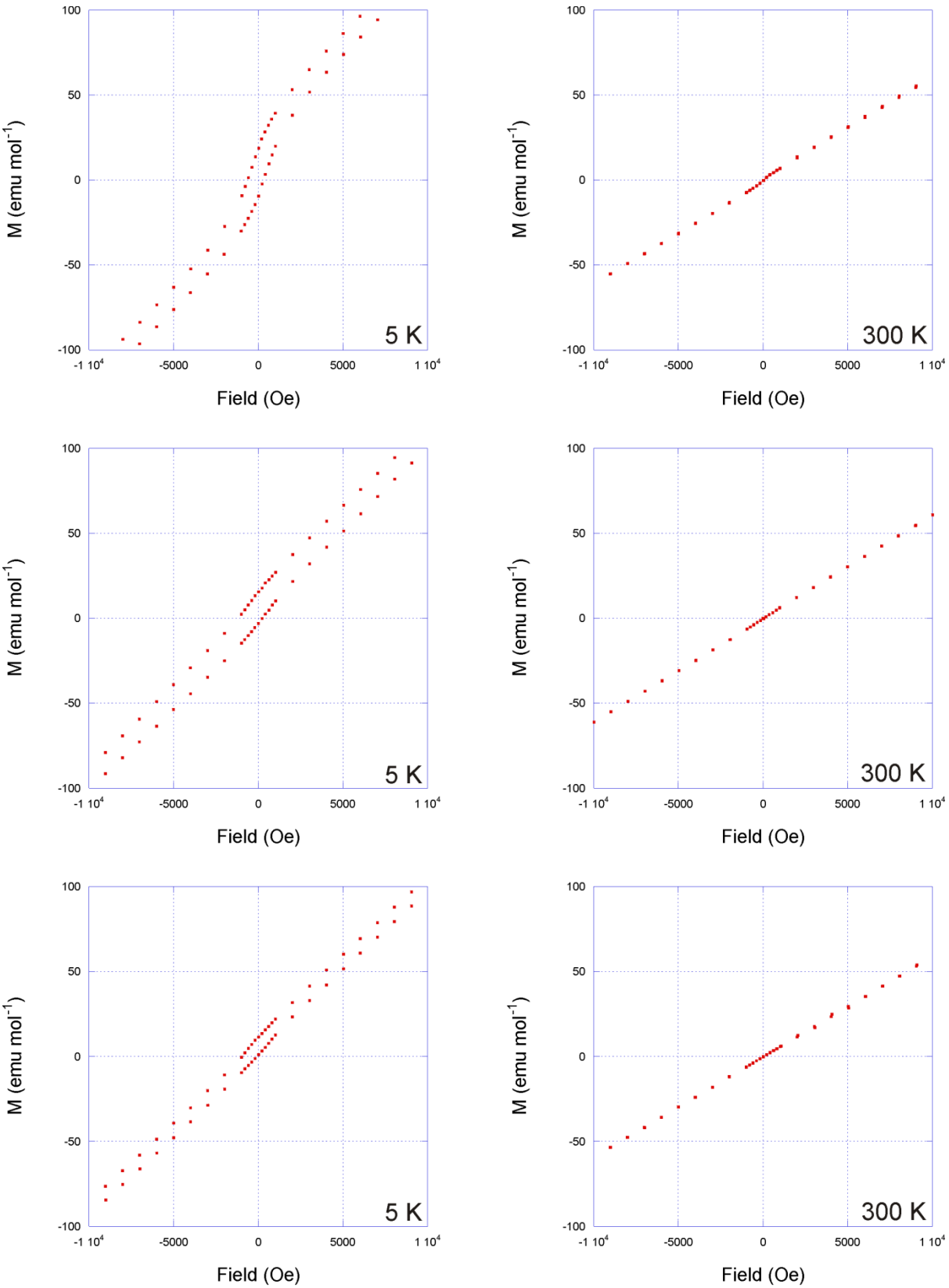


Figure 4.28: Magnetisation-field isotherms collected at 5 K and 300 K from $La_{0.33}Sr_{0.67}MnO_{2.42}$ (top), $La_{0.3}Sr_{0.7}MnO_{2.4}$ (2nd top), $La_{0.25}Sr_{0.75}MnO_{2.35}$ (3rd top) and $La_{0.17}Sr_{0.83}MnO_{2.33}$ (bottom).

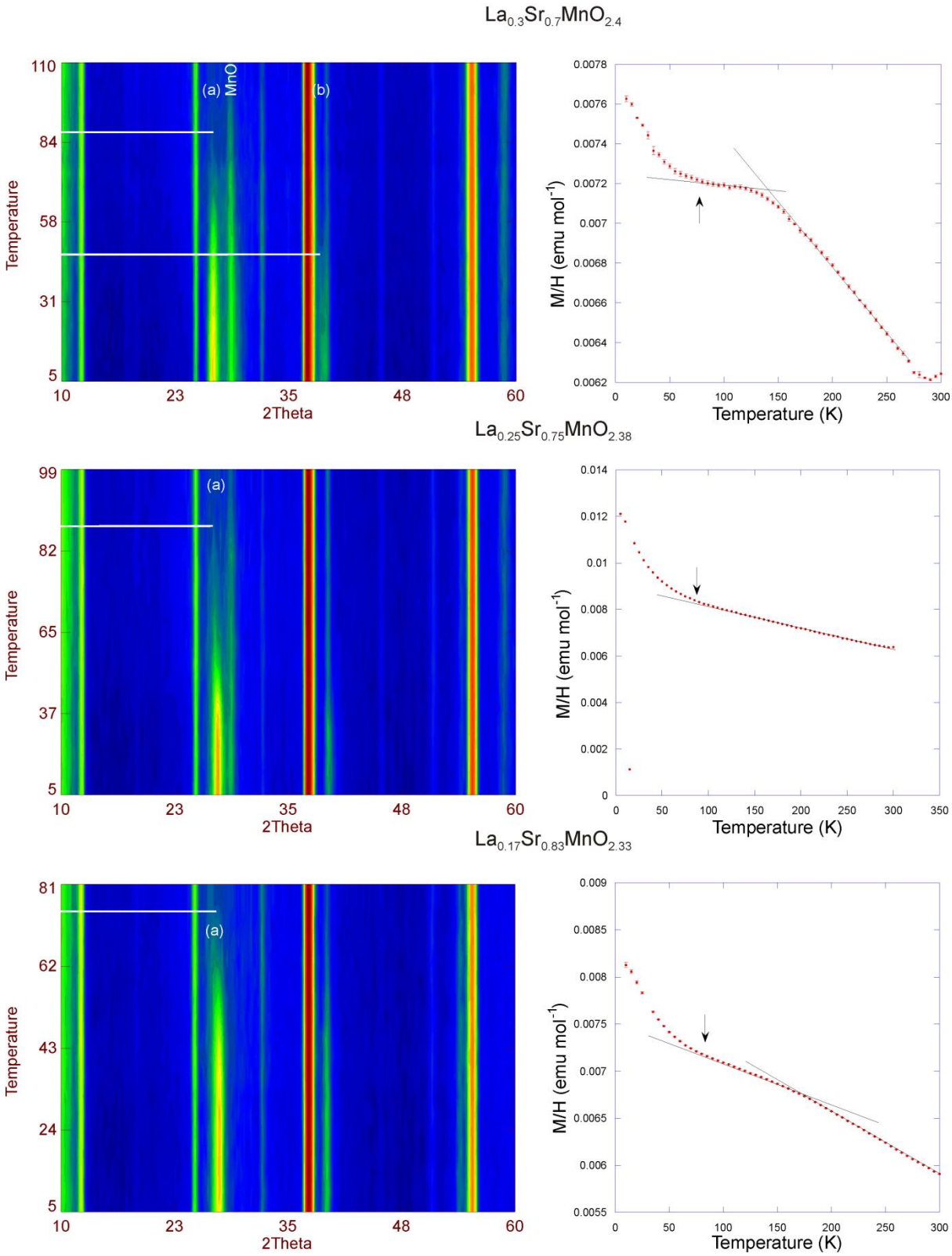


Figure 4.29: Variable temperature neutron powder diffraction data and paramagnetic susceptibility data collected from $La_{1-x}Sr_xMnO_{3-(0.5+x)/2}$ phases

Interaction	Type of Interaction	Nature of Interaction[52]
Mn^{III} $(d_{z^2})^1$ – O(2*p*) – Mn^{III} $(d_{z^2})^1$	Superexchange	AFM
Mn^{III} $(d_{z^2})^1$ – O(2*p*) – Mn^{II} $(d_{z^2})^1$	Superexchange	AFM
Mn^{II} $(d_{z^2})^1$ – O(2*p*) – Mn^{II} $(d_{z^2})^1$	Superexchange	AFM
Mn^{III} $(d_{z^2})^1$ – Mn^{III} $(d_{z^2})^1$	Direct exchange	AFM
Mn^{III} $(d_{z^2})^1$ – Mn^{II} $(d_{z^2})^1$	Direct exchange	AFM
Mn^{II} $(d_{z^2})^1$ – Mn^{II} $(d_{z^2})^1$	Direct exchange	AFM

Table 4.13: Predicted magnetic interactions between manganese centres in neighbouring 'octahedral' layers in the $La_{1-x}Sr_xMnO_{3-(0.5+x)/2}$ (x = 0.67, 0.7 and 0.75) phases

Chapter 5: Characterisation of $La_{1-x}Sr_xMnO_{3-(0.5+x)/2}$ (x = 0.83, 0.9 and 1)

5.1. Introduction

The topotactic reduction reactions of the $La_{1-x}Sr_xMnO_3$ (x = 0.67, 0.7 and 0.75) phases using NaH as a reducing agent result in the formation of anion-deficient phases with an empirical composition of $La_{1-x}Sr_xMnO_{3-(0.5+x)/2}$. The reduced phases adopt 6-layer structures best described as containing an OOTOOT' stacking sequence of the 'octahedral' (O) and tetrahedral (T) layers (labelled as the '6-layer manganate' structure). As detailed in section 4.3.2, analogous topotactic reduction reactions of $La_{1-x}Sr_xMnO_3$ (x = 0.83, 0.9 and 1) phases also result in the formation of products with an empirical stoichiometry of $La_{1-x}Sr_xMnO_{3-(0.5+x)/2}$ consistent with a common average manganese oxidation state of +2.5. A fuller structural investigation of the $La_{1-x}Sr_xMnO_{3-(0.5+x)/2}$ (x = 0.83, 0.9 and 1) phases is detailed in this chapter.

5.2. Results

5.2.1. X-ray diffraction data

X-ray powder diffraction data collected from the reduced $La_{1-x}Sr_xMnO_{3-(0.5+x)/2}$ (x = 0.83, 0.9 and 1) phases are shown in Figure 5.1 along with X-ray powder diffraction data collected from $La_{0.25}Sr_{0.75}MnO_{2.38}$ for comparison. By inspection of Figure 5.1, it can be seen that the diffraction patterns collected from the $La_{1-x}Sr_xMnO_{3-(0.5+x)/2}$ (x = 0.83, 0.9 and 1) phases are very similar to the pattern collected from $La_{0.25}Sr_{0.75}MnO_{2.38}$, suggesting that the Sr^{2+}-rich phases adopt structures closely related to the '6-layer manganate' structure of $La_{0.25}Sr_{0.75}MnO_{2.38}$.

However, closer analysis of the diffraction data collected from the $La_{1-x}Sr_xMnO_{3-(0.5+x)/2}$ (x = 0.83, 0.9 and 1) phases reveals that only the reflections in the data set collected from $La_{0.17}Sr_{0.83}MnO_{2.33}$ can be fully indexed using a unit cell analogous to those of the structures

of the $La_{1-x}Sr_xMnO_{3-(0.5+x)/2}$ (x = 0.67, 0.7 and 0.75) phases. Indeed, diffraction data collected from $La_{0.1}Sr_{0.9}MnO_{2.3}$ and $SrMnO_{2.25}$ contain additional weak reflections (marked with an asterisk in Figure 5.1) inconsistent with this structural model.

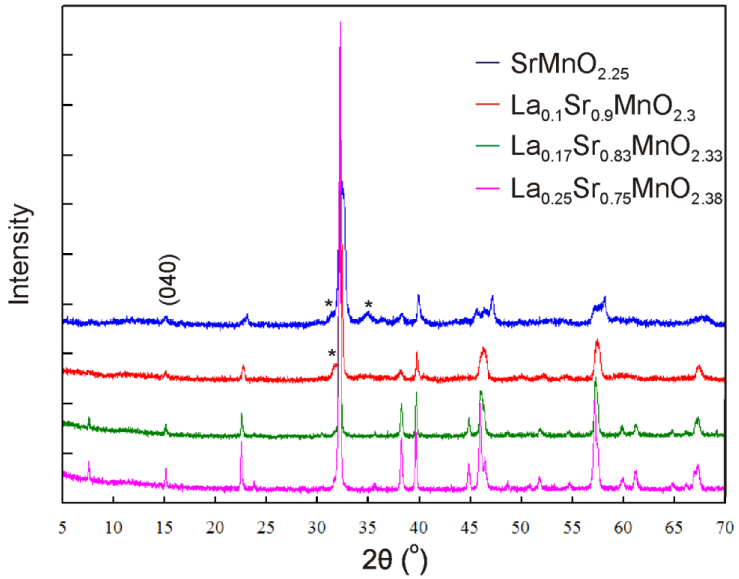


Figure 5.1: X-ray powder diffraction data collected from (from top to bottom) $SrMnO_{2.25}$, $La_{0.1}Sr_{0.9}MnO_{2.3}$, $La_{0.17}Sr_{0.83}MnO_{2.33}$ and $La_{0.25}Sr_{0.75}MnO_{2.38}$.

In addition, the diffraction reflections become increasingly broad with increasing Sr^{2+}-content, consistent with a general decrease in crystallinity. This observation is illustrated by inspection of Figure 5.2 which contains the full width at half maximum (FWHM) for the (040) reflection in the X-ray powder diffraction data.

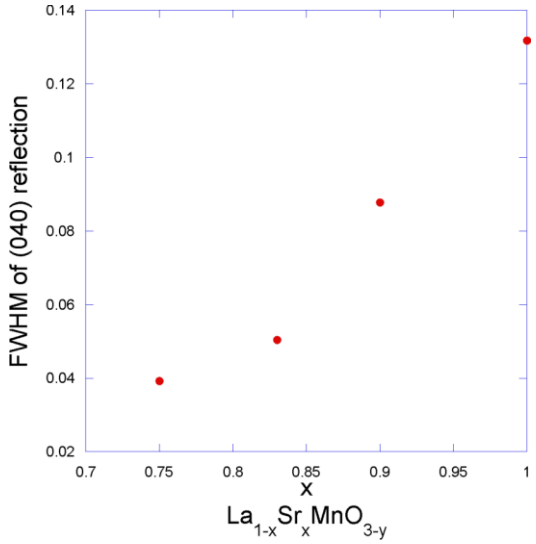


Figure 5.2: FWHM of (040) reflection in X-ray powder diffraction data collected from $La_{1-x}Sr_xMnO_{3-(0.5+x)/2}$ ($x \geq 0.75$)

5.2.2. Neutron diffraction data

Neutron powder diffraction data were collected from $La_{1-x}Sr_xMnO_{3-(0.5+x)/2}$ (x = 0.83, 0.9 and 1) phases using the D1a instrument (see section 2.3.2.1.2) to determine the anion vacancy ordering arrangements in the structures. The data are shown in Figure 5.3 along with those collected from $La_{0.25}Sr_{0.75}MnO_{2.38}$ for comparison.

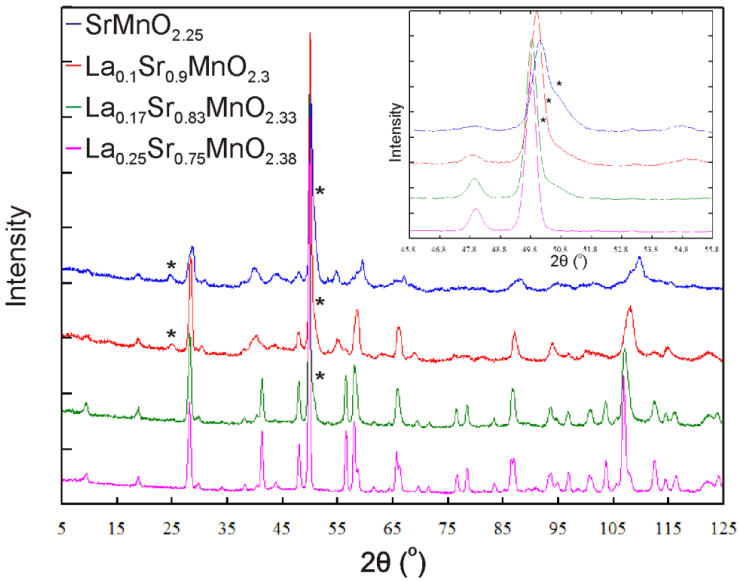


Figure 5.3: Neutron powder diffraction data collected (from top to bottom) from $SrMnO_{2.25}$, $La_{0.1}Sr_{0.9}MnO_{2.3}$ and $La_{0.17}Sr_{0.83}MnO_{2.33}$ and $La_{0.25}Sr_{0.83}MnO_{2.38}$ for comparison. The asterisks mark reflections inconsistent with the '6-layer manganate' structural models

In common with the X-ray powder diffraction data sets, neutron powder diffraction data collected from the phases in the compositional range $La_{1-x}Sr_xMnO_{3-(0.5+x)/2}$ ($0.75 \leq x \leq 1$) change in 2 ways as the Sr^{2+}-content increases:

1. The FWHM of the diffraction reflections increase with increasing Sr^{2+}-content, consistent with decreasing crystallinity.
2. There are a number of additional reflections in the data sets collected from the $La_{1-x}Sr_xMnO_{3-(0.5+x)/2}$ (x = 0.83, 0.9 and 1) phases which are inconsistent with structural models based on the '6-layer manganate' structure. The most intense of these reflections is a 'shoulder' (marked with an asterisk) on the reflections centred at

approximately $2\theta = 50^{o}$. The relative intensities of these additional reflections increase with increasing Sr^{2+}-content.

Variable temperature neutron powder diffraction data collected using the D1b instrument (see section 2.3.2.1.3) shown in Figure 5.19 in Appendix 5 confirmed that the intensities of these additional reflections are independent of temperature, invalidating the hypothesis that these reflections are attributable to the presence of long range magnetic order. Furthermore, the positions of these reflections are inconsistent with the structures of obvious impurity phases. It was therefore clear that the structures of the $La_{1-x}Sr_xMnO_{3-(0.5+x)/2}$ (x = 0.83, 0.9 and 1) reduced phases are incompletely described using the '6-layer manganate' structural model.

5.2.3. Structural refinement

5.2.3.1. $La_{0.17}Sr_{0.83}MnO_{2.33}$

Given the similarity in the bulk diffraction data sets collected from $La_{0.17}Sr_{0.83}MnO_{2.33}$ and the '6-layer manganate' $La_{1-x}Sr_xMnO_{3-(0.5+x)/2}$ (x = 0.67, 0.7 and 0.75) phases, structural elucidation of $La_{0.17}Sr_{0.83}MnO_{2.33}$ using neutron powder diffraction data was attempted using the same refinement strategy as used to elucidate the structures of the latter set of phases (see section 3.3.4).

'6-layer' structural models containing the 5 simplest arrangements of the twisted tetrahedral chains (i.e. models with *I*2*mb*, *Imma*, *Pnma*, *C*2/*c* and *Pcmb* symmetries) were constructed and refined against neutron powder diffraction data collected from $La_{0.17}Sr_{0.83}MnO_{2.33}$. In an analogous fashion to the $La_{1-x}Sr_xMnO_{3-(0.5+x)/2}$ (x = 0.67, 0.7 and 0.75) phases, it is clear from the goodness of fit statistics shown in Table 5.1 that, of the models described above, the model based on *Pcmb* symmetry gives the best fit to the data collected from $La_{0.17}Sr_{0.83}MnO_{2.33}$.

Space group	χ^2	*wRp*	*Rp*	*f*(Td)
I2mb	5.726	6.52 %	4.62 %	
Imma	5.543	6.43 %	4.32 %	
Pnma	5.459	6.37 %	4.49 %	
C2/c	5.527	6.39 %	4.52 %	
Pcmb	4.808	6.00 %	4.34 %	
'Pcmb disorder'	3.708	5.23 %	3.78 %	50 %
'Pcmb disorder varying *f*(Td)'	3.708	5.23 %	3.78 %	53(3) %

Table 5.1: Fitting statistics for the refinement of different 6-layer structural models against neutron powder diffraction data collected from $La_{0.17}Sr_{0.83}MnO_{2.33}$.

In addition to the 5 models described above, 2 additional models accounting for the disorder in the arrangement of the twisted tetrahedral chains ('*Pcmb* disorder' and *'Pcmb* disorder varying *f*(Td)' – see section 3.3.6) were created and refined against the collected neutron powder diffraction data. Both models resulted in an improvement in the quality of the fit to the data relative to the ordered model with *Pcmb* symmetry. However, refinement of the fractional occupancies of the superimposed twisted tetrahedral chains (see section 3.3.6) in the *'Pcmb* disorder varying *f*(Td)' structural model resulted in no measurable improvement in the quality of the fit to the data and the fractional occupancies of the superimposed tetrahedral chains refined to 50 % within error. Therefore both the '*Pcmb* disorder' and *'Pcmb* disorder varying *f*(Td)' models are essentially equivalent.

The equivalence of the '*Pcmb* disorder' and *'Pcmb* disorder varying *f*(Td)' models and the improvement in the fit to the data using these models relative to the ordered model with *Pcmb* symmetry indicates that there is a large amount of disorder in the arrangement of the twisted tetrahedral chains in the structure of $La_{0.17}Sr_{0.83}MnO_{2.33}$. The observed, calculated and difference plots for the refinement of the *'Pcmb* disorder varying *f*(Td)' structural model and the refined structure are shown in Figure 5.4. The refined structural parameters are shown in Table 5.2 in Appendix 5. While it is clear that the shoulder of the reflection centred at $2\theta = 50^{o}$ (marked with an asterisk) is unaccounted for using this '6-layer manganate' structural model, the observable fit to the vast majority of the data is satisfactory; thereby indicating

that the '6-layer manganate' structural model is a good approximation to the true structure of $La_{0.17}Sr_{0.83}MnO_{2.33}$.

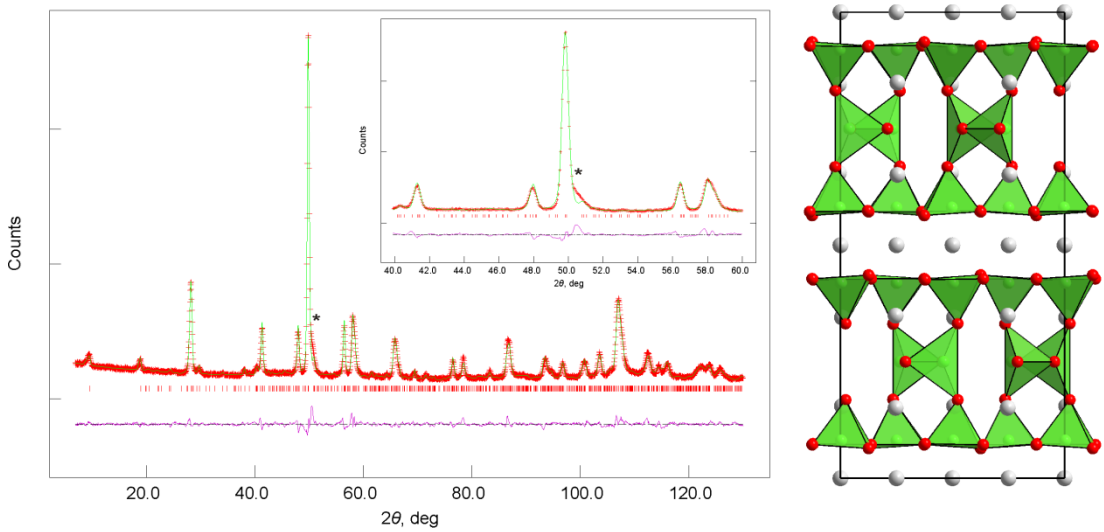


Figure 5.4: Left: observed, calculated and difference plots for refinement of '6-layer manganate' structural model against neutron powder diffraction data collected from $La_{0.17}Sr_{0.83}MnO_{2.33}$ (χ^2 = 3.715, *wRp* = 5.24 %, *Rp* = 3.79 %). Right: refined structure of $La_{0.17}Sr_{0.83}MnO_{2.33}$.

In contrast to the structures of the $La_{1-x}Sr_xMnO_{3-(0.5+x)/2}$ (x = 0.67, 0.7 and 0.75) reduced phases which contain partially occupied anion sites within the $AO(1)/(8)_{1-y}$ layers, the structure of $La_{0.17}Sr_{0.83}MnO_{2.33}$ contains a fully anion-vacant A-cation layer between the MnO_2 layers, in an analogous fashion to the structure of $RESr_2Cu_2GaO_7$.[61]

Following the logic based on the cancellation of the relatively large dipole moments associated with the twisted tetrahedral chains (see section 4.4.2) and the similarity in the structures of phases in the range $La_{1-x}Sr_xMnO_{3-(0.5+x)/2}$ ($0.67 \leq x \leq 0.83$), the structure of $La_{0.17}Sr_{0.83}MnO_{2.33}$ is also predicted to contain an intralayer ordered arrangement of the tetrahedral chains, consistent with *Pcmb* symmetry. However, as discussed in section 4.4.3, the interaction between neighbouring tetrahedral layers is likely to be very weak due to the anion-vacant A-cation layer limiting potential through-bond interactions. There is therefore unlikely to be any long range interlayer ordering of the twisted tetrahedral chains in the structure of $La_{0.17}Sr_{0.83}MnO_{2.33}$. Instead the structure of $La_{0.17}Sr_{0.83}MnO_{2.33}$, in an analogous fashion to the predicted structure of $Ca_2MnAlO_{5.5}$ (see section 4.4.4.2), can be described as

containing an 'intralayer ordered but interlayer disordered' arrangement of the twisted tetrahedral chains.

This predicted arrangement of the twisted tetrahedral chains is fully consistent with the observation that the '*Pcmb* disorder with varying *f*(Td)' model with *f*(Td) 50 % and the '*Pcmb* disorder' model are the most accurate descriptions of the structure of $La_{0.17}Sr_{0.83}MnO_{2.33}$.

5.2.3.2. $La_{0.1}Sr_{0.9}MnO_{2.3}$ and $SrMnO_{2.25}$

Analogous refinements of the 5 simple 6-layer structural variants detailed in section 3.3.4 against neutron powder diffraction data collected from $La_{0.1}Sr_{0.9}MnO_{2.3}$ yielded relatively poor fits to the data. Use of the model based on *Pcmb* symmetry resulted in the best fit to the data and the observed, calculated and difference plots for this refinement are shown in Figure 5.5. Analogous refinements against neutron powder diffraction data collected from $SrMnO_{2.25}$ were highly unstable and so the refinements were abandoned.

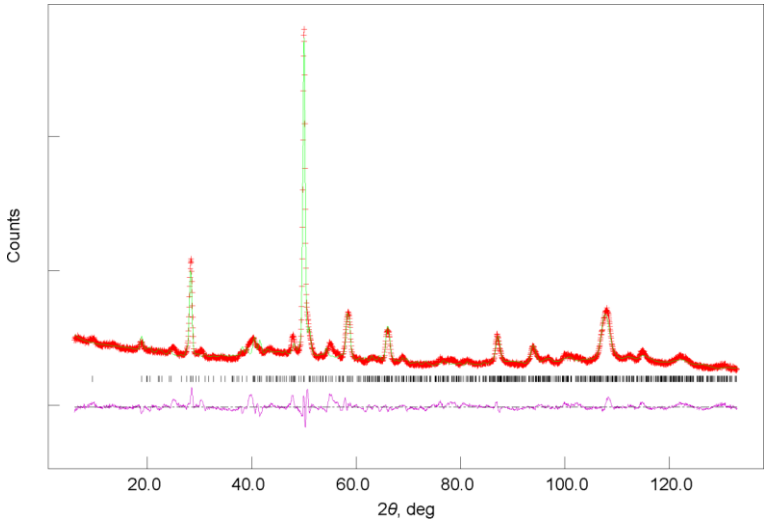


Figure 5.5: Observed, calculated and difference plots for refinement of '6-layer manganate' structural model against neutron powder diffraction data collected from $La_{0.1}Sr_{0.9}MnO_{2.3}$. χ^2 = 6.598, *wRp* = 5.30 %, *Rp* = 4.00 %

It is therefore clear that while the $La_{0.1}Sr_{0.9}MnO_{2.3}$ and $SrMnO_{2.25}$ phases clearly adopt similar structures to those of the $La_{1-x}Sr_xMnO_{3-(0.5+x)/2}$ (x = 0.67, 0.7 and 0.75) phases, the '6-layer manganate' structural model is an incomplete description of their structures. It was

hypothesised that the departure away from the‘6-layer manganate’ structural models for the $La_{1-x}Sr_xMnO_{3-(0.5+x)/2}$ (x = 0.83, 0.9 and 1) phases may be attributable to microstructure effects, including ‘step defects’ or other non-translational defects.

5.2.4. Imaging

5.2.4.1. Introduction

As discussed in section 2.3.3.4, HAADF-STEM micrographs can be used to directly ‘image’ crystals on a nanometre length scale, thereby allowing a detailed study of defects in the structure. Therefore, HAADF-STEM images were collected parallel to a number of crystallographic axes from the $La_{1-x}Sr_xMnO_{3-(0.5+x)/2}$ (x = 0.83, 0.9 and 1) phases and $La_{0.25}Sr_{0.75}MnO_{2.38}$ for comparison. For clarity, all *hkl* planes and directions referred to in the following sections are based on the unit cell of the ‘6-layer manganate’ structure ($\sqrt{2}a_p$ x $6a_p$ x $2\sqrt{2}a_p$) regardless of whether a doubling of the *c*-lattice parameter is crystallographically required or not.

5.2.4.2. [102] direction

5.2.4.2.1. $La_{0.25}Sr_{0.75}MnO_{2.38}$

Figure 5.6 a) – c) show images collected from the [102] zone (i.e. 45^o to the propagation direction of the tetrahedral chains) of $La_{0.25}Sr_{0.75}MnO_{2.38}$. The brightness of particular rows or columns of atoms within an HAADF-STEM image depends on the electron density of that region of the crystallite. It therefore follows that the brightest dots in the images collected from $La_{1-x}Sr_xMnO_{3-(0.5+x)/2}$ phases correspond to the A-cations, the grey stripes correspond to the MnO_2 layers and the dark stripes correspond to the MnO layers within the tetrahedra. In these images it was not possible to differentiate between an eclipsed or staggered arrangement of the tetrahedral layers up the stacking direction. Therefore, as shown in Figure 5.6 d), the HAADF-STEM images consist of 3-layer repeat units (OTO stacking) marked with a white box in Figure 5.6 c). This 3-layer repeat unit corresponds to half the unit cell of

the 6-layer structure of $La_{0.25}Sr_{0.75}MnO_{2.38}$. The HAADF-STEM images collected from $La_{0.25}Sr_{0.75}MnO_{2.38}$ are consistent with large regions (75 nm x 75 nm) of ordered material with 3-layer OTO stacking.

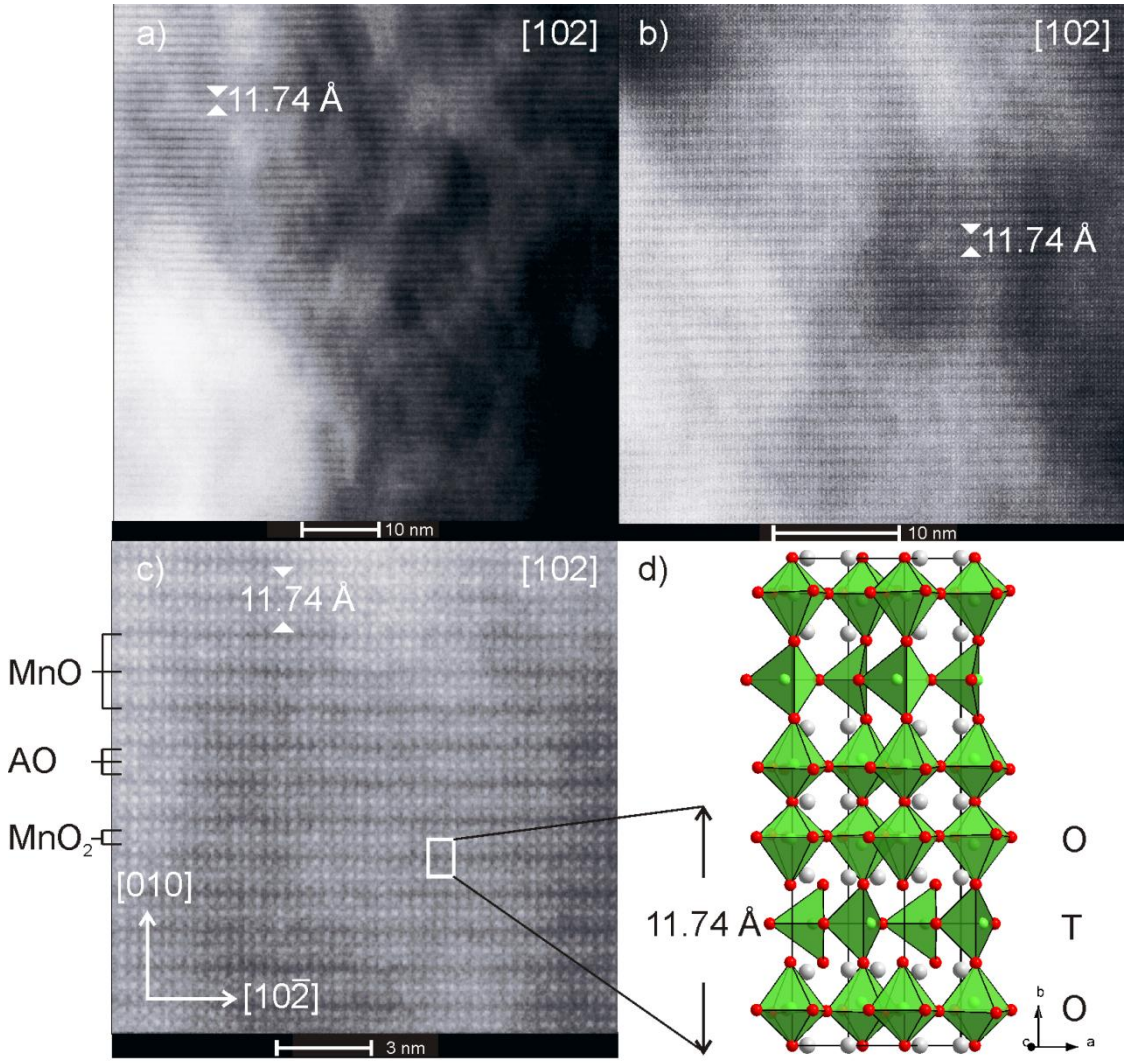


Figure 5.6: a) – c) show HAADF-STEM images collected from the [102] zone of $La_{0.25}Sr_{0.75}MnO_{2.38}$ at different magnifications using a JEOL 3000F microscope, the white box represents the 3-layer (OTO) repeat unit. Figure d) shows the structure of $La_{0.25}Sr_{0.75}MnO_{2.38}$ with the 3-layer (OTO) repeat unit.

5.2.4.2.2. Sr^{2+}-rich phases

Figure 5.7 a) and b) show images collected from a sample of $La_{0.17}Sr_{0.83}MnO_{2.33}$ again down the [102] zone. Figure 5.7 a) shows that crystallites of $La_{0.17}Sr_{0.83}MnO_{2.33}$ also contain large regions of material with an ordered 3-layer repeat unit in an analogous fashion to $La_{0.25}Sr_{0.75}MnO_{2.38}$. As shown in Figure 5.7 c), the structure of $La_{0.17}Sr_{0.83}MnO_{2.33}$ contains a fully anion-deficient A-cation layer; therefore the 3-layer repeat unit corresponds to an STS

stacking sequence of the square-based pyramidal and tetrahedral layers rather than an OTO stacking sequence as in the structure of $La_{0.25}Sr_{0.75}MnO_{2.38}$.

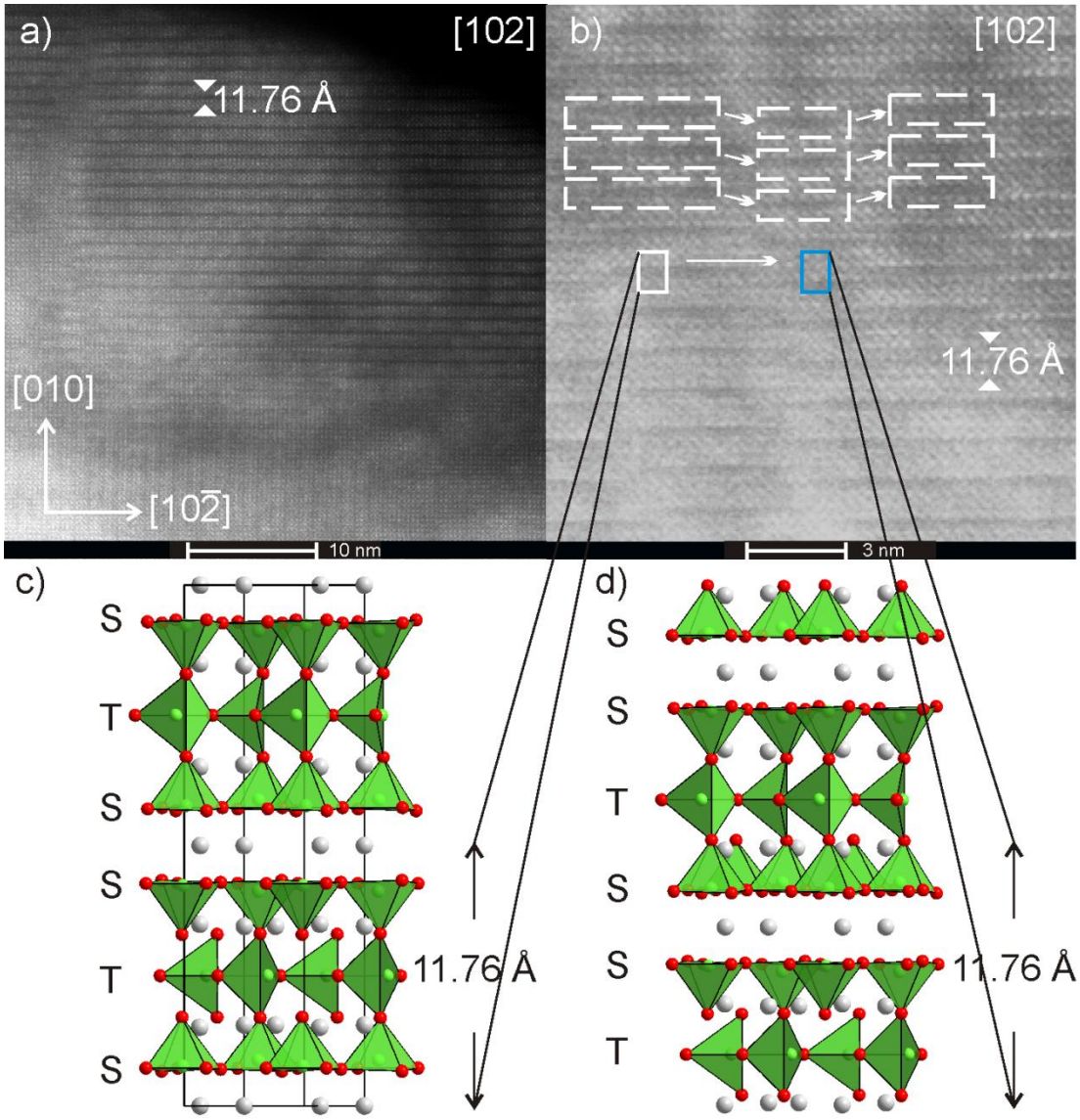


Figure 5.7: HAADF-STEM images collected from [102] zone of $La_{0.17}Sr_{0.83}MnO_{2.33}$ using a JEOL 3000F microscope, the white box represents the 3-layer (STS) repeat unit. In addition, the structure of $La_{0.17}Sr_{0.83}MnO_{2.33}$ is shown with the 3-layer (STS) repeat unit. The hashed boxes in Figs. b) and c) mark portions of the tetrahedral layers and highlight the 'step' in the stacking sequence.

Figure 5.7 b) shows that the crystallites of $La_{0.17}Sr_{0.83}MnO_{2.33}$ also contain regions of STS-stacked material (marked with a white box). However, close inspection reveals that the layers in the structure (for example the tetrahedral layers marked with hashed boxes) are not 'infinite' in the [10] direction. It is clear that the material in the blue box (formed by a translation of the white box in the [10] direction) contains the same relative stacking

sequence but the repeat unit is shifted by approximately 3.92 Å in the [010] direction (⅓ of the length of the 3-layer repeat unit or 1/6*b* of the '6-layer manganate unit cell). An alternative description of this shift is that STSSTS stacking in the white box becomes TSSTSS stacking in the blue box.

These 'step defects' appear to occur with varying frequency and no obvious structural periodicity. As a result, attempts to model their occurrence as a simple modulation superimposed on top of the underlying 3D structure were unsuccessful. In addition, there appears to be no long range order to the direction of the 'step' of the stacking sequence, i.e. STS-stacked material can neighbour TSS-stacked material ('down step') or SST-stacked material ('up step').

As shown in Figure 5.8 a) and b), $La_{0.1}Sr_{0.9}MnO_{2.3}$ and $SrMnO_{2.25}$ also contain similar 'step defects' between regions of STS-stacked material. The frequency of these 'step defects' appears to increase with increasing Sr^{2+}-content, consistent with the formation of these 'step defects' being driven by changes in the empirical composition.

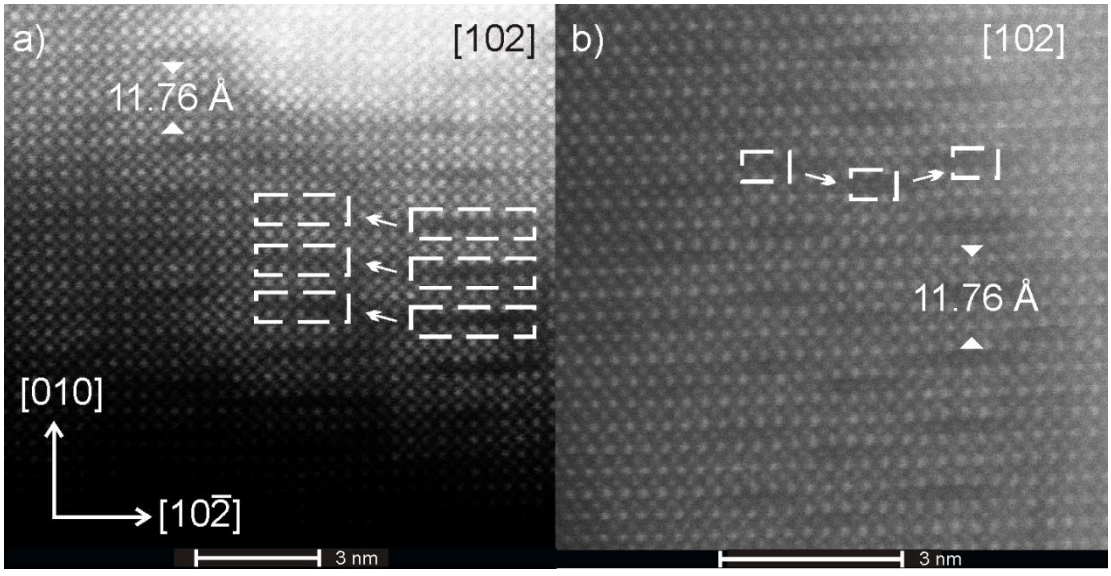


Figure 5.8: HAADF-STEM images collected down the [102] zone of $La_{0.1}Sr_{0.9}MnO_{2.33}$ using a JEOL 3000F microscope (left) and $SrMnO_{2.25}$ using a FEI TITAN 50-80 microscope (right). As in the previous figure, the hashed white boxes mark portions of the tetrahedral layers and highlight the 'step' in the stacking sequence.

5.2.4.3. Other directions

The 'step defects' were not visible in HAADF-STEM images collected from other zones of the $La_{1-x}Sr_xMnO_{3-(0.5+x)/2}$ (x = 0.83, 0.9 and 1) phases, e.g. the [100] zone (tetrahedral chain propagation direction) of $La_{0.1}Sr_{0.9}MnO_{2.3}$ (see Figure 5.9).

It is clear from inspection of the HAADF-STEM images collected from the [102] zones that the $La_{1-x}Sr_xMnO_{3-(0.5+x)/2}$ (x = 0.83, 0.9 and 1) phases contain 'slabs' of ordered material that run along the [102] direction (i.e. into the plane of the paper). However, as demonstrated by the HAADF-STEM images collected parallel to other crystallographic directions (e.g. the [100] direction), the 'step defects' are not observed if the view of the structure is not parallel to the 'interface' planes between the ordered 'slabs'. HAADF-STEM images collected along zones other than the [102] zone display an 'average' structure in which different sections of ordered material are superimposed on top of each other.

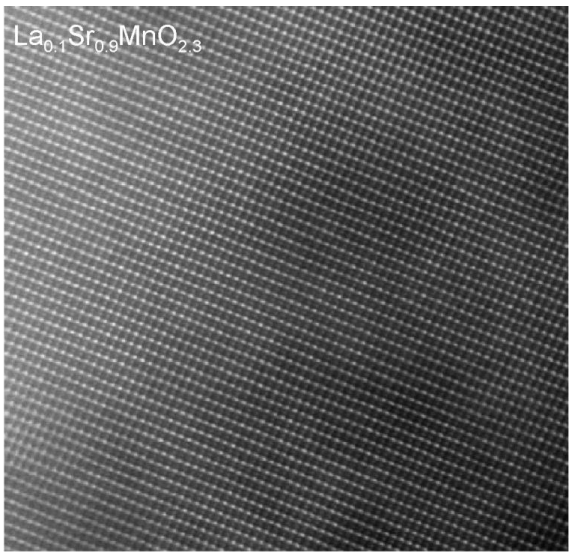


Figure 5.9: HAADF-STEM image collected from $La_{0.1}Sr_{0.9}MnO_{2.3}$ down the [100] zone of the '6-layer manganate' unit cell using a FEI Titan 50-80 microscope

5.3. Discussion

5.3.1. Proposed Model

Figure 5.10 and Figure 5.12 show the proposed model for the 'step defects' in the $La_{1-x}Sr_xMnO_{3-(0.5+x)/2}$ (x = 0.83, 0.9 and 1) phases in 2 different orientations. The different

coloured polyhedra represent the different manganese-based polyhedral layers, i.e. the blue and the orange layers represent the square-based pyramidal layers and the green polyhedra represent the tetrahedral layers. It should be noted that Figure 5.10 and Figure 5.12 are only representations of the 'step defects' and contain atomic positions consistent with those in a simple cubic perovskite, e.g. undistorted tetrahedral chains. In addition, neither figure makes an attempt to represent the frequency of the 'step defects'.

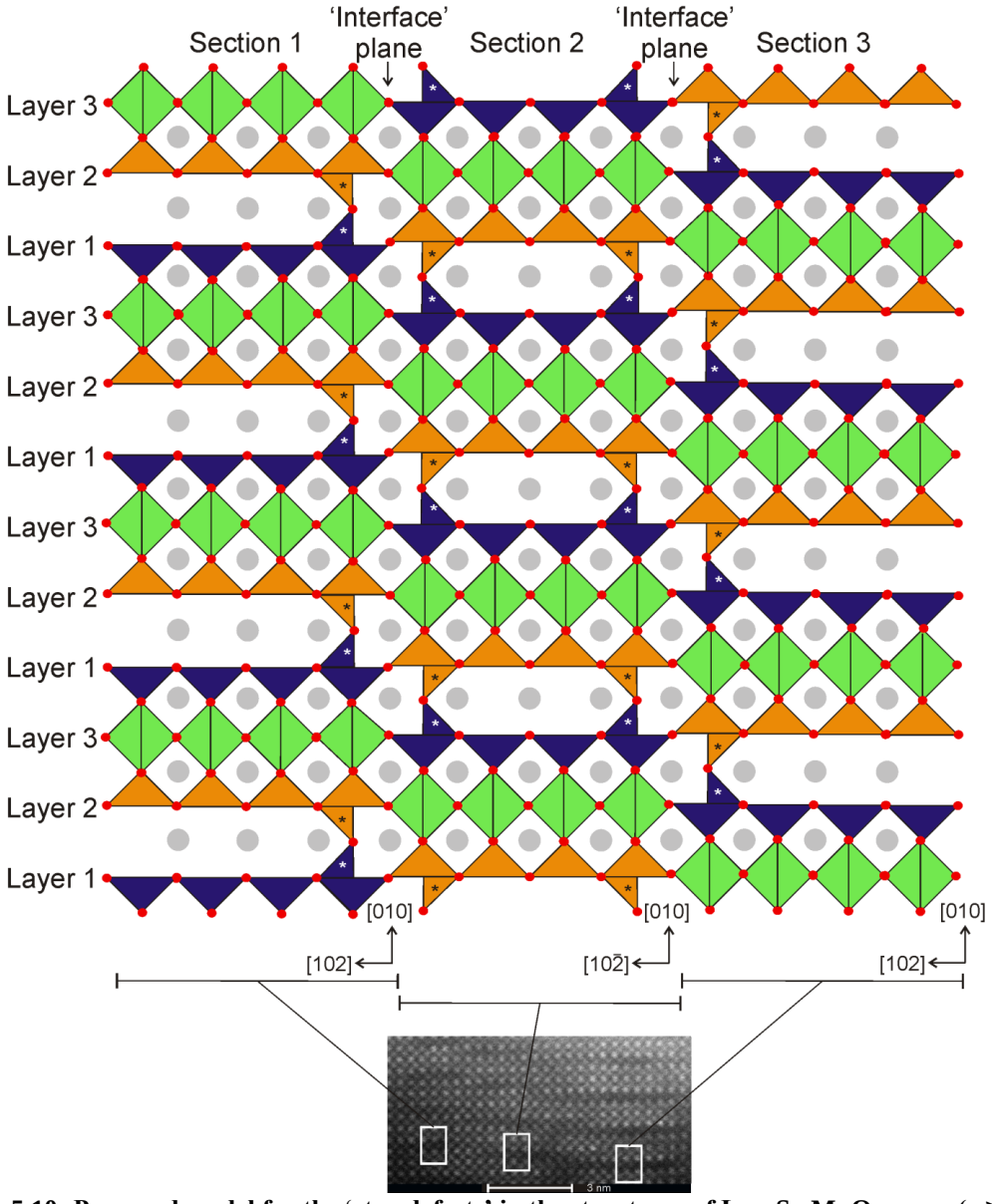


Figure 5.10: Proposed model for the 'step defects' in the structures of $La_{1-x}Sr_xMnO_{3-(0.5+x)/2}$ ($x \geq 0.83$) viewed down either the [10] direction or the [102] direction. The red and the grey spheres represent the oxide ions and the A-cations respectively. The polyhedra marked with an asterisk represent 'square-based pyramidal units' with apical oxide ions in the MnO_2 layer. The HAADF-STEM image collected down the [102] zone of $SrMnO_{2.25}$ demonstrates how the proposed model accounts for the data.

5.3.2. Explanation of Figure 5.10

Figure 5.10 shows a view of the proposed structural model down either the [10] or the [102] direction of the '6-layer manganate' structure (i.e. 45^{o} to the tetrahedral chain propagation direction) which effectively become equivalent in this structural model. The view of the structure in Figure 5.10 is thus the same as that shown in the HAADF-STEM images which highlight the 'step defects' in the structure.

The equivalence of the [10] and [102] directions is due to the propagation direction of the tetrahedral chains rotating by 90^{o}, i.e. changing from parallel to the *a*-axis to parallel to the *c*-axis or vice versa, at the 'interface planes' resulting in a twinning of the stacked sections in the crystallites. The rotation of the tetrahedral chain propagation direction is more clearly shown in Figure 5.12.

The structure contains sections, e.g. Section 2, with 3-layer STS-stacked units repeating up the [010] direction (orange layer, green layer, blue layer). However, in agreement with HAADF-STEM data collected from these phases, the neighbouring STS-stacked sections have a stacking sequence shifted by ⅓ of the length of the 3-layer repeat unit along the [010] direction resulting in a 'step defect' between the sections. The 'step defects' result in the destruction of the 'infinite' layers running along the [10] direction observed in crystallites of $La_{0.25}Sr_{0.75}MnO_{2.38}$. This results in the formation of 'interface planes' between the STS-stacked sections in the crystallites of the $La_{1-x}Sr_xMnO_{3-(0.5+x)/2}$ (x = 0.83, 0.9 and 1) phases. Therefore, the coordination environment of the manganese centres in Layer 2 of the proposed structural model, for example, changes from 'square-based pyramidal' (S) to tetrahedral (T) and then back to 'square-based pyramidal' across the figure.

As discussed in the previous section, only HAADF-STEM images collected down the [102] zone contain the 'step defects', therefore the 'interface' planes between the sections of ordered material must lie along the (102)/(10) direction.

Given the symmetry of the proposed model, the 'step' in the stacking sequence can either shift 'up' (+1/3 of the repeat unit, representing a change in stacking sequence from STSSTS to SSTSST) or 'down' (-1/3 of the repeat unit, representing a change in stacking sequence from STSSTS to TSSTSS) in agreement with HAADF-STEM data collected from these phases. A section of an HAADF-STEM image collected from $SrMnO_{2.25}$ down the [102] zone (extracted from Figure 5.8 b)) is also shown in Figure 5.10 and the relationship between the 'step defects' in the proposed structural model and the defects observed in the data can be observed.

Due to the absence of a suitable local probe, it was not possible to unequivocally determine the coordination environments of the manganese centres adjacent to the 'interface' planes of the 'step defects'. The proposed model contains columns of tetrahedra and square-based pyramids adjacent to the 'interface' plane. However, every second square-based pyramid is rotated by 90^{o} so that the apical oxide ion moves from the AO layer to the MnO_2 layer (see Figure 5.11).

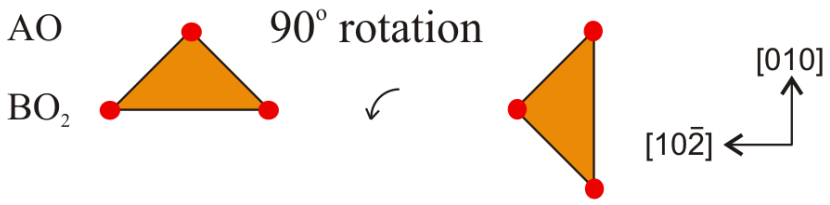


Figure 5.11: Rotation of MnO_5 square based pyramid

The triangles marked with asterisks in Figure 5.10 represent the 'visible' half of the square-based pyramids which have apical oxide ions in the MnO_2 layer. This arrangement of polyhedra allows the local empirical stoichiometry of the material, and consequently the average manganese oxidation state of +2.5, to be maintained at the 'interface plane' of the 'step defect' whilst minimising the structural disruption associated with the fault.

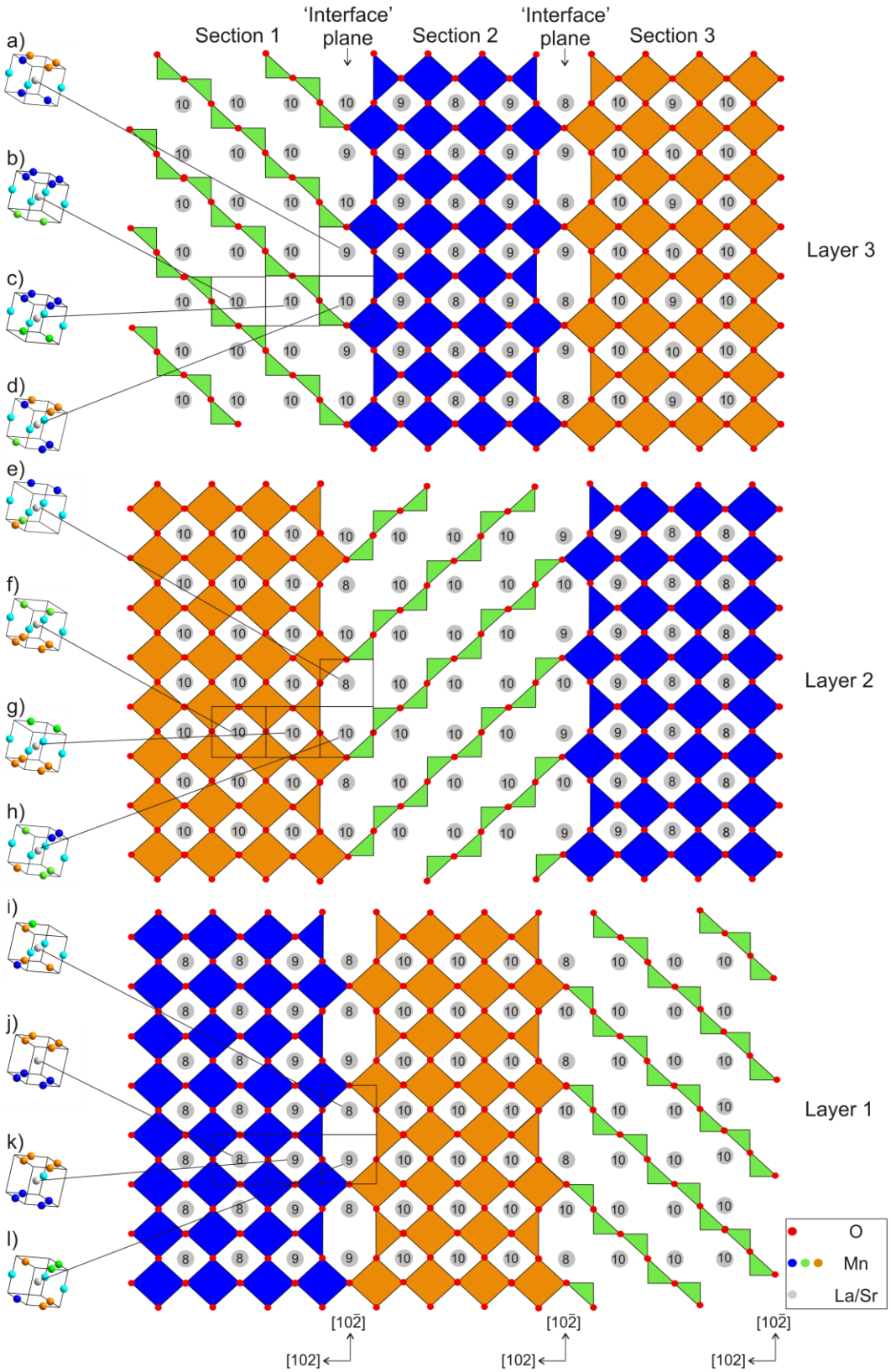


Figure 5.12: The image shows 3 consecutive manganese-containing layers down the [010] direction in the proposed models for the 'step defects' in $La_{1-x}Sr_xMnO_{3-(0.5+x)/2}$ ($x \geq 0.83$) phases. The A-cations are located above each layer shown, i.e. A-cations shown depicted in Layer 1 are in between Layer 1 and Layer 2, and their coordination numbers are shown inside. Images of the coordination environments for selected A-cations in the structure of $La_{0.17}Sr_{0.83}MnO_{2.33}$ are shown on the left in which the colour of the oxide ions relates to which layer they are in.

5.3.3. Explanation of Figure 5.12

The main image in Figure 5.12 shows 3 consecutive manganese-containing layers of the proposed model viewed down the [010] direction (i.e. 90^{o} rotation of Figure 5.10 out of the plane of the paper). Section 2, as an example, contains a stacking sequence of MnO_2 (Layer 1) - MnO (Layer 2) - MnO_2 (Layer 3) layers corresponding to the STS-stacking observed in Figure 5.10. However, across each layer the manganese coordination environment changes, e.g. 'square-based pyramidal' (MnO_2) – tetrahedral (MnO) – 'square-based pyramidal' (MnO_2) across Layer 2.

The grey spheres in the main image in Figure 5.12 represent the A-cations above each manganese-containing layer with the numbers inside detailing the number of oxide ions in their immediate coordination sphere. It should be noted that, for clarity, the oxide ions in the A-cation layers (coloured cyan in Figure 5.12 a)-f)) are not shown in the main diagram in Figure 5.12.

As shown in the left hand column of Section 1 in Figure 5.12, the coordination numbers of the A-cations in the regions of the $La_{0.17}Sr_{0.83}MnO_{2.33}$ structure with no 'step defects' are 8 (when located between the MnO_2 layers, e.g. Figure 5.12 j)) and 10 (when located between the MnO and MnO_2 layers Figure 5.12 b)). However, as shown in the main image of Figure 5.12, the 'step defects' have a significant effect on the coordination environments of the neighbouring A-cations.

The shift in the stacking sequence and the partial filling of the 'bridging' anion site between the MnO_2 layers (due to the 90^{o} rotation of half of the square-based pyramids) generates 3 distinct sets of stripes of A-cation coordination environments adjacent to the 'step defect', i.e. stripes containing 9-coordinate (e.g. Figure 5.12 k)), 8-/10-coordinate (e.g. Figure 5.12 f) and g)) and 8-/9- coordinate (e.g. Figure 5.12 i) and l)) environments.

Therefore, there are fewer highly anion-deficient 8-coordinate A-cation sites adjacent to the ‘interface’ planes than the regions of STS-stacked material with no ‘step defects’. Consequently, the ‘interface’ planes act to increase the lattice energy, thereby providing a driving force for their formation.

5.3.4. Proposed presence of twinning

It should be noted that there is no experimental evidence collected in the course of this investigation which verifies the presence of the 90^{o} rotation in the propagation direction of the tetrahedral chains (twinning) in the structures of the $La_{1-x}Sr_xMnO_{3-(0.5+x)/2}$ (x = 0.83, 0.9 and 1) phases. Indeed, by inspection of Figure 5.12, it surprising that there is no evidence for such twinning in the HAADF-STEM images taken down the [010] zone. It was therefore proposed that the projection of the structure when viewed down the [010] direction contains the superposition of different regions of ordered material with the ‘average’ structure hiding the presence of the twinning.

However, twinning has been included in the structural model for the ‘step defects’ for 2 reasons:

1. Twinning allows the structural equivalence of the crystallographically related (102) and (10) ‘interface’ planes. As shown in Figure 5.13, the unit cells of the $La_{1-x}Sr_xMnO_{3-(0.5+x)/2}$ (x = 0.83, 0.9 and 1) structures, $\sqrt{2}a_p$ x $6a_p$ x $2\sqrt{2}a_p$, are approximately metrically tetragonal, i.e. $(a)/(c/2) \sim 1$. There appears therefore to be no apparent structural motivation for the ‘step defects’ to exist along the (102) ‘interface’ planes but not the (10) ‘interface’ planes. The twinning allows both ‘interface’ planes to be incorporated in equal proportions into the structural model.
2. Twinning creates a structural motivation for the presence of sharp ‘interface planes’ all the way along the [102] plane through the whole crystal (i.e. into the plane of the paper), thereby making the ‘step defects’ visible in the HAADF-STEM images taken

down the [102] zone. The '6-layer manganate' structure contains a significant amount of strain due to the mismatch between the bond lengths in the manganese-based tetrahedra and 'square-based pyramids'. However, the twinning planes relieve some strain in the *ac*-plane of the crystal due to the rotation in the tetrahedral chain propagation direction. For efficient strain relief in the structure, the twinning plane should run through the whole crystal and therefore result in the formation of 'sharp interface' planes.

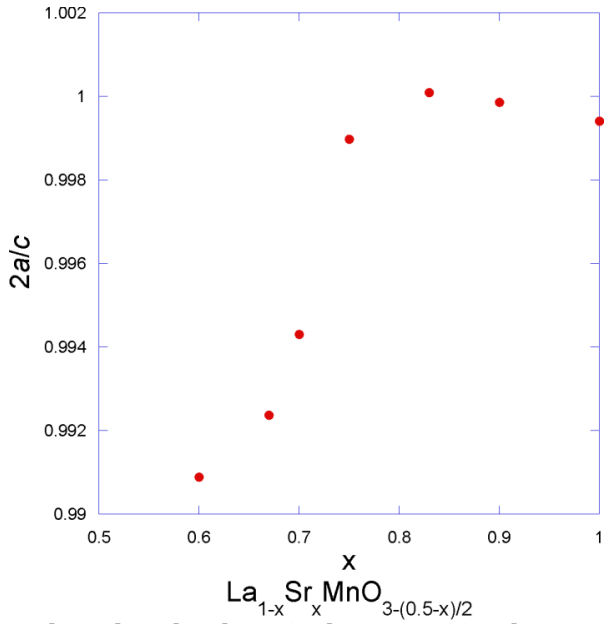


Figure 5.13: Graph depicting how close the phases in the compositional range $La_{1-x}Sr_xMnO_{3-(0.5+x)/2}$ ($0.6 \leq x \leq 1$) are to being metrically tetragonal (i.e. *a*/(*c*/2) = 1 using the cell with *Pcmb* symmetry) using lattice parameters extracted from refinement against X-ray powder diffraction data.

Similar twinning effects have been previously observed in related 6-layer structures, e.g. $YSr_2Cu_2CoO_7$.[63] As shown in Figure 5.14, the basic structure of $YSr_2Cu_2CoO_7$ contains a SSTSST stacking sequence of CuO_5 square-based pyramids (S) and CoO_4 tetrahedra (T).[76] A structural investigation by Krekels *et al*. based on electron microscopy data showed that $YSr_2Cu_2CoO_7$ actually contains twin boundaries at which the propagation direction of the tetrahedral chains rotates by 90°.[63] However, as shown in Figure 5.14 b), there is no 'step' in the stacking sequence at the point at which the tetrahedral chain propagation direction rotates by 90° in the structure of $YSr_2Cu_2CoO_7$.

It was proposed in this structural investigation by Krekels *et al*. that the presence of square-planar copper centres (shown in cyan in Figure 5.14 b)) in the cobalt-containing tetrahedral layers of the structure of $YSr_2Cu_2CoO_7$ act as point defects which allow the propagation direction of the tetrahedral chains to rotate.[63] It was hypothesised that this twinning mechanism was unavailable in the $La_{1-x}Sr_xMnO_{3-(0.5+x)/2}$ (x = 0.83, 0.9 and 1) phases due to the absence of transition metal centres which are known to adopt square planar coordination.

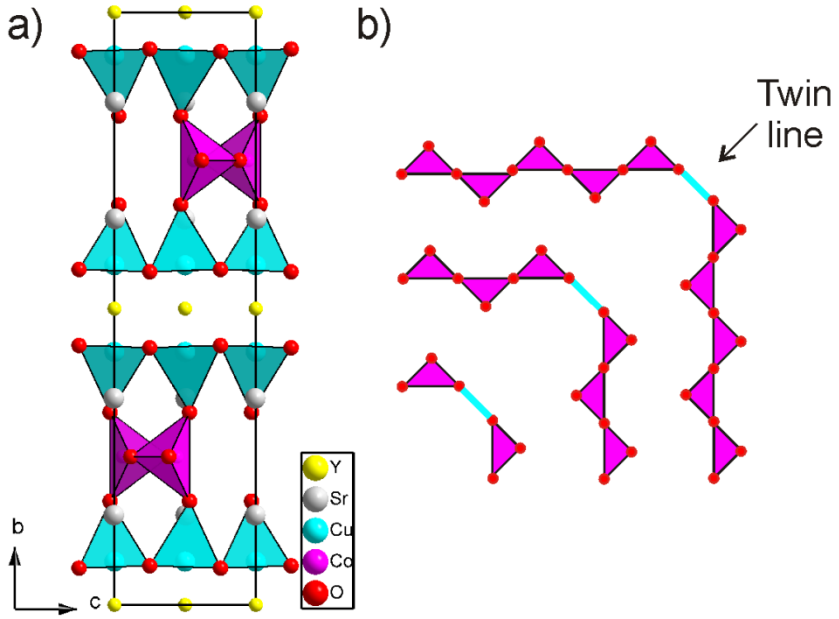


Figure 5.14: a) reported structure of $YSr_2Cu_2CoO_7$.[76] Figure b) shows the proposed mechanism for the 90° rotation of the propagation direction of the cobalt-containing tetrahedral chains in $YSr_2Cu_2CoO_7$ down the (010) direction. The cyan line indicates the presence of square-planar copper centres.[63] Figure b) is adapted from Figure 4 b) in a publication by Krekels *et al.* [63]

5.3.5. Effect of Sr^{2+}-content on the structure

While the structure of $La_{0.17}Sr_{0.83}MnO_{2.33}$ contains layers of MnO_5 square-based pyramids and tetrahedra, the empirical compositions of $La_{0.1}Sr_{0.9}MnO_{2.3}$ and $SrMnO_{2.25}$ require additional anion vacancies to be present relative to the structure of $La_{0.17}Sr_{0.83}MnO_{2.33}$. The location of these additional vacancies can be predicted by considering the bonding requirements of the constituent cations. The additional oxide anion vacancies could be located in the remaining AO layers (O(2)/(7) in Figure 5.15), the MnO layers (O(3)/(4)) or

the MnO_2 layers (O(5)/(6)/(9)/(10)). Vacancies in the AO or MnO layers would result in the formation of some 3-coordinate manganese centres. While there are reported examples of 3-coordinate transition metal centres in extended solid-state systems,[77] it is clear that the formation of such highly anion-deficient transition metal centres is energetically unfavourable.

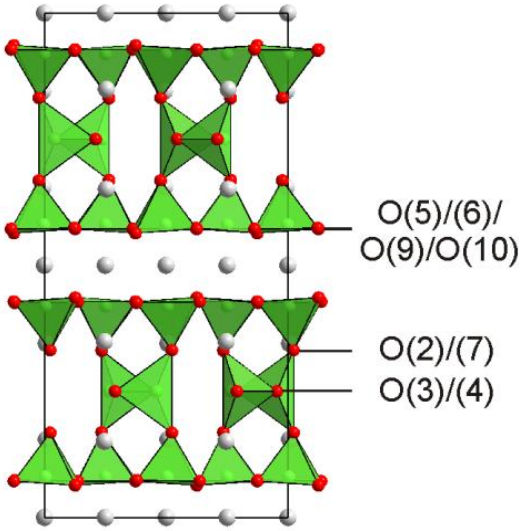


Figure 5.15: Predicted structures for the $La_{1-x}Sr_xMnO_{3-(0.5+x)/2}$ (x = 0.83, 0.9 and 1) phases

In contrast, the presence of vacancies in the MnO_2 layers would avoid the formation of such anion-deficient manganese centres by the formation of a combination of MnO_4 tetrahedra and MnO_5 square-based pyramids instead. Therefore, it seems reasonable to suggest that additional anion vacancies are located in the MnO_2 layers in the structures of $La_{0.1}Sr_{0.9}MnO_{2.3}$ and $SrMnO_{2.25}$.

As shown in Figure 5.7 and Figure 5.8, there is a gradual increase in the frequency of the 'step defects' in structures of the $La_{1-x}Sr_xMnO_{3-(0.5+x)/2}$ (x = 0.83, 0.9 and 1) phases as the Sr^{2+}-content increases. As the Sr^{2+}-content increases and the oxygen content in the empirical stoichiometry decreases, the coordination spheres of all the A-cations, especially the A-cation site between the MnO_{2-y} layers, become highly anion-deficient. Therefore, it is unsurprising that the frequency of the 'step defects' increases so as to increase the coordination numbers of more A-cations and improve the lattice energy of the overall structure.

In addition, the transformation from a ‘square-based pyramidal’ to a tetrahedral layer at the ‘step defect’ requires significant structural rearrangement at the ‘interface planes’ (see Figure 5.12). However, additional oxide anion vacancies in the MnO_{2-y} layer makes the transformation of the manganese coordination environment from ‘square-base pyramidal’ to tetrahedral more facile, thereby lowering the ‘activation energy’ for the formation of the stacking fault and increasing the frequency of the ‘step defects’ throughout the crystal.

5.4. Conclusion

The $La_{1-x}Sr_xMnO_{3-(0.5+x)/2}$ (x = 0.83, 0.9 and 1) phases adopt structures closely related to the ‘6-layer manganate structure’ of the more La^{3+}-rich members of the same anion-deficient series. However, HAADF-STEM data collected from the $La_{1-x}Sr_xMnO_{3-(0.5+x)/2}$ (x = 0.83, 0.9 and 1) phases indicate that the square-based pyramidal and tetrahedral layers are not ‘infinite’ throughout the structure. While the STSSTS stacking sequence of the ‘square based pyramidal’ and tetrahedral layers is maintained throughout the structure, there are ‘step defects’ which result in the shift of the stacking sequence, i.e. ‘step down’ to TSSTSS-stacked material or ‘step up’ SSTSST-stacked material. It was proposed that the formation of the ‘step defects’ is driven by 2 factors: the desire to increase the coordination number of the strontium cations between the ‘square-based pyramidal layers’ and to the need to partially relieve the strain in the structure brought about by the mismatch of the Mn-O bond lengths in the ‘square-based’ pyramidal and tetrahedral layers.

Appendix 5

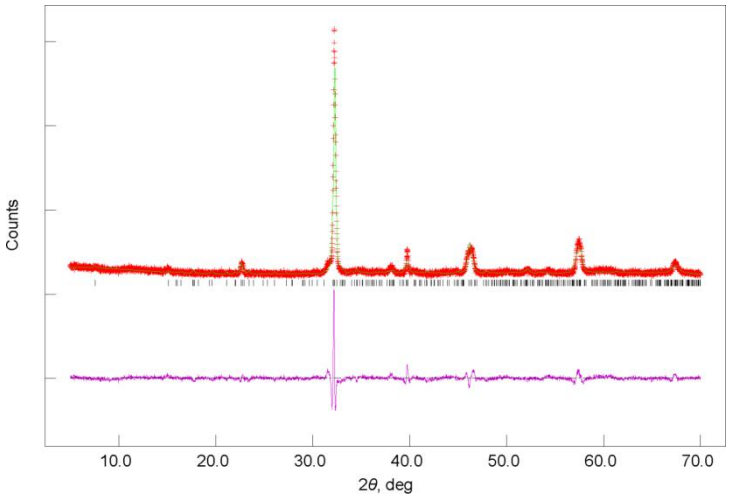


Figure 5.16: Observed, calculated and difference plots for refinement of '6-layer manganate' structural model against X-ray powder diffraction data collected from $La_{0.1}Sr_{0.9}MnO_{2.3}$. *a* = 5.5667(7) Å, *b* = 23.4608(33) Å and *c* = 11.1350(15) Å. χ^2 = 1.982, *wRp* = 8.31 %, *Rp* = 5.98 %

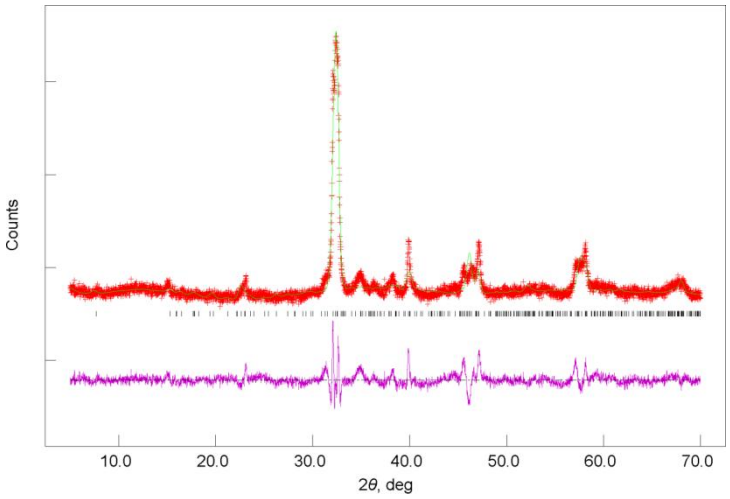


Figure 5.17: Observed, calculated and difference plots for refinement of '6-layer manganate' structural model against X-ray powder diffraction data collected from $SrMnO_{2.25}$. *a* = 5.5757(19) Å, *b* = 23.1645(71) Å and *c* = 11.0843(41) Å. χ^2 = 1.830, *wRp* = 6.80 %, *Rp* = 5.01 %

Atom	Wyckoff position	*x*	*y*	*z*	Occupancy	U_{iso} (Å^3)
Sr/La(1)	4*a*	½	0	0	0.83/0.17	0.012(1)
Sr/La(2)	4*c*	0.999(3)	0	¼	0.83/0.17	0.012(1)
Sr/La(3)	8*e*	0.463(2)	0.158(1)	0.993(2)	0.83/0.17	0.012(1)
Sr/La(4)	8*e*	0.981(1)	0.146(1)	0.249(1)	0.83/0.17	0.012(1)
Mn(1)	8*e*	0.008(1)	0.083(1)	0.001(1)	1	0.004(1)
Mn(2)	4*d*	0.469(1)	¾	0.290(1)	0.51(2)	0.004(1)
Mn(2')	4*d*	0.531(1)	¾	0.290(2)	0.49(2)	0.004(1)
Mn(3)	4*d*	0.050(1)	¼	0.020(1)	0.51(2)	0.004(1)
Mn(3')	4*d*	0.950(1)	¼	0.020(1)	0.49(2)	0.004(1)
Mn(4)	8*e*	0.485(1)	0.083(1)	0.251(1)	1	0.004(1)
O(2)	8*e*	0.002(2)	0.169(1)	0.981(1)	1	0.013(1)
O(3)	4*d*	0.934(1)	¼	0.202(1)	0.51(2)	0.013(1)
O(3')	4*d*	0.066(1)	¼	0.202(1)	0.49(2)	0.013(1)
O(4)	4*d*	0.434(1)	¼	0.029(1)	0.51(2)	0.013(1)
O(4')	4*d*	0.566(1)	¼	0.029(1)	0.49(2)	0.013(1)
O(5)	8*e*	0.749(1)	0.069(1)	0.373(1)	1	0.013(1)
O(6)	8*e*	0.250(1)	0.075(1)	0.375(1)	1	0.013(1)
O(7)	8*e*	0.501(2)	0.169(1)	0.236(1)	1	0.013(1)
O(9)	8*e*	0.229(1	0.072(1)	0.124(1)	1	0.013(1)
O(10)	8*e*	0.732(1)	0.075(1)	0.127(1)	1	0.013(1)
$La_{0.3}Sr_{0.7}MnO_{2.4}$: space group *Pcmb*, *a* = 5.5906(6) Å, *b* = 23.204(1) Å, *c* = 11.1548(1) Å, cell volume = 1466.78(16) Å^3						
χ^2 = 3.702, wR_p = 5.23 %, R_p = 3.78 %						

Table 5.2: Refined structural parameters of $La_{0.17}Sr_{0.83}MnO_{2.33}$

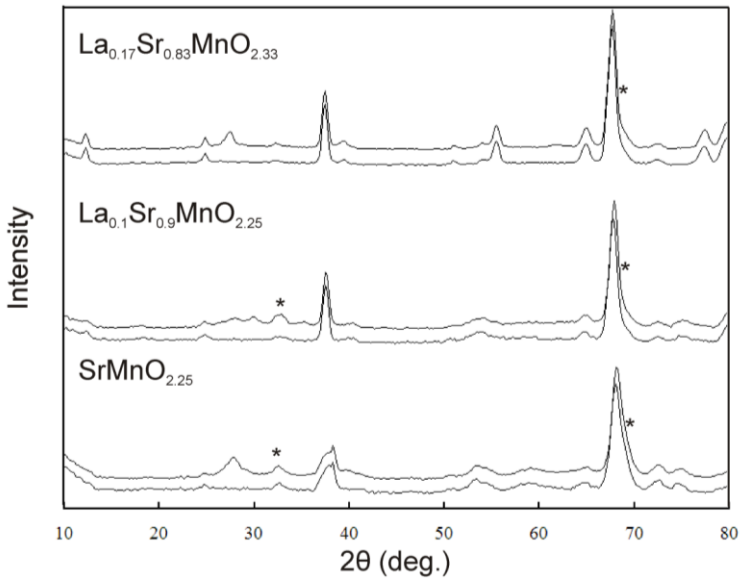


Figure 5.19: Neutron powder diffraction data collected from the Sr^{2+}-rich phases of the $La_{1-x}Sr_xMnO_{3-(0.5-x)/2}$ series at 298 K (bottom) and 5 K (top) using the D1b instrument. The reflections marked with asterisks are inconsistent with the '6-layer manganate' unit cell

Chapter 6: $La_{0.4}Sr_{0.6}MnO_{3-y}$ and Conclusions Regarding the '6-layer Manganates'

6.1. Introduction

As discussed in sections 4.3.2 and 4.3.1, the topotactic reduction reaction of $La_{0.4}Sr_{0.6}MnO_3$ using NaH as a solid-state reducing agent results in the formation of a reduced phase with an empirical composition of $La_{0.4}Sr_{0.6}MnO_{2.45}$ and an average manganese oxidation state of +2.5. While a '6-layer manganate' structural model for $La_{0.4}Sr_{0.6}MnO_{2.45}$ can be successfully refined against X-ray powder diffraction data (see Figure 4.24 in Appendix 4), electron diffraction data collected from $La_{0.4}Sr_{0.6}MnO_{2.45}$ are inconsistent with this phase adopting a structure analogous to the $La_{1-x}Sr_xMnO_{3-(0.5+x)/2}$ (x = 0.67, 0.7 and 0.75) phases. This chapter details a fuller structural investigation of $La_{0.4}Sr_{0.6}MnO_{2.45}$ and some conclusions regarding the structures of the $La_{1-x}Sr_xMnO_{3-(0.5+x)/2}$ ($x \geq 0.6$) phases.

6.2. Results

6.2.1. Neutron diffraction data

Neutron powder diffraction data were collected from a sample of $La_{0.4}Sr_{0.6}MnO_{2.45}$ using the POLARIS instrument (see section 2.3.2.2). The majority of the observed diffraction reflections could be indexed using a unit cell consistent with the '6-layer manganate' structure (a = 5.6105(2) Å, b = 23.2893(10) Å, c = 11.3279(5) Å). However, close inspection of the data revealed several additional weak reflections which are inconsistent with this unit cell. The d-spacings of some of these additional reflections are consistent with the presence of MnO and vanadium (marked with red and blue tick marks in Figure 6.1 respectively), the latter being attributable to the sample holder. However, the rest of these additional reflections, including the large d-spacing reflection marked with an asterisk in Figure 6.1, could not be assigned to obvious impurity phases. Variable temperature neutron powder diffraction data collected using the D1b instrument (see Figure 6.6 in Appendix 6) confirmed

that the intensities of these additional reflections were independent of temperature, invalidating the hypothesis that these reflections were attributable to the presence of long range magnetic order.

6.2.2. Structural refinement

Elucidation of the structure of $La_{0.4}Sr_{0.6}MnO_{2.45}$ using neutron powder diffraction data was attempted using the same refinement strategy used to determine the structures of the $La_{1-x}Sr_xMnO_{3-(0.5+x)/2}$ (x = 0.67, 0.7 and 0.75) phases (see section 3.3.4).

'6-layer' structural models describing the 5 simplest arrangements of twisted tetrahedral chains (i.e. models with *I*2*mb*, *Imma*, *Pnma*, *C*2/*c* and *Pcmb* symmetries) were constructed and refined against neutron powder diffraction data. In addition to these 5 models, 2 additional models accounting for the disorder in the arrangement of the twisted tetrahedral chains ('*Pcmb* disorder' and '*Pcmb* disorder varying *f*(Td)' – see section 3.3.6) were also created and refined against neutron diffraction data. In agreement with observations based on data collected from the $La_{1-x}Sr_xMnO_{3-(0.5+x)/2}$ (x = 0.67, 0.7 and 0.75) phases, the '*Pcmb* disorder varying *f*(Td)' model gives the best statistical fit to the data (see Table 6.1). However, given the imperfect observable fit to the data (see Figure 6.1) and the similarity in the fitting statistics between the models, it is not possible to unequivocally determine the ordering arrangement of the twisted tetrahedral chains within the structure of $La_{0.4}Sr_{0.6}MnO_{2.45}$ using neutron powder diffraction data.

Space group	χ^2	*wRp*	*Rp*	*f*(Td)
I2mb	2.228	3.36 %	5.75 %	
Imma	1.939	3.13 %	5.14 %	
Pnma	2.305	3.41 %	6.03 %	
C2/c	2.056	3.33 %	6.13 %	
Pcmb	1.817	3.08 %	6.09 %	
'*Pcmb* disorder'	2.041	3.27 %	6.22 %	50 %
'*Pcmb* disorder varying *f*(Td)'	1.797	3.07 %	5.92 %	89(2) %

Table 6.1: Fitting statistics for the refinement of different 6-layer structural models against neutron powder diffraction data collected from $La_{0.4}Sr_{0.6}MnO_{2.45}$.

The observed, calculated and difference plots for the refinement of the '*Pcmb* disorder varying *f*(Td)' structural model are shown in Figure 6.1. The observable fit to the vast majority of the observable reflections is good, however as discussed above, several large *d*-spacing reflections are unaccounted for using the '6-layer manganate' structural model. This suggests that while the '6-layer manganate' structural model is a reasonably accurate approximation to the actual structure of $La_{0.4}Sr_{0.6}MnO_{2.45}$, additional order is present.

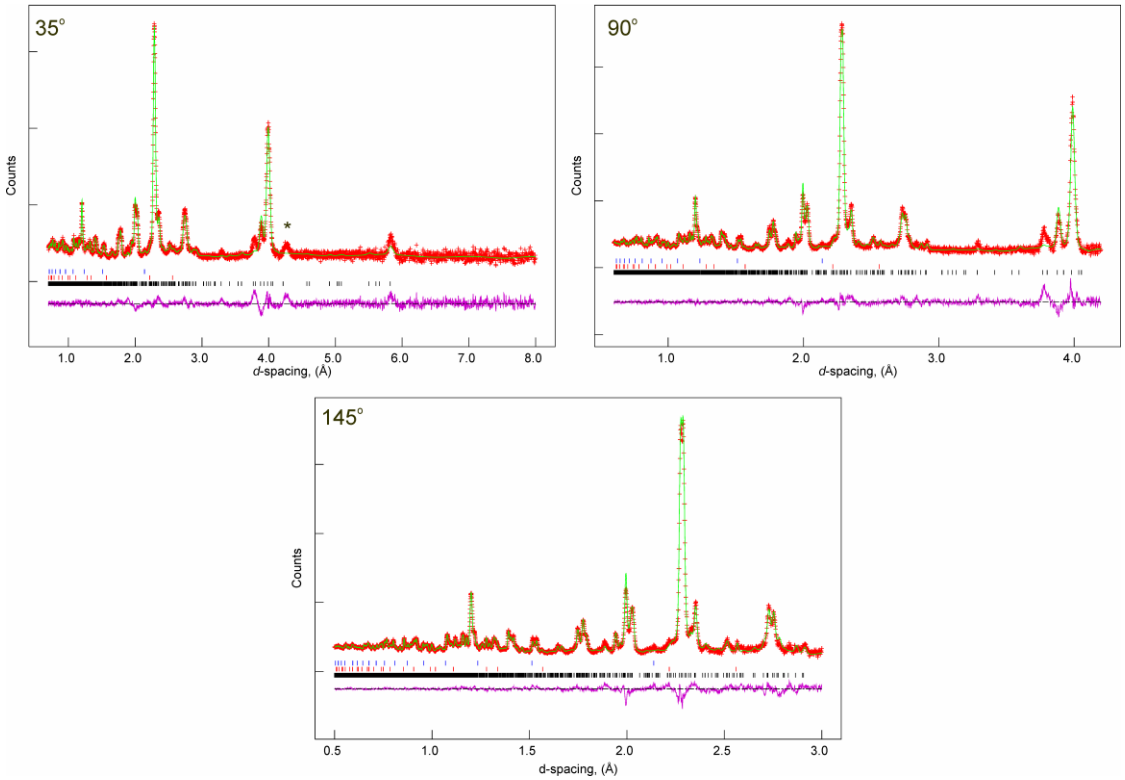


Figure 6.1: Observed, calculated and difference plots for the refinement of a '6-layer manganate' structural model against data collected from $La_{0.4}Sr_{0.6}MnO_{2.45}$. Tick marks show reflection positions for $La_{0.4}Sr_{0.6}MnO_{2.45}$ (black), MnO (red) and vanadium (blue). The most intense reflection inconsistent with the '6-layer manganate' structural model is marked with an asterisk.

6.2.3. Electron diffraction data

In order to evaluate the presence of additional order in the structure of $La_{0.4}Sr_{0.6}MnO_{2.45}$, electron diffraction data were collected. It should be noted at the outset that the data are complicated due to twinning of the crystallites. The electron diffraction data collected down the majority of the zones (e.g. the [101] zone shown in Figure 6.2 a)) could be indexed using a unit cell based on a $\sqrt{2}a_p$ x $6a_p$ x $\sqrt{2}a_p$ expansion of the unit cell of a simple cubic perovskite structure and *I*2*mb*/*Imma* symmetry, i.e. the *c*-lattice parameter is halved relative to the unit cell of the '6-layer manganate' structure ($\sqrt{2}a_p$ x $6a_p$ x $2\sqrt{2}a_p$).

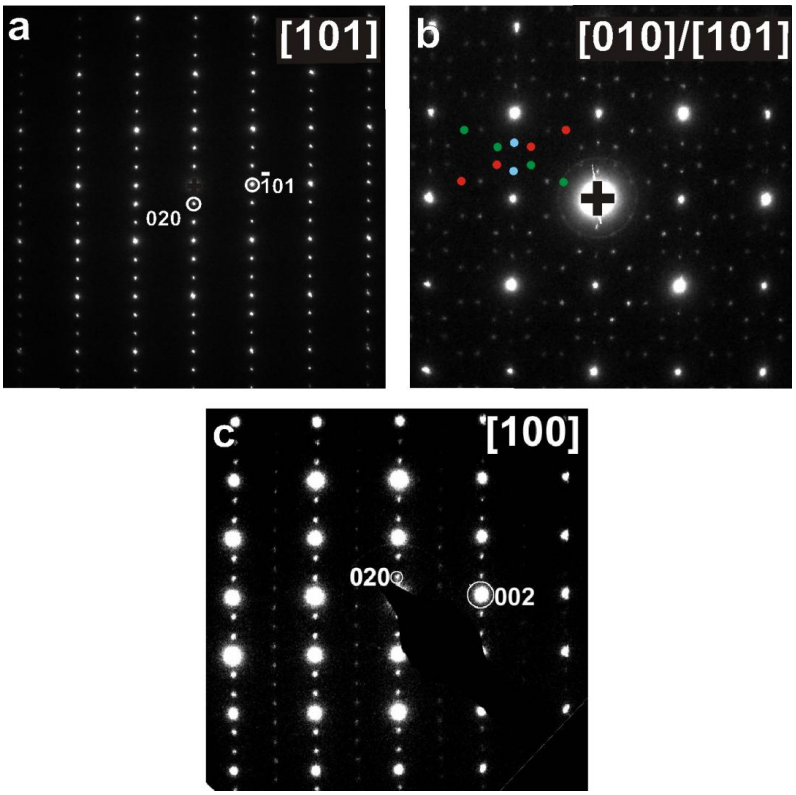


Figure 6.2: Electron diffraction data collected from the a) [101], b) [010] (twinned with [101]) and c) [100] zone axes of $La_{0.4}Sr_{0.6}MnO_{2.45}$ by Prof. Dr. Joke Hadermann.

However, Figure 6.2 b) contains reflections inconsistent with this unit cell. The reflections marked with red and green circles come from a mirror twin of the [010] zone. However, the reflections marked with blue circles indicate additional order in the *ac*-plane. All the data can be accounted for using a unit cell based on a $\sqrt{10}a_p$ x $6a_p$ x $\sqrt{10}a_p$ expansion of the simple cubic perovskite structure (a = 12.54 Å, b = 23.29 Å, c = 12.66 Å) proposed by Prof. Dr. Joke

Hadermann.[78] A $\sqrt{10}a_p$ expansion, along with other 'simple' expansions, of the simple cubic perovskite structure is shown in Figure 6.3. Unfortunately, attempts to determine the space group of the structure of $La_{0.4}Sr_{0.6}MnO_{2.45}$ were unsuccessful.

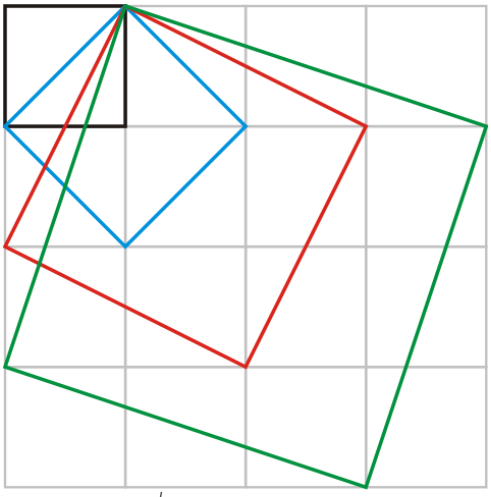


Figure 6.3: $\sqrt{2}a_p$ (blue line), $\sqrt{5}a_p$ (red line) $\sqrt{10}a_p$ (green line) of simple cubic perovskite unit cell (black line)

The large *d*-spacing reflection in the neutron powder diffraction data collected from $La_{0.4}Sr_{0.6}MnO_{2.45}$ which can't be indexed using the unit cell of the '6-layer manganate' structural model (marked with an asterisk in Figure 6.6) can be indexed using the $\sqrt{10}a_p$ x $6a_p$ x $\sqrt{10}a_p$ expanded unit cell. This suggests that this additional order is observable over the long range.

This additional order could be associated with a number of different structural features; however the most likely source involves in-plane ordering within the 'octahedral' layers. Given the empirical stoichiometry of the $La_{0.4}Sr_{0.6}MnO_{2.45}$ phase, the average coordination number of the manganese centres in the 'octahedral' layers is 5.35, therefore the 'octahedral' layers are comprised of a 35:65 ratio of MnO_y square-based pyramids and octahedra. The square-based pyramids and octahedra may order in a number of arrangements, the 2 simplest of which are described below:

Firstly, the modulation of the fractional occupancy of the 'bridging' anion site between the MnO_2 layers would result in an in-plane ordered arrangement of the MnO_y octahedra and

square-based pyramids. One possibility is that the MnO_y octahedra and square-based pyramids are ordered in a manner resembling the ordering patterns of NiO_y octahedra and square-planar units in one of the anion-deficient $LaNiO_{3-y}$ phases shown in Figure 6.4.[79]

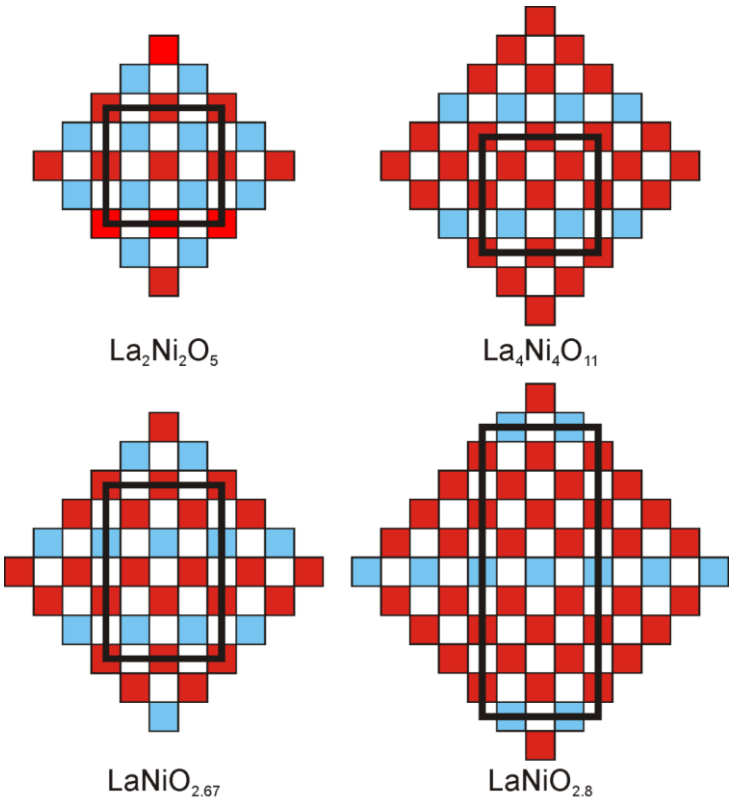


Figure 6.4 (adapted from a publication by Sayagués *et al.*)[79]: The structures of some anion deficient $LaNiO_{3-x}$ phases. It should be noted that a refined structure of $LaNiO_{2.67}$ has not been reported. The red and the blue squares represent nickel in octahedral and square planar sites respectively.

Alternatively, the square-based pyramids in the structure of $La_{0.4}Sr_{0.6}MnO_{2.45}$ could rotate by 90° about the *a*- or *c*-axis such that their apical oxide ions are located in the manganese-containing layers (i.e. the Mn-O_{apical} vector is parallel to the *a*- or the *c*- axis). The MnO_y octahedra and rotated square-based pyramids could then order in an analogous fashion to that observed in the structure of $La_{0.1}Sr_{0.9}MnO_{2.74}$ (see Figure 6.5).[55]

However, the proposed ordering scheme based on $La_{0.1}Sr_{0.9}MnO_{2.74}$ requires oxide anion vacancies to be located within the MnO_2 layer of the $La_{0.4}Sr_{0.6}MnO_{2.45}$ structure. During the refinement of the structural model for $La_{0.4}Sr_{0.6}MnO_{2.45}$, these oxide anion sites remained fully occupied within error - effectively ruling out the adoption of this ordering scheme.

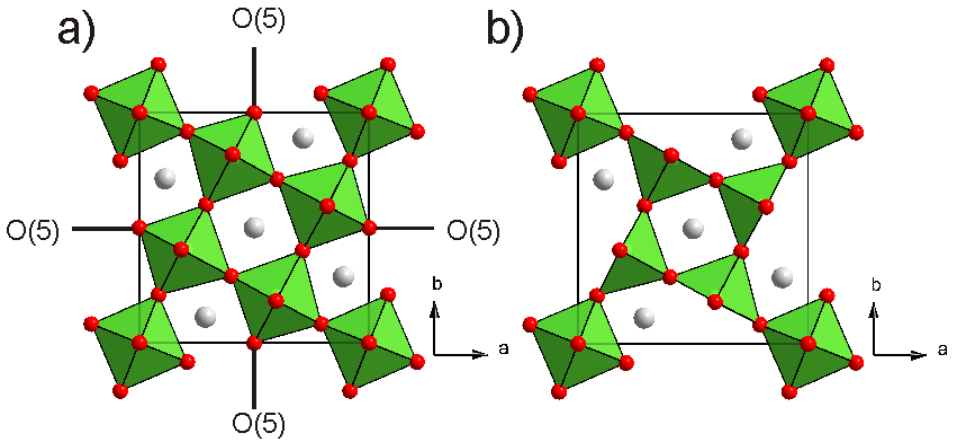


Figure 6.5 a) Structure of $La_{0.1}Sr_{0.9}MnO_{2.74}$ with partially occupied O(5) sites b) structure with O(5) sites removed to highlight anion vacancy ordering arrangement.

Unfortunately, the determination of the ordering arrangement of the MnO_y octahedra and square-based pyramids in the structure of $La_{0.4}Sr_{0.6}MnO_{2.45}$, and therefore full structural characterisation, was unsuccessful. However, it is clear that the 35:65 ratio of MnO_y square-based pyramids and octahedra is not consistent with a unit cell containing a simple ordered arrangement of the MnO_y polyhedra. It is therefore likely that the oxygen content is not uniform throughout the material with small domains of subtly different structures present

6.3. Conclusions regarding '6-layer manganate' structure

6.3.1. Level of reduction

There is a strong contrast between the structures of the products of the topotactic reduction reactions of the $La_{1-x}Sr_xMnO_3$ ($0.2 \leq x \leq 1$) substrate phases as a function of the Sr^{2+}-content:

1. $0.2 \leq x \leq 0.5$. The products adopt the $A_2B_2O_5$ brownmillerite structure with no partially occupied anion sites.[17, 20] Given the invariance of the anion content in the empirical composition, the average manganese oxidation state increases with increasing Sr^{2+}-content (i.e. Mn^{2+x}).
2. $0.6 \leq x \leq 0.75$. The phases adopt the '6-layer manganate' structure with the empirical composition ($La_{1-x}Sr_xMnO_{3-(0.5+x)/2}$) dependent on the Sr^{2+}-content. These phases contain an invariant manganese oxidation state of +2.5. In contrast to the $A_2B_2O_5$

brownmillerite phases, the '6-layer manganate' structure contains partially occupied anion sites (O(1)/(8) in Figure 3.6).

3. $0.83 \leq x \leq 1$. The phases adopt highly anion-deficient structures closely related to the '6-layer manganate' structure but contain 'step defects' (see Chapter 5). In common with the $0.6 \leq x \leq 0.75$ phases, the reduced phases also adopt empirical compositions with varying anion content ($La_{1-x}Sr_xMnO_{3-(0.5+x)/2}$ $(0.83 \leq x \leq 1)$) but an invariant manganese oxidation state of +2.5.

The contrast in the empirical compositions (i.e. constant or variable anion contents) of the $0.2 \leq x \leq 0.5$ and $x \geq 0.6$ reduced phases indicates that the topotactic reduction reactions which form these phases are controlled by different factors. The constant empirical composition of the phases in the compositional range $La_{1-x}Sr_xMnO_{2.5}$ $(0.2 \leq x \leq 0.5)$ suggests that the structures of the reduced phases control the anion content. In contrast, phases within the compositional range $La_{1-x}Sr_xMnO_{3-(0.5+x)/2}$ $(x \geq 0.6)$ exhibit a variable anion content and an invariant manganese oxidation state of +2.5. On initial inspection there appears to be no direct structural motivation for this behaviour, it is therefore pertinent to ask: what leads to the preparation of $La_{1-x}Sr_xMnO_{3-(0.5+x)/2}$ $(0.6 \leq x \leq 1)$ reduced phases which contain manganese centres with this constant average oxidation state?

One hypothesis is that the level of reduction is controlled by the 'reducing power' of the reducing agent (NaH). This hypothesis is given credence by the fact that a broad of array of less anion-deficient $La_{1-x}Sr_xMnO_{3-y}$ (see Figure 3.1) phases have previously been reported using H_2/He gas as a reducing agent, known to be a weaker reducing agent than NaH.[54-56, 80] In these instances, the anion content of the reduced phases is strongly dependent on the strength of the reducing conditions employed.

It has been demonstrated that binary metal hydrides can effect topotactic reduction reactions which form complex manganese-based oxides with manganese oxidation states as

low as +2, e.g. $BaMnO_2$.[29] This suggests that the 'reducing power' of NaH is unlikely to limit the level of reduction of the $La_{1-x}Sr_xMnO_3$ ($x \geq 0.6$) phases.

An alternative proposal is that the level of reduction of the $La_{1-x}Sr_xMnO_{3-y}$ ($x \geq 0.6$) phases is controlled by some electronic stability associated with the formation of materials which contain manganese with an average oxidation state of +2.5. This proposal is supported by the fact that the manganese centres in the $La_{1-x}Sr_xMnO_{3-(0.5+x)/2}$ ($x = 0.83$, 0.9 and 1) phases contain such an average oxidation state even though the structures have to incur relatively severe structural disruption (i.e. the formation of 'step defects') to simultaneously maintain the empirical composition, and thus average manganese oxidation state, and satisfy the bonding requirements of the highly anion-deficient A-cations.

The most chemically reasonable explanation for the constant average manganese oxidation state in the '6-layer manganate' phases is charge ordering in the 'octahedral' layers. As discussed in section 3.4.1, the '6-layer manganate' phases contain tetrahedral Mn^{2+} centres and so the average manganese oxidation state in the 'octahedral' layers is +2.75. However, as discussed in section 4.3.4, there is no evidence in any of the diffraction data sets (X-ray, neutron and electron) for any $3Mn^{3+}$:$1Mn^{2+}$ charge ordering in the 'octahedral' layers in the '6-layer manganate' phases. Therefore, it is unlikely that the formation of such a charge ordered arrangement determines the level of reduction, especially at the elevated reaction temperatures (210 ^oC). Further work is required on this subject to determine the reasoning behind the apparent stability associated with the formation of '6-layer manganate' phases which contain manganese centres with an average oxidation state of +2.5.

6.3.2. Structure of $La_{0.5}Sr_{0.5}MnO_{2.5}$

As discussed in section 4.3.2, $La_{0.5}Sr_{0.5}MnO_{2.5}$, whether prepared by heating the $La_{0.5}Sr_{0.5}MnO_3$ substrate phase under an H_2/He atmosphere or with NaH,[20] adopts the brownmillerite structure. While the empirical stoichiometry of, and average manganese

oxidation state in, $La_{0.5}Sr_{0.5}MnO_{2.5}$ are consistent with the adoption of the '6-layer manganate' structure, there is a clear preference for the adoption of the brownmillerite structure.

Given the apparent stability of the brownmillerite structure relative to the '6-layer manganate' structure for $La_{0.5}Sr_{0.5}MnO_{2.5}$, it can be hypothesised that the topotactic reduction of phases in the range $La_{1-x}Sr_xMnO_3$ ($x \geq 0.6$) should result in the formation of reduced phases which adopt the brownmillerite structure rather than the observed '6-layer manganate' structure. However, as previously described in section 3.4.1, the proposed resistance to the formation of tetrahedral manganese centres with an average oxidation state above +2 precludes the formation of brownmillerite phases. Instead the topotactic reduction reactions of the $La_{1-x}Sr_xMnO_3$ ($x \geq 0.6$) phases results in the formation of reduced phases which adopt the '6-layer manganate' structure.

Appendix 6

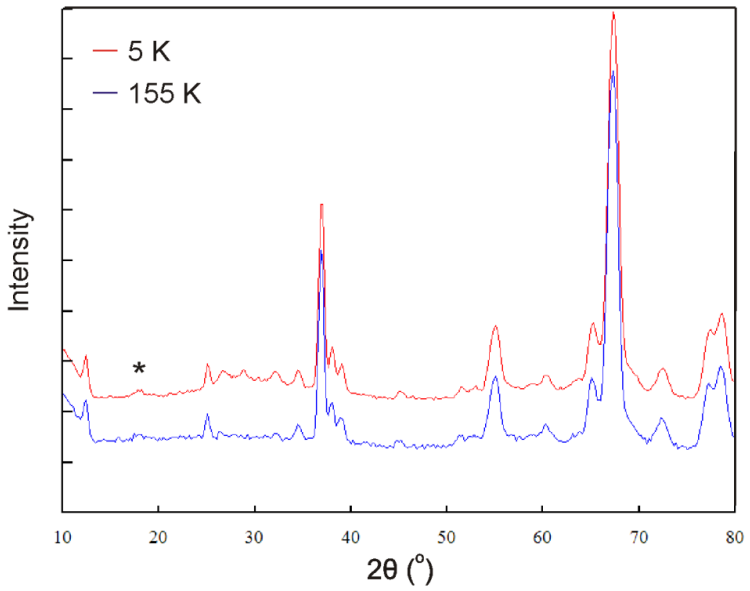


Figure 6.6: Neutron powder diffraction data collected from $La_{0.4}Sr_{0.6}MnO_{2.45}$ using the D1b instrument at 155 K (bottom) and 5 K (red). The *d*-spacing of the reflection centred at $2\theta = 18^o$ (marked with an asterisk) is the same as that marked with an asterisk in Figure 6.1.

Chapter 7: Reduction of $La_{1-x}Ca_xMnO_3$ ($0.6 \leq x \leq 1$) phases

7.1. Introduction

While the topotactic reduction reactions of the La^{3+}-rich $La_{1-x}Sr_xMnO_3$ phases form $A_2B_2O_5$ brownmillerite reduced phases,[17, 20] the reduction reactions of the Sr^{2+}-rich $La_{1-x}Sr_xMnO_3$ phases form '6-layer manganate' phases (see Chapters 3-6). In a similar fashion, the topotactic reduction reactions of the La^{3+}-rich $La_{1-x}Ca_xMnO_3$ substrate phases also result in the formation of reduced phases which adopt the brownmillerite structure.[17, 21] Therefore it is pertinent to ask, what are the structures of the reduced phases formed by topotactic reduction reactions of the $La_{1-x}Ca_xMnO_3$ ($0.6 \leq x \leq 1$) substrate phases?

While the reduction chemistry of substrate phases in the range $La_{1-x}Ca_xMnO_3$ ($0.6 \leq x \leq 0.9$) is poorly studied, the topotactic reduction of $CaMnO_3$ has been the subject of more detailed investigation (see Figure 7.1). The topotactic reduction reaction of $CaMnO_3$ to form $Ca_2Mn_2O_5$ was reported by Poeppelmeier *et al*.[81] The structure of the latter phase contains an ordered array of vertex-linked MnO_5 square-based pyramids. More recently, Varela *et al*. detailed the reduction of $CaMnO_3$ to form $Ca_{0.5}Mn_{0.5}O$, which adopts the rock salt structure with a disordered arrangement of calcium and manganese cations.[82]

The most notable feature about the reaction of $CaMnO_3$ to form $Ca_{0.5}Mn_{0.5}O$ is the 'non-topotactic' nature of the reaction, in the sense that there is a significant rearrangement of the cation framework upon reaction. The calcium and manganese cations are located on distinct crystallographic sites (4*c* and 4*b* respectively) in $CaMnO_3$, whereas both cations are located on the same site (4*b*) in $Ca_{0.5}Mn_{0.5}O$. This demonstrates that there is, at least, partial cation mobility at the relatively modest reaction temperature (665 ^oC) used to form $Ca_{0.5}Mn_{0.5}O$.

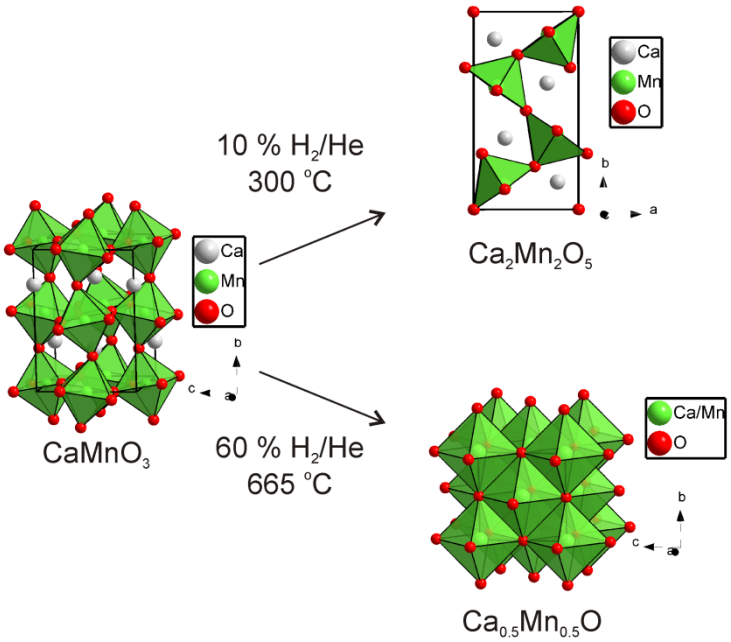


Figure 7.1: Reduction chemistry of $CaMnO_3$.[82, 83]

To allow structural comparison to the '6-layer manganate' $La_{1-x}Sr_xMnO_{3-(0.5-x)/2}$ ($x \geq 0.6$) phases and the previously reported $Ca_{0.5}Mn_{0.5}O$ disordered rock salt phase, the reduction reactions of phases in the range $La_{1-x}Ca_xMnO_3$ ($x \geq 0.6$) were performed using NaH as a reducing agent.

7.2. Experimental

7.2.1. Synthesis of perovskite starting materials

5 g samples of $La_{1-x}Ca_xMnO_3$ (x = 0.6, 0.67, 0.7, 0.8, 0.9 and 1) were prepared using a synthetic procedure based on that previously reported by Radaelli *et al.*[84] The appropriate stoichiometric ratios of La_2O_3 (99.999 %, dried at 900 °C), $CaCO_3$ (99.999 %) and MnO_2 (99.999 %) were ground with an agate pestle and mortar and then heated at 900 °C in air. The resulting powders were reground, pressed into 2-3 g, 13 mm pellets and heated at 1400 °C for 3 x 48 hours in air. After each heating cycle the materials were reground and pressed into pellets as before. After the final heating cycle, the samples were cooled at 1 °C/min to ensure that the materials were oxide stoichiometric rather than anion deficient. X-ray powder diffraction patterns confirmed that phase-pure samples of all the target materials had been

obtained with lattice parameters in good agreement with published values (see Table 7.11 in Appendix 7).[84, 85]

7.2.2. Low temperature reduction with metal hydrides

Low temperature reduction reactions of phases in the compositional range $La_{1-x}Ca_xMnO_3$ ($x \geq 0.6$) were carried out using the same method utilised for the reduction of $La_{0.33}Sr_{0.67}MnO_3$ (see section 3.2.2). 5 g samples of $La_{1-x}Ca_xMnO_3$ were ground thoroughly with 2 mole equivalents of NaH in an argon-filled glovebox and then sealed under vacuum in a Pyrex ampoule. The mixtures were then heated at 180 ^oC for 12 hours and then 210 ^oC for 4 x 48 hours with the mixture being ground in an argon-filled glovebox after each heating cycle. The samples were then washed with 4 x 100 ml of CH_3OH under nitrogen to remove sodium-containing phases (NaOH and NaH) before being dried under vacuum.

7.3. Results

7.3.1. X-ray diffraction data

Inspection of X-ray powder diffraction data collected from the washed products of the reaction between NaH and $La_{1-x}Ca_xMnO_3$ ($x \geq 0.6$) substrate phases (see Figure 7.2 and Figure 7.3) revealed that the products fall into 2 general classes as a function of the La:Ca ratio.

1. x = 0.9 and 1. The reflections in each data set can be indexed using a face-centred cubic unit cell (see Table 7.1).
2. x = 0.6, 0.67, 0.7 and 0.8. The reflections in each data set can be indexed using a tetragonal unit cell with the lattice parameters shown in Table 7.1.

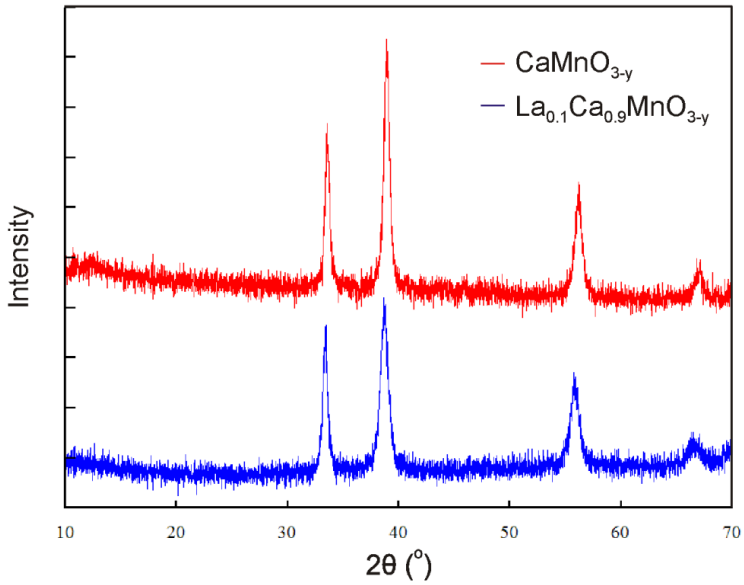


Figure 7.2: X-ray powder diffraction data collected from $(La_{0.1}Ca_{0.9})_{0.5}Mn_{0.5}O$ (red) and $Ca_{0.5}Mn_{0.5}O$ (blue)

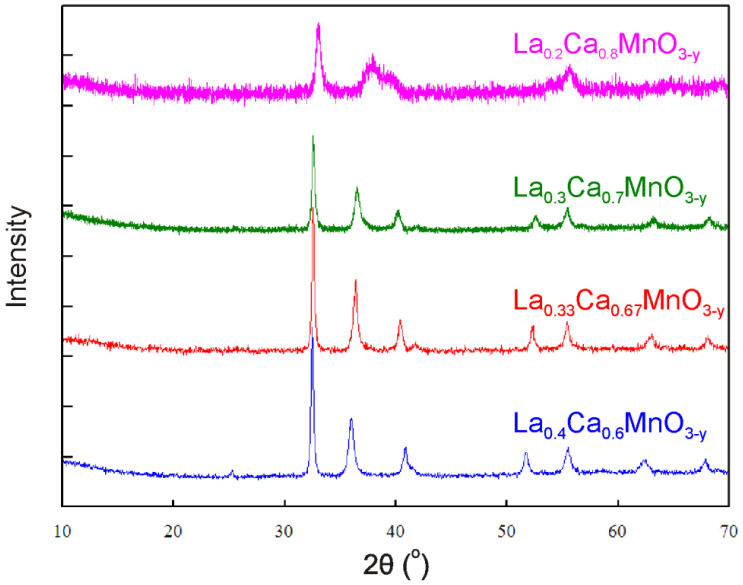


Figure 7.3: X-ray powder diffraction data collected from the washed products of the reaction between NaH and $La_{1-x}Ca_xMnO_3$ ($0.6 \leq x \leq 0.8$) substrate phases

$La_{1-x}Ca_xMnO_{3-y}$	*a* (Å)	*c* (Å)	*V* (Å^3)
0.6	3.539(1)	4.428(1)	55.479(46)
0.67	3.508(1)	4.555(1)	54.852(21)
0.7	3.480(1)	4.489(1)	54.378(31)
0.8	3.382(2)	4.602(3)	52.651(98)
0.9	4.661(1)		101.308(79)
1	4.637(1)		99.709(56)

Table 7.1: Lattice parameters used to index reflections in X-ray powder diffraction data collected from $La_{1-x}Ca_xMnO_{3-y}$ ($0.6 \leq x \leq 0.8$) and $(La_{1-x}Ca_x)_{0.5}Mn_{0.5}O$ (x = 0.9 and 1) phases.

The face-centred unit cells of the products of reaction between $La_{1-x}Ca_xMnO_3$ (x = 0.9 and 1) substrate phases and NaH are consistent with disordered rock salt structures previously

reported for $Ca_{0.5}Mn_{0.5}O$ (see Figure 7.1).[82] Therefore models based on this disordered rock salt structure were constructed and refined against X-ray powder diffraction data collected from $(La_{0.1}Ca_{0.9})_{0.5}Mn_{0.5}O$ and $Ca_{0.5}Mn_{0.5}O$.[82] As shown in Figure 7.4 and Figure 7.5, the refinements result in good observable fits to the collected data. The refined structural parameters for $(La_{0.1}Ca_{0.9})_{0.5}Mn_{0.5}O$ and $Ca_{0.5}Mn_{0.5}O$ are shown in Table 7.13 and Table 7.12 in Appendix 7. It is clear that an empirical composition of $(La_{0.1}Ca_{0.9})_{0.5}Mn_{0.5}O$ requires the presence of some Mn(I) centres. To the best of the author's knowledge, $(La_{0.1}Ca_{0.9})_{0.5}Mn_{0.5}O$ is the first reported example of an extended oxide containing manganese centres with an average oxidation state below 2.

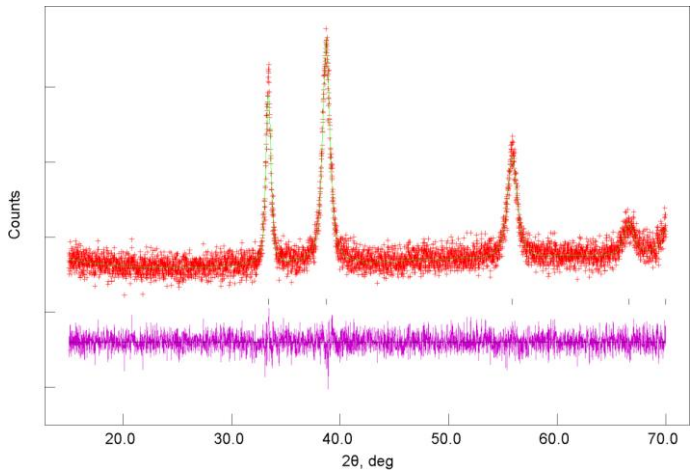


Figure 7.4: Observed, calculated and difference plots from the refinement of a disordered rock salt model against X-ray diffraction data collected from $(La_{0.1}Ca_{0.9})_{0.5}Mn_{0.5}O$, χ^2 = 1.1162, *wRp* = 5.62 % and *Rp* = 4.43 %

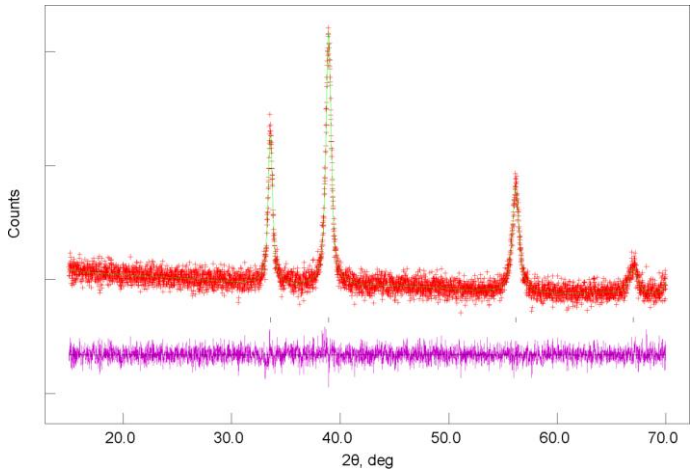


Figure 7.5: Observed, calculated and difference plots from the refinement of a disordered rock salt model against X-ray diffraction data collected from $Ca_{0.5}Mn_{0.5}O$, χ^2 = 1.1059, *wRp* = 5.27 % and *Rp* = 4.12 %

In contrast, from inspection of the X-ray powder diffraction data sets shown in Figure 7.3, it is clear that $La_{1-x}Ca_xMnO_{3-y}$ ($0.6 \leq x \leq 0.8$) phases do not adopt the rock salt structure.

7.3.2. Electron diffraction data

In order to confirm the size and symmetry of the unit cell, electron diffraction patterns were collected from a sample of $La_{0.4}Ca_{0.6}MnO_{3-y}$, as a representative member of the $La_{1-x}Ca_xMnO_{3-y}$ ($0.6 \leq x \leq 0.8$) series (see Figure 7.6). The reflections in each data set shown in Figure 7.6 are consistent with the tetragonal unit cell shown in Table 7.1. However, some of the patterns (e.g. Figure 7.6.d) contain additional scattering outside of the Bragg reflections. This diffuse scattering is consistent with additional order in the structure that is coherent over too small a range to result in Bragg reflections in the electron diffraction patterns.

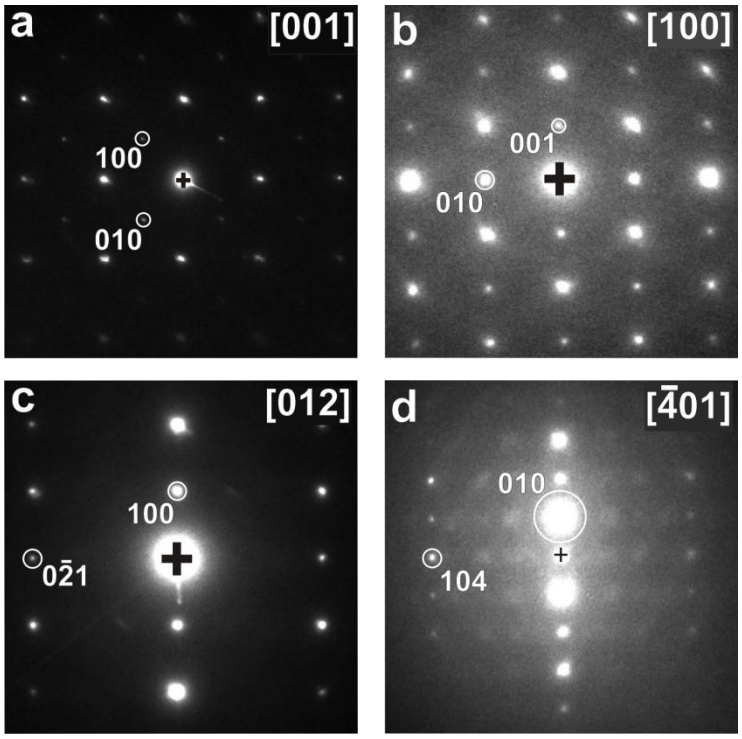


Figure 7.6: Electron diffraction patterns collected from the a) [001], b) [100], c) [012] and d) [01] zones axes of $La_{0.4}Ca_{0.6}MnO_{3-y}$ by Prof. Dr. Joke Hadermann.

7.3.3. Neutron diffraction data

In order to establish the long range anion-vacancy ordered structure, neutron powder diffraction data were collected from the $La_{1-x}Ca_xMnO_{3-y}$ ($0.6 \leq x \leq 0.8$) phases. Data were collected from $La_{0.2}Ca_{0.8}MnO_{3-y}$ using the D2b instrument (see Figure 7.7) and from $La_{0.3}Ca_{0.7}MnO_{3-y}$, $La_{0.33}Ca_{0.67}MnO_{3-y}$ and $La_{0.4}Ca_{0.6}MnO_3$ using the POLARIS instrument (see Figure 7.8).

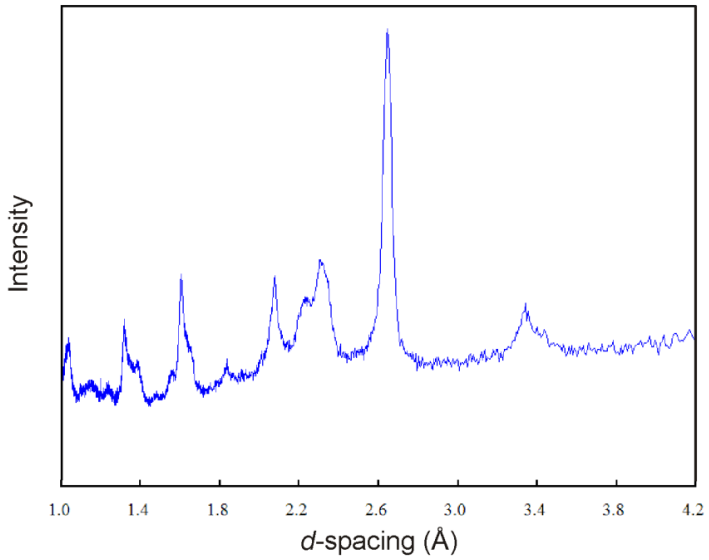


Figure 7.7: Neutron powder diffraction data collected from $La_{0.2}Ca_{0.8}MnO_{3-y}$ using the D2b instrument

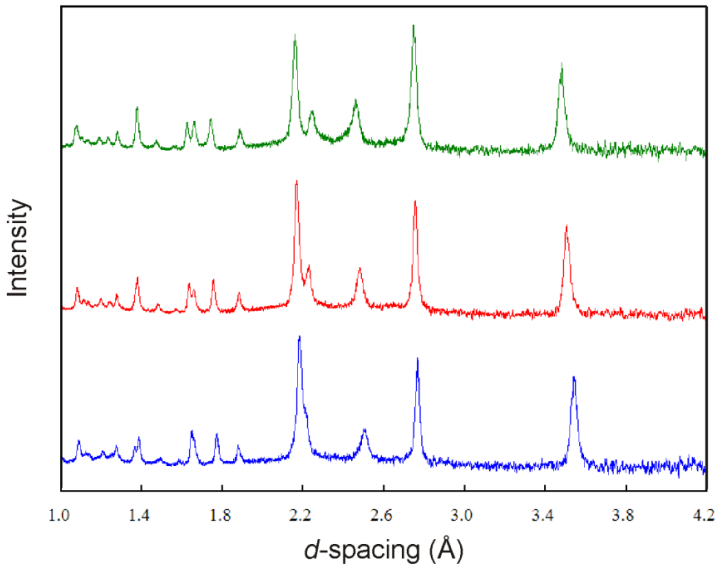


Figure 7.8: Neutron powder diffraction data collected from $La_{0.3}Ca_{0.67}MnO_{3-y}$ (top), $La_{0.33}Ca_{0.7}MnO_{3-y}$ (middle) and $La_{0.4}Ca_{0.6}MnO_{3-y}$ (bottom) using the 90° detector bank of the POLARIS instrument.

All the reflections in the neutron powder diffraction data sets collected from the $La_{1-x}Ca_xMnO_{3-y}$ ($0.6 \leq x \leq 0.8$) phases can be indexed with the unit cells shown in Table 7.1. Given the similarity in the data sets collected from $La_{0.2}Ca_{0.8}MnO_{3-y}$ and $La_{1-x}Ca_xMnO_{3-y}$ (x = 0.6, 0.67 and 0.7), it clear that all these reduced phases adopt closely related structures. However, the reflections in the data set collected from $La_{0.2}Ca_{0.8}MnO_{3-y}$ are very broad, consistent with poor crystallinity.

7.3.4. Structural Refinement (x = 0.6, 0.67 and 0.7)

Structural models based on the perovskite structure but with tetragonal unit cells (see Table 7.1) and *P*4/*mmm* symmetry were constructed and refined against neutron powder diffraction data collected from the $La_{1-x}Ca_xMnO_{3-y}$ (x = 0.6, 0.67 and 0.7) phases. The model which yielded the best fit to the data contained the same cationic arrangement as in the perovskite structure (i.e. La/Ca - (½,½,½), Mn – (0,0,0)) with an anion sublattice containing 3 distinct anion sites: O(1) – (0,0,½), O(2) - (½,½,0) and O(3) - (*x*, ½, 0). The model is shown in Figure 7.12 with the refined atomic parameters for the $La_{1-x}Ca_xMnO_{3-y}$ (x = 0.6, 0.67 and 0.7) phases shown in Table 7.2 - Table 7.4. The observed, calculated and difference plots for these refinements are shown in Figure 7.9 - Figure 7.11 below. The visual fit to the data is clearly poor - a fact consistent with added complexity with the structure.

Atom	***Wyckoff position***	***x***	***y***	***z***	U_{iso}	U_{11} = U_{22}	U_{33}	**Frac. Occ.**
La	1*d*	½	½	½		0.016(1)	0.112(1)	0.4
Ca	1*d*	½	½	½		0.016(1)	0.112(1)	0.6
Mn	1*a*	0	0	0		0.049(1)	0.025(1)	1
O(1)	1*b*	0	0	½		0.022(1)	0.015(1)	1
O(2)	1*c*	½	½	0	0.035(1)			0.541(4)
O(3)	4*n*	0.114(1)	½	0	0.022(1)			0.115(1)

Table 7.2: Structural parameters for refined structure of $La_{0.4}Ca_{0.6}MnO_2$

Atom	*Wyckoff position*	*x*	*y*	*z*	U_{iso}	U_{11} = U_{22}	U_{33}	Frac. Occ.
La	1*d*	½	½	½		0.010(1)	0.105(1)	0.33
Ca	1*d*	½	½	½		0.010(1)	0.105(1)	0.67
Mn	1*a*	0	0	0		0.055(1)	0.033(1)	1
O(1)	1*b*	0	0	½		0.018(1)	0.020(1)	1
O(2)	1*c*	½	½	0	0.032(1)			0.572(3)
O(3)	4*n*	0.107(1)	½	0	0.019(1)			0.118(1)

Table 7.3: Structural parameters for refined structure of $La_{0.33}Ca_{0.67}MnO_2$

Atom	*Wyckoff position*	*x*	*y*	*z*	U_{iso}	U_{11} = U_{22}	U_{33}	Frac. Occ.
La	1*d*	½	½	½		0.051(4)	0.119(1)	0.3
Ca	1*d*	½	½	½		0.051(4)	0.119(1)	0.7
Mn	1*a*	0	0	0		0.055(1)	0.025(1)	1
O(1)	1*b*	0	0	½		0.014(1)	0.012(1)	1
O(2)	1*c*	½	½	0	0.030(1)			0.662(4)
O(3)	4*n*	0.123(1)	½		0.031(2)			0.085(1)

Table 7.4: Structural parameters for refined structure of $La_{0.3}Ca_{0.7}MnO_2$

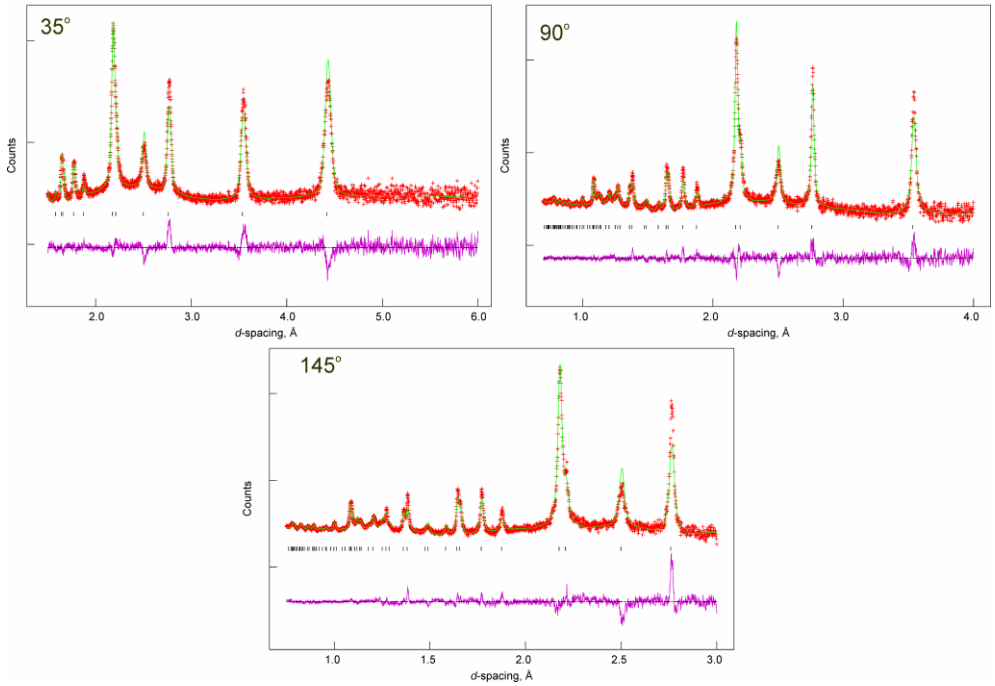


Figure 7.9: Observed, calculated and difference plots for refinement against neutron powder diffraction data collected from $La_{0.4}Ca_{0.6}MnO_2$ using the POLARIS instrument. χ^2 = 1.453, *wRp* = 3.53 %, *Rp* = 6.30 %

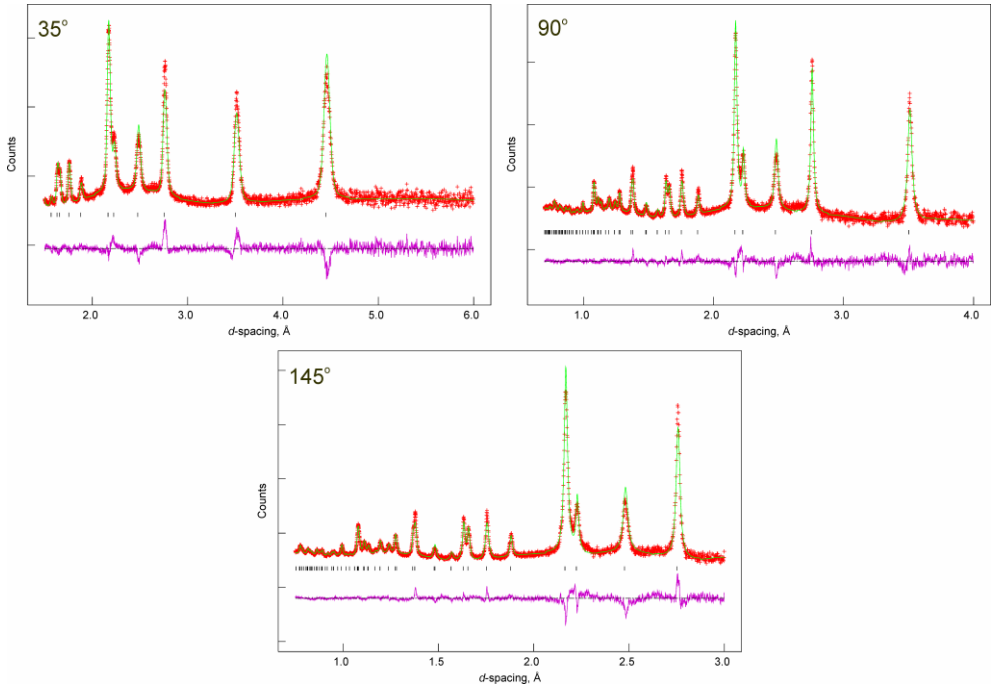


Figure 7.10: Observed, calculated and difference plots for refinement against neutron powder diffraction data collected from $La_{0.33}Ca_{0.67}MnO_2$ using the POLARIS instrument. χ^2 = 1.866, *wRp* = 3.38 %, *Rp* = 5.76 %

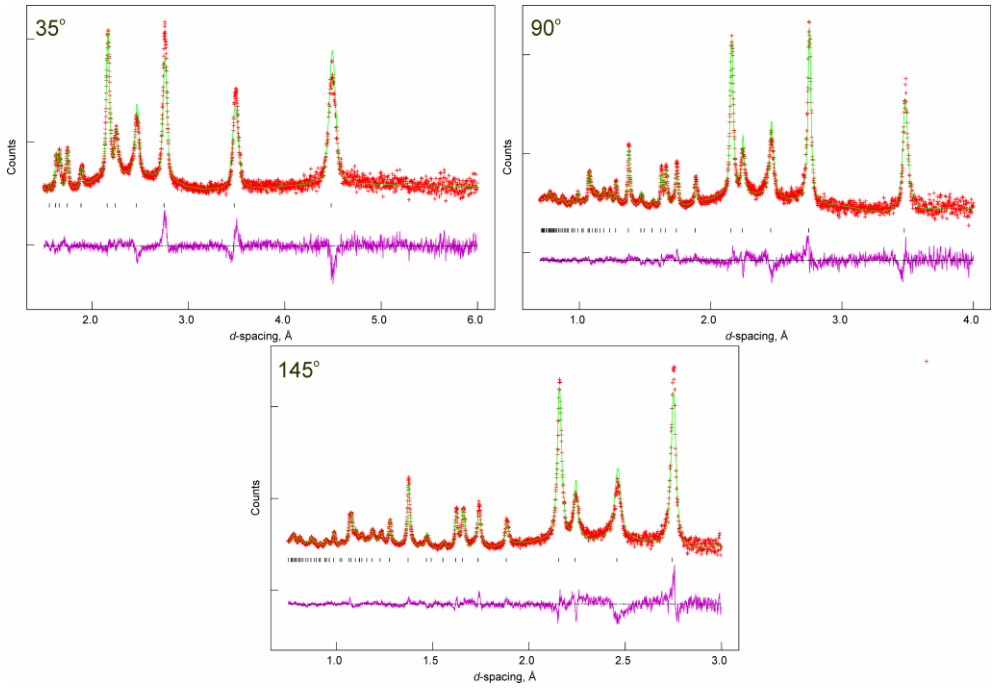


Figure 7.11: Observed, calculated and difference plots for refinement against neutron powder diffraction data collected from $La_{0.3}Ca_{0.7}MnO_2$ using the POLARIS instrument. χ^2 = 1.677, *wRp* = 3.27 %, *Rp* = 5.76 %

Determination of the exact anion content of the reduced phases is not possible from refinement against neutron diffraction data due to the strong correlations between thermal displacement factors and fractional occupancies. However, some insight into the anion

content can be gained by consideration of the local coordination environments of the manganese polyhedra. Given the anion positions in the unit cell, the most chemically reasonable model for the reduced phases contains a disordered array of edge-sharing MnO_6 octahedra and chains of vertex-sharing MnO_4 tetrahedra, leading to an empirical composition of $La_{1-x}Ca_xMnO_2$.

Anion-deficient ABO_{3-y} perovskite phases tend to form layered structures with each layer containing just one type of BO_n polyhedron.[10] Therefore it was hypothesised that the structures of the $La_{1-x}Ca_xMnO_{3-y}$ reduced phases contain a disordered arrangement of layers of edge-sharing MnO_6 octahedra like slices of the rock salt structure and, in an analogous fashion the brownmillerite and '6-layer manganate' phases, layers that consist of chains of tetrahedra running parallel to the $[101]_p$ direction (see Figure 7.12).

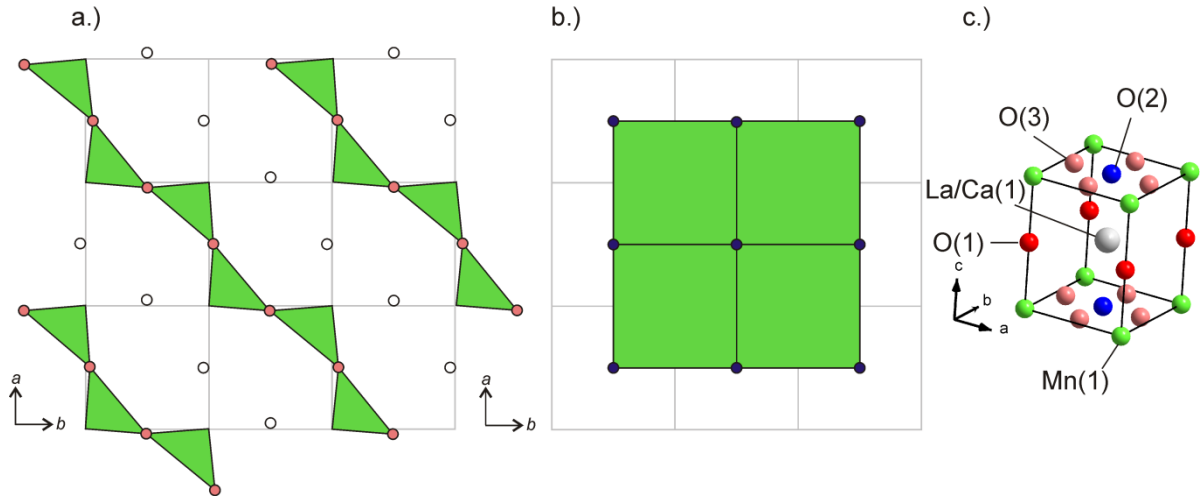


Figure 7.12: Proposed unit cell structure of $La_{1-x}Ca_xMnO_2$ phases (c.)) containing edge sharing octahedra (b.)) and chains of tetrahedra (a.)). N.B. The O(3) sites are only 50 % occupied with the other 50 % (marked with blank circles in a.)) vacant to allow for the formation of tetrahedra.

Figure 7.13 shows a possible model for a single layer of tetrahedra within the proposed structures of the $La_{1-x}Ca_xMnO_{3-y}$ reduced phases. As shown in Table 7.5, the separation between the oxide ions within the basal plane of the tetrahedra is very small considering the ionic radius of an oxide ion (1.4 Å).[86] However, at this juncture it should be noted that, given the disorder in the structure, the local structure, including oxygen-oxygen separations,

may differ from the average structure determined by Rietveld refinement against bulk diffraction data.

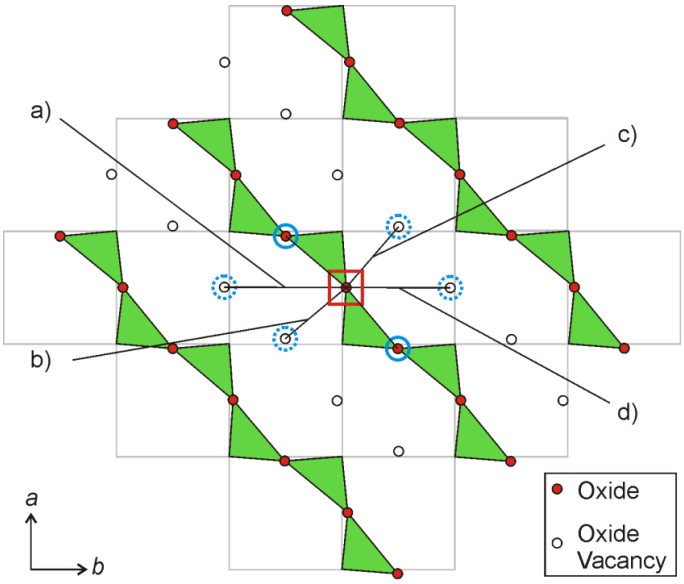


Figure 7.13: Cartoon showing tetrahedral chains in structure of $La_{1-x}Ca_xMnO_{3-y}$ phases. Positions of oxide vacancies are also indicated. The grey boxes indicate the unit cell of the disordered structure. The oxide-oxide and oxide-oxide vacancy lengths for the oxide boxed in red are shown in Table 7.5

Phase	Contact	Length to oxide vacancy		
		a)	b) = c)	d)
$La_{0.4}Ca_{0.6}MnO_2$	2 x 2.568(4) Å	4.353(6) Å	2.568(4) Å	2.725(6) Å
$La_{0.33}Ca_{0.67}MnO_2$	2 x 2.594(3) Å	4.339(5) Å	2.549(3) Å	2.674(5) Å
$La_{0.3}Ca_{0.7}MnO_2$	2 x 2.533(6) Å	4.335(9) Å	2.533(6) Å	2.622(9) Å

Table 7.5: The refined oxide-oxide and oxide-oxide vacancy lengths for the oxide ion boxed in red in Figure 7.13

Increasing the anion content above $La_{1-x}Ca_xMnO_2$ would result in filling some of the oxide vacancies in the manganese-containing layer. As shown in Table 7.5, this would result in a greater number of close oxygen-oxygen contacts (especially contact d)) which would destabilise the structure. Given this consideration, it is very hard to envisage a stable structure in which the anion content of the manganese-containing layer is above MnO, i.e. an anion content above that in $La_{1-x}Ca_xMnO_2$. It is clear that empirical compositions of $La_{1-x}Ca_xMnO_2$ require the presence of some Mn(I) centres in the La^{3+}-containing reduced phases. Further data are clearly therefore required to substantiate this proposed empirical composition.

7.3.5. Iodometric titrimitry

In order to confirm the stoichiometries of the $La_{1-x}Ca_xMnO_{3-y}$ ($x \geq 0.6$) reduced phases, iodometric titrations were performed using the method described in section 2.9. The results of these titrations are consistent with average manganese oxidation states of Mn(II) or below across the entire $La_{1-x}Ca_xMnO_{3-y}$ ($x \geq 0.6$) compositional range.

7.3.6. Thermogravimetric analysis

Thermogravimetric data collected during the reoxidation of the washed products of the reaction between $La_{1-x}Ca_xMnO_3$ ($x \geq 0.6$) substrate phases and NaH are shown in Figure 7.26, with the most pertinent results shown in Table 7.6.

$La_{1-x}Ca_xMnO_{3-y}$	Mass gain (%)	Empirical stoichiometry
0.6	6.71(4)	$La_{0.4}Ca_{0.6}MnO_{2.28(4)}$
0.67	7.35(3)	$La_{0.33}Ca_{0.67}MnO_{2.25(3)}$
0.7	7.63(3)	$La_{0.3}Ca_{0.7}MnO_{2.24(3)}$
0.8	8.29(3)	$La_{0.2}Ca_{0.8}MnO_{2.22(3)}$
0.9	8.80(3)	$La_{0.1}Ca_{0.9}MnO_{2.23(3)}$
1	8.38(3)	$CaMnO_{2.30(3)}$

Table 7.6: Relevant data from thermogravimetric analysis of washed products of the reaction between $La_{1-x}Ca_xMnO_3$ ($x \geq 0.6$) substrate phases and NaH

The empirical stoichiometries of the refined disordered rock salt structural models for $(La_{0.1}Ca_{0.9})_{0.5}Mn_{0.5}O$ and $Ca_{0.5}Mn_{0.5}O$ are inconsistent with those extracted from reoxidative thermogravimetric data. Given the high quality of the fit to the diffraction data collected from $(La_{0.1}Ca_{0.9})_{0.5}Mn_{0.5}O$ and $Ca_{0.5}Mn_{0.5}O$ (see Figure 7.4 and Figure 7.5), analysis of thermogravimetric data clearly leads to inaccurate values for the oxygen contents of these reduced phases, possibly due to auto-oxidation of the reduced phases on exposure to air or incomplete reoxidation to the perovskite starting materials. In addition, the reoxidation process of the disordered rock salt reduced phases to the corresponding perovskite starting material is clearly not a topotactic process as significant rearrangement of both the cation and anion sublattices is required. The non-topotactic nature of the reoxidation process may lead to errors in the determination of the empirical compositions from thermogravimetric data.

In conclusion, it is clear that in this instance thermogravimetric reoxidation data do not yield an accurate determination of the anion content of the $(La_{1-x}Ca_x)_{0.5}Mn_{0.5}O$ (x = 0.9 and 1) phases. Therefore, given the discrepancy in the empirical compositions extracted from thermogravimetric data and Rietveld refinement against diffraction data, further evidence is required to confirm the anion contents of the $La_{1-x}Ca_xMnO_2$ ($0.6 \leq x \leq 0.8$) phases.

7.3.7. XANES spectroscopy

7.3.7.1. Experimental

As discussed in section 2.10, the energies of the absorption edges in X-ray absorption spectra are sensitive to the oxidation state of the absorbing atom; lower energy photons are required to eject electrons from lower oxidation states. Therefore XANES spectra were collected from the Mn K-edge of $La_{1-x}Ca_xMnO_2$ ($0.6 \leq x \leq 0.8$) and $(La_{1-x}Ca_x)_{0.5}Mn_{0.5}O$ (x = 0.9 and 1) phases to provide evidence for the manganese oxidation state.

Due to the air- and moisture-sensitive nature of the reduced phases, samples suitable for characterisation by XANES spectroscopy were prepared under an inert atmosphere. In an argon-filled glovebox, 5 mg samples of each reduced phase were ground together with 100 mg of cellulose (dried at 120 ^{o}C to prevent the introduction of water into the sample) with an agate pestle and mortar. The purpose of the cellulose was to act as an inert matrix which allows robust pellets to be pressed - cellulose was chosen due to its low X-ray absorption. Then, the pellet die was loaded inside a glovebox and sealed inside two tied plastic bags, thus keeping the sample under an argon atmosphere. After the pellets had been pressed outside of the glovebox, the press was returned to the glovebox and the sample removed. Data were collected at the manganese K-edge (i.e. ionisation from the 1*s* orbital) from each sample using the B18 instrument at the Diamond facility. The measurements and data handling were performed by Dr Silvia Ramos.

7.3.7.2. Results

Figure 7.14 a) shows the Mn K-edge X-ray absorption spectra collected from the $La_{1-x}Ca_xMnO_2$ and $(La_{1-x}Ca_x)_{0.5}Mn_{0.5}O$ phases. Figure 7.14 b) and c) show the XANES region of the absorption spectra. Figure 7.14 d) shows the first derivative of the absorption spectra over the same energy range as Figure 7.14 c) to highlight the trend in the Mn K-edge absorption energies with increasing La^{3+}-content.

$Ca_{0.5}Mn_{0.5}O$ unequivocally contains Mn(II) cations and can therefore be used as a standard to compare spectra collected from the other $La_{1-x}Ca_xMnO_2$ and $(La_{1-x}Ca_x)_{0.5}Mn_{0.5}O$ phases. The Mn K-edge absorption spectrum collected from the Mn(II) $Ca_{0.5}Mn_{0.5}O$ phase is shown in Figure 7.14 with a cyan line.

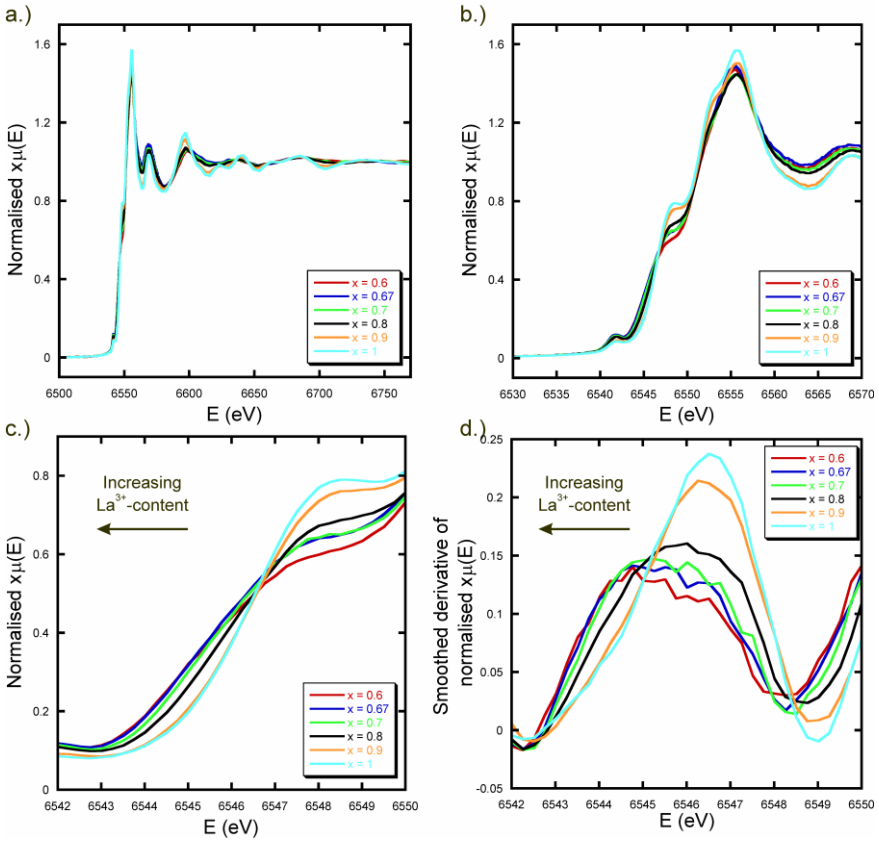


Figure 7.14: Mn K-edge absorption spectra collected from $La_{1-x}Ca_xMnO_2$ ($0.6 \leq x \leq 0.8$) and $(La_{1-x}Ca_x)_{0.5}Mn_{0.5}O$ (x = 0.9 and 1) reduced phases; a.) Full spectra; b) XANES spectra; c.) Section of data collected between 6542 eV and 6550 eV to highlight trend with increasing Ca^{2+}-content; d.) 1st derivative of XANES spectra between 6542 eV and 6550 eV.

As shown most clearly in Figure 7.14 c.), the energy of the Mn K-edge of the $La_{1-x}Ca_xMnO_2$ phases decreases with increasing La^{3+}-content, indicating a decrease in the average manganese oxidation states below +2. This trend is highlighted by inspecting the first derivative of the XANES spectra (see Figure 7.14 d.)). The data therefore provide clear evidence for average manganese oxidation states consistent with empirical compositions of $La_{1-x}Ca_xMnO_2$ ($0.6 \leq x \leq 0.8$) and $(La_{0.1}Ca_{0.9})_{0.5}Mn_{0.5}O$. These findings are in agreement with the predictions made regarding the most anion-rich stable structures for the $La_{1-x}Ca_xMnO_{3-y}$ phases (see section 7.3.4).

7.3.8. Local structure determination

7.3.8.1. Introduction

The models for the average structures of the $La_{1-x}Ca_xMnO_2$ (x = 0.6, 0.67 and 0.7) phases (see Figure 7.12) contain no long range order in the arrangement of the MnO_4 and MnO_6 polyhedra. However, the local structures of these materials are proposed to contain layers of edge-sharing octahedra and layers of vertex-sharing tetrahedra. To test this hypothesis, a more 'local probe', such as the Pair Distribution Function (PDF), is required to give information on the local structures of these materials.

7.3.8.2. Pair Distribution Function

Neutron powder diffraction data collected from samples of the $La_{1-x}Ca_xMnO_2$ (x = 0.6, 0.67 and 0.7) phases using the POLARIS instrument (see section 2.3.2.2) over the range of scattering vectors of magnitude $1.5\ Å^{-1} \leq Q \leq 40\ Å^{-1}$ were corrected to take into account the effects of background scattering, absorption and beam intensity variations.[87] These corrected data were then converted into PDFs (see the left hand pane of Figure 7.16).

As discussed in section 2.5, Reverse Monte-Carlo (RMC) simulations, guided by fits to experimental data, can be used to generate atomic configurations that are more accurate representations of the local structures of materials. In this investigation, RMC simulations

were performed guided simultaneously by the fit to the corresponding PDF and Bragg diffraction data collected using the "90 ^{o} detector bank" of the POLARIS instrument.

7.3.8.3. Reverse Monte Carlo Simulation

Starting atomic configurations for the RMC process were produced from 20 x 20 x 26 supercells of the crystallographic unit cells previously determined by Rietveld refinement against neutron diffraction data (see Table 7.1). These supercells each contain 41600 atoms. The supercell contained a 26-fold expansion along the *c*-direction to allow the starting configurations to contain an integer number of octahedral and tetrahedral layers while keeping the ratios of octahedral:tetrahedral layers as close as possible to those in the structures refined using the Rietveld method ($La_{0.4}Ca_{0.6}MnO_2$ = 14:12; $La_{0.33}Ca_{0.67}MnO_2$ = 15:11; $La_{0.3}Ca_{0.7}MnO_2$ = 17:9).

As discussed in section 1.3, the tetrahedral chains in the brownmillerite and '6-layer manganate' structures run parallel to the $[101]_p$ direction. Given the tetragonal nature of the unit cells observed for the $La_{1-x}Ca_xMnO_2$ (x = 0.6, 0.67 and 0.7) phases, the chains of tetrahedra can propagate parallel to either of the crystallographically equivalent [1 0] or [110] directions. In addition, as described in section 1.4, the chains of tetrahedra can twist in 2 different senses (L and R). This leads to the possibility of 4 types of tetrahedral chain as shown in Figure 7.15.

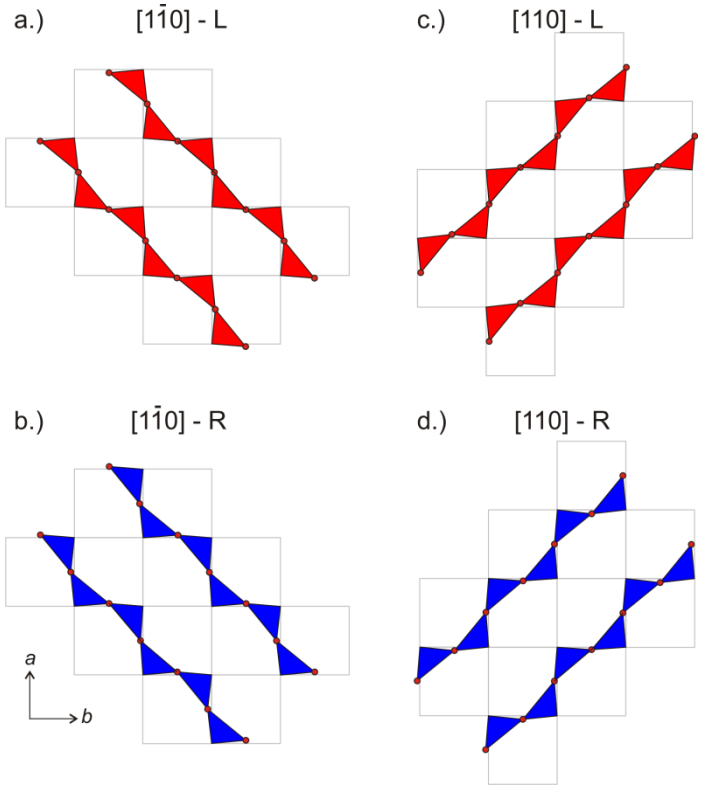


Figure 7.15: The 4 orientations of tetrahedral chains in the starting ensemble for the RMC calculations. There are 2 different propagation directions for the chains ([10] or [101]) and 2 different twist directions of the tetrahedral chains (L or R – see Chapter 1). The grey boxes indicate the unit cell of the disordered structure.

In the starting ensemble, each tetrahedral layer contained just one type of tetrahedral chain, thereby creating 4 types of tetrahedral layer. The 4 different types of tetrahedral layers and the octahedral layers were then randomly distributed within the starting ensemble. To model the disordered arrangement of the lanthanum and calcium cations, 'hybrid' A-cation sites were used in the ensemble with neutron scattering lengths equal to the weighted average of the A-cations in the empirical composition.[30]

Two key constraints were added to the simulations to maintain chemically reasonable atomic configurations throughout the refinement process: Firstly the closest approaches between atoms were constrained to be above a minimum value, with the value depending on the identity of the atoms (see Table 7.7). Secondly, the Mn-O bond length was constrained to be within limits of 1.7 Å and 3.0 Å. This allowed the connectivity of the Mn/O framework to be conserved throughout the RMC process. The values for the closest approach of atoms and

the limiting values for the lengths of the Mn-O bonds were determined either directly from the PDF of by analysis of the evolution of partial PDFs during the refinement, with the caveat that the values were chemically sensible.

Atom Pair	Closest Approach (Å)
La/Ca-La/Ca	2.5
La/Ca-Mn	2.5
La/Ca-O	2.16
Mn-Mn	2.5
Mn-O	1.7
O-O	2.0

Table 7.7: Closest approach of atoms in RMC simulations

For each composition, 5 completely separate configurations were generated each with their own random distribution of MnO_n polyhedra layers (within the constraints detailed above). Then 2 separate RMC simulations were performed using each configuration for each composition, leading to an improvement in the reliability of the final atomic configurations. The refinement processes were allowed to continue until no further improvements in the fits to the data were observed.

7.3.8.4. Results

As shown in Figure 7.16, the final atomic configurations generated by the RMC simulations yielded good fits for each composition to the experimental differential correlation functions ($D(r)$ - an alternative representation to $G(r)$, see section 2.5.2). These final atomic configurations also yielded satisfactory fits to the corresponding neutron diffraction data set, with better fits most likely prevented by incomplete description of the peak shapes in the diffraction data. There are only minor differences between the atomic configurations generated in each of the 10 RMC simulations for each composition, suggesting that the overall result is largely independent of the starting configuration.

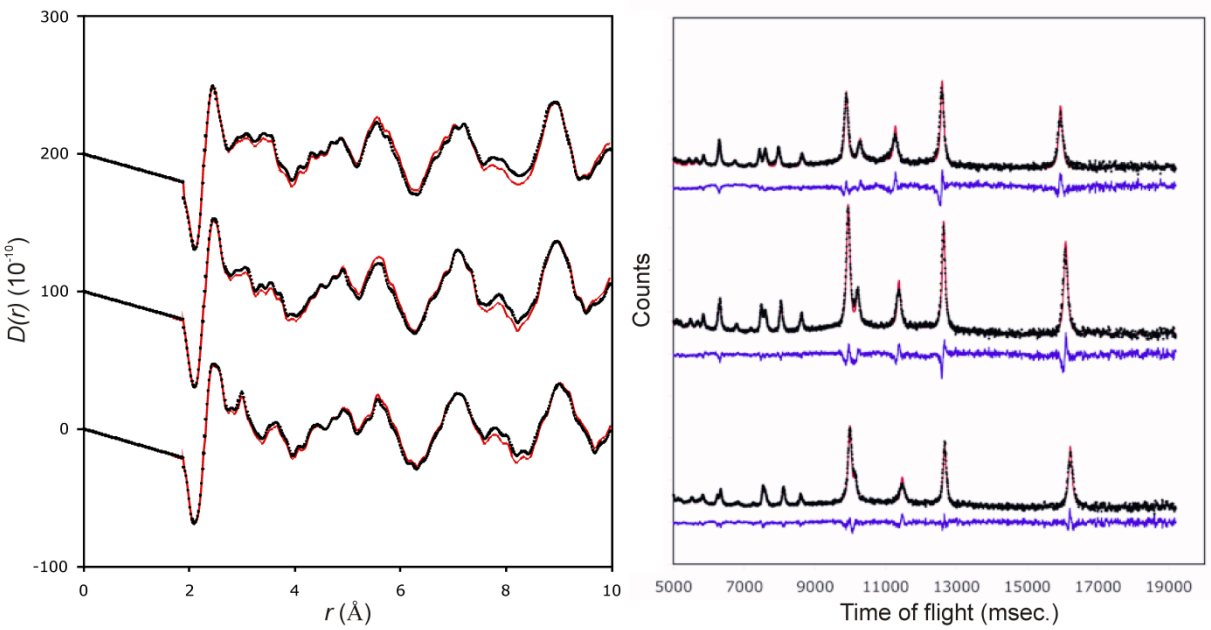


Figure 7.16: Left - RMC fits (red) to the pair distribution functions (black - left) and diffraction data (black - right) collected from $La_{0.3}Ca_{0.7}MnO_2$ (top), $La_{0.33}Ca_{0.67}MnO_2$ (middle) and $La_{0.4}Ca_{0.6}MnO_2$ (bottom) collected using the POLARIS instrument.

As a final check of the quality of the RMC models, inspection of slices though the MnO layers (see Figure 7.17) reveals that the refinement has proceeded without the inclusion of any anomalous regions of 'damage' to produce atomic configurations with chemically reasonable atomic separations. As shown in Figure 7.17, the overall topologies of the MnO layers are similar to those in the starting atomic configuration, suggesting that segregation into the 2 types of polyhedral layer is a real feature of the structures. More specifically, the tetrahedral layers (top panes in Figure 7.17) mostly comprise of regular tetrahedral chains, however, there is a certain degree of cross linking between the chains in the final atomic configuration. In addition, the edge-sharing octahedral framework (bottom panes in Figure 7.17) is generally maintained. However, it is clear that the shared oxide ions within the basal plane of the edge-sharing MnO_6 octahedra have relaxed away from their 'ideal' starting positions.

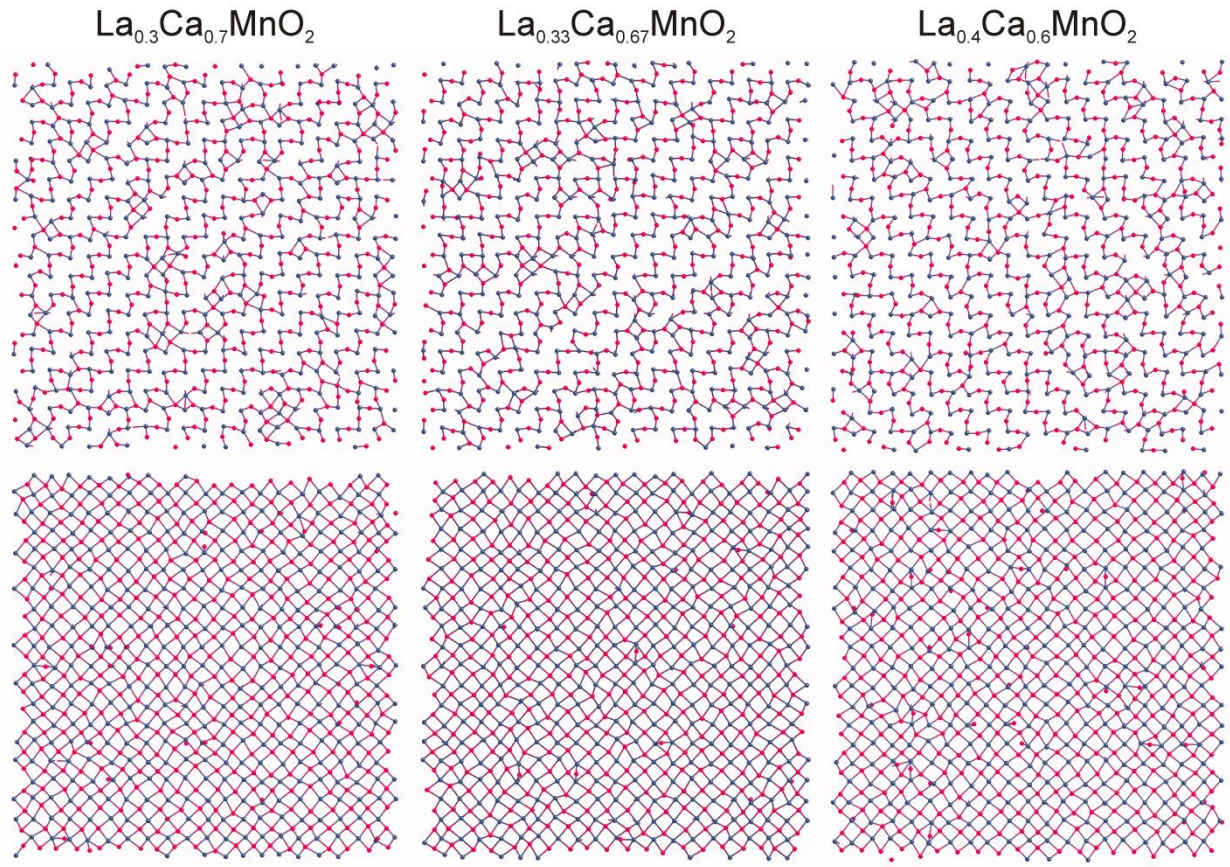


Figure 7.17: Slices through the MnO layers of the tetrahedral (top) and edge-sharing octahedral (bottom) layers in the final atomic configurations for the $La_{1-x}Ca_xMnO_2$ ($0.6 \leq x \leq 0.7$). The blue and red spheres represent the manganese and oxide ions respectively.

By inspection of Figure 7.17, it is clear that the distortion in the octahedral layers away from the 'ideal' geometry in the starting atomic configuration decreases, while that in the tetrahedral layers increases with increasing Ca^{2+}-content. This observation is consistent with the fact that the most Ca^{2+}-rich $La_{1-x}Ca_xMnO_2$ phases adopt the rock salt structure with 'undistorted' edge-sharing MnO_6 octahedra.

The final atomic configuration from the RMC simulation for $La_{0.4}Ca_{0.6}MnO_2$ 'collapsed' into the simple disordered crystallographic unit cell is shown in Figure 7.18. In addition, Figure 7.18 shows a description of this 'collapsed' structure using displacement ellipsoids. Reassuringly, the 'collapsed' structure is very similar to the average structure extracted from Rietveld refinement against bulk diffraction data (see Figure 7.12); however, a much more accurate representation of the local structure has clearly been produced.

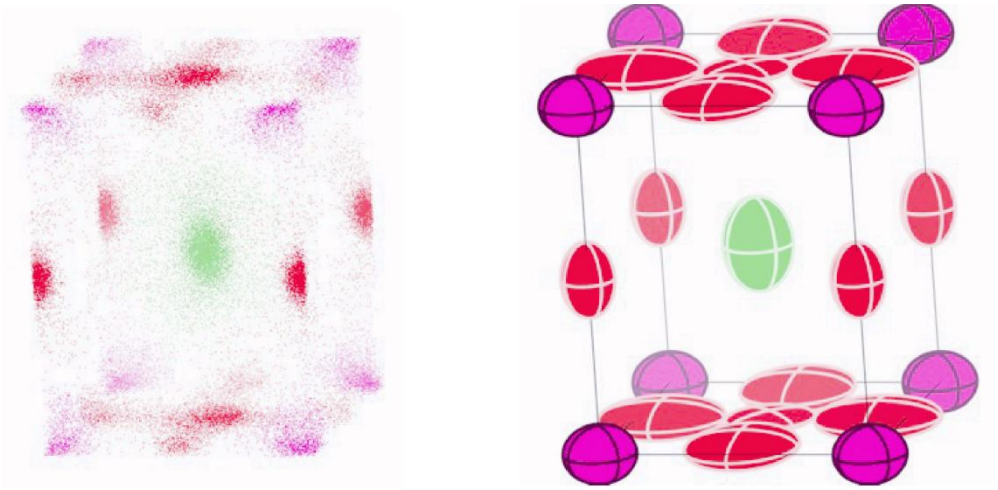


Figure 7.18: Left - 'Collapsed' structure from RMC simulation for $La_{0.4}Ca_{0.6}MnO_2$. Right – Description of 'collapsed' structure using displacement ellipsoids.

7.3.8.5. Bond Lengths

The "bond lengths" calculated from average-structure determinations (e.g. Rietveld refinement against diffraction data) only represent the separations between average atomic positions, defined as <A>-<B>.[88] In contrast, RMC refinement against total scattering data allows a much more accurate description of the true average bond lengths, defined as <A-B>. Both <A>-<B> and <A-B> lengths between selected atom pairs in structures of the $La_{1-x}Ca_xMnO_2$ ($0.6 \leq x \leq 0.7$) phases are shown in Table 7.8.

x	Length	Tetrahedral (Å)			Octahedral (Å)	
		Mn-O(3) (eq.)	Mn-O(1) (ax.)	O(3)-O(3)	Mn-O(1) (ax.)	Mn-O(2) (eq.)
0.6	<A>-<B>	1.816(1)	2.212(1)	2.568(4)	2.212(1)	2.502(1)
	<A-B>	2.115(3)	2.401(7)	2.807(6)	2.214(2)	2.554(2)
0.67	<A>-<B>	1.802(1)	2.227(1)	2.594(3)	2.227(1)	2.480(1)
	<A-B>	2.083(3)	2.390(5)	2.739(7)	2.220(2)	2.525(2)
0.7	<A>-<B>	1.791(1)	2.243(1)	2.533(6)	2.243(1)	2.459(1)
	<A-B>	2.076(3)	2.433(6)	2.760(9)	2.250(3)	2.510(2)

Table 7.8: Selected distances in the local and average structures of $La_{1-x}Ca_xMnO_2$

It should be emphasised that, given the low *Q*-range and lack of suitable background correction, the POLARIS instrument is not optimised for the collection of data suitable for measurement of the PDF. Therefore, it is important not to "over-analyse" the <A-B> lengths in the final atomic configurations generated by the RMC process. However, several key features are apparent from analysis of the <A>-<B> and<A-B> lengths: Firstly, the

description of the edge-sharing MnO_6 octahedra in the average structure is a good approximation to that in the local structure. In contrast, there is a much larger difference in the local and average structure description of the MnO_4 tetrahedra. Indeed, the tetrahedra are much more 'relaxed' in the local structure with the <O(3)-O(3)> separation in particular much larger, and more chemically reasonable, than the unrealistically close <O(3)>-<O(3)> separation in the average structure. Finally, the axial <Mn-O(1)> bonds are longer in the MnO_4 tetrahedra than in the MnO_6 octahedra. Therefore, given that the both polyhedra contain the same Mn and O(1) sites in the average structure, it is unsurprising that the displacement ellipsoids for these atoms in the refined structure are so large (see Table 7.2 - Table 7.4).

7.3.9. Structure of $La_{0.2}Ca_{0.8}MnO_2$

Given the similarity in the bulk diffraction data collected from $La_{0.2}Ca_{0.8}MnO_2$ and $La_{1-x}Ca_xMnO_2$ (x = 0.6, 0.67 and 0.7) phases, it is highly likely that all these phases adopt similar structures. Therefore, a structural model based the structures of the $La_{1-x}Ca_xMnO_2$ (x = 0.6, 0.67 and 0.7) phases was constructed and refined against neutron powder diffraction data collected from $La_{0.2}Ca_{0.8}MnO_2$. However, as shown in Figure 7.19, the fit to the data is poor, thereby preventing the extraction of reliable structural parameters.

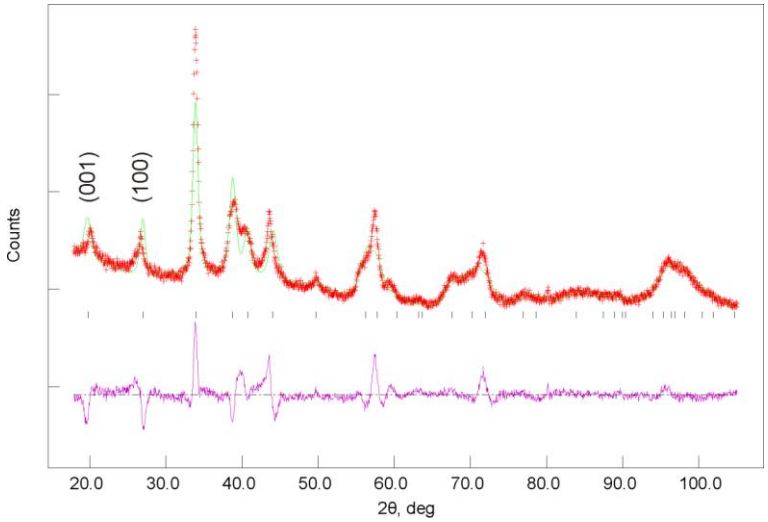


Figure 7.19: Observed, calculated and difference plots for the refinement of a structural model of $La_{0.2}Ca_{0.8}MnO_2$ against neutron powder diffraction data.

There is a change in the structures adopted by the reduced phases formed upon reduction of the $La_{1-x}Ca_xMnO_3$ ($0.6 \leq x \leq 1$) phases. The more La^{3+}-rich phases adopt structures with a disordered arrangement of layers of edge-sharing octahedra and layers of vertex-sharing tetrahedra, while the x = 0.9 and x = 1 members adopt the disordered rock salt structure.

As shown in Figure 7.20, the reflections from the (110) and (002) planes in the X-ray powder diffraction data collected from the $La_{1-x}Ca_xMnO_2$ phases converge with increasing calcium content and coalesce to 'form' the (200) reflection in the data set collected from the disordered rock salt x = 0.1 member. Thus, given the close structural similarity between the 2 structure types, it is likely that $La_{0.2}Ca_{0.8}MnO_2$ is close to the phase boundary between the 2 structure types and represents a 'hybrid' between the two structure types. It is therefore unsurprising that the structure of $La_{0.2}Ca_{0.8}MnO_2$ is so poorly crystalline.

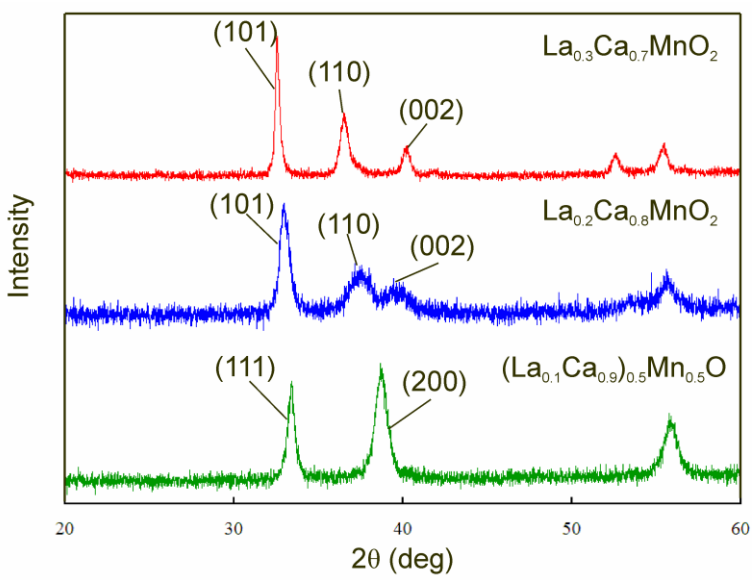


Figure 7.20: X-ray powder diffraction data collected from $La_{1-x}Ca_xMnO_2$ (x = 0.7 and 0.8) and $(La_{0.1}Ca_{0.9})_{0.5}Mn_{0.5}O$ with the (*hkl*) values for the most intense reflections marked.

7.4. Discussion

The topotactic reduction reactions of phases in the compositional range $La_{1-x}Ca_xMnO_3$ ($0.6 \leq x \leq 1$) using NaH as a solid state reducing agent result in the formation of reduced phases with structures which depend on the La:Ca ratio. Reactions of $La_{0.1}Ca_{0.9}MnO_3$ and $CaMnO_3$ with NaH result in the formation of phases which adopt the rock salt structure. However, reduction reactions of phases in the range $La_{1-x}Ca_xMnO_3$ ($0.6 \leq x \leq 0.8$) result in the formation of reduced phases with an empirical composition of $La_{1-x}Ca_xMnO_2$ which adopt structures containing layers of edge-sharing octahedra and layers of vertex-sharing tetrahedra.

The disordered rock salt structures of $(La_{0.1}Ca_{0.9})_{0.5}Mn_{0.5}O$ and $Ca_{0.5}Mn_{0.5}O$ contain a single cation site which accommodates manganese, calcium and, in the former phase, lanthanum cations. The stability of $(La_{0.1}Ca_{0.9})_{0.5}Mn_{0.5}O$ and $Ca_{0.5}Mn_{0.5}O$ in this structure type is attributable to the good match in the bonding requirements of the calcium and manganese cations - clearly demonstrated by the fact that CaO and MnO form a fully miscible solid solution ($Ca_{1-x}Mn_xO$ ($0 \leq x \leq 1$)).[89] However, as the La^{3+}-content increases, the $La_{1-x}Ca_xMnO_2$ phases adopt structures with distinct A- and B-cation sites. The La^{3+}-rich phases are prevented from adopting the disordered rock salt structure by the aversion to

forming single crystallographic sites housing a mixture of lanthanum, calcium and manganese cations.

A fruitful comparison can be made to Ba_2LaTaO_6 which adopts the 'double perovskite' structure. The structure of Ba_2LaTaO_6 is a relatively rare example of a structure containing lanthanum cations on the B-site in a cubic perovskite phase (see Figure 7.21).[90]

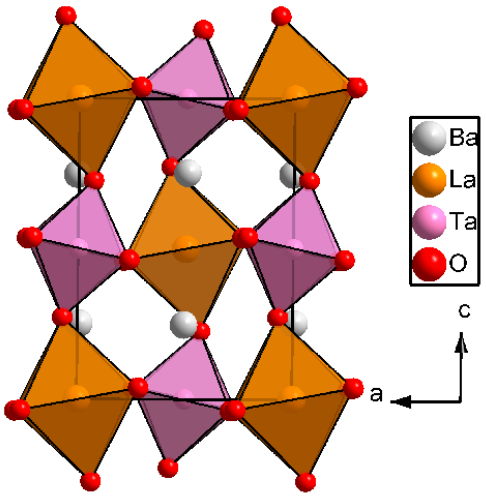


Figure 7.21: Structure of Ba_2LaTaO_6

The 'double perovskite' structure is, by definition, an ordered structure in which the lanthanum and tantalum cations are still housed on distinct crystallographic sites with different coordination environments (<La-O> = 2.378 Å and <Ta-O> = 2.001 Å). It is clear that the discrepancy in the bonding requirements of the lanthanum and transition metal cations, based on the size and charge differences between the cations, prevents the formation of shared crystallographic sites in the structures of both Ba_2LaTaO_6 and the La^{3+}-rich $La_{1-x}Ca_xMnO_2$ phases.

7.4.1. Comparison to infinite-layer structure

Working on the premise that the cation framework of the $La_{1-x}Ca_xMnO_3$ perovskite substrate phases is conserved during the topotactic reduction reactions, the ABO_2 empirical compositions of the $La_{1-x}Ca_xMnO_2$ phases severely limit which structures the reduced phases can adopt. To the best of the author's knowledge, the only ABO_2 structure-type containing

the same cationic arrangement as in cubic perovskite phases is the infinite-layer structure which contains sheets of vertex-linked BO_4 square planar centres (see Figure 7.22 b.)). As an example, the topotactic reduction reaction of the $LaNiO_3$ perovskite phases using NaH results in the formation of $LaNiO_2$ which adopts an infinite-layer structure.[26]

Given their empirical compositions, it is initially surprising that $La_{1-x}Ca_xMnO_2$ ($0.6 \leq x \leq 0.8$) phases do not adopt the infinite-layer structure with square planar manganese centres. Indeed, there are a small number of reported examples of structures containing such square planar manganese centres, e.g. Ce_2MnN_3 [91] and $Sr_2MnO_2Cu_{1.5}S_2$ [92] (see Figure 7.22).

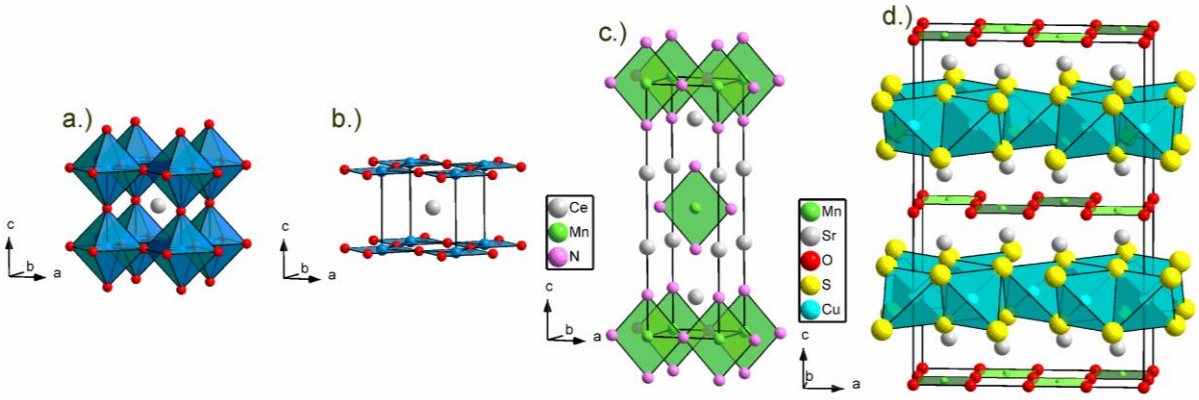


Figure 7.22: a.) Cubic perovskite structure; b.) Infinite-layer structure; c.) Structure of Ce_2MnN_3; d) Structure of $Sr_2MnO_2Cu_{1.5}S_2$

However, the majority of the MnO_4 square planar units in the hypothetical infinite-layer $La_{1-x}Ca_xMnO_2$ phases would contain high-spin d^5 Mn(II) centres which would be afforded no obvious electronic stabilisation on LFSE grounds. Therefore the $La_{1-x}Ca_xMnO_2$ phases, essentially for want of another structure type, adopt the observed disordered structures containing tetrahedra and edge-sharing octahedra.

7.4.2. '$Sr_{0.5}Mn_{0.5}O$'

Chapter 5 of this investigation details the topotactic reduction reaction of $SrMnO_3$ using NaH as a reducing agent which results in the formation of $SrMnO_{2.25}$. The analogous reaction of $CaMnO_3$ results in the formation of $Ca_{0.5}Mn_{0.5}O$, with a much lower anion content than $SrMnO_{2.25}$. Therefore, it is pertinent to ask: why does the topotactic reduction of $SrMnO_3$

using NaH as a reducing agent not result in the formation of the hypothetical disordered rock salt phase '$Sr_{0.5}Mn_{0.5}O$'?

The structure of '$Sr_{0.5}Mn_{0.5}O$' would require the strontium and manganese cations to share the same crystallographic site. The greater average radius of the strontium cations ($r(Sr^{2+})$ = 1.18 Å)[86] compared to that of the manganese cations ($r(Mn^{2+})$ = 0.83 Å)[86] prevents the formation of a disordered arrangement of strontium and manganese cations. Further confirmation of this size mismatch can be seen in the calculated bond valences for the cations in the hypothetical '$Sr_{0.5}Mn_{0.5}O$' rock salt phase.

By considering the ratio of the volume per manganese cation in the structures of the $CaMnO_3$ and $SrMnO_3$ perovskite substrate phases ($V_{Mn(CaMnO_3)}/V_{Mn(SrMnO_3)}$ = 51.888 $Å^3$/55.050 $Å^3$ = 0.943)[58, 81] and the cubic lattice parameter of the structure of $Ca_{0.5}Mn_{0.5}O$ (a = 4.637 Å), the cubic lattice parameter for the hypothetical disordered rock salt '$Sr_{0.5}Mn_{0.5}O$' phase can be estimated as a = 4.920 Å. A structural model for the hypothetical rock salt '$Sr_{0.5}Mn_{0.5}O$' phase can be constructed, thereby allowing a comparison between the bond valences of the cations in the $Ca_{0.5}Mn_{0.5}O$ and '$Sr_{0.5}Mn_{0.5}O$' phases.

As shown in Table 7.9, the coordination requirements of neither cation would be 'met' with such an arrangement with the strontium cations highly 'overbonded' and the manganese cations highly 'underbonded'. In contrast, the better size match of the calcium ($r(Ca^{2+})$ = 1.06 Å)[86] and manganese cations allows the calculated bond valences of both cations in $Ca_{0.5}Mn_{0.5}O$ to be much more chemically reasonable than in the hypothetical strontium-based analogue.

Phase	Contact	Length	Number of contacts	BVS contribution per contact	BVS
$Ca_{0.5}Mn_{0.5}O$	Mn - O	2.319 Å	6	0.240	**1.438**
	Ca - O	2.319 Å	6	0.387	**2.320**
'$Sr_{0.5}Mn_{0.5}O$'	Mn - O	2.460 Å	6	0.164	**0.982**
	Sr - O	2.460 Å	6	0.397	**2.382**

Table 7.9: Bond valence sums for cations in $Ca_{0.5}Mn_{0.5}O$ and '$Sr_{0.5}Mn_{0.5}O$'

7.4.3. Oxidation state

Phases in the range $La_{1-x}Ca_xMnO_2$ ($0.6 \leq x \leq 0.8$) and $(La_{0.1}Ca_{0.9})_{0.5}Mn_{0.5}O$ contain manganese centres with an average manganese oxidation state of below 2. There are examples of organometallic complexes containing manganese centres with such a low average oxidation state, e.g. *trans*-[Mn(CO)dppe$_2$NCMe]ClO_4 where dppe = 1,2-Bis(diphenylphosphino)ethane,[93] with the common feature being the presence of π-acceptor ligands to stabilise the low manganese oxidation state. In addition there is evidence to suggest that Ce_2MnN_3 contains Mn(I) cations, although unequivocal determination of the oxidation states of the cerium, manganese and nitride ions has not yet been achieved.[91, 94, 95] However, the $La_{1-x}Ca_xMnO_2$ ($0.6 \leq x \leq 0.8$) and $(La_{0.1}Ca_{0.9})_{0.5}Mn_{0.5}O$ phases are, to the best of the author's knowledge, the first examples of extended oxides containing manganese centres with an average oxidation state below +2.

7.4.4. Structural conclusion

Analysis of data collected from a wide range of experimental techniques has led to the conclusion that the structures of the phases formed upon the topotactic reduction reactions of the $La_{1-x}Ca_xMnO_3$ ($0.6 \leq x \leq 1$) phases are dependent on the La:Ca ratio. The structures of $(La_{0.1}Ca_{0.9})_{0.5}Mn_{0.5}O$ and $Ca_{0.5}Mn_{0.5}O$ are based on the disordered rock salt structure, while the structures of the more La^{3+}-rich reduced phases contain layers of edge-sharing octahedra and layers of vertex-sharing tetrahedra.

RMC simulations, guided by the fit to PDFs and Bragg diffraction data, have shown that the $La_{1-x}Ca_xMnO_2$ (x = 0.6, 0.67 and 0.7) phases, while lacking long-range order, posses longer-range structures than indicated by the diffraction data alone. It is clear that the structures of the $La_{1-x}Ca_xMnO_2$ phases contain layers of tetrahedral chains, albeit with significant cross-linking between the chains, analogous to those in the structures of the $La_{1-x}A_xMnO_{2.5}$ brownmillerite phases and the $La_{1-x}Sr_xMnO_{3-(0.5-x)/2}$ '6-layer manganate' phases.

The most notable feature regarding the $La_{1-x}Ca_xMnO_2$ and $(La_{1-x}Ca_x)_{0.5}Mn_{0.5}O$ phases is clearly the surprisingly low average manganese oxidation states of Mn^{1+x}.

7.5. Magnetic properties of $La_{1-x}Ca_xMnO_2$ ($0.6 \leq x \leq 0.7$)

7.5.1. Introduction

As a comparison to the magnetic properties of the $La_{1-x}Ca_xMnO_2$ ($0.6 \leq x \leq 0.7$) phases, magnetic susceptibility data collected from $Ca_{0.5}Mn_{0.5}O$ can be fitted with the Curie-Weiss law between 200 K and 300 K with θ = -174.1 K and $C \approx 4.06$ cm^3 K mol^{-1}.[82] This value for the Curie constant is in good agreement with that expected for a material containing high-spin S = 5/2 Mn(II) centres ($C_{expected}$ = 4.38 cm^3 K mol^{-1}). In addition, Varela *et al*. reported that neutron powder diffraction data collected from $Ca_{0.5}Mn_{0.5}O$ at 5 K are consistent with this phase adopting a G-type antiferromagnetically ordered arrangement with a refined ordered moment of 3.83 μ_B per manganese centre.[82]

7.5.2. Results

7.5.2.1. Magnetic susceptibility data

Zero field cooled and field cooled magnetic susceptibility data collected from samples of the $La_{1-x}Ca_xMnO_2$ ($0.6 \leq x \leq 0.7$) phases are shown in Figure 7.27 in Appendix 7. The susceptibility data are consistent with the presence of a trace amounts of the corresponding

perovskite starting materials which adopt magnetically ordered structures with ferromagnetic components, thereby preventing satisfactory fits to the Curie-Weiss law.[96, 97]

7.5.2.2. Neutron Diffraction Data

Variable temperature neutron powder diffraction data were collected from $La_{0.4}Ca_{0.6}MnO_2$, $La_{0.33}Ca_{0.67}MnO_2$ and $La_{0.3}Ca_{0.7}MnO_2$ using the POLARIS instrument to characterise the long range magnetic order in these phases. As shown in Figure 7.23, low temperature neutron powder diffraction data sets collected from the $La_{1-x}Ca_xMnO_2$ ($0.6 \leq x \leq 0.7$) phases contain an intense additional reflection at approximately 4.4 Å relative to the analogous data sets collected at room temperature.

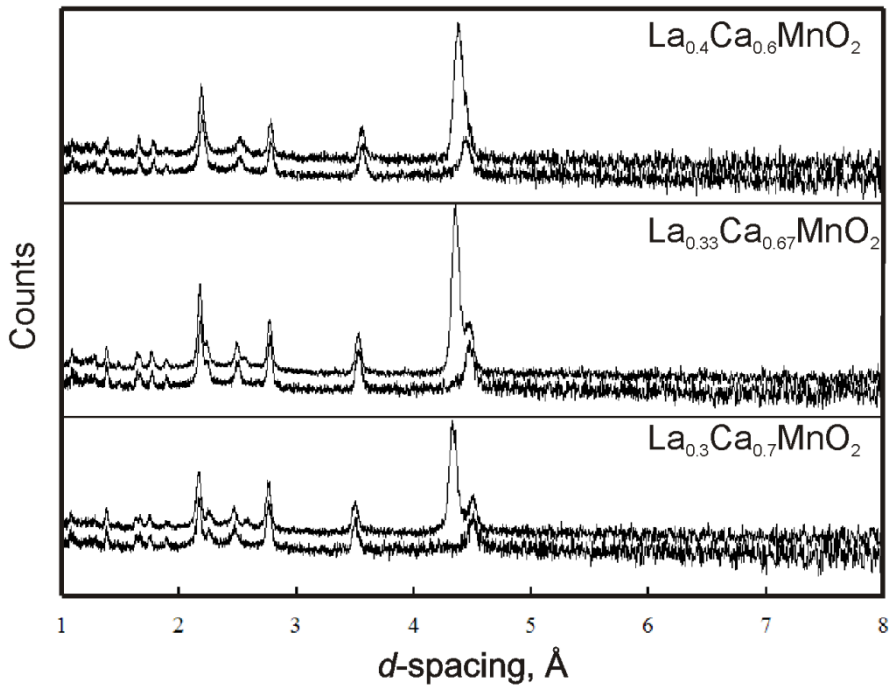


Figure 7.23: Neutron powder diffraction data collected from $La_{0.4}Ca_{0.6}MnO_2$, $La_{0.33}Ca_{0.67}MnO_2$ and $La_{0.3}Ca_{0.7}MnO_2$ at 5 K (top in each pane) and 298 K (bottom in each pane) using the 35° detector bank of the POLARIS instrument.

This additional diffraction reflection can be indexed in each case using a unit cell related to the crystallographic unit cell by an $a' = \sqrt{2}a$, $b' = \sqrt{2}b$, $c' = 2c$ geometric expansion. A series of magnetically ordered models consistent with the crystallographic symmetry were compared to the 5 K data sets. In each case, the best fit was obtained with a simple G-type antiferromagnetically ordered model with the moments aligned parallel to the *c*-axis, as

shown in Figure 7.25. The refinements converged readily to yield the ordered moments shown in Table 7.10.

Phase	$\mu_{observed}$ at 5 K	$\mu_{expected}$	T_N	β
$La_{0.4}Ca_{0.6}MnO_2$	4.07(6) μ_B	4.60 μ_B	231 K	0.548
$La_{0.33}Ca_{0.67}MnO_2$	3.91(4) μ_B	4.67 μ_B	221 K	0.508
$La_{0.3}Ca_{0.7}MnO_2$	3.96(5) μ_B	4.70 μ_B	214 K	0.442

Table 7.10: Pertinent magnetic data for the $La_{0.4}Ca_{0.6}MnO_2$, $La_{0.33}Ca_{0.67}MnO_2$ and $La_{0.3}Ca_{0.7}MnO_2$ phases

The fits to the data collected from the $La_{1-x}Ca_xMnO_2$ (x = 0.6, 0.67 and 0.7) phases at 5 K using the '35 ^{o} detector bank' of the POLARIS instrument are shown in Figure 7.24.

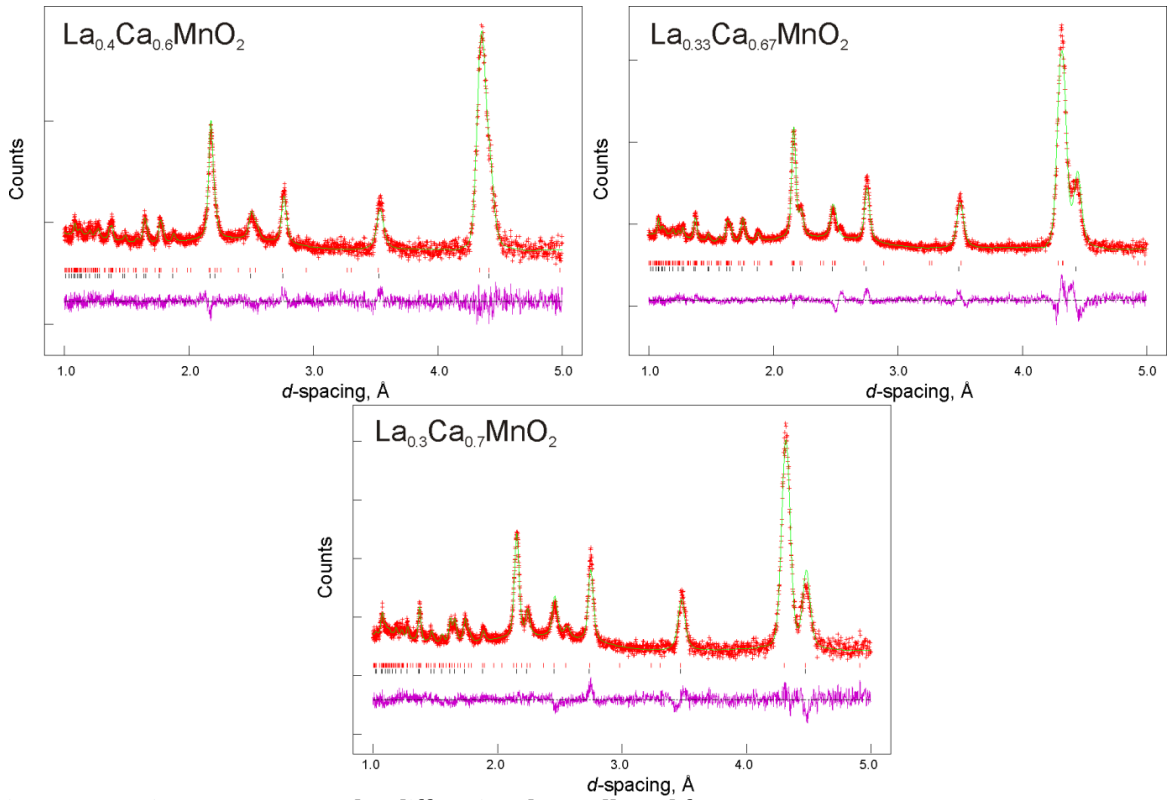


Figure 7.24: Fit to neutron powder diffraction data collected from $La_{0.4}Ca_{0.6}MnO_2$, $La_{0.33}Ca_{0.67}MnO_2$ and $La_{0.3}Ca_{0.7}MnO_2$ at 5 K using the 35^o detector bank of the POLARIS instrument.

Figure 7.25 shows a plot of the ordered magnetic moments per manganese centre in $La_{0.4}Ca_{0.6}MnO_2$, $La_{0.33}Ca_{0.67}MnO_2$ and $La_{0.3}Ca_{0.7}MnO_2$ as a function of temperature.

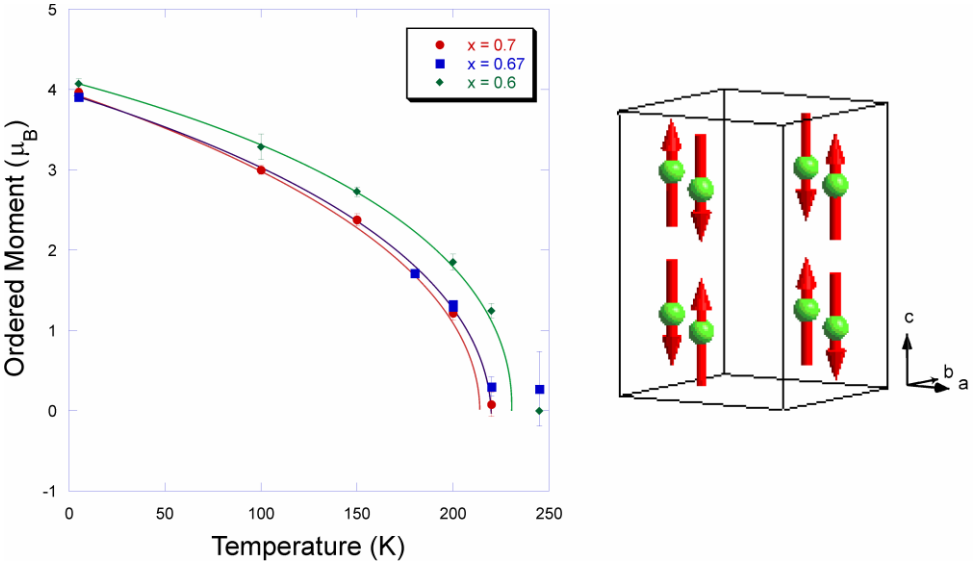


Figure 7.25: Plot of ordered moment as a function of temperature (left) and magnetic structure (right) for the $La_{1-x}Ca_xMnO_2$ ($0.6 \leq x \leq 0.7$) phases.

The thermal dependence of the ordered moments could be fitted with an $I = A(1-(T/T_N))^{\beta}$ power law with the values shown Table 7.10. In addition, the ordered moments expected for magnetic systems containing the corresponding mixture of Mn(I) and Mn(II) cations are also shown in Table 7.10.

7.5.3. Discussion

Given the fact that the observed moments are the same within error and the imperfect fit to the neutron diffraction data collected at 5 K, it is hard to make meaningful comparisons between the magnetic properties of the $La_{1-x}Ca_xMnO_2$ (x = 0.6, 0.67 and 0.7) phases. However, it is surprising that the ordered moment and antiferromagnetic ordering temperature slightly decrease as the Ca^{2+}-content and, thus, the number of unpaired electrons on the manganese centres increase.

$La_{1-x}Ca_xMnO_2$ (x = 0.6, 0.67 and 0.7) phases contain manganese centres with an average oxidation states of between 1.6 and 1.7, consistent with a mixture of high-spin Mn(I) S = 2 and Mn(II) S = 5/2 centres. Given the disordered nature of all the structures (both in terms of stacking of the layers of MnO_y polyhedra and lack of the Mn^I/Mn^{II} charge order), there are clearly a large number of possible magnetic interactions in the $La_{1-x}Ca_xMnO_2$ phases.

However, the majority of the magnetic interactions in the structures are strong 180°, σ-type superexchange interactions between half-filled Mn 3*d* orbitals. By consideration of the Goodenough-Kanamori rules,[52] it is therefore unsurprising that these reduced phases adopt G-type antiferromagnetically ordered schemes.

The disordered nature of the structures of the $La_{1-x}Ca_xMnO_2$ phases may also lead to magnetic frustration in the systems, thereby leading to a reduction in the observed ordered moments in the 5 K neutron diffraction data sets relative to those predicted based on the number of unpaired electrons on the manganese centres.

Appendix 7

$La_{1-x}Ca_xMnO_3$	Space group	*a* (Å)	*b* (Å)	*c* (Å)
0.6	*Pnma*	5.398(1)	7.593(1)	5.404(1)
0.67	*Pnma*	5.377(1)	7.565(1)	5.377(1)
0.7	*Pnma*	5.371(1)	7.561(1)	5.368(1)
0.8	*Pnma*	5.335(1)	7.529(2)	5.331(3)
0.9	*Pnma*	5.307(4)	7.498(1)	5.301(1)
1	*Pnma*	5.282(1)	7.459(1)	5.268(1)

Table 7.11: Lattice parameters from refinement of $La_{1-x}Ca_xMnO_3$ structural models against X-ray powder diffraction data.

Atom	Wyckoff position	*x*	*y*	*z*	Occupancy	U_{iso} (Å^2)
Ca/Mn(1)	4*b*	½	½	½	0.5/0.5	0.035(1)
O(1)	4*a*	0	0	0	1	0.015(2)
$Ca_{0.5}Mn_{0.5}O$: space group *Fm m* *a* = 4.6370(8) Å, cell volume = 99.70(5) Å^3 $Ca_{0.5}Mn_{0.5}O$[82]: *a* = 4.6313(1) Å						

Table 7.12: Refined structural parameters for $Ca_{0.5}Mn_{0.5}O$. The previously reported lattice parameter for $Ca_{0.5}Mn_{0.5}O$ is also shown for comparison.

Atom	Wyckoff position	*x*	*y*	*z*	Occupancy	U_{iso} (Å^2)
La/Ca/Mn(1)	4*b*	½	½	½	0.05/0.45/0.5	0.018(2)
O(1)	4*a*	0	0	0	1	0.001(2)
$(La_{0.1}Ca_{0.9})_{0.5}Mn_{0.5}O$: space group *Fm m* *a* = 4.6617(12) Å, cell volume = 101.30(7) Å^3						

Table 7.13: Refined structural parameters for $(La_{0.1}Ca_{0.9})_{0.5}Mn_{0.5}O$

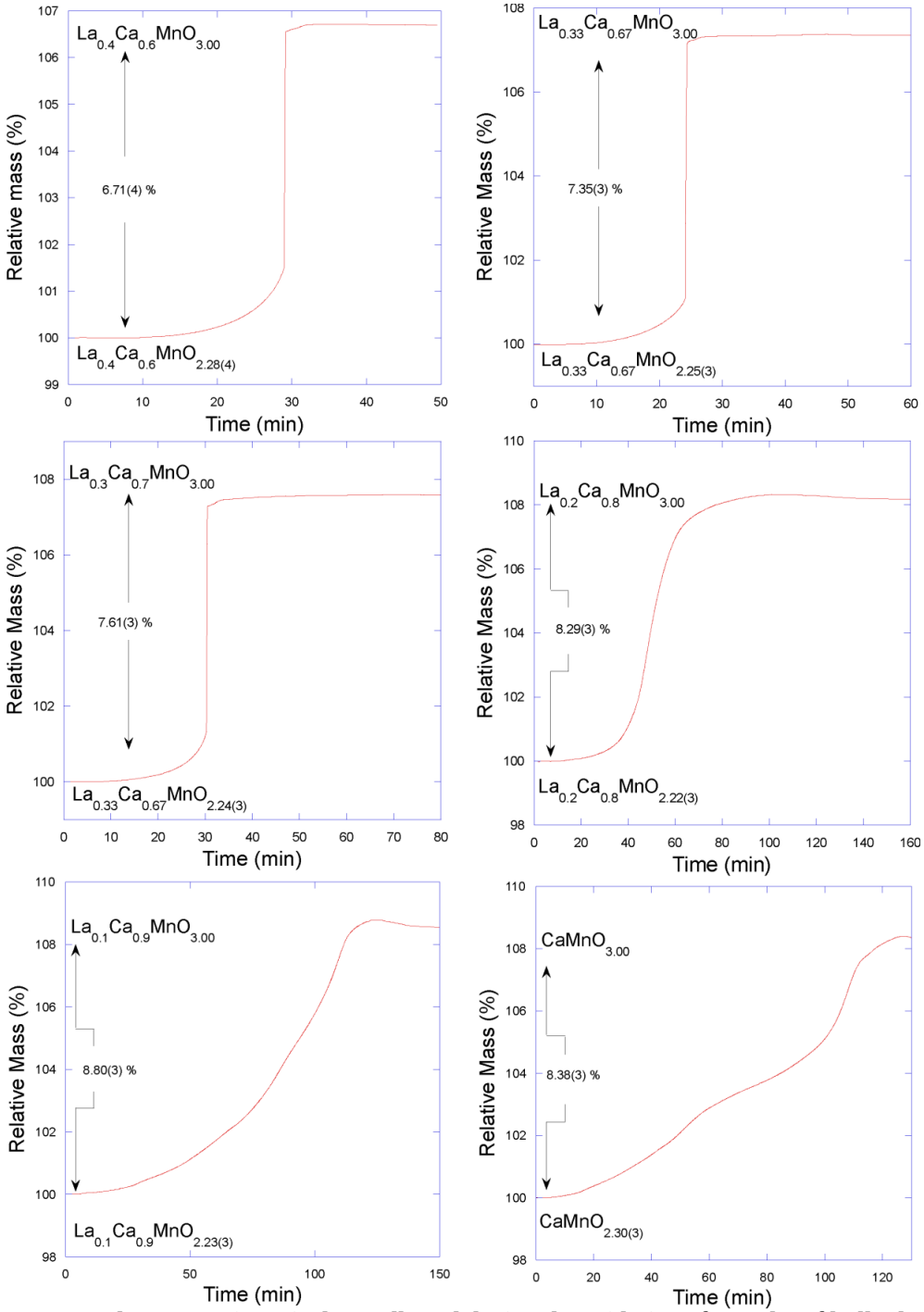


Figure 7.26: Thermogravimetric data collected during the oxidation of samples of bulk phases formed upon reaction of $La_{1-x}Ca_xMnO_3$ substrate phases and NaH

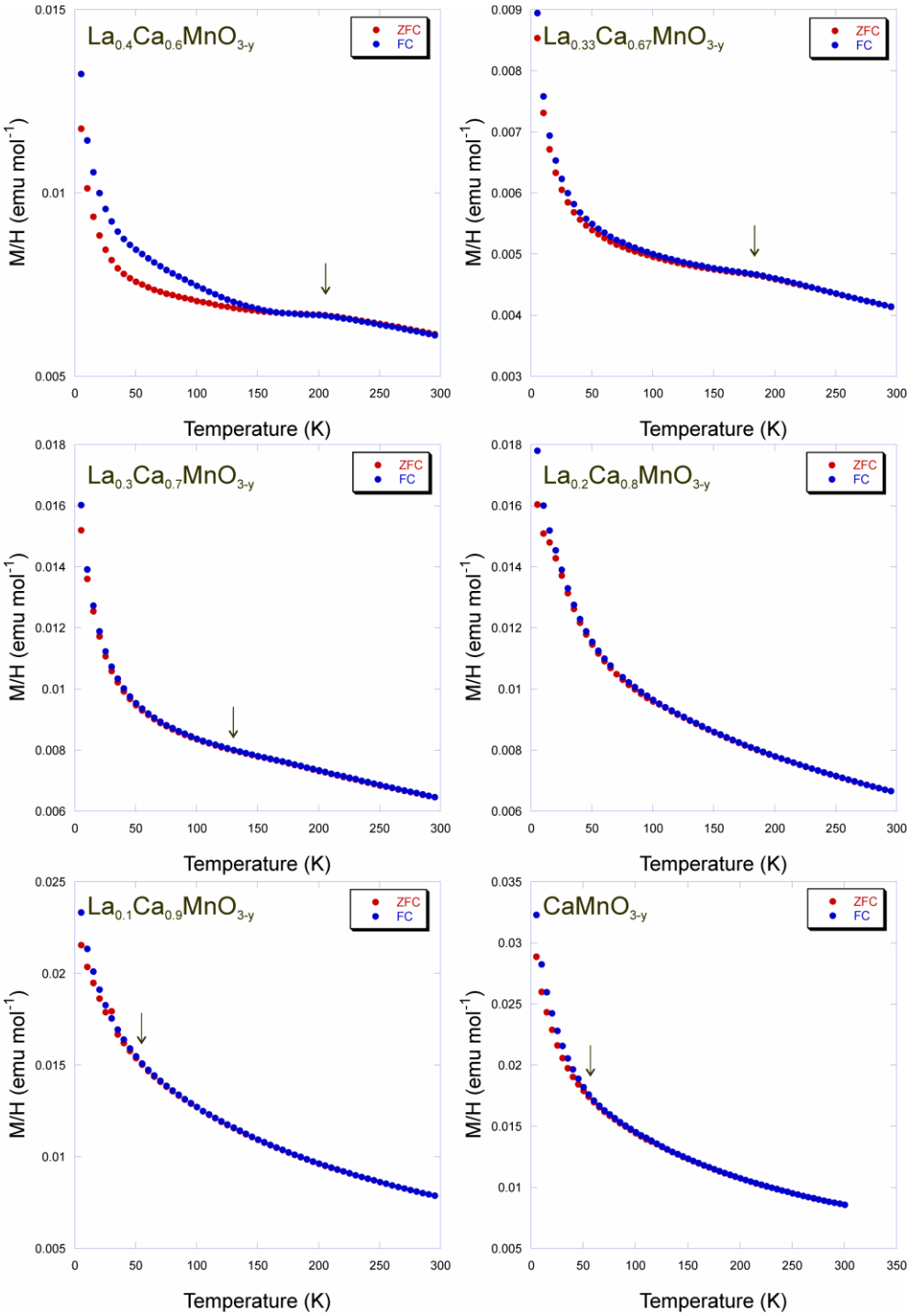


Figure 7.27: Zero field cooled (ZFC) and field (FC) cooled susceptibility data collected from $La_{1-x}Ca_xMnO_2$ ($0.6 \leq x \leq 0.8$) and $(La_{1-x}Ca_x)_{0.5}Mn_{0.5}O$ (x = 0.9 and 1) phases.

Chapter 8: Topotactic Reduction of $Sr_3Fe_2O_5Cl_2$

8.1. Introduction

There are a large number of published examples of successful topotactic reduction reactions using binary metal hydrides as solid state reducing agents; many of which result in the formation of novel compounds and corresponding electronic states. In contrast, there has been relatively little study of the directing influences of heteroanions on the progress of topotactic reductions in mixed anion solids. This chapter is primarily concerned with the topotactic reduction reaction of $Sr_3Fe_2O_5Cl_2$, the first reported example of anion deintercalation from an oxychloride system.

$Sr_3Fe_2O_5Cl_2$ adopts an n = 2 Ruddlesden-Popper (RP) structure closely related to that of $Sr_3Fe_2O_7$ (see Figure 8.1), in which double layers of FeO_5 square based pyramids are separated by SrCl rock salt-type layers. Therefore the structure of $Sr_3Fe_2O_5Cl_2$ contains 3 distinct anion sites: 'bridging axial' O(1), 'equatorial' O(2) and 'axial' Cl(1) sites. As a result, $Sr_3Fe_2O_5Cl_2$ provides an apposite system to monitor the structural and chemical selectivity of topotactic reduction reactions.

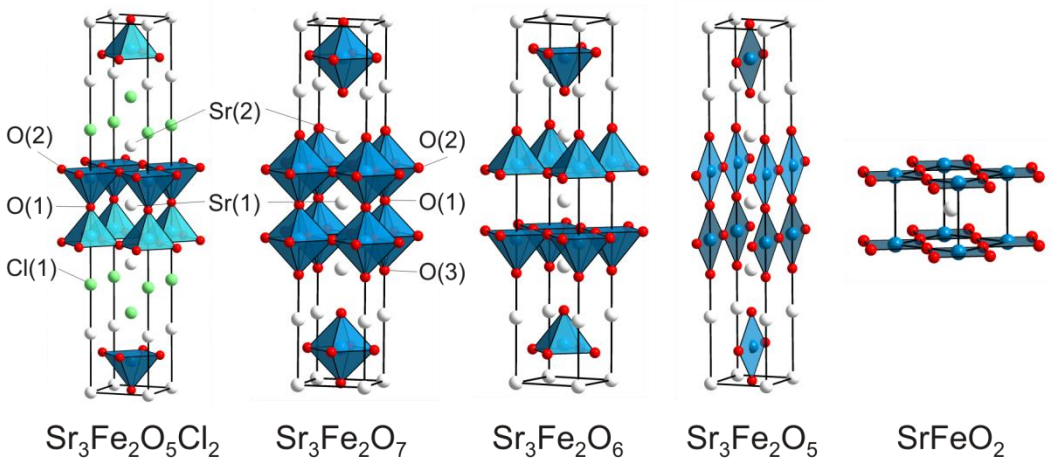


Figure 8.1: Structures of some complex iron-based phases

Furthermore, interest in the topotactic reduction reactions of iron-based complex oxides has recently been sparked by the reduction of $SrFeO_3$, a cubic perovskite phase, to form the infinite-layer phase $SrFeO_2$ - the first reported example of a phase containing linked Fe(II)

square planar units (see Figure 8.1).[98] Subsequent work by the same authors reported the synthesis of $Sr_3Fe_2O_5$, the structure of which also contains linked Fe(II) square planar units, by the topotactic reduction of $Sr_3Fe_2O_{7-\delta}$, via the formation of $Sr_3Fe_2O_6$ as an intermediate (see Figure 8.1).[99] Prior to the structural characterisation of $SrFeO_2$, the only reported example of a material containing square planar Fe(II) cations was the mineral gillespite, $BaFeSi_4O_{10}$, which contains isolated $Fe(II)O_4$ units housed within Si_4O_{10} rings.[100]

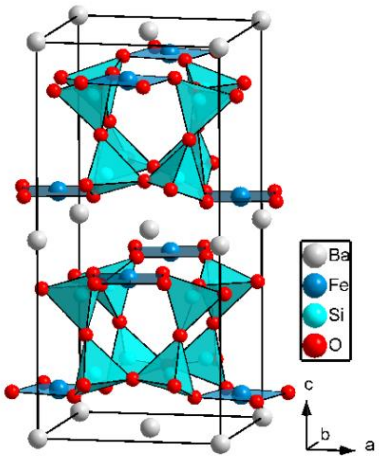


Figure 8.2: Structure of $BaFeSi_4O_{10}$ (Gillespite)

Therefore topotactic reduction reactions of $Sr_3Fe_2O_5Cl_2$ were performed to allow comparison to similar reactions of the structurally related n = 2 RP $Sr_3Fe_2O_{7-\delta}$ and perovskite $SrFeO_3$ phases.

8.2. Experimental

8.2.1. Synthesis of $Sr_3Fe_2O_5Cl_2$

Samples of $Sr_3Fe_2O_5Cl_2$ were prepared by a direct-combination route that has previously been described by Weller *et al.*[25] Due to the air- and moisture-sensitive nature of SrO, $SrCl_2$ and $Sr_3Fe_2O_5Cl_2$, all samples were kept under an inert atmosphere at all times. Suitable quantities of SrO (prepared by the decomposition of $SrCO_3$ at 1100 ^oC under vacuum), $SrCl_2$ (dried at 180 ^oC under vacuum) and Fe_2O_3 (Alfa Aesar, 99.99 %) were thoroughly mixed using an agate pestle and mortar in an argon filled glovebox (O_2 and H_2O levels < 1 ppm). The mixture was then heated in an evacuated silica ampoule at 850 ^oC for 2 periods of 24

hours with one intermediate grinding. X-ray powder diffraction data collected from this material were consistent with a single phase with lattice parameters a = 3.947(1) Å and c = 23.786(1) Å in good agreement with previously reported values (a = 3.946(1) Å and c = 23.786(1) Å).[25]

8.2.2. Low temperature reduction with metal hydrides

Previous research has shown that NaH, CaH_2 and LiH can act as effective solid state topotactic reducing agents for oxide-based materials.[26-28] Therefore, the topotactic reduction of $Sr_3Fe_2O_5Cl_2$ was attempted using each of these binary metal hydrides as reducing agents. Small samples (~ 300 mg) of $Sr_3Fe_2O_5Cl_2$ were ground together in an argon-filled glovebox with 1:2, 1:2 and 1:4 molar ratios of NaH, CaH_2 and LiH, respectively. These mixtures were then sealed under vacuum in Pyrex ampoules and heated at a series of temperatures in the range $180 \leq T\ (^oC) \leq 210$ when using NaH and $300 \leq T\ (^oC) \leq 400$ when using CaH_2 or LiH. The products of the reactions were checked using X-ray powder diffraction data.

Due to the hazards associated with the production of hydrogen gas as a by-product when using CaH_2 or LiH as a reducing agent,[27, 28] large-scale samples suitable for characterisation by neutron powder diffraction were prepared by means of a spring-loaded venting apparatus described in section 2.2.3.

The samples were then washed using 2 different procedures depending on the identity of the metal hydride used: Samples containing either NaH or LiH were washed with 4 x 100 ml of CH_3OH under nitrogen to remove sodium- or lithium-containing phases (NaOH or Li_2O and unreacted NaH or LiH) before being dried under vacuum. Samples containing CaH_2 were washed under nitrogen with 4 × 100 ml of a 0.25 M solution of NH_4Cl in CH_3OH to remove the calcium-containing phases (CaH_2 and CaO). Samples were then washed with 4 × 80 ml of clean CH_3OH to remove any remaining NH_4Cl before being dried under vacuum. Average

iron oxidation states in all phases were determined by iodometric titration, details of this technique are covered in section 2.9.

8.3. Results

8.3.1. Reactivity of $Sr_3Fe_2O_5Cl_2$

X-ray powder diffraction data were collected from the washed products of the various reactions detailed above, the results of which are shown in Table 8.1.

Metal Hydride	Temperature	Result
NaH	180 ^oC	No reaction
NaH	200 ^oC	Partial Decomposition
NaH	210 ^oC	Decomposition
CaH_2	300 ^oC	No reaction
CaH_2	350 ^oC	No reaction
CaH_2	400 ^oC	Formation of Sr_2FeO_3Cl[101]
LiH	300 ^oC	No reaction
LiH	350 ^oC	Lattice parameter change
LiH	400 ^oC	Formation of Sr_2FeO_3Cl[101]

Table 8.1: Results of reactions of $Sr_3Fe_2O_5Cl_2$ with a series of binary metal hydrides at a series of temperatures.

Due to the decomposition of $Sr_3Fe_2O_5Cl_2$ to poorly crystalline binary metal compounds when using NaH as a reducing agent, the attempted topotactic reduction of $Sr_3Fe_2O_5Cl_2$ using NaH was discontinued. Heating $Sr_3Fe_2O_5Cl_2$ with LiH or CaH_2 at 400 ^oC results in the formation of the n = 1 RP Sr_2FeO_3Cl phase along with some by-products. Owing to the poor crystallinity of the phases formed as by-products upon formation of Sr_2FeO_3Cl, it was not possible to unequivocally determine the identity of some of the by-products (highlighted in bold below) of the reactions. However the most chemically reasonable reactions for each case are shown below:

A fuller discussion of these 2 reactions is covered in section 8.4.3. In contrast, the reaction of $Sr_3Fe_2O_5Cl_2$ with LiH at 350 ^oC results in the formation of a majority phase with a body-centred tetragonal unit cell, consistent with the topotactic reduction of $Sr_3Fe_2O_5Cl_2$. As shown in Figure 8.3, X-ray diffraction data collected from this sample prior to the CH_3OH washing procedure contain reflections (marked with an asterisk) consistent with the presence of Li_2O with no evidence for the presence of LiCl. The formation of Li_2O rather than LiCl as a by-product in this reaction is a clear indication that the oxide anion sublattice has been manipulated over the course of the reaction with the chloride anion sublattice remaining intact.

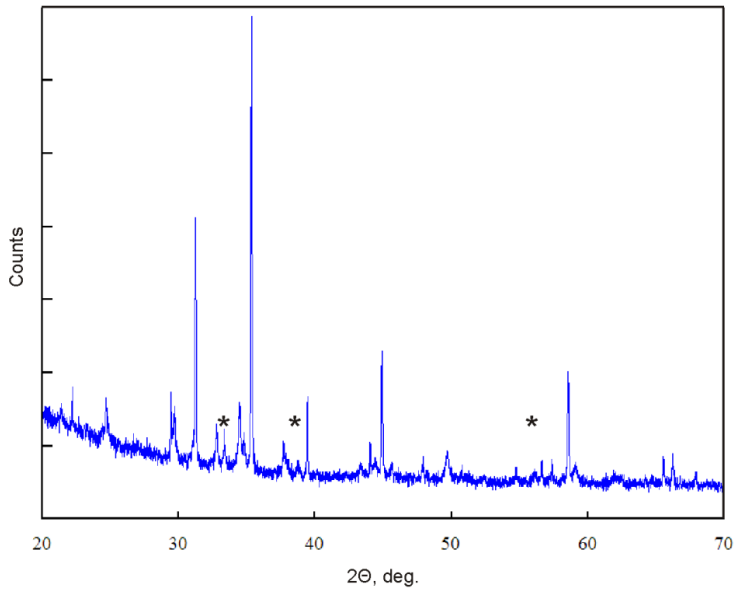


Figure 8.3: X-ray powder diffraction data collected from the products of the reaction between $Sr_3Fe_2O_5Cl_2$ with LiH at 350 ^oC. The asterisks mark reflections consistent with the presence of Li_2O.

8.3.2. Structural characterisation

8.3.2.1. X-ray diffraction data

X-ray powder diffraction data collected from the washed product of the reaction between $Sr_3Fe_2O_5Cl_2$ and LiH at 350 ^oC along with those collected from the $Sr_3Fe_2O_5Cl_2$ substrate phase are shown in Figure 8.4.

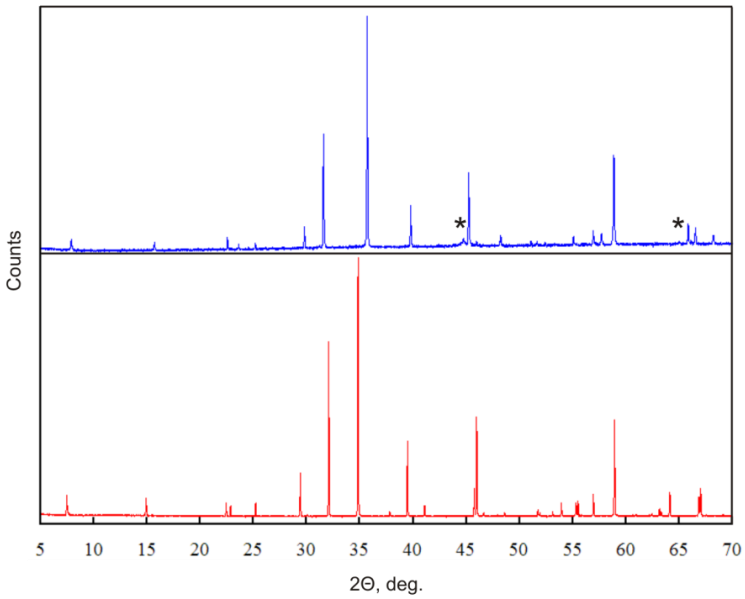


Figure 8.4: X-ray powder diffraction patterns collected from $Sr_3Fe_2O_5Cl_2$ (red) and the washed product of the reaction between $Sr_3Fe_2O_5Cl_2$ and LiH at 350 °C (blue). The reflections marked with an asterisk denote the presence of elemental iron.

The reflections in the data could be readily indexed on the basis of a body-centred tetragonal unit cell (a = 4.009(1) Å, c = 22.638(1) Å). Close inspection of the data revealed a set of weak diffraction reflections consistent with the presence of metallic iron (labelled with an asterisk in Figure 8.4), indicating mild decomposition had occurred during the reaction.

8.3.2.2. Electron diffraction data

Electron diffraction data were collected from $Sr_3Fe_2O_{5-x}Cl_2$ to confirm the size and symmetry of the crystallographic unit cell. As can be seen in Figure 8.5, the data can be readily indexed using the body-centred tetragonal unit cell determined using X-ray powder diffraction data.

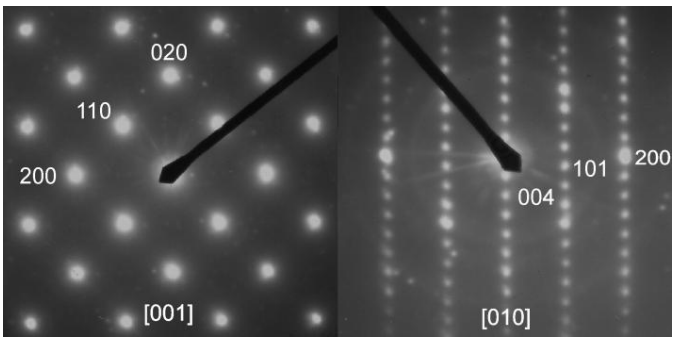


Figure 8.5: Electron diffraction data collected from $Sr_3Fe_2O_{5-x}Cl_2$

8.3.2.3. Neutron diffraction data

Neutron powder diffraction data were collected from $Sr_3Fe_2O_{5-x}Cl_2$ at room temperature using the D2b instrument at the ILL to determine the structure of the reduced phase. The majority of the reflections in the data could be indexed using the body-centred unit cell consistent with the X-ray and electron diffraction data sets. However, as shown in Figure 8.6, neutron diffraction data collected from $Sr_3Fe_2O_{5-x}Cl_2$ contain a series of additional large *d*-spacing diffraction features inconsistent with this unit cell (marked with arrows).

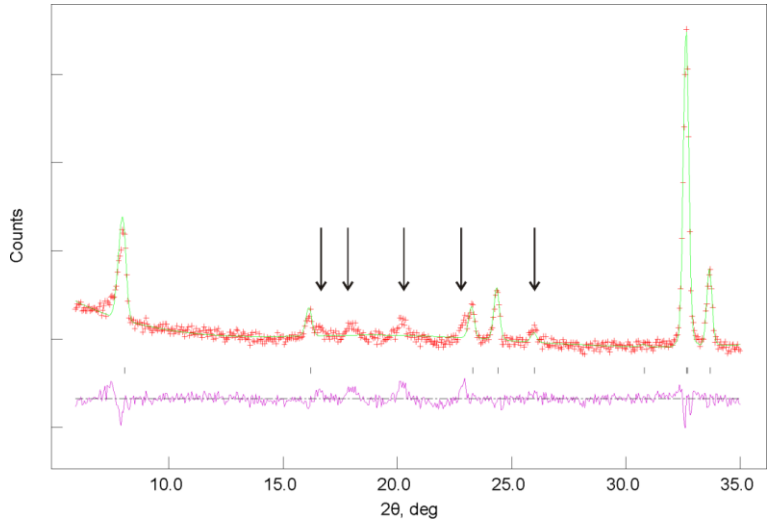


Figure 8.6: Magnetic reflections (marked by arrows) in neutron powder diffraction data collected from $Sr_3Fe_2O_{5-x}Cl_2$ at room temperature using the D2b instrument.

These additional reflections could be indexed using a unit cell related to the tetragonal cell described above by an $a' = \sqrt{2}a$, $b' = \sqrt{2}b$, $c' = c$ geometric expansion, suggesting these reflections are attributable to long range magnetic order. In order to confirm this hypothesis, variable temperature neutron powder diffraction data were collected to monitor the temperature dependence of the intensities of these additional reflections. Neutron powder diffraction data sets were collected at 5 K using the D2b instrument (see section 2.3.2.1.1) and in the temperature range 298 K $\leq$ T (K) $\leq$ 388 K using the POLARIS instrument (see section 2.3.2.2). The intensities of these additional neutron diffraction features diminish with increasing temperature such that at 388 K their intensities were zero (see Figure 8.7), consistent with a loss of magnetic order at this temperature.

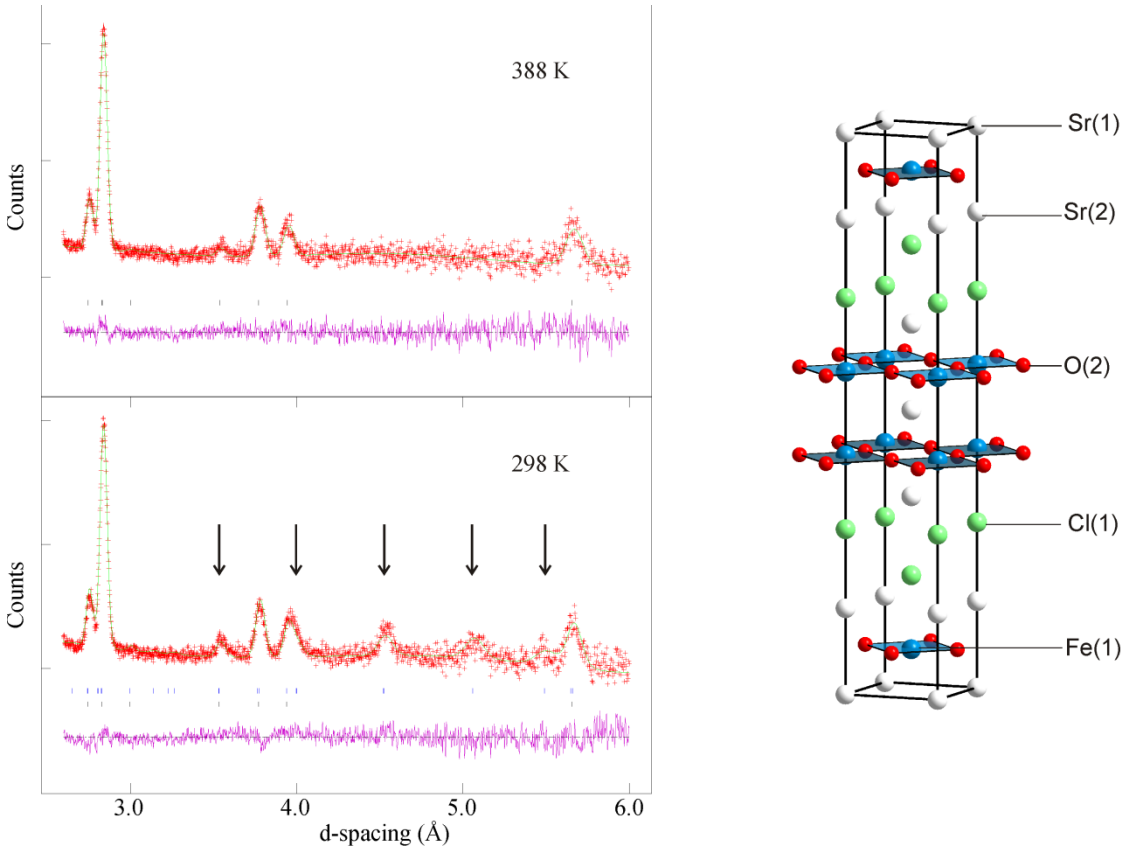


Figure 8.7: Section of neutron powder diffraction data collected from $Sr_3Fe_2O_{5-x}Cl_2$ using the POLARIS at 298 K and 388 K (the major magnetic reflections are marked with arrows) and the refined structure of $Sr_3Fe_2O_4Cl_2$

To avoid the complications of simultaneous structural and magnetic refinements, the structural refinement of $Sr_3Fe_2O_{5-x}Cl_2$ was performed against neutron powder diffraction data collected at 388 K. A structural model based on that of $Sr_3Fe_2O_5Cl_2$ but with altered lattice parameters was refined against this data set. During the refinement all atomic positional and thermal parameters were allowed to vary and, to account for the non-stoichiometry of the reduced phase, the fractional occupancies of all the anion sites (both oxide and chloride) were also allowed to vary. The occupancy of the O(1) 'bridging axial' anion site (see Figure 8.1) rapidly declined to zero within error with an associated improvement in the fit to the data, whereas both the O(2) and Cl(1) sites remained fully occupied within error.

In the final stages of the refinement the fractional occupancies of all the atomic sites were allowed to vary but all other atomic positions remained fully occupied within error indicating

a composition of $Sr_3Fe_2O_4Cl_2$. To account for the presence of metallic iron in the sample, a structural description of this phase was added to the refinement model. In addition, several weak diffraction reflections consistent with the diffraction by the vanadium sample holder. A structural description of vanadium was also added to the refinement model. The final refinement readily converged to give a good statistical fit to the data ($\chi^2 = 1.858$).

Full details of the refined structural parameters are given in Table 8.2. The refined structure of $Sr_3Fe_2O_4Cl_2$ is shown in Figure 8.7. Selected bond lengths are shown in Table 8.3, with percentage differences between the corresponding lengths in $Sr_3Fe_2O_5Cl_2$ included for comparison. Observed, calculated and difference plots are shown in Figure 8.8.

Atom	**Wyckoff position**	***x***	***y***	***z***	U_{iso} **(Å^2)**
Sr(1)	2*a*	0	0	0	0.0036(5)
Sr(2)	4*e*	0	0	0.153(1)	0.0038(4)
Fe(1)	4*e*	0	0	0.425(1)	0.0028(2)
O(2)	8*g*	0.5	0	0.078(1)	0.0058(2)
Cl(1)	4*e*	0	0	0.294(1)	0.0087(2)
Space group: *I*4/*mmm*, a = 4.008(1) Å, c = 22.653(1) Å, cell volume = 364.01(1) Å^3 χ^2= 1.858, wR_p = 2.14 %, R_p = 3.77 %					

Table 8.2: Refined structural model for $Sr_3Fe_2O_4Cl_2$ at 388 K

Cation	**Anion**	**Length (Å)**	**% change upon reduction**	**BVS contribution**	**Total BVS**
Fe(1)	O(2)	4 x 2.006(1)	+0.753	4 x 0.479	2.002
	Cl(1)	1 x 2.977(2)	-0.700	1 x 0.079	
Sr(1)	O(2)	8 x 2.674(1)	-8.078	8 x 0.223	1.780
Sr(2)	O(2)	4 x 2.632(2)	+3.541	4 x 0.249	2.031
	Cl(1)	1 x 3.192(2)	-2.950	4 x 0.219	
	Cl(1)	4 x 3.072(1)	+2.026	1 x 0.158	
	a	4.009(1)	+1.597		
	c	22.638(1)	-4.75 %		

Table 8.3: Selected bond lengths and bond valence parameters from the refined structure of $Sr_3Fe_2O_4Cl_2$

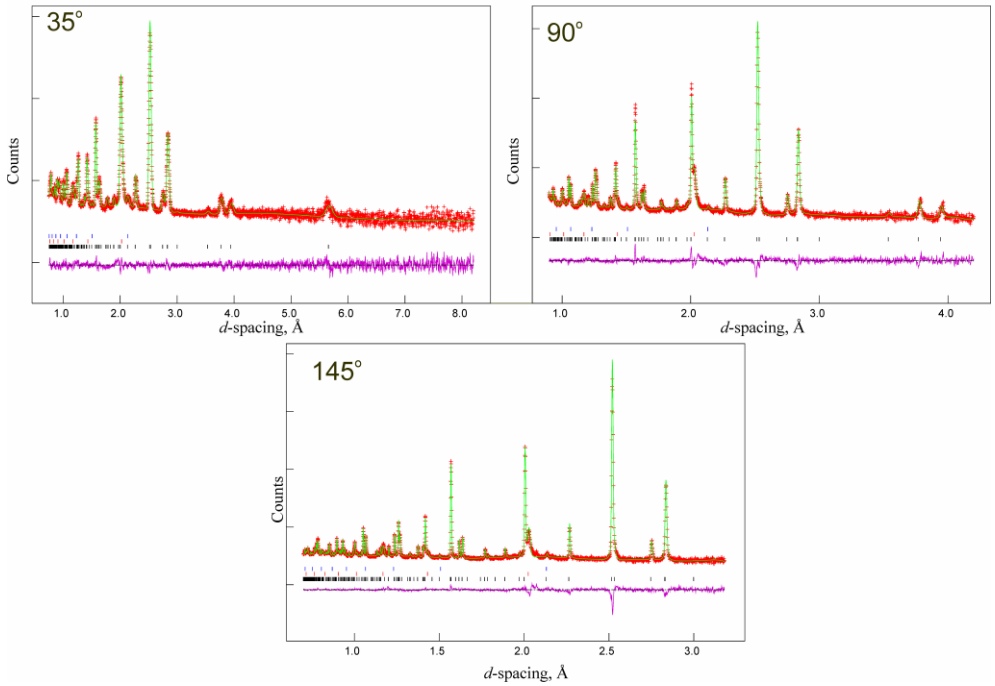


Figure 8.8: Observed, calculated and difference plots for refinement of the structural model for $Sr_3Fe_2O_4Cl_2$ at 298 K, including the magnetic model, against neutron powder diffraction data collected using the POLARIS instrument (35° bank – top, 90° bank– middle and 145° bank - bottom).

8.3.2.4. Iodometric titrimetry

Due to the highly-air sensitive nature of $Sr_3Fe_2O_{5-x}Cl_2$, it was not possible to determine the stoichiometry of the reduced phase using reoxidative thermogravimetric data. Indeed, bulk samples of this material are highly pyrophoric and should be handled with care. X-ray powder diffraction data collected from a bulk sample of $Sr_3Fe_2O_{5-x}Cl_2$ exposed to air are consistent with complete reoxidation to $Sr_3Fe_2O_5Cl_2$. This provides another clear indication that the topotactic reduction reaction of $Sr_3Fe_2O_5Cl_2$ has been completed with the removal of oxide anions rather than chloride anions.

In order to confirm the refined stoichiometry of the reduced phase, iodometric titrations were performed using the method described in section 2.9. The results of these titrations are consistent with an average iron oxidation state of Fe(II) in the bulk phase.

8.3.3. Magnetic characterisation

As discussed above, neutron powder diffraction data collected from $Sr_3Fe_2O_4Cl_2$ at 5 K show additional features relative to the 388 K data set which are attributable to long range

magnetic order. A series of magnetically ordered models consistent with the crystallographic symmetry were compared to the 5 K data and the best fit was obtained by a simple G-type antiferromagnetically ordered model with moments aligned parallel to the *z*-axis (see Figure 8.9). The refinement converged readily to yield an ordered moment of 2.81(9) μ_B per iron centre at 5 K. Complete details of the magnetic refinement and fits to the data at 5 K are shown in Table 8.11 and Figure 8.16 respectively in Appendix 8.

Analogous models were refined against neutron diffraction data collected in the temperature range 5 < T (K) < 388. Figure 8.9 shows a plot of the refined ordered moment as a function of temperature, indicating a magnetic ordering temperature of T_N ~ 378(10) K for $Sr_3Fe_2O_4Cl_2$.

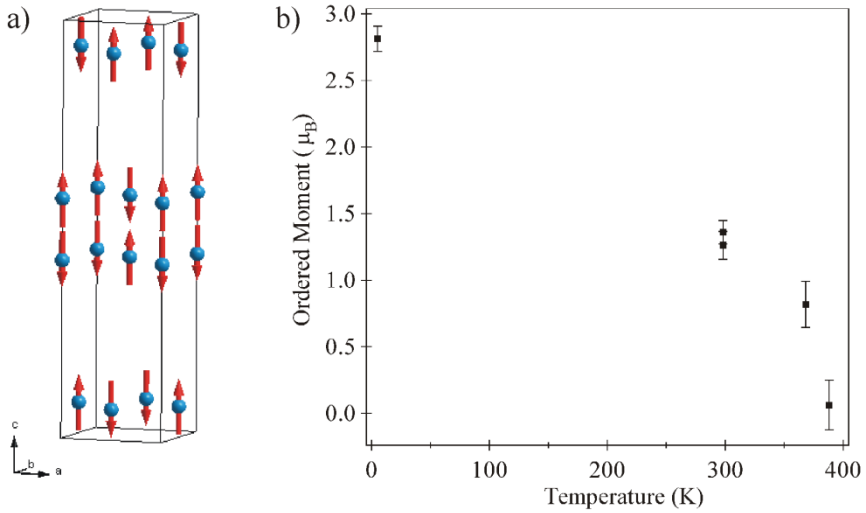


Figure 8.9: a) The G-type antiferromagnetically ordered model refined for $Sr_3Fe_2O_4Cl_2$.b) A plot of the refined magnetic moment per iron centre as a function of temperature for $Sr_3Fe_2O_4Cl_2$, indicating a magnetic ordering temperature of T_N ~ 378 K.

Due to the presence of metallic iron in the sample, it was not possible to confirm the magnetic ordering temperature from magnetic susceptibility measurements.

8.4. Discussion

The topotactic reduction of $Sr_3Fe_2O_5Cl_2$ with LiH results in the deintercalation of oxide ions from the SrO(1) layer of the material and the formation of $Sr_3Fe_2O_4Cl_2$ as shown in Figure 8.10. Bond valence sums (BVS) calculated for the iron centres in $Sr_3Fe_2O_4Cl_2$ (see

Table 8.3) are consistent with the presence of Fe(II). In addition they reveal that the long Fe-Cl bond (2.977(2) Å) contributes only 3.9 % to the BVS total of the iron centre so the iron coordination geometry is effectively square planar. The structure of $Sr_3Fe_2O_4Cl_2$ can therefore be described as containing double layers of vertex-sharing FeO_4 square planar units separated by a SrCl rock salt-type layer (see Figure 8.10).

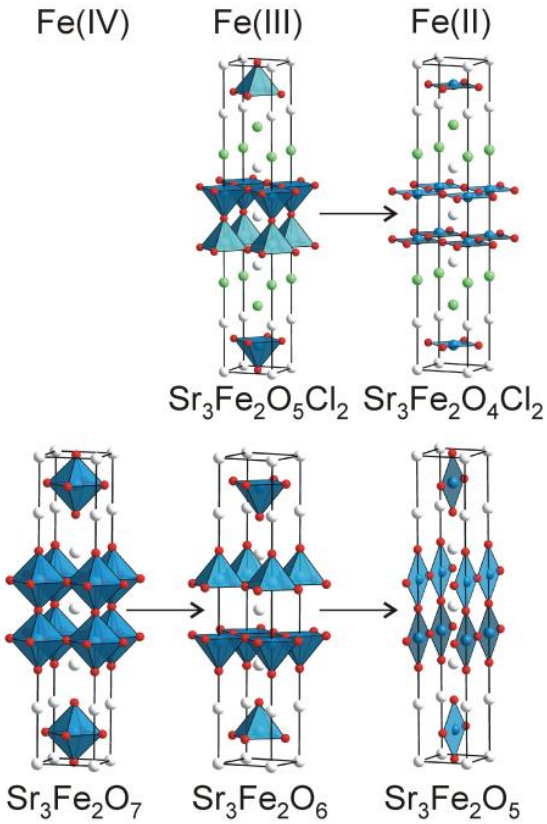


Figure 8.10: Reduction of $Sr_3Fe_2O_5Cl_2$ proceeds via the removal of oxide ions from bridging axial sites to yield $Sr_3Fe_2O_4Cl_2$. Reduction of $Sr_3Fe_2O_7$ proceeds initially by the removal of ions from bridging axial sites to form $Sr_3Fe_2O_6$.[99] A subsequent removal of equatorial oxide ions and rearrangement of the anion lattice leads to the formation of the spin-ladder phase $Sr_3Fe_2O_5$.[99]

There are relatively few examples in the literature of square planar Fe(II) centres in extended solids for comparison. As discussed in the introduction to this chapter, those that are reported have been prepared by similar topotactic reduction syntheses as $Sr_3Fe_2O_4Cl_2$. The infinite-layer phases $SrFeO_2$, for example, has been prepared by the topotactic reduction of $SrFeO_{3-\delta}$ with CaH_2.[98] Comparison of the structural parameters of $Sr_3Fe_2O_4Cl_2$ and $SrFeO_2$ reveals a remarkable similarity in the in-plane Fe-O bond lengths of 2.006(1) Å and 1.996(1) Å respectively, consistent with near equivalent chemical sites.[98] In addition, as described

above, the structure of $Sr_3Fe_2O_5$ (formed by the topotactic reduction of $Sr_3Fe_2O_{7-\delta}$)[99] also contains square planar Fe(II) centres.

8.4.1. Magnetic behaviour

Neutron powder diffraction data show that $Sr_3Fe_2O_4Cl_2$ adopts a G-type antiferromagnetically ordered arrangement below $T_N \sim 378$ K, exhibiting an ordered moment of 2.81(9) μ_B per iron centre at 5 K. The magnitude of the ordered moment at 5 K is consistent with a d^6 high-spin electronic configuration as expected for Fe(II) centres ($S = 2$, $\mu_{ordered\ exp.} = 4\ \mu_B$). The reduction in the observed moment with respect to the expected moment is attributable to covalency within the iron-anion contacts and/or slight disorder within the magnetic system.

In order to rationalise the adoption of the magnetic ordering scheme in $Sr_3Fe_2O_4Cl_2$, it is necessary to establish the ordering of the *d*-orbital energies on the Fe(II) centres in $Sr_3Fe_2O_4Cl_2$. As shown in Figure 8.11, simple MO considerations produce 3 possible ordering sequences of the *d*-orbital energies on the Fe(II) centres in $Sr_3Fe_2O_4Cl_2$.

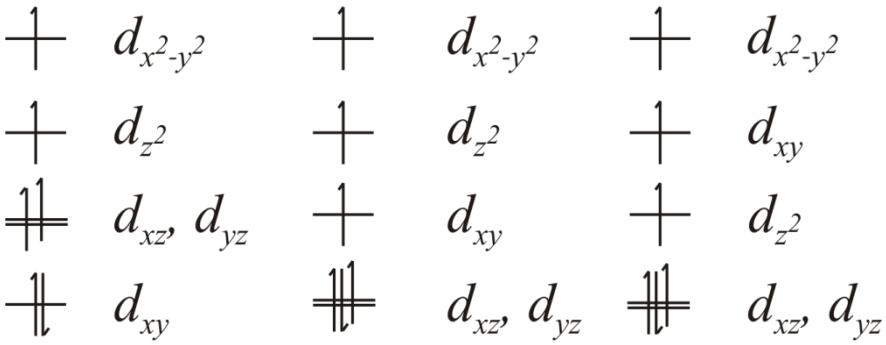


Figure 8.11: Potential electronic configurations of the iron centres in $Sr_3Fe_2O_4Cl_2$

Neutron powder diffraction data show that $Sr_3Fe_2O_4Cl_2$ retains tetragonal symmetry on cooling to 5 K. This suggests that in common with $SrFeO_2$, $Sr_3Fe_2O_4Cl_2$ does not adopt a degenerate electronic ground state, as such a state would be susceptible to a Jahn-Teller-like distortion.[102] This observation and the similarity of the iron coordination environments in the two phases, make it reasonable to assume that the iron centres in $Sr_3Fe_2O_4Cl_2$ will adopt

the same *d*-orbital energy ordering scheme as the iron centres in $SrFeO_2$. Previous reports on the electronic structure of $SrFeO_2$ indicate that the $S = 2$ ground state contains Fe(II) centres with an electronic configuration of: $(d_{z^2})^2(d_{xz}, d_{yz})^2(d_{xy})^1(d_{x^2-y^2})^1$.[98, 102]

By consideration of the Goodenough-Kanamori rules,[52] the iron *d*-orbital expected to have the strongest contribution to the superexchange interactions is the $d_{x^2-y^2}$ orbital. Therefore, the 180º, σ-type Fe $(d_{x^2-y^2})^1$ – O $(2p)$ – Fe $(d_{x^2-y^2})^1$ superexchange interaction accounts for the strong antiferromagnetic coupling between iron centres within each FeO_2 layer of $Sr_3Fe_2O_4Cl_2$.

Coupling between FeO_2 layers is more complex. In the case of adjacent FeO_2 layers (separated by 3.364(2) Å) within the $SrFe_2O_4$ blocks (see Figure 8.12), direct Fe $(d_{z^2})^2$ – Fe $(d_{z^2})^2$ exchange interactions result in G-type antiferromagnetic ordering. However in order for the FeO_2 layers separated by SrCl rock salt layers (separated by 7.874(2) Å) to couple, and full 3D antiferromagnetic order to result, a through space mechanism is most likely employed (although a through bond mechanism may still be present).

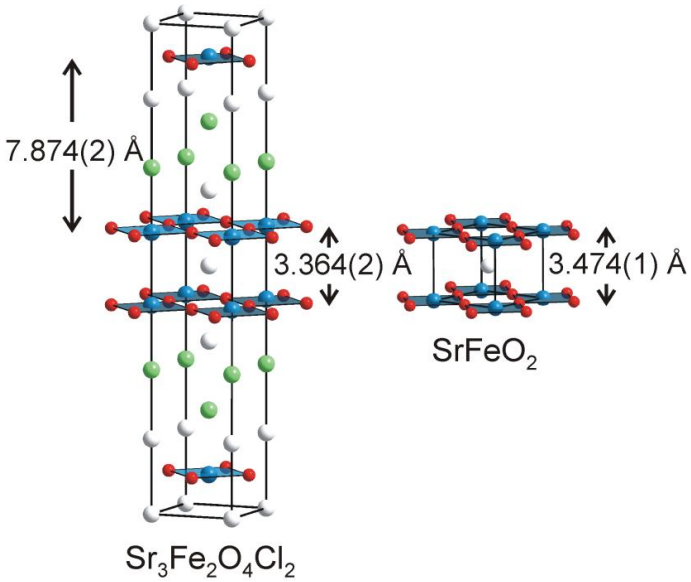


Figure 8.12: Distances between FeO_2 planes in $Sr_3Fe_2O_4Cl_2$ and $SrFeO_2$

As discussed above, square-planar Fe(II) centres in extended oxides are rare. However, the few examples present in the literature allow for fruitful electronic comparisons. Table 8.4

shows the pertinent magnetic data for the isoelectronic series $SrFeO_2$, $Sr_3Fe_2O_4Cl_2$ and $Sr_3Fe_2O_5$. Of particular interest is the comparison between $Sr_3Fe_2O_4Cl_2$ and the structurally similar infinite-layer phase $SrFeO_2$ (see Figure 8.12) as both adopt G-type antiferromagnetically ordered arrangements below T_N.[98]

Phase	Moment per iron centre at low T	T_N (K)
$SrFeO_2$[98]	3.6	473
$Sr_3Fe_2O_4Cl_2$	2.81(9)	378
$Sr_3Fe_2O_5$[103, 104]	2.76(5)	296

Table 8.4: Pertinent magnetic data for a some phases containing square planar Fe(II) centres

$SrFeO_2$, $Sr_3Fe_2O_5$ and $Sr_3Fe_2O_4Cl_2$ all adopt antiferromagnetically ordered structures with high ordering temperatures. Studies based on Mossbauer spectroscopy concluded that the high magnetic ordering temperatures in $SrFeO_2$ and $Sr_3Fe_2O_5$ are in part due to the strong hybridisation in the Fe-O contacts.[98, 99, 104] Given the structural similarities and the high magnetic ordering temperature, it seems likely that similarly strong hybridisation exists in the Fe-O contacts in $Sr_3Fe_2O_4Cl_2$

The lower ordering temperature and smaller ordered moment observed for $Sr_3Fe_2O_4Cl_2$, compared to $SrFeO_2$, suggests that the through space coupling mechanism discussed above is a limiting factor. The insertion of SrCl layers into the structure of $Sr_3Fe_2O_4Cl_2$ to form isolated $SrFe_2O_4$ blocks and a more two-dimensional structure (see Figure 8.12) leads to a reduction in the strength of the magnetic interactions between these double layer blocks compared to the regularly spaced FeO_2 layers within the structure of $SrFeO_2$. This results in a reduction in both the magnetic ordering temperature and ordered moment. Analogous arguments based on dimensionality can be used to rationalise the reduction in the magnetic ordering temperatures of the isoelectronic and structurally related n = 2 RP $Sr_3Mn_2O_7$ and perovskite $SrMnO_3$ phase (see Table 8.5).[105, 106]

Phase	Moment per manganese centre at low T	T_N (K)
cubic-$SrMnO_3$[106]	2.6(2) at 77 K	260
$Sr_3Mn_2O_7$[105]	2.31(7)	160

Table 8.5: Pertinent magnetic data for $SrMnO_3$ and $Sr_3Mn_2O_7$

As shown in Figure 8.1, $Sr_3Fe_2O_5$ also contains Fe(II) centres in square planar coordination. However, in contrast to $SrFeO_2$ and $Sr_3Fe_2O_4Cl_2$, $Sr_3Fe_2O_5$ adopts a 'ladder' type structure in which the dominant magnetic exchange pathways can be considered one-dimensional. Thus it is no surprise that while $Sr_3Fe_2O_5$ also adopts a G-type antiferromagnetically ordered structure, it has a lower magnetic ordering temperature (T_N = 296 K) than $SrFeO_2$ and $Sr_3Fe_2O_4Cl_2$.[99, 104]

8.4.2. Structural selectivity

The reduction of $Sr_2Fe_2O_5Cl_2$ to form $Sr_2Fe_2O_4Cl_2$ proceeds with the selective removal of O(1) ions, demonstrating an apparent 'preference' over the removal of O(2) or Cl(1) ions. The following sections rationalise the 'preference' for the removal of O(1) over the other anions; the barrier to the reduction/rearrangement process to form the hypothetical '$Sr_2Fe_2O_3Cl_2$' phase in an analogous fashion to the formation of $Sr_3Fe_2O_5$ from $Sr_3Fe_2O_6$;[99] and the selective removal of oxide ions over chloride ions.

8.4.2.1. Selective removal of O(1)

The selective removal of the oxide anions from the 'bridging' axial or O(1) site from $Sr_2Fe_2O_5Cl_2$ is in direct contrast to the selective nature of topotactic reduction reactions of a number of other RP phases. For example, the reduction of $Sr_3Mn_2O_7$ to form $Sr_3Mn_2O_{6+x}$ proceeds with the removal of oxide anions from the 'equatorial' anion site (i.e. from the BO_2 layers) of the substrate phase (see Figure 1.10).[23] Following logic described previously,[27] the contrasting selectivity for these reactions can be rationalised on the basis of the formation energies of point vacancy defects at the various anion sites.

At the outset it is worth noting that this logic contains two major assumptions: firstly it is assumed that upon removal of an anion, the system does not relax to a more

thermodynamically stable state. Secondly, it is assumed that no electronic interactions between the metals and the anions are present, e.g. no LFSE contribution, which may raise the point vacancy formation energy of one anion over another. Taking these assumptions into account, removal of the anion with the lowest associated point defect formation energy should produce the most stable product with the restriction that the cation framework remains undisturbed throughout the reaction.

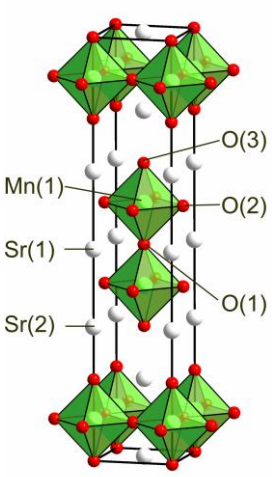
Upon reduction, the iron oxidation state drops, so the ideal geometry around the iron centres will contain longer/fewer anion contacts. In contrast, the ideal geometry around the strontium centres will remain unchanged throughout the reduction process. Therefore, the least amount of disruption to the structure would be caused by the removal of an anion with strong Fe-X contacts but with no Sr-X contacts. This situation is unrealistic as such a structure is hard to 'design'; however in the case of $Sr_3Fe_2O_5Cl_2$ is clear that the anion that most closely fits this relationship, i.e. strong Fe-X contacts and weak Sr-X contacts, will incur the lowest point vacancy defect formation energy.

To allow facile comparisons across a variety of phases, bond valence sum (BVS)[50] contributions can be used as a crude approximation to the bond strengths in a material and consequently the point anion vacancy formation energies. Therefore the anions with the lowest point vacancy defect formation energy will have the most positive Fe BVS contribution – Sr BVS contribution. Contributions made by the iron and strontium to the bond valence of the anion sites in $Sr_3Fe_2O_5Cl_2$ are shown in Table 8.6.

	O(1)	O(2)	Cl(1)
Fe(1) BVS	1.474	1.068	0.086
Sr(1) BVS	0.649	0.235	
Sr(2) BVS		0.636	1.155
Fe BVS – Sr BVS total	0.825	0.197	-1.069

Table 8.6: Bond valence sums calculated for the anion sites of $Sr_3Fe_2O_5Cl_2$

Therefore, in agreement with observation, it is predicted that the reduction reaction of $Sr_3Fe_2O_5Cl_2$ should proceed with the selective removal of the 'bridging axial' O(1) site.[107] Analogous calculations for the reduction of $Sr_3Mn_2O_7$ predict the opposite, and experimentally observed, selectivity.[23]



	O(1)	O(2)	O(3)
Mn(1) BVS	1.171	1.344	0.661
Sr(1) BVS	0.859	0.416	
Sr(2) BVS		0.546	1.201
Mn BVS – Sr BVS total	0.312	0.382	-0.540

Figure 8.13: Structure of $Sr_3Mn_2O_7$
Table 8.7: Bond valence sums calculated for the anion sites of $Sr_3Mn_2O_7$

8.4.2.2. Barrier to further reaction

As discussed above, $Sr_3Fe_2O_4Cl_2$, $SrFeO_2$ and $Sr_3Fe_2O_5$ all contain square planar Fe(II) centres, clearly demonstrating a common end point in the topotactic reduction reactions of the relevant substrate phases. Furthermore reduction reactions of $SrFeO_3$ and $Sr_3Fe_2O_{7-\delta}$ both proceed with a reduction/rearrangement of an apparently stable intermediate, i.e. the brownmillerite $Sr_2Fe_2O_5$ phase and $Sr_3Fe_2O_6$,[98, 99] a clear indication of the stability of the end products. It seems unlikely that this stability is purely attributable to effective crystal packing; indeed recent work has associated some electronic stability with this particular electronic state.[102] However, it is unclear why these high-spin Fe(II) d^6 systems adopt this

electronic state on LFSE grounds alone and further work is required to establish the origin of the stability of this electronic state.

The topotactic reduction of the *n* = 2 RP $Sr_3Fe_2O_7$ phase provides an interesting comparison to that of its oxychloride analogue. As discussed above, the reduction of $Sr_3Fe_2O_7$ to form $Sr_3Fe_2O_5$ proceeds via the formation of $Sr_3Fe_2O_6$ (a direct structural analogue of $Sr_3Fe_2O_4Cl_2$) as an intermediate.[99] While it is clear that both $Sr_3Fe_2O_4Cl_2$ and $Sr_3Fe_2O_6$ adopt strongly related structures, there is no evidence for an analogous reduction/rearrangement process in $Sr_3Fe_2O_4Cl_2$. Calculations based on BVS contributions shown in Table 8.8 predict that the reduction of $Sr_3Fe_2O_4Cl_2$ would occur with the partial removal of the 'equatorial' O(2) ions, in an analogous fashion to the formation of $Sr_3Fe_2O_5$ from $Sr_3Fe_2O_6$.

	O(2)	**Cl(1)**
Fe(1) BVS	0.959	0.083
Sr(1) BVS	0.445	
Sr(2) BVS	0.497	1.038
Fe BVS – Sr BVS	0.017	-0.955

Table 8.8: Bond valence sums calculated for the anion sites of $Sr_3Fe_2O_4Cl_2$

The reasons for the inhibition of this reduction/rearrangement process in $Sr_3Fe_2O_4Cl_2$ are two-fold: Firstly, further reduction of $Sr_3Fe_2O_4Cl_2$ would require the formation of iron centres with an average oxidation state of below +2. Extensive searches in the literature provide no evidence for the formation of extended solid state materials containing iron centres with such an oxidation state. Secondly, the formation of the hypothetical '$Sr_3Fe_2O_3Cl_2$' ladder-type structure would leave the strontium cations in the SrCl rock salt layers (Sr(2)) significantly 'under-bonded' in large anion-deficient O_2Cl_5 coordination spheres.

8.4.2.3. Chemical selectivity

Complex transition metal oxyhalides provide an opportunity to evaluate the ability of binary metal hydrides to selectively deintercalate anions other than oxide anions. As described above it is clear that during the reduction of $Sr_3Fe_2O_5Cl_2$ there is complete

selectivity for the removal of oxide ions over chloride ions. This selectivity can be rationalised on the basis of two factors: the strength of the Sr-Cl contacts compared to the Fe-Cl contacts and the magnitude of the lattice energy of the potential by-products (Li_2O vs. LiCl). These factors will be discussed in turn in the following sections.

8.4.2.3.1. Strength of the Sr-Cl contacts

The arguments based on BVS contributions described above clearly predict that anions with the largest Fe BVS – strontium BVS contribution will be selectively removed during the topotactic reduction reaction. BVS calculations (see Table 8.6) indicate that the chloride ions contribute only 4.2 % of the total valence sum of the iron centres in $Sr_3Fe_2O_5Cl_2$, but are 'bonded' much more strongly to the Sr(2) cation, i.e. the chloride ions have highly negative Fe BVS – Sr BVS. Removal of chloride ions from the structure of $Sr_3Fe_2O_5Cl_2$ as part of the reduction process would therefore have little effect on the valence of the iron centres. In contrast, each Sr(2) cation resides in a 9-coordinate coordination site of stoichiometry O_4Cl_5. Removal of the chloride ions from the structure would therefore leave the Sr(2) coordination sphere exceptionally anion-deficient, with a large destabilising effect on the lattice energy of the solid.

Using these considerations, it is clear that $Sr_3Fe_2O_5Cl_2$ does not adopt a structure amenable to the removal of chloride ions. Indeed, it is difficult to 'design' a mixed anion system from which anions other than oxide ions are predicted to be removed, i.e. the anion with the largest B BVS – A BVS contribution is not an oxide anion. Mixed-anion phases tend to form layered structures in which the anions segregate based on size and polarisability.[108] In these structures, the layers can usually be classed as BO_x and AX_y ($X \neq O$) with the strength of the of the B-O contacts clearly preventing such a system from meeting the bond strength condition stated above.

8.4.2.3.2. Lattice energy of the by-product

The removal of chloride ions from a complex oxyhalide would presumably occur via reaction (1) leading to the formation of LiCl as a by-product, compared to the observed reaction in which the removal of oxide ions leads to the formation of Li_2O.

Given that the conversion of the thermally unstable LiH ($\Delta H_{lattice\ per\ Li^+\ ion}$ = -916 $kJmol^{-1}$) to Li_2O ($\Delta H_{lattice\ per\ Li^+\ ion}$ = -2799/2 $kJmol^{-1}$ = 1399.5 $kJmol^{-1}$) or LiCl ($\Delta H_{lattice\ per\ Li^+\ ion}$ = -834 $kJmol^{-1}$) provides the thermodynamic driving force for the topotactic reduction reactions,[109] the greater lattice energy of Li_2O compared to LiCl is clearly a deciding factor for the course of the reaction. This further suggests that in general, topotactic reduction reactions will occur with the preferential deintercalation of oxide ions, rather than chloride ions, from the majority of complex oxyhalide hosts.

8.4.3. Sr_2FeO_3Cl formation

Heating $Sr_3Fe_2O_5Cl_2$ with CaH_2 or LiH at 400 ^oC results in the formation of Sr_2FeO_3Cl along with several by-products (see section 8.3.1). X-ray powder diffraction data collected from the sample formed on heating $Sr_3Fe_2O_5Cl_2$ with LiH at 400 ^oC and subsequent washing in CH_3OH could be successfully fitted using a multi-phase refinement containing Sr_2FeO_3Cl as a bulk phase in combination with $LiFeO_2$, $Sr_3Fe_2O_5Cl_2$ starting material and elemental iron.[25, 101, 110, 111] The details of this refinement are shown in Table 8.9 and the observed, calculated and difference plots for the refinement are shown in Figure 8.14.

Atom	Wyckoff position	*x*	*y*	*z*	U_{iso} (Å^2)	Occupancy
Sr(1)	2*c*	¾	¾	0.094(1)	0.041(1)	1
Sr(2)	2*c*	¾	¾	0.347(1)	0.008(1)	1
Fe(1)	2*c*	¼	¼	0.210(1)	0.061(2)	1
O(1)	2*c*	¼	¼	0.098(1)	0.063(7)	1
O(2)	4*f*	¼	¾	0.243(1)	0.034(3)	1
Cl(1)	2*c*	¼	¼	0.431(1)	0.019(2)	1
Sr_2FeO_3Cl:[101] space group *P*4/*nmmz*, *a* =3.9237(1) Å, *c* = 14.3298(3) Å, cell volume = 220.615(12) Å^3 $LiFeO_2$:[110] space group *Fm m*, *a* = 4.1562(1) Å; wt. frac. = 32.8(14) % $Sr_3Fe_2O_5Cl_2$:[25] space group *I*4/*mmm*, *a* =3.9466(5) Å, *c* = 23.8330(62); wt. frac = 0.7(1) % Fe:[111] space group *Im m*, *a* = 2.8660(1) Å, wt. frac. 20.1(13) % χ^2 = 1.138, wR_p = 4.68 %, R_p = 3.50 %						

Table 8.9: Details for refinement of multi-phase refinement with a majority phase of Sr_2FeO_3Cl

Sr_2FeO_3Cl adopts an *n* = 1 RP structure as shown in Figure 8.15.[101] Therefore, the transformation of $Sr_3Fe_2O_5Cl_2$ to Sr_2FeO_3Cl is highly unusual as it involves a major structural rearrangement from an *n* = 2 to an *n* = 1 RP structure. Several key points arising from this transformation are detailed in the following sections.

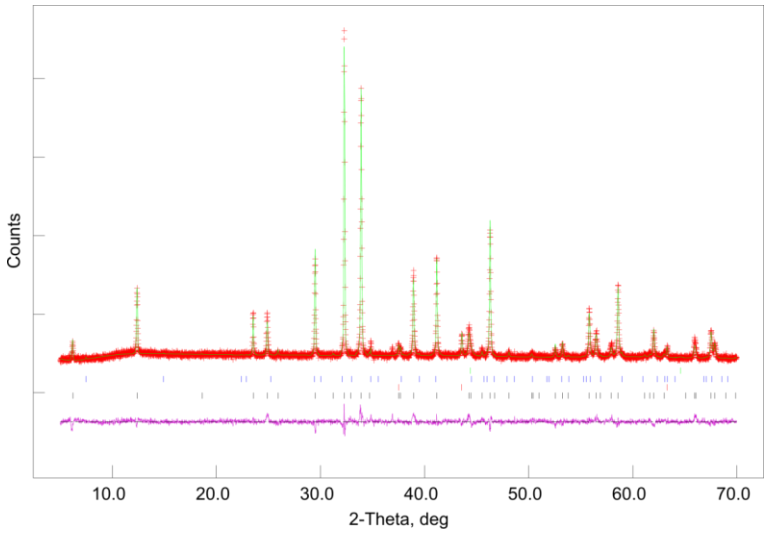


Figure 8.14: Observed, calculated and difference plots for multi-phase refinement of the washed products of the reaction of $Sr_3Fe_2O_5Cl_2$ and LiH at 400 °C.

8.4.3.1. Possible reaction routes

Both $Sr_3Fe_2O_5Cl_2$ and Sr_2FeO_3Cl contain iron with an oxidation state of +3. The *n* = 2 to *n* =1 RP transformation could proceed through a variety of different pathways: Firstly, the transformation could proceed with the formation of $Sr_3Fe_2O_4Cl_2$ (Fe(II)) as an intermediate,

followed by a disproportionation reaction to form Sr_2FeO_3Cl and elemental iron. Alternatively, the reaction could proceed by a direct route with no observable intermediate.

In an effort to determine the route of the reaction, a sample of $Sr_3Fe_2O_4Cl_2$ (Fe(II)), the formation of which is described in section 8.3.1, was ground together with a 1:2 molar ratio with CaH_2 in an argon-filled glovebox and heated at 400 ^oC in a sealed silica ampoule. X-ray powder diffraction data collected from the resultant phase are consistent with decomposition to binary metal compounds rather than the formation of Sr_2FeO_3Cl. Therefore, it seems reasonable to suggest that, despite the presence of strong reducing agents, the n = 2 to n =1 RP transformation reaction proceeds via a direct route with a constant iron oxidation state (Fe(III)) throughout. It is possible that the presence of the SrCl rock salt layer acts as an intrinsic flux for the n = 2 to n = 1 transformation, thereby favouring the n = 2 to n =1 RP transformation over the removal of the 'bridging' O(1) oxide anion at 400 ^oC.

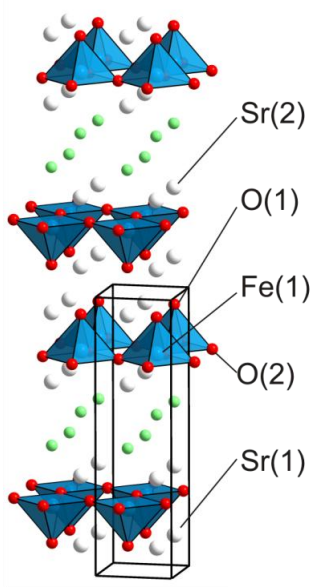
8.4.3.2. Driving force

The n = 2 to n = 1 RP transformation reaction does not occur when pure $Sr_3Fe_2O_5Cl_2$ is heated under vacuum at 400 ^oC. Therefore, the greater lattice energies of the by-products formed in each reaction, most notably Li_2O ($\Delta H_{lattice\ per\ Li^+\ ion}$ = 1399.5 $kJmol^{-1}$) and CaO ($\Delta H_{lattice\ per\ Ca^{2+}\ ion}$ = -3414 $kJmol^{-1}$), with respect to the binary metal hydrides, LiH ($\Delta H_{lattice\ per\ Li^+\ ion}$ = -916 $kJmol^{-1}$) and CaH_2 ($\Delta H_{lattice\ per\ Ca^{2+}\ ion}$ = -2410 $kJmol^{-1}$), must provide the thermodynamic driving force for the n = 2 to n = 1 transformation.[109]

8.4.3.3. Relative stabilities of the oxychlorides

The product of the n = 2 to n = 1 RP transformation reaction, Sr_2FeO_3Cl, does not react with LiH or CaH_2 at 400 ^oC. Using the logic based on BVS contributions described above, the most likely anion to be removed from Sr_2FeO_3Cl were a topotactic reduction reaction to occur would be the O(2) 'equatorial' anion (see Table 8.10). However, the reduced phase formed by the removal of the 'equatorial' anion is demonstrably unstable and there is no

facile rearrangement to a stable structure. As discussed above, the structures of $Sr_3Fe_2O_4Cl_2$, $SrFeO_2$ and $Sr_3Fe_2O_5$ all benefit from unexpected stabilisation associated with the formation of square planar Fe(II) centres. However there is no 'energetically available' and stable phase containing this electronic state formed by the topotactic reduction of Sr_2FeO_3Cl.



	O(1)	O(2)	Cl(1)
Fe(1) BVS	0.704	1.068	0.063
Sr(1) BVS	1.051	0.362	
Sr(2) BVS		0.804	1.058
Fe BVS – Sr BVS	-0.347	-0.098	-0.995

Figure 8.15: Structure of Sr_2FeO_3Cl
Table 8.10: Bond valence sums calculated for the anion sites of Sr_2FeO_3Cl

8.5. Conclusion

In conclusion, the topotactic reduction reaction of $Sr_3Fe_2O_5Cl_2$ using LiH at 400 ^oC results in the formation of $Sr_3Fe_2O_4Cl_2$, a structure containing sheets of vertex-sharing $Fe(II)O_4$ square planar units. This structure is closely related to $SrFeO_2$ and $Sr_3Fe_2O_5$ which both contain similar $Fe(II)O_4$ square planar units. $Sr_3Fe_2O_4Cl_2$ adopts a G-type antiferromagnetically ordering structure below $T_N \sim 378(10)$ K.

The topotactic reduction reaction of $Sr_3Fe_2O_5Cl_2$ proceeds with precise selectivity over the removal of the 'bridging axial' oxide anion (O(1)) from the structure. This chapter contains several comparisons between the structures of $Sr_3Fe_2O_4Cl_2$, $SrFeO_2$ and $Sr_3Fe_2O_5$ and their magnetic behaviour; most notably the reduction in magnetic ordering temperature with decreasing dimensionality of the structure.

The topotactic reduction reaction of $Sr_3Fe_2O_5Cl_2$ and the isoelectronic all-oxide analogue ($Sr_3Fe_2O_7$) proceed to different extents. This contrast results in the formation of an isoelectronic pair of phases with different anion frameworks. This observation suggests that by careful selection of the substrate phase the structure of the reduced phase can controlled. The research and findings detailed in this chapter have been reported in a recent publication.[107]

Appendix 8

Atom	***x***	***y***	***z***	**Moment (μ_B)**
Fe(1)	0	0.5	0.074	2.81(9)
Fe(2)	0.5	0	0.074	-2.81(9)
Fe(3)	0.5	0.5	0.426	2.81(9)
Fe(4)	0	0	0.426	-2.81(9)
Fe(5)	0.5	0.5	0.574	-2.81(9)
Fe(6)	0	0	0.574	2.81(9)
Fe(7)	0	0.5	0.926	-2.81(9)
Fe(8)	0.5	0	0.926	2.81(9)
Space group: *P*1, *a* = *b* = 5.669 Å, c = 22.653 Å, cell volume = 728.012 Å^3				

Table 8.11: Details of magnetic model for $Sr_3Fe_2O_4Cl_2$ at 5 K.

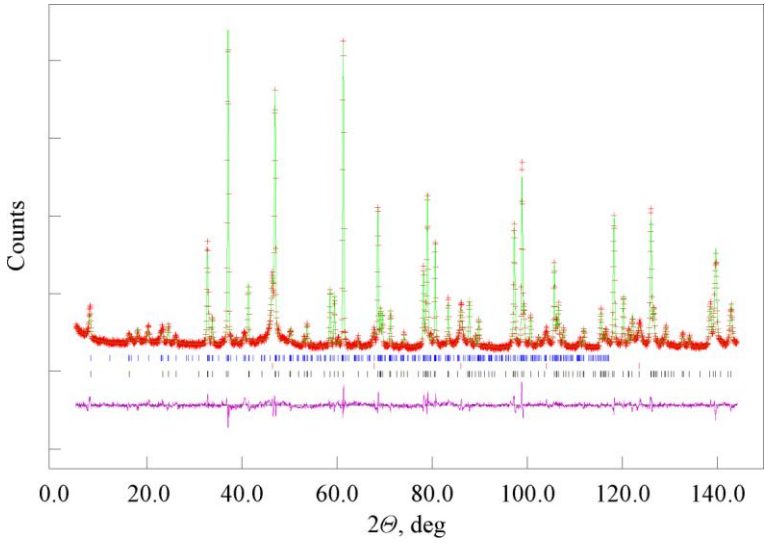


Figure 8.16: Observed, calculated and difference plots for the refinement of the structural model for $Sr_3Fe_2O_4Cl_2$ at 5 K, including the magnetic model, against neutron powder diffraction data collected using the D2b instrument

Chapter 9: Topotactic Reduction of $Sr_3Fe_{2-x}Co_xO_5Cl_2$

9.1. Introduction

Since the discovery of high-temperature superconductivity in complex copper oxides,[112] there has been great interest in preparing materials which contain square-planar MO_4 transition-metal centres. In particular, interest has focused on the synthesis of materials in which these centres are arranged into corner-linked sheets, analogous to the CuO_2 sheets present in the superconducting cuprate phases.[113] However despite extensive investigations, there are very few reports of thermodynamically stable phases which are not based on copper but still contain such MO_4 centres.

Given the apparent low thermodynamic stability of extended oxide phases containing square-planar transition metal centres, a logical synthetic approach is to use kinetically controlled chemical processes to prepare suitable metastable phases. There are several examples of topotactic reduction reactions resulting in the formation of materials containing square-planar MO_4 centres. For example, the reduction reactions of the Ni(III) oxides $LaNiO_3$ and $LaSrNiO_4$ at low-temperature yield the Ni(I) phases $LaNiO_2$ and $LaSrNiO_3$ respectively,[26, 114] which both contain extended arrays of corner-linked $Ni^{I}O_4$ square-planes. Specifically $LaNiO_2$ forms the so-called 'infinite-layer' structure and is isostructural with $Ca_{0.84}Sr_{0.16}CuO_2$,[115] while $LaSrNiO_3$ adopts a one-dimensional structure isostructural with Sr_2CuO_3 [116] as shown in Figure 9.1. The formation of anion-deficient phases such as $LaNiO_2$ and $LaSrNiO_3$, which contain $Ni^{I}O_4$ centres, is attributable to the favourable crystal-field stabilisation energy associated with the d^9 electron count of these ions in such a coordination environment.

However, as discussed in Chapter 8, it is possible to prepare phases containing vertex-linked square planar MO_4 centres in the absence of such favourable crystal-field stabilisation energies. The topotactic reduction reactions of $SrFeO_3$, $Sr_3Fe_2O_{7-\delta}$ and $Sr_3Fe_2O_5Cl_2$ result in

the formation of $SrFeO_2$, $Sr_3Fe_2O_5$ and $Sr_3Fe_2O_4Cl_2$ respectively which all contain corner-linked $Fe^{II}O_4$ square planar centres as shown in Figure 9.1.[98, 103]

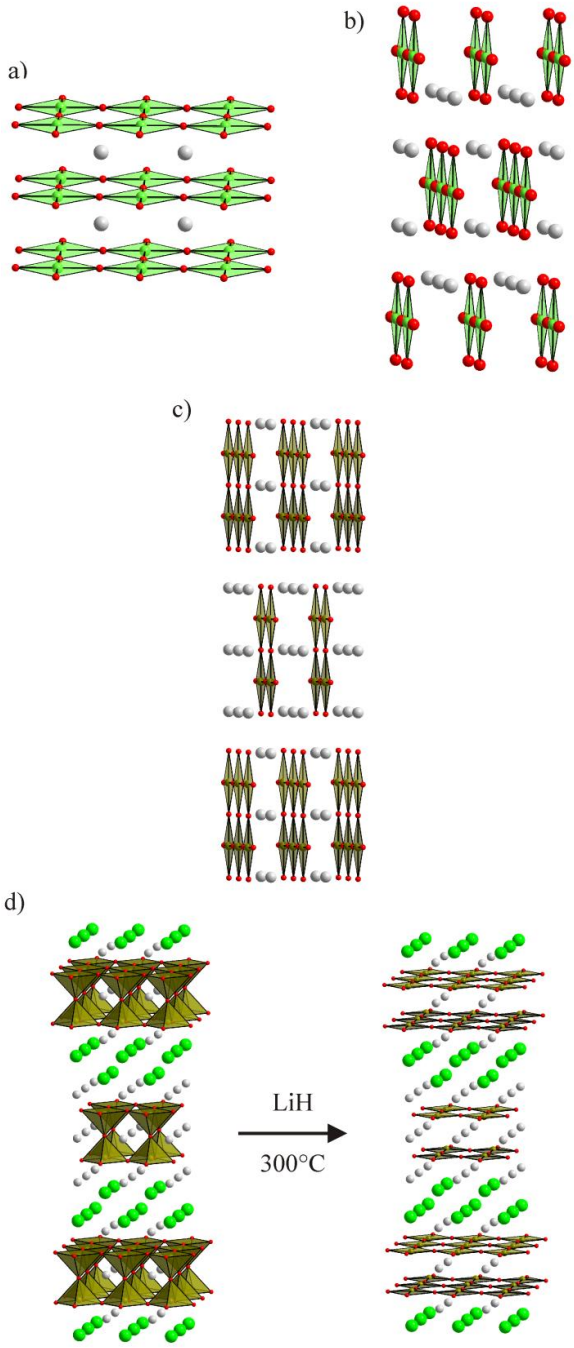


Figure 9.1: a) Infinite-layer structure of $LaNiO_2$, $SrFeO_2$ and $Ca_{0.64}Sr_{0.16}O_2$; b) Structure of $LaSrNiO_3$ and Sr_2CuO_3; c) Structure of $Sr_3Fe_2O_5$ and d) The topotactic reduction reaction of $Sr_3Fe_2O_5Cl_2$ to form $Sr_3Fe_2O_4Cl_2$, the latter containing sheets of $Fe^{II}O_4$ square planar units.[117]

As discussed in section 8.4.2.2, it is not clear what directs $SrFeO_2$, $Sr_3Fe_2O_5$ and $Sr_3Fe_2O_4Cl_2$ to adopt anion deficient structures which contain Fe(II) centres in these highly unusual square-planar coordination sites. The high-spin d^6 electronic configuration adopted

by the Fe(II) centres in these phases is offered no obvious stabilisation by square-planar coordination geometries. As detailed in section 8.4.2.1, the structures of the products of the majority of topotactic reduction reactions can be rationalised by considering the bonding requirements of the A-cations.[9, 27] However, the reduction reactions of $SrFeO_3$ and $Sr_3Fe_2O_{7-\delta}$ both proceed through apparently stable intermediates (the $Sr_2Fe_2O_5$ brownmillerite phase and anion-deficient n =2 $Sr_3Fe_2O_6$ RP phase shown in Figure 1.10 respectively)[24, 118] with the formation of the final products requiring large scale rearrangements of the anion lattice. Therefore, it is hard to rationalise the structures adopted by the $SrFeO_2$ and $Sr_3Fe_2O_5$ reduced phases on the basis of the coordination preferences of the Sr^{2+} A-cations.

A recent study by Kageyama *et al*. has attempted to rationalise the structural selectivity associated with the topotactic reduction reaction of $SrFeO_2$.[119] The authors performed the topotactic reduction reactions of $SrFe_{1-x}M_xO_{3-\delta}$ (M = Co, Mn; $0 < x \leq 0.4$) phases to determine the effect of the B-site composition, and thus *d*-electron count, on the structural selectivity of the reduction reaction.[119] It was observed that at substitution levels of 30 % or below, the reduction of $SrFe_{1-x}(Mn/Co)_xO_{3-\delta}$ substrate phases led, as expected, to the formation of the corresponding 'infinite-layer' $SrFe_{1-x}(Mn/Co)_xO_2$ phases. However at substitution levels of greater than 30 % the reduction reactions led to the formation of alternative products which are yet to be identified. The sensitivity of the structure of the reduced phases to B-site composition does suggest that the d^6 electronic configuration of the Fe(II) centres plays some role in directing the formation of anion deficient structures with square-planar $Fe^{II}O_4$ coordination sites.

In this work Kageyama *et al.* also noted that the magnetic properties of the 'infinite-layer' $SrFe_{1-x}(Mn/Co)_xO_2$ phases are affected by the B-site composition.[119] While the cobalt-doped materials retain the G-type antiferromagnetically ordered structure exhibited by $SrFeO_2$, the manganese-doped materials adopt frustrated magnetic systems.[119]

As discussed in section 9.4.1, the topotactic reduction reaction of $Sr_3Fe_2O_5Cl_2$ to form $Sr_3Fe_2O_4Cl_2$ is directed by the coordination preferences of the Sr^{2+} A-cations. As a result the reactions which form $Sr_3Fe_2O_4Cl_2$ are expected to be much more tolerant to B-cation substitution than those which form $SrFeO_2$. Therefore the topotactic reduction reactions of $Sr_3Fe_{2-x}Co_xO_5Cl_2$ ($0 \leq x \leq 1$) phases were performed to analyse the effect of cobalt substitution on the crystal structure and magnetic behavior of the isostructural $Sr_3Fe_{2-x}Co_xO_4Cl_2$ ($0 \leq x \leq 1$) series of reduced phases, thereby allowing comparison to the analogous $SrFe_{1-x}Co_xO_2$ ($0 \leq x \leq 0.3$) phases.

9.2. Experimental

9.2.1. Preparation of $Sr_3Fe_{2-x}Co_xO_5Cl_2$ phases

Samples of $Sr_3Fe_{2-x}Co_xO_5Cl_2$ (x = 0.2, 0.6, 0.8 and 1) were prepared by the direct-combination route previously described by Weller *et al.* for the synthesis of $Sr_3FeCoO_5Cl_2$.[25] Suitable quantities of SrO (prepared by the decomposition of $SrCO_3$ at 1100 ^oC under vacuum), $SrCl_2$ (dried at 180 ^oC under vacuum), Fe_2O_3 (Alfa Aesar, 99.99 %) and $Sr_2Co_2O_5$ (prepared using the method described by Grenier *et al.*)[120] were thoroughly mixed in an agate pestle and mortar in an argon filled glovebox (O_2 and H_2O levels < 1 ppm). The resulting mixtures were then sealed under vacuum in silica ampoules and heated at 850 ^oC for 2 periods of 24 hours with one intermediate grinding. X-ray powder diffraction data sets collected from $Sr_3Fe_{2-x}Co_xO_5Cl_2$ samples were consistent with single phase materials with lattice parameters which span the range between the values reported for $Sr_3Fe_2O_5Cl_2$ and $Sr_3FeCoO_5Cl_2$ as shown in Table 9.7 in Appendix 9.[25]

9.2.2. Reduction of $Sr_3Fe_{2-x}Co_xO_5Cl_2$ phases

The reduction reactions of the $Sr_3Fe_{2-x}Co_xO_5Cl_2$ (x = 0.2, 0.6, 0.8 and 1) phases were performed using LiH as a solid state reducing agent[28] in a similar manner to that reported for the topotactic reduction reaction of $Sr_3Fe_2O_5Cl_2$ (see section 8.2.2). Small samples

(~ 300 mg) of the required $Sr_3Fe_{2-x}Co_xO_5Cl_2$ (x = 0.2, 0.6, 0.8 and 1) phase were ground together in a 1:4 molar ratio with LiH in an argon filled glovebox. These mixtures were then sealed under vacuum in Pyrex ampoules and heated at temperatures between 210 ^oC and 400 ^oC to monitor the temperature dependence of the reduction reactions.

Due to the hazards associated with the production of hydrogen gas when using LiH as a reducing agent,[28] large-scale samples suitable for characterisation by neutron powder diffraction were synthesised in a sealed Parr Series 4740 Pressure Vessel (see section 2.2.2) which is capable of withstanding the pressures generated by the hydrogen gas produced in these reactions. Approximately 4 g of the required $Sr_3Fe_{2-x}Co_xO_5Cl_2$ (x = 0.2, 0.6, 0.8, 0.9 and 1) phase was mixed, in an argon filled glovebox, with 4 mole equivalents of LiH and loaded into an alumina finger which was then sealed in the pressure vessel. The pressure vessel was then evacuated, sealed and heated so that the sample was held at 300 ^oC for 4 periods of 24 hours with intermediate grinding. After reaction, samples were washed with 4 x 100 ml aliquots of CH_3OH, under nitrogen, to remove any lithium containing phases (unreacted LiH and Li_2O) before being dried under vacuum.

9.3. Results

9.3.1. Reactivity of $Sr_3Fe_{2-x}Co_xO_5Cl_2$

X-ray powder diffraction data collected from the products of the reactions between $Sr_3Fe_{2-x}Co_xO_5Cl_2$ phases and LiH reveal that at temperatures below 300 ^oC no reactions occur. Reactions performed at temperatures above 350 ^oC result in decomposition of the $Sr_3Fe_{2-x}Co_xO_5Cl_2$ substrate phases to form a complex mixture of binary metal oxides, chlorides and elemental iron and cobalt. However, in the temperature range $300 < T\ (°C) \leq 350$ reactions result in the formation of body-centred tetragonal phases with lattice parameters similar to that of $Sr_3Fe_2O_4Cl_2$, indicating that topotactic reduction reactions of the $Sr_3Fe_{2-x}Co_xO_5Cl_2$ substrate phases had occurred.

Examination of X-ray powder diffraction data collected from samples before and after the CH_3OH washing procedure (see Figure 9.9 - Figure 9.12 in Appendix 9) revealed the presence of a number of weak additional reflections in the data sets collected after the CH_3OH washing procedure had been completed. These additional reflections are consistent with the presence of small amounts of $Sr_3Fe_{2-x}Co_xO_5Cl_2$ starting material formed by mild oxidation during the washing procedure. The relative phase fractions of these re-oxidised $Sr_3Fe_{2-x}Co_xO_5Cl_2$ phases with respect to the $Sr_3Fe_{2-x}Co_xO_4Cl_2$ target phases can be minimised by the use of dry solvents and rigorously anaerobic conditions. However, with the exception of the x = 1 member, their presence could not be eliminated. The highly air-sensitive nature of the $Sr_3Fe_{2-x}Co_xO_4Cl_2$ phases is consistent with the pyrophoric behaviour of $Sr_3Fe_2O_4Cl_2$ (see section 8.3.2.4).[107][107][107][107][107][107][107][107][107][106][106]

9.3.2. Structural refinement

9.3.2.1. Neutron diffraction data

Table 9.1 shows the details of the neutron powder diffraction experiments used to collect data from the washed products of the reactions described above.

	Instrument in temperature range		
Reduced phase	**5 < T (K) < 300**	**298 K**	**300 < T (K) < 323**
$Sr_3Fe_{1.8}Co_{0.2}O_4Cl_2$	D1b, ILL λ = 2.52 Å	D1a, ILL λ = 1.91 Å	D2b, ILL λ = 1.59 Å
$Sr_3Fe_{1.4}Co_{0.6}O_4Cl_2$	D1b, ILL λ = 2.52 Å	D1a, ILL λ = 1.91 Å	N/A
$Sr_3Fe_{1.2}Co_{0.8}O_4Cl_2$	D2b, ILL λ = 1.59 Å	D2b, ILL λ = 1.59 Å	N/A
$Sr_3FeCoO_4Cl_2$	POLARIS, ISIS	POLARIS, ISIS	N/A

Table 9.1: Details of the neutron powder diffraction experiments used to collect data from $Sr_3Fe_{2-x}Co_xO_4Cl_2$ phases – see section 2.3.2 for details of instruments

9.3.2.2. Room temperature neutron diffraction data

The majority of the reflections in the neutron diffraction data collected from the reduced $Sr_3Fe_{2-x}Co_xO_4Cl_2$ samples at room temperature could be readily indexed on the basis of body-

centred tetragonal cells (see Table 9.2), with lattice parameters similar to those of $Sr_3Fe_2O_4Cl_2$. Structural models based on the refined structure of $Sr_3Fe_2O_4Cl_2$ (see Table 8.3) were therefore constructed for the $Sr_3Fe_{2-x}Co_xO_4Cl_2$ phases and refined against these neutron diffraction data sets. However, as in the X-ray diffraction data sets, the neutron diffraction data sets also contained additional weak reflections, consistent with the presence of small amounts of $Sr_3Fe_{2-x}Co_xO_5Cl_2$ starting material in the samples. Therefore, structural models for the $Sr_3Fe_{2-x}Co_xO_5Cl_2$ starting materials were added to the refinements to account for these additional diffraction features.[25]

Further diffraction features were observed in the neutron diffraction data set collected from $Sr_3Fe_{1.8}Co_{0.2}O_4Cl_2$, consistent with the presence of long range magnetic order, as observed previously in $Sr_3Fe_2O_4Cl_2$ (see section 8.4.1). A magnetically ordered model, more fully described in section 9.3.3, was therefore added to the refinement performed against this data set.

In the final stages of all 5 refinements, the fractional occupancies of all the anion sites (both oxide and chloride) were refined to confirm the stoichiometries of the bulk phases. However, all the anion sites remained fully occupied within error, thereby confirming the $Sr_3Fe_{2-x}Co_xO_4Cl_2$ compositions. The structural refinements against all 5 room temperature data sets converged readily to give good statistical fits to the data (see Table 9.2).

As discussed previously, the topotactic reduction reactions of $Sr_3Fe_{2-x}Co_xO_4Cl_2$ phases proceed with the removal of the O(1) oxide ion at (½, ½, 0). In order therefore to model partial oxidation of the bulk phases which may have occurred during the washing procedure, an extra oxide ion site was added into each structural model at (½, ½, 0). However, the fractional occupancy of this site refined to zero occupancy in each refinement, demonstrating that the mild oxidation during the washing procedure resulted in a mixture of the

$Sr_3Fe_{2-x}Co_xO_4Cl_2$ bulk phase and the $Sr_3Fe_{2-x}Co_xO_5Cl_2$ starting material, rather than a partially oxidized $Sr_3Fe_{2-x}Co_xO_{5-y}Cl_2$ ($0 < y < 1$) phase.

The observed, calculated and difference plots from the structural refinement against the room temperature neutron diffraction data set collected from $Sr_3Fe_{1.4}Co_{0.6}O_4Cl_2$ (as an example of the $Sr_3Fe_{2-x}Co_xO_4Cl_2$ series) and the refined structure are shown in Figure 9.2. The fits to the data sets collected from the other $Sr_3Fe_{2-x}Co_xO_4Cl_2$ phases are shown in Figure 9.13 - Figure 9.15 in Appendix 9. In addition, the refined structural parameters and goodness of fit statistics for all the synthesised $Sr_3Fe_{2-x}Co_xO_4Cl_2$ ($0 \leq x \leq 1$) phases are shown in Table 9.2.

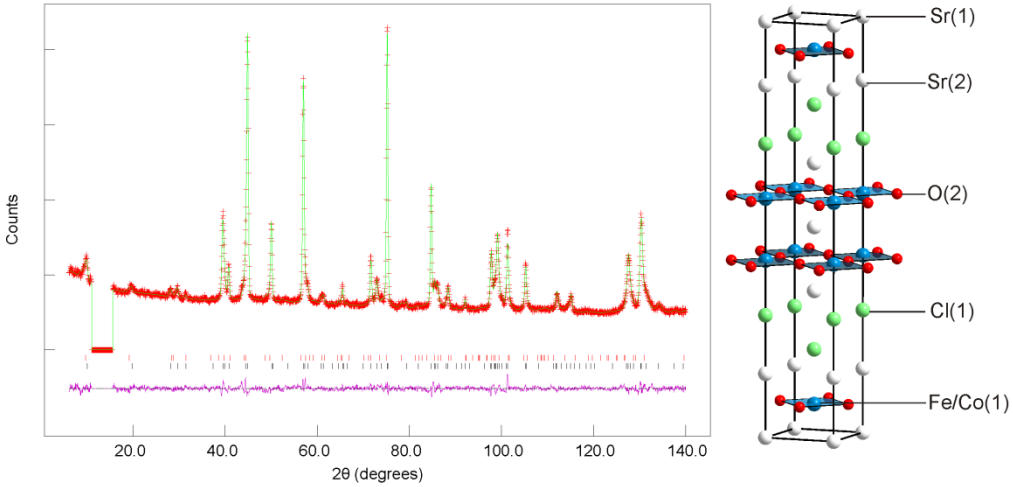


Figure 9.2: Observed, calculated and difference plots (left) from the structural refinement against neutron diffraction data collected from $Sr_3Fe_{1.4}Co_{0.6}O_4Cl_2$ at room temperature. The red tick marks relate to the $Sr_3Fe_{1.4}Co_{0.8}O_5Cl_2$ starting material. The excluded region between $11^o \leq 2\theta \leq 15.5^o$ contains a broad reflection due to the presence of glass in the sample. The refined structure is shown on the right.

$Sr_3Fe_{2-x}Co_xO_4Cl_2$	x = 0	x = 0.2	x = 0.6	x = 0.8	x = 1
a (Å)	4.0095(1)	4.0160(1)	4.0178(1)	4.0162(1)	4.0145(1)
c(Å)	22.6365(5)	22.6275(9)	22.552(1)	22.595(1)	22.4795(7)
Sr(1) U_{iso} (Å^2)	0.0054(2)	0.0072(18)	0.0136(21)	0.0104(15)	0.0038(4)
Sr(2) *z*	0.1524(1)	0.1526(1)	0.1526(2)	0.1528(2)	0.15309(7)
Sr(2) U_{iso} (Å^2)	0.0087(1)	0.0093(13)	0.0082(15)	0.0141(12)	0.0066(3)
Fe/Co *z*	0.4263(1)	0.4250(1)	0.4258(2)	0.4263(2)	0.42676(9)
Fe/Co U_{iso} (Å^2)	0.0048(1)	0.0061(7)	0.0032(8)	0.0023(2)	0.0021(2)
O *z*	0.4214(1)	0.4215(1)	0.4218(2)	0.4218(1)	0.42152(6)
O U_{iso} (Å^2)	0.0128(4)	0.0167(8)	0.0141(8)	0.0135(6)	0.0110(2)
Cl *z*	0.2950(1)	0.2948(1)	0.2954(1)	0.2956(1)	0.29492(6)
Cl U_{iso} (Å^2)	0.0135(3)	0.0121(7)	0.0122(8)	0.0134(6)	0.0129(2)
Wt. % $Sr_3Fe_{2-x}Co_xO_5Cl_2$	0	15%	17%	13%	0
χ^2	3.6	1.88	1.529	2.318	1.284
Diffractometer	D2B	D1A	D1A	D2B	POLARIS

Table 9.2: Structural parameters refined for $Sr_3Fe_{2-x}Co_xO_4Cl_2$ phases against room-temperature neutron powder diffraction data. Sr(1) is located at (0, 0, 0); Sr(2) at (0, 0, *z*); Fe/Co at (0, 0, *z*); O at (½, 0, *z*); Cl at (0, 0, *z*).

9.3.3. Magnetic characterisation

Variable temperature neutron powder diffraction data were collected from the $Sr_3Fe_{2-x}Co_xO_4Cl_2$ samples to characterise the long range magnetic order in these phases. As detailed in section 8.3.3, $Sr_3Fe_2O_4Cl_2$ adopts a G-type antiferromagnetically ordered structure below 378(10) K. Inspection of the data sets collected from $Sr_3Fe_{1.8}Co_{0.2}O_4Cl_2$ and $Sr_3Fe_{1.4}Co_{0.6}O_4Cl_2$ at 5 K revealed diffraction features consistent with the $a' = \sqrt{2} \times a$, $b' = \sqrt{2} \times b$, $c' = \sqrt{2} \times c$ magnetic cell for $Sr_3Fe_2O_4Cl_2$. Therefore, magnetic models analogous to that refined for $Sr_3Fe_2O_4Cl_2$ were refined against these 5 K data sets. The refinements converged readily to yield ordered moments of 3.00(16) μ_B and 2.90(21) μ_B per transition metal centre for $Sr_3Fe_{1.8}Co_{0.2}O_4Cl_2$ and $Sr_3Fe_{1.4}Co_{0.6}O_4Cl_2$ respectively. The observed, calculated and difference plots for these refinements are shown in Figure 9.3 and Figure 9.4.

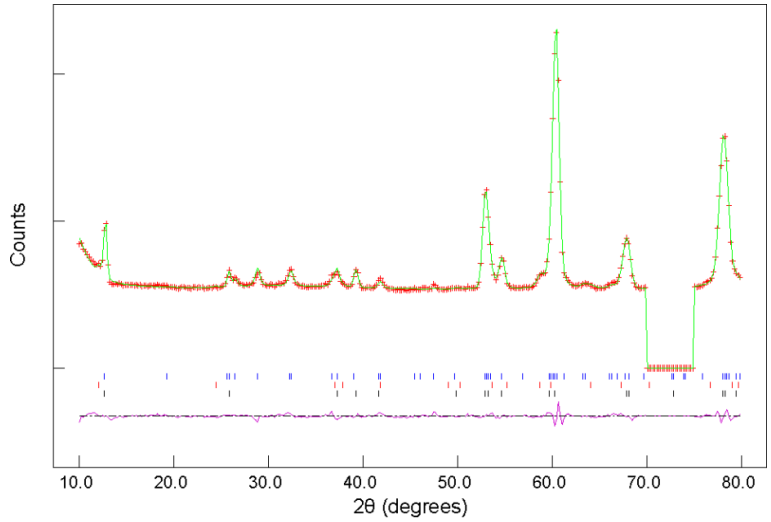


Figure 9.3: Observed, calculated and difference plots from the structural refinement against neutron diffraction data collected from $Sr_3Fe_{1.8}Co_{0.2}O_4Cl_2$ at 5 K. The red tick marks relate to the $Sr_3Fe_{1.8}Co_{0.2}O_5Cl_2$ starting material and the blue relate to the magnetic structure. The excluded region from $70^o \leq 2\theta \leq 76^o$ contains a major reflection from the vanadium sample holder.

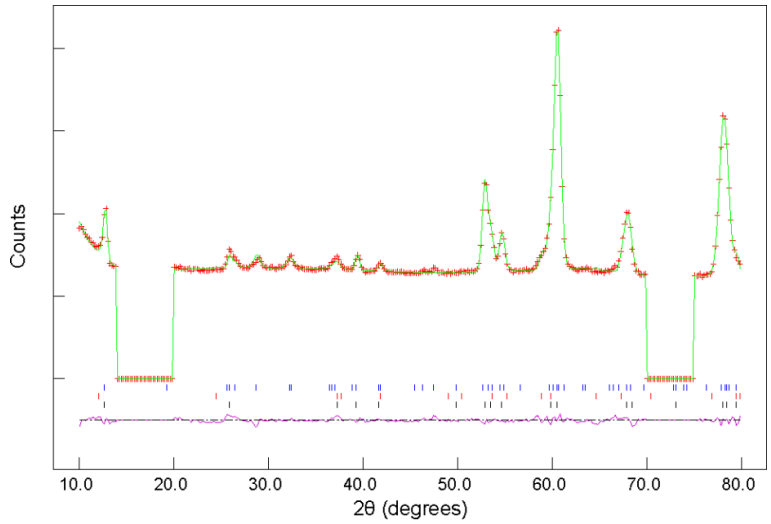


Figure 9.4: Observed, calculated and difference plots from the structural refinement against neutron diffraction data collected from $Sr_3Fe_{1.4}Co_{0.6}O_4Cl_2$ at 5 K. The red tick marks relate to the $Sr_3Fe_{1.4}Co_{0.6}O_5Cl_2$ starting material and the blue relate to the magnetic structure. The excluded region from $70^o \leq 2\theta \leq 76^o$ contains a major reflection from the vanadium sample holder. The excluded region between $11^o \leq 2\theta \leq 15.5^o$ contains a broad reflection due to the presence of glass in the sample.

Figure 9.5 shows a plot of the ordered magnetic moments per transition metal centre in $Sr_3Fe_{1.8}Co_{0.2}O_4Cl_2$ and $Sr_3Fe_{1.4}Co_{0.6}O_4Cl_2$ phases and, for comparison, $Sr_3Fe_2O_4Cl_2$ (see section 8.3.3) as a function of temperature.

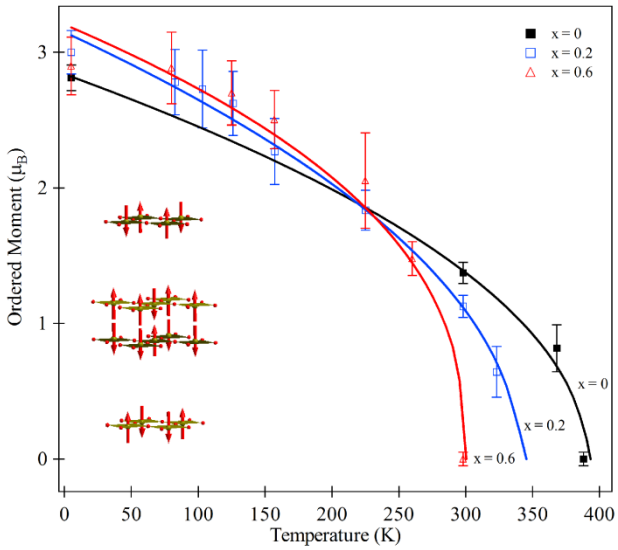


Figure 9.5: Plot of the refined ordered magnetic moment as a function of temperature for $Sr_3Fe_{2-x}Co_xO_4Cl_2$ (x = 0, 0.2, 0.6) phases. Inset shows the antiferromagnetically ordered structure of the $Sr_3Fe_{2-x}Co_xO_4Cl_2$ (x = 0, 0.2, 0.6) phases. Data for the x = 0 sample are taken from section 8.3.3.

The thermal dependence of the ordered moments could be fitted with an $I = A(1-(T/T_N))^{\beta}$ power law with the values shown in Table 9.3. In contrast, there was no indication of long range magnetic order in $Sr_3Fe_{1.2}Co_{0.8}O_4Cl_2$ and $Sr_3FeCoO_4Cl_2$ down to the lowest temperature measured (5 K).

Phase	β	T_N
$Sr_3Fe_2O_4Cl_2$	0.494	378 K
$Sr_3Fe_{1.8}Co_{0.2}O_4Cl_2$	0.495	340 K
$Sr_3Fe_{1.4}Co_{0.6}O_4Cl_2$	0.394	300 K

Table 9.3: Pertinent magnetic data for $Sr_3Fe_{2-x}Co_xO_4Cl_2$ (x = 0, 0.2, 0.6) phases

Magnetic susceptibility data collected from $Sr_3FeCoO_4Cl_2$, as a representative member of the $Sr_3Fe_{2-x}Co_xO_4Cl_2$ series, using the 'ferromagnetic subtraction' method described in section 2.7 are shown in Figure 9.6. Data in the temperature range 35 < T (K) < 300 can be fitted to the Curie–Weiss law ($\chi = C/(T-\theta)$) yielding values of C = 0.778(4) cm^3 K mol^{-1} and θ = -9.7(3) K K. This value of the Curie constant is significantly lower than would be expected for a simple paramagnet ($C_{expected}$ = 4.87 cm^3 K mol^{-1} assuming high-spin, S = 2 Fe^{2+} and high-spin, $S = {}^3/_2$ Co^{2+} centres). In addition, inspection of Figure 9.6 reveals that there is a maximum in the susceptibility data at approximately 25 K, indicative of a magnetic transition. As can be seen in the bottom pane of Figure 9.6, this feature at 25 K is associated

with a sharp increase in the saturated ferromagnetic moment of the sample from an essentially temperature independent value of ~1000 emu mol^{-1} in the range 35 < T (K) < 300 (attributable to the presence of elemental iron and cobalt) to 2500 emu mol^{-1} at 5 K.

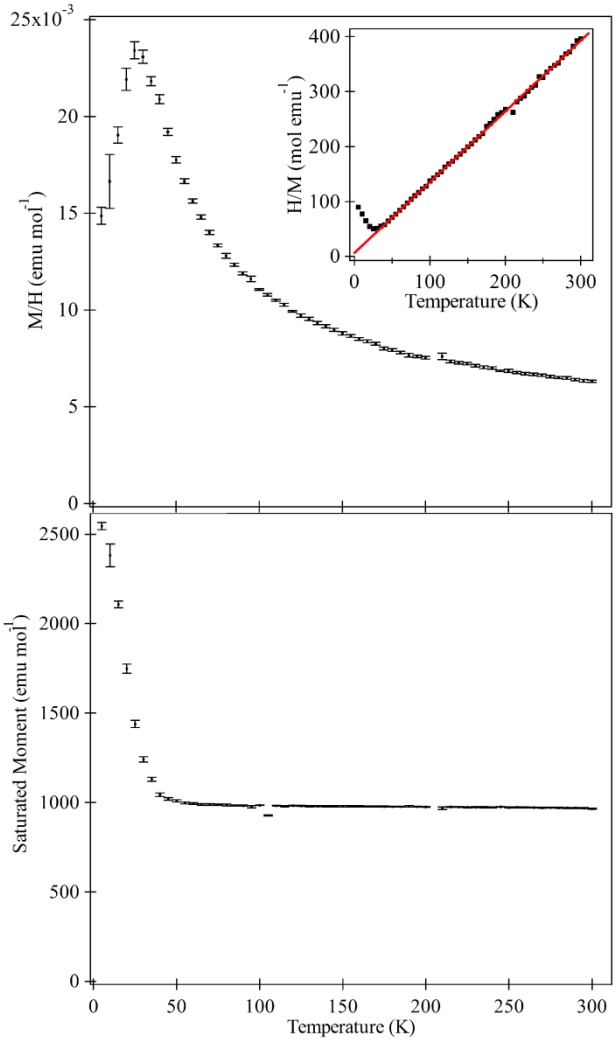


Figure 9.6: Magnetisation data collected from $Sr_3FeCoO_4Cl_2$ using the 'ferromagnetic subtraction' method. Upper panel shows the paramagnetic susceptibility as a function of temperature with the inset showing a fit to the Curie-Weiss law in the temperature range 35 ≤ T (K) ≤ 300. Lower panel shows the saturated ferromagnetic moment as a function of temperature.

As shown in Figure 9.7, this large increase in the saturated ferromagnetic moment in $Sr_3FeCoO_4Cl_2$ at low temperature is reflected in the magnetisation-field isotherms collected from $Sr_3FeCoO_4Cl_2$. In addition, close inspection of the field cooled magnetisation-field isotherm collected at 5 K reveals that the magnetisation-field loop is displaced to higher magnetisations. This observation is consistent with the maximum in the magnetisation data

collected from $Sr_3FeCoO_4Cl_2$ at approximately 25 K being associated with a transition to spin-glass type behaviour.

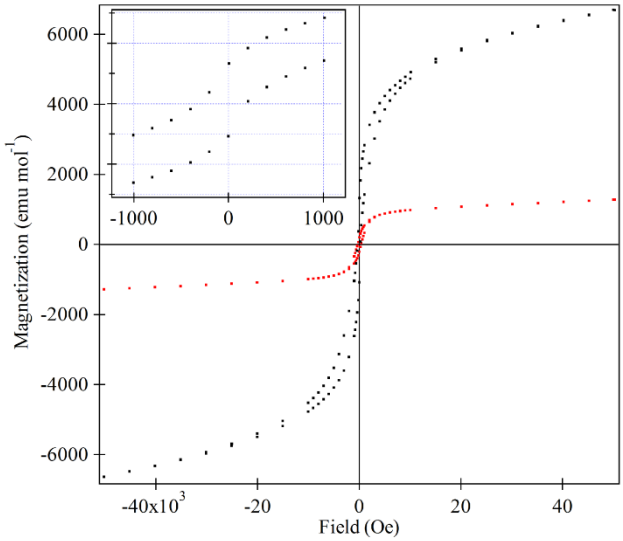


Figure 9.7: Magnetisation-field isotherms collected at 300 K (red) and 5 K (black) from $Sr_3FeCoO_4Cl_2$. Inset shows an expanded region of the 5 K isotherm emphasising that the data are displaced to higher magnetisations.

The magnetic susceptibility data collected from the $Sr_3Fe_{2-x}Co_xO_4Cl_2$ (x = 0.2, 0.6 and 0.8) phases show the same general features as those collected from $Sr_3FeCoO_4Cl_2$ (see Figure 9.16 - Figure 9.18 in Appendix 9). The Curie constants and Weiss temperatures extracted from the fits to these data in the range 35 < T (K) < 300 are shown in Table 9.4.

$Sr_3Fe_{2-x}Co_xO_4Cl_2$	$C_{obs.}$ (cm^3 K mol^{-1})	$C_{exp.}$ (cm^3 K mol^{-1})	θ (K)
x= 0.2	0.357(3)	5.775	-2.4(6)
x = 0.6	1.213(5)	5.325	-2.3(3)
x = 0.8	0.732(9)	5.10	-5.6(4)
x = 1	0.788(4)	4.875	-9.7(3)

Table 9.4: Pertinent magnetic information for the $Sr_3Fe_{2-x}Co_xO_4Cl_2$ (x = 0.2, 0.6, 0.8 and 1) phases

9.4. Discussion

9.4.1. Structural discussion

The reactions of phases in the compositional range $Sr_3Fe_{2-x}Co_xO_5Cl_2$ ($0.2 \leq x \leq 1$) with LiH result in the removal of oxide ions from the central SrO(1) layer. These reactions result in the formation of reduced phases with an empirical composition $Sr_3Fe_{2-x}Co_xO_4Cl_2$ which are isostructural with $Sr_3Fe_2O_4Cl_2$. While the $Sr_3Fe_{2-x}Co_xO_4Cl_2$ reduced phases are rare examples of materials containing square-planar $Fe^{II}O_4$ centres, there are a greater number of

materials containing $Co^{II}O_4$ centres, including the thermodynamically stable $Ba_2CoO_2Cu_2S_2$ and $Sr_2CoO_2Cl_2$ phases (see Figure 9.8).[121, 122]

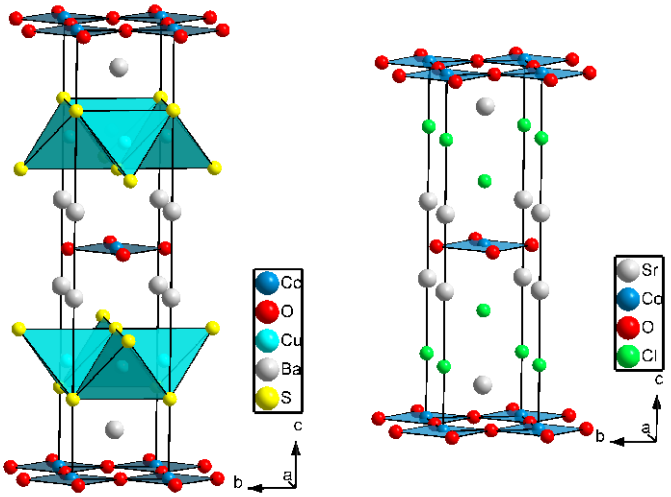


Figure 9.8: Structures of $Ba_2CoO_2Cu_2S_2$ (left) and $Sr_2CoO_2Cl_2$ (right)

Given the structural similarity between the $Sr_3Fe_{2-x}Co_xO_5Cl_2$ ($0 \leq x \leq 1$) substrate phases,[25] the similarity in the reactivity across the series is unsurprising. The same logic used to rationalise the selectivity of the topotactic reduction reaction of $Sr_3Fe_2O_5Cl_2$ (see section 8.4.2.1) can be applied to the reduction of $Sr_3FeCoO_5Cl_2$ (see Table 8.6). In agreement with the experimental findings, the 'bridging' or O(1) oxide ion is predicted to be removed from $Sr_3FeCoO_5Cl_2$.

	O(1)	**O(2)**	**Cl(1)**
Fe(1) BVS	**1.494**	1.104	0.082
Sr(1) BVS	**0.684**	0.342	
Sr(2) BVS		0.651	1.209
Fe BVS – Sr BVS total	**0.809**	0.121	-1.127

Table 9.5: Bond valence sums calculated for the anion sites of $Sr_3FeCoO_5Cl_2$

As discussed in the introduction to this chapter, the B-site in 'infinite-layer' $SrFe_{1-x}M_xO_2$ (M = Co, Mn) reduced phases can only accommodate 30 % manganese or cobalt before the structure changes. In contrast, the $Sr_3Fe_{2-x}Co_xO_4Cl_2$ reduced phases can accommodate a much wider range of cobalt-doping ($0 \leq x \leq 1$). This strongly suggests that the anion vacancy ordering patterns in $Sr_3Fe_{2-x}Co_xO_4Cl_2$ and $SrFe_{1-x}M_xO_2$ phases are controlled by different factors – the A-cation lattice in the former case and some electronic factor in the latter.[123]

The effect of the cobalt composition on the structures of the $Sr_3Fe_{2-x}Co_xO_4Cl_2$ reduced phases is minimal. As shown in Table 9.6, the *a*-lattice parameter and in-plane Co-O bonds are essentially unchanged within error across the series. The *c*-lattice parameter contracts by 0.7 % across the compositional range associated with a general contraction of the structure in this direction.

$Sr_3Fe_{2-x}Co_xO_4Cl_2$	Fe-O (Å)	Fe-Cl (Å)	Sr(1)-O (Å)	Sr(2)-O (Å)	Sr(2)-Cl (Å)	Sr(2)-Cl (Å)
x = 0	2.008(1)	2.972(3)	2.680(2)	2.610(2)	3.075(1)	3.228(3)
x = 0.2	2.010(1)	2.946(3)	2.681(1)	2.616(2)	3.079(1)	3.218(3)
x = 0.6	2.011(1)	2.941(5)	2.673(3)	2.617(4)	3.074(2)	3.220(5)
x = 0.8	2.011(1)	2.940(5)	2.670(1)	2.617(3)	3.068(2)	3.212(5)
x = 1	2.011(1)	2.964(2)	2.672(1)	2.616(1)	3.070(1)	3.188(2)

Table 9.6: Selected bond lengths extracted from the refinements of $Sr_3Fe_{2-x}Co_xO_4Cl_2$ phases. Data for the x = 0 sample are taken from Table 8.3 for comparison

The slight scatter in the data in Table 9.6 as a function of cobalt concentration is attributable to the systematic errors introduced by collecting the neutron powder diffraction data utilized in the structural refinements, using three different diffractometers (see Table 9.1).

9.4.2. Magnetic discussion

While the effect of the cobalt content on the structures of the $Sr_3Fe_{2-x}Co_xO_4Cl_2$ phases is negligible, the effect on the magnetic behaviour is more pronounced. As shown in Figure 9.5, the substitution of cobalt for iron leads to a steady reduction of the antiferromagnetic ordering temperature followed by a complete suppression of long range magnetic order for samples with $x \geq 0.8$. The mechanism for the general suppression of long range magnetic order across the series can be elucidated by inspection of the paramagnetic susceptibility data collected from $Sr_3Fe_{2-x}Co_xO_4Cl_2$ samples and consideration of the magnetic coupling interactions present in the sample, as follows:

9.4.2.1. Paramagnetic susceptibility data

As shown in Table 9.4, the Curie constants extracted from the paramagnetic susceptibility data collected from $Sr_3Fe_{2-x}Co_xO_4Cl_2$ samples are between 6 - 25 % of the values predicted for spin-only behaviour, representing a significant departure from simple paramagnetic behaviour. As discussed above, $Sr_3Fe_{1.8}Co_{0.2}O_4Cl_2$ and $Sr_3Fe_{1.4}Co_{0.6}O_4Cl_2$ adopt long-range antiferromagnetically ordered magnetic structures below 340 K and 300 K respectively. Therefore, the low values of the Curie constants for $Sr_3Fe_{1.8}Co_{0.2}O_4Cl_2$ and $Sr_3Fe_{1.4}Co_{0.6}O_4Cl_2$ are unsurprising. In these instances, the observed paramagnetic susceptibility is attributable to uncoupled spins at grain boundaries and other defect or surface sites.

In contrast, as discussed above, there is no evidence for any long range magnetic order in neutron powder diffraction data collected from $Sr_3Fe_{1.2}Co_{0.8}O_4Cl_2$ and $Sr_3FeCoO_4Cl_2$ phases. Therefore the low values for the Curie constants of the x = 0.8 and 1 members suggest that even in the absence of long range magnetic order, there are still strong antiferromagnetic interactions between spins. The combination of the lack of long range magnetic order and the displaced magnetisation-field loops at 5 K (see Figure 9.7) suggests that $Sr_3Fe_{1.2}Co_{0.8}O_4Cl_2$ and $Sr_3FeCoO_4Cl_2$ display spin-glass type behaviour. Therefore it is logical to suggest that the substitution of cobalt for iron in $Sr_3Fe_{2-x}Co_xO_4Cl_2$ adds competing magnetic interactions into the system leading to suppression of the long range antiferromagnetic order; initially leading to a reduction in the antiferromagnetic ordering temperature in cobalt-poor samples and ultimately leading to spin-glass type behaviour as the cobalt-content increases.

9.4.2.2. Magnetic interactions

As discussed in section 8.4.1, the local electronic configuration at the Fe(II) centres in $Sr_3Fe_2O_4Cl_2$ is $(d_{z^2})^2(d_{xz}, d_{yz})^2(d_{xy})^1(d_{x^2-y^2})^1$.[123] By consideration of the Goodenough-Kanamori rules,[52] the 180°, σ-type Fe $(d_{x^2-y^2})^1$ - O (2*p*) - Fe $(d_{x^2-y^2})^1$ interaction is predicted to bring about in-plane antiferromagnetic order. In addition, direct Fe $(d_{z^2})^2$ - Fe $(d_{z^2})^2$ exchange

interactions bring about antiferromagnetic order within the $SrFe_2O_4$ block. The great strength of these magnetic interactions is demonstrated by the high antiferromagnetic ordering temperature (378 K) observed in $Sr_3Fe_2O_4Cl_2$ (see section 8.4.1).

By analogy to other structurally related phases containing $Co^{II}O_4$ centres,[121] the ordering of the *d*-orbital energies on the Co(II) centres is predicted to be the same as that on the Fe(II) centres in $Sr_3Fe_2O_4Cl_2$. Therefore the Co(II) d^7 centres will have a local electronic configuration of $(d_{z^2})^2(d_{xz}, d_{yz})^3(d_{xy})^1(d_{x^2-y^2})^1$. The partial substitution of cobalt for iron leaves the population of the orbitals which participate in strong σ-type antiferromagnetic interactions unaffected (i.e. half-full $d_{x^2-y^2}$ orbitals and full d_{z^2} orbitals).

However, the substitution of cobalt for iron places an extra electron in the degenerate d_{xz} and d_{yz} orbital set relative to $Sr_3Fe_2O_4Cl_2$. This introduces the possibility of π-type Co $(d_{xz}/d_{yz})^2$ – O $(2p_z)$ – Fe $(d_{xz}/d_{yz})^1$ superexchange interactions which, by consideration of the Goodenough-Kanamori rules,[52] are predicted to be ferromagnetic. This ferromagnetic interaction is predicted to compete with other in-plane π-type magnetic interactions which are predicted to be antiferromagnetic (e.g. Co $(d_{xz}/d_{yz})^1$ – O $(2p_z)$ – Fe $(d_{xz}/d_{yz})^1$) and the underlying σ-type antiferromagnetic framework, thereby leading to magnetic frustration. This frustration leads to a reduction in the antiferromagnetic ordering temperature with increasing cobalt-content in $Sr_3Fe_{2-x}Co_xO_5Cl_2$ ($0 \leq x \leq 0.6$) phases and spin-glass type behavior in the ($0.8 \leq x \leq 1$) phases.

9.4.3. Comparison to $SrFe_{1-x}Co_xO_2$ ($x \leq 0.3$)

As discussed in the introduction to this chapter, Kageyama *et al.* observed that there is a reduction in the antiferromagnetic ordering temperatures of infinite-layer $SrFe_{1-x}Co_xO_2$ phases, the 3D structural analogues of $Sr_3Fe_{2-x}Co_xO_4Cl_2$, with increasing cobalt content.[119] It was reported that the antiferromagnetic ordering temperature of $SrFe_{0.7}Co_{0.3}O_2$ is "no more than 50 K" below that of $SrFeO_2$ ($T_N(SrFeO_2)$ = 473 K).[119] As a comparison, 30 %

substitution of the cobalt for iron in $Sr_3Fe_2O_4Cl_2$ results in an 80 K reduction in the antiferromagnetic ordering temperature. Therefore it is clear that the antiferromagnetic order in the $SrFe_{1-x}Co_xO_2$ ($x \leq 0.3$) phases is more robust with respect to cobalt substitution than in the $Sr_3Fe_{2-x}Co_xO_4Cl_2$ ($0 \leq x \leq 1$) phases. This is most likely attributable to the higher dimensionality of the structures of the $SrFe_{1-x}Co_xO_2$ phases (3D) compared to structures of the $Sr_3Fe_{2-x}Co_xO_4Cl_2$ ($0 \leq x \leq 1$) phases (2D).

As discussed in section 8.4.1, analogous arguments based on dimensionality can be used to explain the reduction in the antiferromagnetic ordering temperatures with decreasing dimensionality in the isoelectronic series $SrFeO_2$ (3D),[98] $Sr_3Fe_2O_4Cl_2$ (2D) and $Sr_3Fe_2O_5$ (1D):[103, 104] 473 K, 378 K and 296 K respectively. Therefore, it seems logical to predict that the substitution of the iron centres in $Sr_3Fe_2O_5$ would result in a much more pronounced effect on the magnetic behaviour than that observed in $SrFe_{1-x}Co_xO_2$ and $Sr_3Fe_{2-x}Co_xO_4Cl_2$ phases.

9.4.4. Comparison to high pressure $SrFeO_2$ and $Sr_3Fe_2O_5$ phases

Further work by Kageyama *et al*. has shown that $SrFeO_2$ exhibits a spin transition from a high-spin ($S = 2$) to an intermediate spin ($S = 1$) state when subjected to pressures in excess of 38 GPa.[124, 125] This transition is accompanied by a change from antiferromagnetic (AFM) to ferromagnetic metallic (FMM) behaviour. Furthermore, it has recently been shown that $Sr_3Fe_2O_5$ (see Figure 9.1) also exhibits an analogous spin and AFM-FMM transition at approximately the same critical pressure (34 GPa), indicating that the dimensionality of the structure has little effect on the spin transition.[125]

The high pressures required to induce this spin transition in $SrFeO_2$ and $Sr_3Fe_2O_5$ result in a large decrease in the volume of the unit cell. For example, the increase from ambient pressure to the pressure required for the transition results in an 11 % decrease (3.47 Å to 3.09 Å) in the distance between iron centres in neighbouring face-to-face FeO_4 units in

$SrFeO_2$.[124] Whangbo and Köhler have shown that the origin of the spin transition is dependent on the increased strength of the Fe-O-Fe interactions in linked FeO_4 units and Fe···Fe interactions between neighbouring face-to-face FeO_4 units brought about by the decrease in the interatomic distances.[126] The increase in the strength of these interactions leads to "electronic instability towards the depopulation of iron $d_{x^2-y^2}$ and oxygen p_σ antibonding states".[124] This leads to an increase in the iron *d*-electron count to '$d^{6.5}$' with the electronic configuration of the iron centres changing to "$(d_{z^2})^1(d_{xz}, d_{yz})^2(d_{xy})^1(d_{x^2-y^2})^{0.25}$ for the spin-up channel and $(d_{z^2})^1(d_{xz}, d_{yz})^1(d_{xy})^0(d_{x^2-y^2})^{0.25}$ for the spin-down channel".[124]

In an analogous fashion to this pressure-induced spin transition in $SrFeO_2$ and $Sr_3Fe_2O_5$, the substitution of cobalt for iron in $Sr_3Fe_2O_4Cl_2$ also results in an increase in both the *d*-electron count and population of the degenerate (d_{xz}, d_{yz}) orbitals of the transition metal centres. However there is no evidence to suggest that the cobalt-doped $Sr_3Fe_2O_4Cl_2$ materials display similar ferromagnetic metallic behaviour. The most logical explanation for this difference in behaviour is that cobalt-doped $Sr_3Fe_2O_4Cl_2$ phases retain half-occupied $d_{x^2-y^2}$ orbitals, while the population of the $d_{x^2-y^2}$ orbitals is reduced upon the transition to the high pressure $S = 1$ $SrFeO_2$ and $Sr_3Fe_2O_5$ phases. Therefore the strong σ-type Fe/Co $(d_{x^2-y^2})^1$ – O (2*p*) – Fe $(d_{x^2-y^2})^1$ superexchange interactions maintain the antiferromagnetic framework within the FeO_2 layers of the $Sr_3Fe_{2-x}Co_xO_4Cl_2$ phases (see section 9.4.2.2), thereby preventing the adoption of 3D ferromagnetically ordered schemes.

An alternative explanation is that the metallic behaviour exhibited by $SrFeO_2$ and $Sr_3Fe_2O_5$ is a result of the increase in the band width associated with the increase in orbital overlap brought about by the application of external pressure. Given the much larger interatomic distances, the $Sr_3Fe_{2-x}Co_xO_4Cl_2$ ($0 \leq x \leq 1$) phases at ambient pressures contain much poorer orbital overlap, and thus narrower bands, leading to insulating rather than metallic behaviour.

9.5. Conclusion

The topotactic reduction reactions of $Sr_3Fe_{2-x}Co_xO_5Cl_2$ ($0.2 \leq x \leq 1$) substrate phases are very similar to the reduction reaction of $Sr_3Fe_2O_5Cl_2$. In each case, the reactions result in the formation of $Sr_3Fe_{2-x}Co_xO_4Cl_2$ phases which adopt structures containing sheets of vertex-linked $Fe^{II}/Co^{II}O_4$ square planar units. The substitution of cobalt for iron results in a suppression in the frustration of the antiferromagnetic order, ultimately leading to spin glass behaviour in $Sr_3Fe_{2-x}Co_xO_4Cl_2$ ($0.8 \leq x \leq 1$) phases. This suppression is attributable to the competing magnetic interactions in the material brought about by the increase in the population of the degenerate d_{xz} and d_{yz} orbital set on the transition metal centres relative to $Sr_3Fe_2O_4Cl_2$. The results and findings detailed in this chapter have recently been published.[117]

Appendix 9

$Sr_3Fe_{2-x}Co_xO_5Cl_2$	*a* (Å)	*c* (Å)
x = 0	3.9470(1)	23.786(1)
x = 0.2	3.9436(1)	23.8043(4)
x = 0.6	3.9388(1)	23.8318(1)
x = 0.8	3.9360(1)	23.851(1)
x = 1	3.9295(4)	23.8676(4)

Table 9.7: Lattice parameters refined for $Sr_3Fe_{2-x}Co_xO_5Cl_2$ phases.

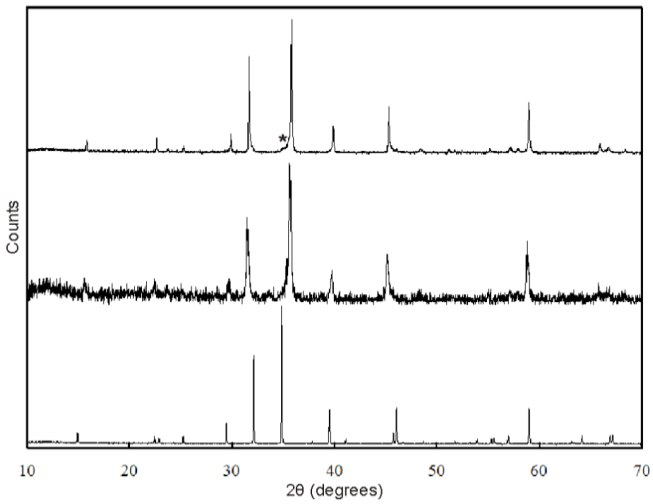


Figure 9.9: (Bottom to top) X-ray powder diffraction data collected from $Sr_3Fe_{1.8}Co_{0.2}O_5Cl_2$; product of the reaction between $Sr_3Fe_{1.8}Co_{0.2}O_5Cl_2$ and LiH at 350 ^oC; and the washed product of said reaction.

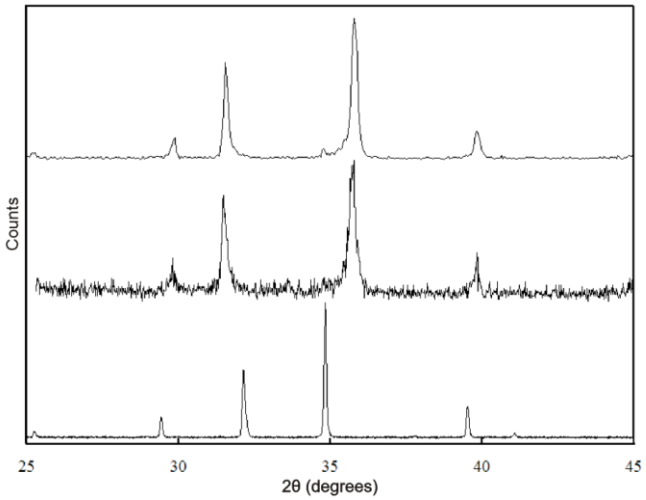


Figure 9.10: (Bottom to top) X-ray powder diffraction data collected from $Sr_3Fe_{1.4}Co_{0.6}O_5Cl_2$; the product of the reaction between $Sr_3Fe_{1.4}Co_{0.6}O_5Cl_2$ and LiH at 350 ^oC; and the washed product of said reaction.

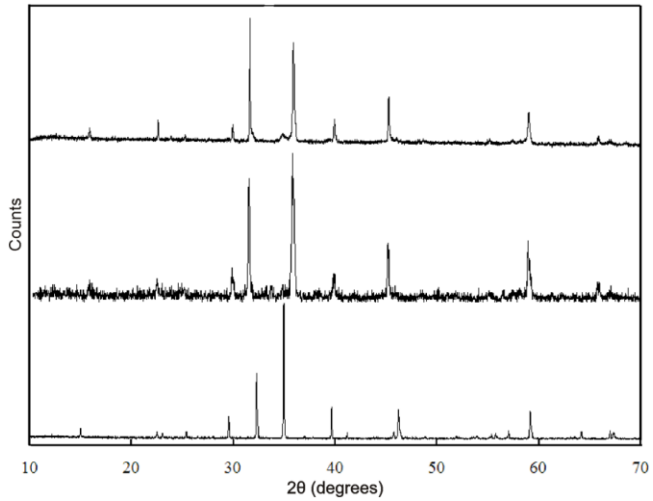


Figure 9.11: (Bottom to top) X-ray powder diffraction data collected from $Sr_3Fe_{1.2}Co_{0.8}O_5Cl_2$; the product of the reaction between $Sr_3Fe_{1.2}Co_{0.8}O_5Cl_2$ and LiH at 350 ^oC; and the washed product of said reaction.

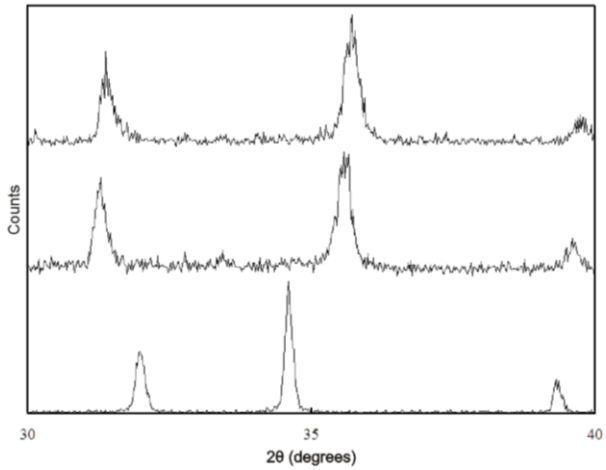


Figure 9.12: (Bottom to top) X-ray powder diffraction data collected from $Sr_3FeCoO_5Cl_2$; the product of the reaction between $Sr_3FeCoO_5Cl_2$ and LiH at 350 ^oC; and the washed product of said reaction.

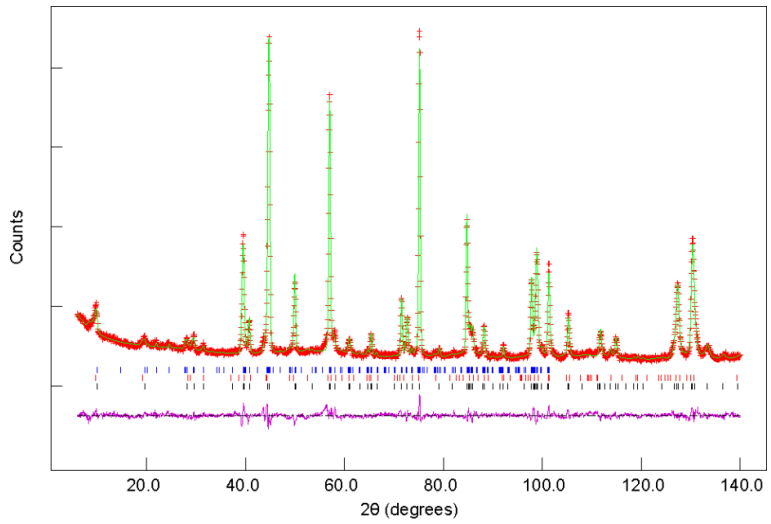


Figure 9.13: Observed, calculated and difference plots from the structural refinement against neutron diffraction data collected from $Sr_3Fe_{1.8}Co_{0.2}O_4Cl_2$ at room temperature. The red tick marks relate to the $Sr_3Fe_{1.8}Co_{0.2}O_5Cl_2$ starting material and the blue tick marks relate to the magnetically ordered model.

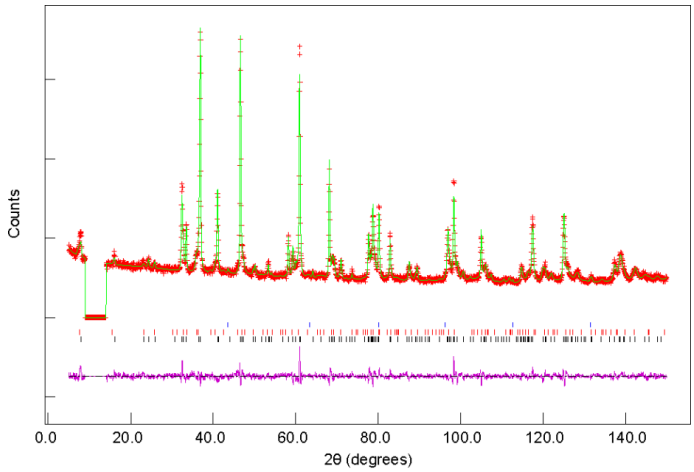


Figure 9.14: Observed, calculated and difference plots from the structural refinement against neutron diffraction data collected from $Sr_3Fe_{1.2}Co_{0.8}O_4Cl_2$ at room temperature. The red tick marks relate to the $Sr_3Fe_{1.2}Co_{0.8}O_5Cl_2$ starting material and the blue relate to the magnetic structure.

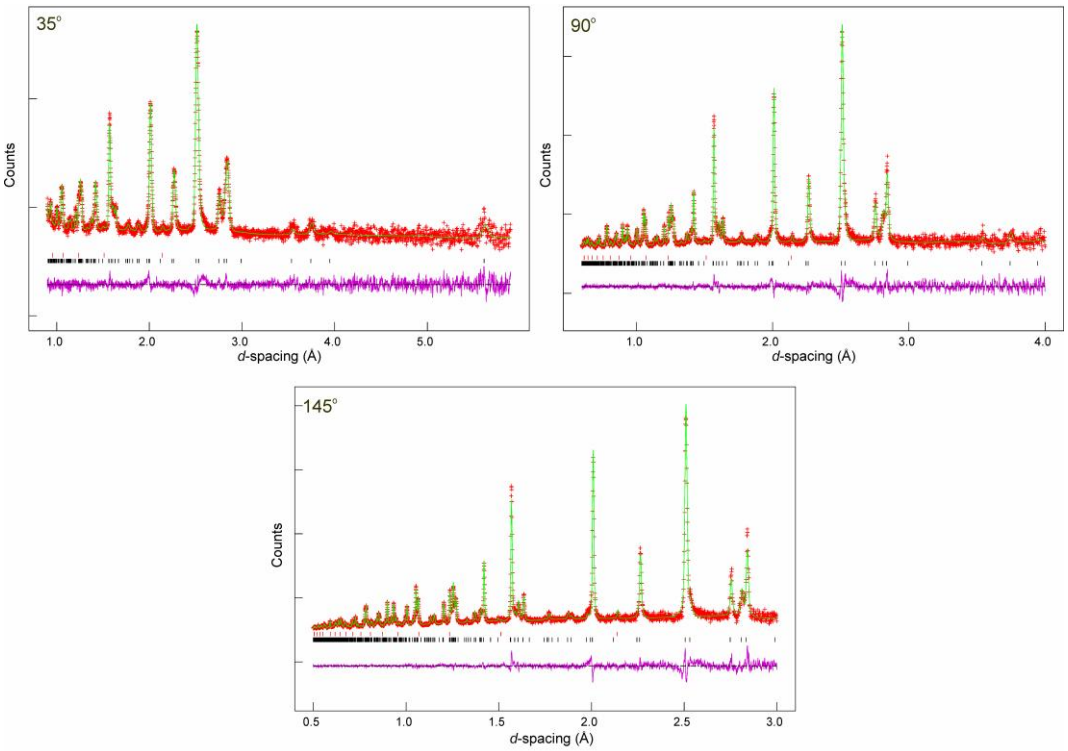


Figure 9.15: Observed, calculated and difference plots from the structural refinement against neutron diffraction data collected from $Sr_3FeCoO_4Cl_2$ at room temperature. The red tick marks relate to vanadium from the sample holder.

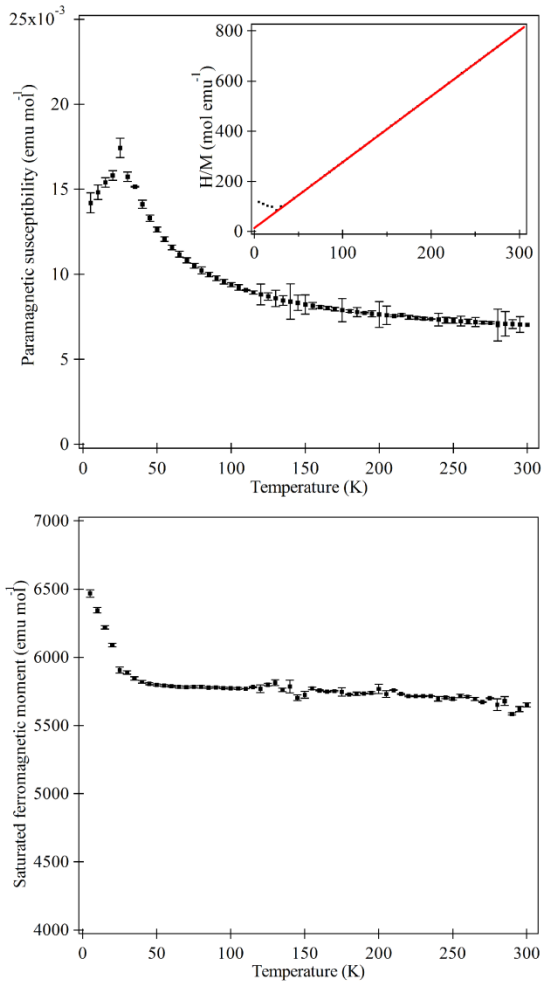


Figure 9.16: Magnetisation data collected from $Sr_3Fe_{1.2}Co_{0.8}O_4Cl_2$ using the 'ferromagnetic subtraction' method. Upper panel shows the paramagnetic susceptibility as a function temperature. Inset shows a fit to the Curie-Weiss law in the temperature range $35 \leq T\ (K) \leq 300$: $C = 0.732(9)\ cm^3\ K\ mol^{-1}$, $\theta = -5.6(4)\ K$. Lower panel shows the saturated ferromagnetic moment as a function of temperature.

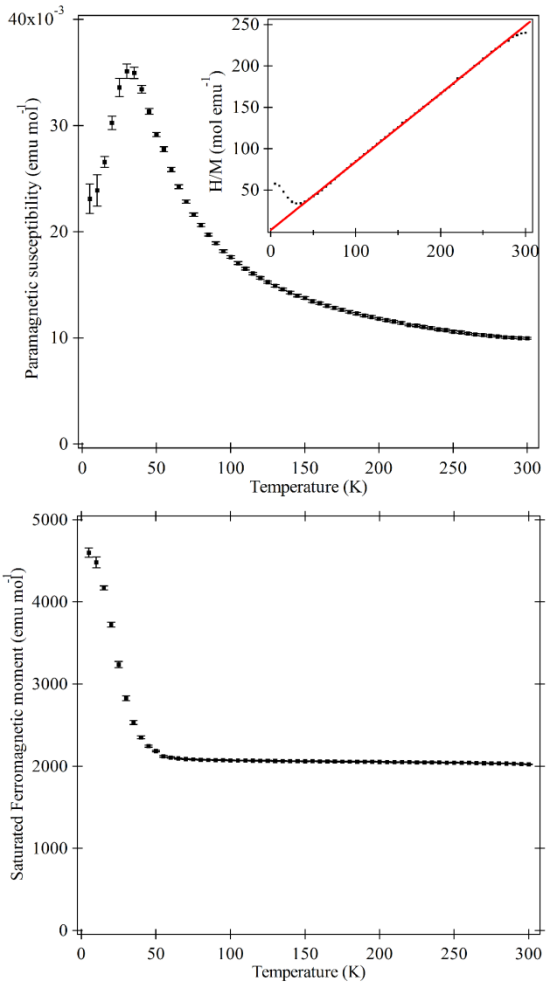


Figure 9.17: Magnetisation data collected from $Sr_3Fe_{1.4}Co_{0.6}O_4Cl_2$ using the 'ferromagnetic subtraction' method. Upper panel shows the paramagnetic susceptibility as a function temperature. Inset shows a fit to the Curie-Weiss law in the temperature range $35 \leq T\ (K) \leq 300$: $C = 1.213(5)\ cm^3\ K\ mol^{-1}$, $\theta = -2.3(3)\ K$. Lower panel shows the saturated ferromagnetic moment as a function of temperature.

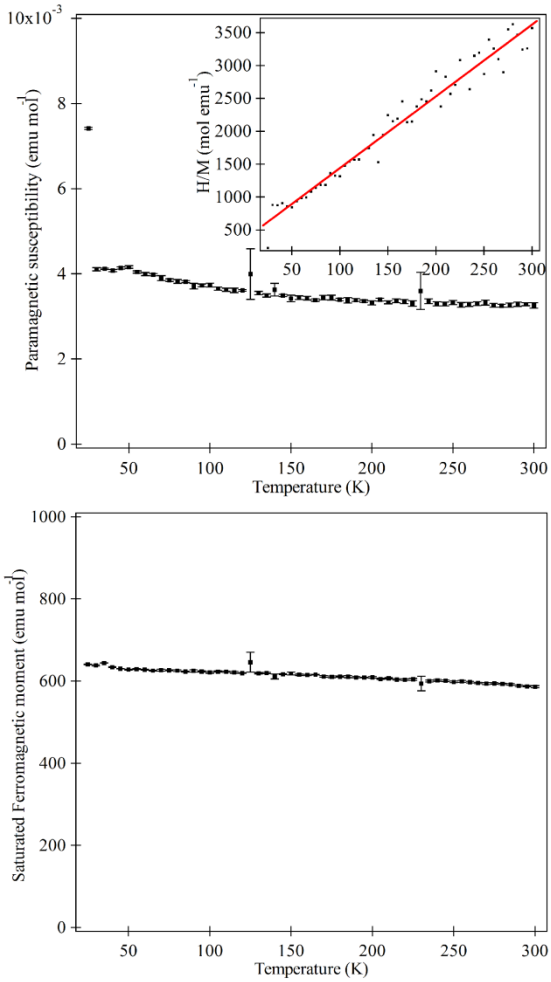


Figure 9.18: Magnetisation data collected from $Sr_3Fe_{1.8}Co_{0.2}O_4Cl_2$ using the 'ferromagnetic subtraction' method. Upper panel shows the paramagnetic susceptibility as a function temperature. Inset shows a fit to the Curie-Weiss law in the temperature range $35 \leq T\ (K) \leq 300$: $C = 0.357(3)\ cm^3\ K\ mol^{-1}$, $\theta = -2.4(6)\ K$. Lower panel shows the saturated ferromagnetic moment as a function of temperature.

Chapter 10: Summary of Findings

10.1. Introduction

This investigation has shown than binary metal hydrides (LiH, NaH and CaH_2) can act as effective solid state reducing agents, removing oxide ions from substrate phases to form novel metastable phases. The majority of these new phases contain transition metal centres in unusual oxidation states and coordination environments, e.g. manganese cations with an average oxidation state of below +2 ($La_{1-x}Ca_xMnO_2$ and $(La_{0.1}Ca_{0.9})_{0.5}Mn_{0.5}O$) and Fe^{2+} cations in square planer coordination sites ($Sr_3Fe_2O_4Cl_2$). This investigation is split into two main sections, each with their own objectives:

- To structurally and magnetically characterise the products of the topotactic reduction reactions of the lanthanum-poor $La_{1-x}A_xMnO_3$ (A = Ca^{2+} and Sr^{2+}) perovskite phases using binary metal hydrides as reducing agents.
- To test the selectivity of the topotactic reduction reactions of mixed anion substrate phases using binary metal hydrides as reducing agents.

A summary of the findings within each of these sections will be covered in the following sections.

10.2. Reduction of $La_{1-x}A_xMnO_3$ (A = Ca^{2+} and Sr^{2+}) Phases

The topotactic reduction of phases in the compositional range $La_{1-x}A_xMnO_3$ ($0.2 \leq x \leq 0.5$) with binary metal hydrides results in the formation of reduced phases with empirical compositions of $La_{1-x}A_xMnO_{2.5}$ which adopt brownmillerite structures.[17, 20, 21] However, the current investigation has shown that analogous topotactic reductions reactions of the lanthanum-poor $La_{1-x}A_xMnO_3$ phases result in the formation of reduced phases which adopt differing structures depending on the A-site composition:

- $A^{2+} = Sr^{2+}$. The reduced phases have an empirical composition of $La_{1-x}Sr_xMnO_{3-(0.5-x)/2}$ and adopt 6-layer OOTOOT' stacked structures closely related to the brownmillerite structure.
- $A^{2+} = Ca^{2+}$ ($0.6 \leq x \leq 0.8$). The reduced phases have an empirical composition of $La_{1-x}Ca_xMnO_2$ and adopt structures containing a disordered arrangement of layers of edge-sharing MnO_6 octahedra and layers of chains of MnO_4 tetrahedra.
- $A^{2+} = Ca^{2+}$ ($x = 0.9$ and 1). The reduced phases adopt the rock salt structure with a disordered arrangement of cations.

The stabilisation of the observed structures rather than the hypothetical '$La_{1-x}A_xMnO_{2.5}$' ($x \geq 0.6$) brownmillerite structures can be rationalised on the basis of an aversion to the formation of tetrahedral Mn^{3+} centres (a requirement for the hypothetical lanthanum-poor brownmillerite phases). This suggests that tetrahedral Mn^{2+} centres can be used as a 'secondary building block' in the 'modular construction' of anion-deficient perovskite structures.[6]

The $La_{1-x}Sr_xMnO_{3-(0.5-x)/2}$ ($x = 0.67$, 0.7 and 0.75) phases adopt structures containing an intralayer ordered arrangement (-L-R-L-R-) of twisted tetrahedral chains. While this arrangement has previously been proposed for 6-layer and 4-layer brownmillerite phases,[63] the structures of the $La_{1-x}Sr_xMnO_{3-(0.5-x)/2}$ ($x = 0.67$, 0.7 and 0.75) phases represent the first examples of refined 6-layer structures containing such intralayer order. As in the structurally-related brownmillerite phases,[17] the adoption of this particular arrangement of the twisted tetrahedral chains can be rationalised on the basis of the cancellation of dipole moments associated with the twisted chains. Furthermore, this logic can be extended to rationalise the adoption of other anion-deficient structures containing tetrahedral layers. As discussed in Chapter 4, further work is required to fully elucidate the magnetic structures of the 6-layer $La_{1-x}Sr_xMnO_{3-(0.5-x)/2}$ ($x \geq 0.6$) phases.

The $La_{1-x}Ca_xMnO_2$ ($0.6 \leq x \leq 0.8$) reduced phases represent the first reported examples of oxide based materials containing an average manganese oxidation state of below +2. Within this investigation significant progress had been made towards the understanding of the effect of the average A-cation radius on the structures of the phases formed upon topotactic reduction reactions of manganese-based perovskite phases. To complement this investigation, further research on this topic should include an investigation into the effect of the variance in the A-site cation radii upon the structures formed upon reduction of such perovskite phases.

10.3. Selectivity

In order to reap the full benefit of topotactic reduction reactions it is necessary to control which of the various anions in a substrate phase are removed and how the resulting anion vacancies order. The topotactic reduction reaction of $Sr_3Fe_2O_5Cl_2$ with LiH is the first reported example of the use of binary metal hydrides to deintercalate oxide ions from a complex transition metal oxychloride and, as such, represents a significant step towards the targeted synthesis of anion-deficient phases.

As discussed in Chapter 1, the relative strengths of the contacts between the anions and the A- and B-cations can be used to predict which anions will be removed from a structure during a topotactic reduction reaction.[27] It therefore follows that the removal of certain anions from a host structure is not possible, thereby precluding the formation of potentially interesting electronic states. For example, the 'apical' oxide ion in the all oxide-analogue of $Sr_3Fe_2O_5Cl_2$ ($Sr_3Fe_2O_{7-\delta}$ – O(3) in Figure 8.1) remains in place upon topotactic reduction.[99] However, by substitution of this 'apical' oxide ion for a chloride ion (Cl(1) in Figure 8.1), the effect of this anion on the transition metal centre can be removed without the need to deintercalate the anion, thereby allowing access to an usual electronic state.

It is clear that $Sr_3Fe_2O_4Cl_2$ is tolerant of extensive B-site doping by cobalt, which is somewhat unusual given the relatively narrow compositional range over which the

$SrFe_{1-x}(Co/Mn)_xO_2$ ($x \leq 0.3$) phases adopt the related infinite layer structure.[119] Indeed the magnetic properties of the $Sr_3Fe_{2-x}Co_xO_4Cl_2$ ($0 \leq x \leq 1$) phases are highly dependent on the B-site composition: while $Sr_3Fe_2O_4Cl_2$ ($0 \leq x \leq 0.6$) phases adopt G-type antiferromagnetically ordered structures below T_N, $Sr_3Fe_{2-x}Co_xO_4Cl_2$ ($0.8 \leq x \leq 1$) phases display spin glass behaviour.

Further work on this topic should extend the cobalt doping level to include all B-site compositions up to $Sr_3Co_2O_4Cl_2$ ($x = 2$) to further monitor the effect of the B-site composition on the magnetic properties of the $Sr_3Fe_{2-x}Co_xO_4Cl_2$ ($0 \leq x \leq 2$) phases. Indeed, incorporation of other metal centres onto the B-site of the $Sr_3Fe_2O_4Cl_2$ phase should also be attempted. Furthermore, topotactic reduction of the bromide analogue of $Sr_3Fe_2O_5Cl_2$, $Sr_3Fe_2O_5Br_2$,[25] should result in the formation of $Sr_3Fe_2O_4Br_2$ – the magnetic properties of which should provide a further probe into the strength of the magnetic coupling between the FeO_2 layers in these phases.

Chapter 11: Bibliography

1. Cox, P. A., *Transition Metal Oxides*. Oxford Science Publications: Oxford, 1992; Vol. 27.
2. Rao, C. N. R.; Raveau, B., *Transition Metal Oxides*. VCH Publishers: New York, 1995.
3. Pena, M. A.; Fierro, J. L. G., *Chemical Reviews* **2001,** 101, (7), 1981-2018.
4. Ishihara, T. E., *Perovskite Oxide for Solid Oxide Fuel Cells*. Springer: 2009.
5. Dawber, M.; Rabe, K. M.; Scott, J. F., *Reviews of Modern Physics* **2005,** 77, (4), 1083.
6. Tenailleau, C.; Allix, M.; Claridge, J. B.; Hervieu, M.; Thomas, M. F.; Hirst, J. P.; Rosseinsky, M. J., *Journal of the American Chemical Society* **2008,** 130, (24), 7570-7583.
7. Goldschmidt, V. M., *Geochemische Verteilungsgesetze der Elemente VII - VIII* **1927,** 1927, 1-156.
8. Woodward, P., *Acta Crystallographica Section B* **1997,** 53, (1), 32-43.
9. Seddon, J.; Suard, E.; Hayward, M. A., *Journal of the American Chemical Society* **2010,** 132, (8), 2802-2810.
10. Anderson, M. T.; Vaughey, J. T.; Poeppelmeier, K. R., *Chemistry of Materials* **1993,** 5, (2), 151-165.
11. Bertaut, E. F.; Blum, P.; Sagnieres, A., *Acta Crystallographica* **1959,** 12, (2), 149-159.
12. Abakumov, A. M.; Alekseeva, A. M.; Rozova, M. G.; Antipov, E. V.; Lebedev, O. I.; Van Tendeloo, G., *Journal of Solid State Chemistry* **2003,** 174, (2), 319-328.
13. Abakumov, A. M.; Kalyuzhnaya, A. S.; Rozova, M. G.; Antipov, E. V.; Hadermann, J.; Van Tendeloo, G., *Solid State Sciences* **2005,** 7, (7), 801-811.
14. Hadermann, J.; Abakumov, A. M.; D'Hondt, H.; Kalyuzhnaya, A. S.; Rozova, M. G.; Markina, M. M.; Mikheev, M. G.; Tristan, N.; Klingeler, R.; Buchner, B.; Antipov, E. V., *Journal of Materials Chemistry* **2007,** 17, (7), 692-698.
15. Lambert, S.; Leligny, H.; Grebille, D.; Pelloquin, D.; Raveau, B., *Chemistry of Materials* **2002,** 14, (4), 1818-1826.
16. D'Hondt, H.; Abakumov, A. M.; Hadermann, J.; Kalyuzhnaya, A. S.; Rozova, M. G.; Antipov, E. V.; Van Tendeloo, G., *Chemistry of Materials* **2008,** 20, (22), 7188-7194.
17. Parsons, T. G.; D'Hondt, H.; Hadermann, J.; Hayward, M. A., *Chemistry of Materials* **2009,** 21, (22), 5527-5538.
18. Abakumov, A. M.; Rozova, M. G.; Pavlyuk, B. P.; Lobanov, M. V.; Antipov, E. V.; Lebedev, O. I.; Van Tendeloo, G.; Sheptyakov, D. V.; Balagurov, A. M.; Bourée, F., *Journal of Solid State Chemistry* **2001,** 158, (1), 100-111.
19. Casey, P. S.; Barker, D.; Hayward, M. A., *Journal of Solid State Chemistry* **2006,** 179, (5), 1375-1382.
20. Cortés-Gil, R.; Ruiz-González, M.; Alonso, J.; Vallet-Regí, M.; Hernando, A.; González-Calbet, J., *Chemistry – A European Journal* **2007,** 13, (15), 4246-4252.
21. Cortés-Gil, R.; Hernando, M.; Ruiz-González, M. L.; Céspedes, E.; Prieto, C.; Alonso, J. M.; Vallet-Regí, M.; Hernando, A.; González-Calbet, J. M., *Chemistry – A European Journal* **2008,** 14, (29), 9038-9045.
22. Parsons, T. G. The Anion Chemistry of Manganese Perovskites. DPhil. Thesis, University of Oxford, Oxford, 2008.
23. Gillie, L. J.; Wright, A. J.; Hadermann, J.; Van Tendeloo, G.; Greaves, C., *Journal of Solid State Chemistry* **2003,** 175, (2), 188-196.

24. Dann, S. E.; Weller, M. T.; Currie, D. B., *Journal of Solid State Chemistry* **1992,** 97, (1), 179-185.
25. Knee, C. S.; Field, M. A. L.; Weller, M. T., *Solid State Sciences* **2004,** 6, (5), 443-450.
26. Hayward, M. A.; Green, M. A.; Rosseinsky, M. J.; Sloan, J., *Journal of the American Chemical Society* **1999,** 121, (38), 8843-8854.
27. O'Malley, M.; Lockett, M. A.; Hayward, M. A., *Journal of Solid State Chemistry* **2007,** 180, (10), 2851-2858.
28. Adkin, J. J.; Hayward, M. A., *Inorganic Chemistry* **2008,** 47, (23), 10959-10964.
29. Hadermann, J.; Abakumov, A. M.; Adkin, J. J.; Hayward, M. A., *Journal of the American Chemical Society* **2009,** 131, (30), 10598-10604.
30. Sears, V. F., *Neutron News* **1992,** 3, (3), 26 - 37.
31. http://www.ill.eu/instruments-support/instruments-groups/instruments/d2b/characteristics/.
32. http://www.ill.eu/instruments-support/instruments-groups/instruments/d2b/.
33. http://www.ill.eu/instruments-support/instruments-groups/instruments/d1a/characteristics/.
34. http://www.ill.eu/instruments-support/instruments-groups/instruments/d1a/.
35. http://www.ill.eu/instruments-support/instruments-groups/instruments/d1b/characteristics/.
36. http://www.ill.eu/instruments-support/instruments-groups/instruments/d1b/.
37. http://www.isis.stfc.ac.uk/about-isis/how-isis-works6313.html.
38. Williams, D. B.; Carter, C. B., *Transmission Electron Microscopy*. Plenum Press: New York, 1996.
39. Hammond, C., *The Basics of Crystallography and Diffraction*. Oxford Science Publications: Oxford, 2001.
40. Rietveld, H. M., *Journal of Applied Crystallography* **1969,** 2, 65.
41. Larson, A. C.; Von Dreele, R. B. *General Structure Analysis System*, Los Alamos National Laboratory Report LAUR 86-748: Los Alamos 2000.
42. Young, R. A., *The Rietveld Method*. 1995.
43. Thompson, P.; Cox, D. E.; Hastings, J. B., *Journal of Applied Crystallography* **1987,** 20, (2), 79-83.
44. Caglioti, G.; Paoletti, A.; Ricci, F. P., *Nuclear Instruments & Methods* **1958,** 3, (4), 223-228.
45. Tucker, M. G.; Keen, D. A.; Dove, M. T.; Goodwin, A. L.; Hui, Q., *Journal of Physics-Condensed Matter* **2007,** 19, (33).
46. Keen, D., *Journal of Applied Crystallography* **2001,** 34, (2), 172-177.
47. Dove, M. T.; Tucker, M. G.; Keen, D. A., *European Journal of Mineralogy* **2002,** 14, (2), 331-348.
48. Goodwin, A. L.; Michel, F. M.; Phillips, B. L.; Keen, D. A.; Dove, M. T.; Reeder, R. J., *Chemistry of Materials* **2010,** 22, (10), 3197-3205.
49. Billinge, S. J. L.; Kanatzidis, M. G., *Chemical Communications* **2004**, (7), 749-760.
50. Brese, N. E.; O'Keeffe, M., *Acta Crystallographica B* **1991,** B47, 192-197.
51. Brown, I. D.; Altermatt, D., *Acta Crystallographica B* **1985,** B41, 244-247.
52. Goodenough, J. B., *Magnetism and the Chemical Bond*. Wiley: New York, 1963.
53. Jiang, S. P., *Journal of Materials Science* **2008,** 43, (21), 6799-6833.
54. Suescun, L.; Dabrowski, B.; Remsen, S.; Mais, J., *Journal of Solid State Chemistry* **2009,** 182, (1), 187-195.
55. Suescun, L.; Dabrowski, B.; Mais, J.; Remsen, S.; Richardson, J. W.; Maxey, E. R.; Jorgensen, J. D., *Chemistry of Materials* **2008,** 20, (4), 1636-1645.

56. Suescun, L.; Chmaissem, O.; Mais, J.; Dabrowski, B.; Jorgensen, J. D., *Journal of Solid State Chemistry* **2007,** 180, (5), 1698-1707.
57. Caignaert, V.; Nguyen, N.; Hervieu, M.; Raveau, B., *Materials Research Bulletin* **1985,** 20, (5), 479-484.
58. Chmaissem, O.; Dabrowski, B.; Kolesnik, S.; Mais, J.; Jorgensen, J. D.; Short, S., *Physical Review B* **2003,** 67, (9).
59. Battle, P. D.; Gibb, T. C.; Jones, C. W., *Journal of Solid State Chemistry* **1988,** 74, (1), 60-66.
60. Hudspeth, J. M.; Goossens, D. J.; Studer, A. J.; Withers, R. L.; Noren, L., *Journal of Physics-Condensed Matter* **2009,** 21, (12).
61. Roth, G.; Adelmann, P.; Heger, G.; Knitter, R.; Wolf, T., *Journal De Physique I* **1991,** 1, (5), 721-741.
62. Battle, P. D.; Gibb, T. C.; Lightfoot, P., *Journal of Solid State Chemistry* **1990,** 84, (2), 237-244.
63. Krekels, T.; Milat, O.; Van Tendeloo, G.; Amelinckx, S.; Babu, T. G. N.; Wright, A. J.; Greaves, C., *Journal of Solid State Chemistry* **1993,** 105, (2), 313-335.
64. Aminoff, G., *Zeitschrift fur Kristallographie* **1926,** 64, 475-490.
65. Sinha, A. P. B.; Sanjana, N. R.; Biswas, A. B., *Acta Crystallographica B* **1957,** 10, (6), 439-440.
66. Dixon, E.; Hadermann, J.; Hayward, M. A., *Journal of Solid State Chemistry* **2011,** 184, (7), 1791-1799.
67. Janssen, T.; Janner, A.; Looijenga, A.; de Wolff, P. M., *International Tables for Crystallography*. Kluwer Academic: Dordrecht, 1992; Vol. C797.
68. Palmer, H. M.; Snedden, A.; Wright, A. J.; Greaves, C., *Chemistry of Materials* **2006,** 18, (5), 1130-1133.
69. Wright, A. J.; Palmer, H. M.; Anderson, P. A.; Greaves, C., *Journal of Materials Chemistry* **2002,** 12, 978-982.
70. Geller, S.; Wood, E. A., *Acta Crystallographica* **1956,** 9, (7), 563-568.
71. H. Hansteen, O.; Fjellvag, H.; C. Hauback, B., *Journal of Materials Chemistry* **1998,** 8, (9), 2081-2088.
72. Mydosh, J. A., *Spin Glasses: An Experimental Introduction*. Taylor and Francis: London, 1993.
73. Kittel, C., *Introduction to Solid State Physics*. 8th ed. ed.; Wiley: New York, 2005.
74. Battle, P. D.; Blundell, S. J.; Santhosh, P. N.; Rosseinsky, M. J.; Steer, C., *Journal of Physics: Condensed Matter* **2002,** 14, 13569-13577.
75. Rodríguez-Carvajal, J.; Vallet-Regí, M.; Calbet, J. M. G., *Materials Research Bulletin* **1989,** 24, (4), 423-430.
76. Babu, T. G. N.; Kilgour, J. D.; Slater, P. R.; Greaves, C., *Journal of Solid State Chemistry* **1993,** 103, (2), 472-480.
77. Bowman, A.; Allix, M.; Pelloquin, D.; Rosseinsky, M. J., *Journal of the American Chemical Society* **2006,** 128, (39), 12606-12607.
78. Hadermann, J., Private Communication. In.
79. Sayagués, M. J.; Vallet-Regí, M.; Caneiro, A.; González-Calbet, J. M., *Journal of Solid State Chemistry* **1994,** 110, (2), 295-304.
80. Mori, T.; Kamegashira, N., *Journal of Alloys and Compounds* **2006,** 408-412, 1210-1213.
81. Poeppelmeier, K. R.; Leonowicz, M. E.; Scanlon, J. C.; Longo, J. M.; Yelon, W. B., *Journal of Solid State Chemistry* **1982,** 45, (1), 71-79.

82. Varela, A.; Dios, S. d.; Parras, M.; Hernando, M.; Fernandez-Diaz, M. T.; Landa-Canovas, A. R.; Gonzalez-Calbet, J. M., *Journal of the American Chemical Society* **2009,** 131, (24), 8660-8668.
83. Poeppelmeier, K. R.; Leonowicz, M. E.; Longo, J. M., *Journal of Solid State Chemistry* **1982,** 44, (1), 89-98.
84. Radaelli, P. G.; Cox, D. E.; Capogna, L.; Cheong, S. W.; Marezio, M., *Physical Review B* **1999,** 59, (22), 14440.
85. Sagdeo, P. R.; Shahid, A.; Lalla, N. P., *Powder Diffraction* **2006,** 21, (1), 40-44.
86. Shannon, R. D., *Acta Crystallographica A* **1976,** A32, (5), 751-67.
87. Hull, S.; Smith, R. I., *User Guide for the Polaris Powder Diffractometer*. 2007.
88. Goodwin, A. L.; Redfern, S. A. T.; Dove, M. T.; Keen, D. A.; Tucker, M. G., *Physical Review B* **2007,** 76, (17), 174114.
89. Poeppelmeier, K. R.; Horowitz, H. S.; Longo, J. M., *Journal of the Less Common Metals* **1986,** 116, (1), 219-227.
90. Saines, P. J.; Spencer, J. R.; Kennedy, B. J.; Avdeev, M., *Journal of Solid State Chemistry* **2007,** 180, (11), 2991-3000.
91. Niewa, R.; Vajenine, G. V.; DiSalvo, F. J.; Luo, H. H.; Yelon, W. B., *Zeitschrift Fur Naturforschung B* **1998,** 53, (1), 63-74.
92. Clarke, S. J.; Adamson, P.; Herkelrath, S. J. C.; Rutt, O. J.; Parker, D. R.; Pitcher, M. J.; Smura, C. F., *Inorganic Chemistry* **2008,** 47, (19), 8473-8486.
93. Garcia-Alonso, F. J.; Riera, V.; Misas, M. J., *Transition Metal Chemistry* **1985,** 10, (1), 19-21.
94. Niewa, R.; Hu, Z.; Grazioli, C.; Rößler, U.; Golden, M. S.; Knupfer, M.; Fink, J.; Giefers, H.; Wortmann, G.; de Groot, F. M. F.; DiSalvo, F. J., *Journal of Alloys and Compounds* **2002,** 346, (1-2), 129-133.
95. Niewa, R.; DiSalvo, F. J., *Chemistry of Materials* **1998,** 10, (10), 2733-2752.
96. Goodenough, J. B., *Physical Review* **1955,** 100, (2), 564.
97. Loudan, J. An Investigation of the Unconventional Phases in the $La_{1-x}Ca_xMnO_3$ system. Univeristy of Cambridge, Cambridge, 2003.
98. Tsujimoto, Y.; Tassel, C.; Hayashi, N.; Watanabe, T.; Kageyama, H.; Yoshimura, K.; Takano, M.; Ceretti, M.; Ritter, C.; Paulus, W., *Nature* **2007,** 450, (7172), 1062-1065.
99. Kageyama, H.; Watanabe, T.; Tsujimoto, Y.; Kitada, A.; Sumida, Y.; Kanamori, K.; Yoshimura, K.; Hayashi, N.; Muranaka, S.; Takano, M.; Ceretti, M.; Paulus, W.; Ritter, C.; André, G., *Angewandte Chemie International Edition* **2008,** 47, (31), 5740-5745.
100. Hazen, R. M.; Burnham, C. W., *American Mineralogist* **1974,** 59, (11-12), 1166-76.
101. Hector, A. L.; Hutchings, J. A.; Needs, R. L.; Thomas, M. F.; Weller, M. T., *Journal of Materials Chemistry* **2001,** 11, (2), 527-532.
102. Xiang, H. J.; Wei, S.-H.; Whangbo, M. H., *Physical Review Letters* **2008,** 100, (16), 167207.
103. Hiroshi, K.; Takashi, W.; Yoshihiro, T.; Atsushi, K.; Yuji, S.; Kazuyoshi, K.; Kazuyoshi, Y.; Naoaki, H.; Shigetoshi, M.; Mikio, T.; Monica, C.; Werner, P.; Clemens, R.; Gilles, A., *Angewandte Chemie International Edition* **2008,** 47, (31), 5740-5745.
104. Hayashi, N.; Kageyama, H.; Tsujimoto, Y.; Watanabe, T.; Muranaka, S.; Ono, T.; Nasu, S.; Ajiro, Y.; Yoshimura, K.; Takano, M., *Journal of the Physical Society of Japan* **2010,** 79, (12), 123709/1-123709/4.
105. Mitchell, J. F.; Millburn, J. E.; Medarde, M.; Short, S.; Jorgensen, J. D.; Fernandez-Diaz, M. T., *Journal of Solid State Chemistry* **1998,** 141, 599-603.

106. Takeda, T.; Komura, S.; Watanabe, N. In *Exchange interactions in cubic perovskite type strontium manganese oxide (SrMnO3) and strontium iron oxide (SrFeO3)*, Ferrites, Proc. ICF, 3rd, 1982; Cent. Acad. Publ. Jpn.: 1982; pp 385-8.
107. Dixon, E.; Hayward, M. A., *Inorganic Chemistry* **2010,** 49, (20), 9649-9654.
108. Helps, R. M.; Rees, N. H.; Hayward, M. A., *Inorganic Chemistry* **2010,** 49, (23), 11062-11068.
109. *Handbook of Chemistry and Physics*. 89th ed.; Boca Raton, 2008.
110. Anderson, J. C.; Schieber, M., *Journal of Physics and Chemistry of Solids* **1964,** 25, (9), 961-968.
111. Giles, P. M.; Longenbach, M. H.; Marder, A. R., *Journal of Applied Physics* **1971,** 42, (11), 4290-4295.
112. Bednorz, J. G.; Muller, K. A., *Zeitschrift Fur Physik B-Condensed Matter* **1986,** 64, (2), 189-193.
113. Prassides, K.; Lappas, A., *Chemistry in Britain* **1994,** 30, (9), 730-732.
114. Crespin, M.; Landron, C.; Odier, P.; Bassat, J. M.; Mouron, P.; Choisnet, J., *Journal of Solid State Chemistry* **1992,** 100, (2), 281-291.
115. Siegrist, T.; Zahurak, S. M.; Murphy, D. W.; Roth, R. S., *Nature* **1988,** 334, (6179), 231-232.
116. Weller, M. T.; Lines, D. R., *Journal of Solid State Chemistry* **1989,** 82, (1), 21-29.
117. Dixon, E.; Hayward, M. A., *Inorganic Chemistry* **2011,** 50, (15), 7250-7256.
118. Greaves, C.; Jacobson, A. J.; Tofield, B. C.; Fender, B. E. F., *Acta Crystallographica Section B* **1975,** 31, (3), 641-646.
119. Seinberg, L.; Yamamoto, T.; Tassel, C.; Kobayashi, Y.; Hayashi, N.; Kitada, A.; Sumida, Y.; Watanabe, T.; Nishi, M.; Ohoyama, K.; Yoshimura, K.; Takano, M.; Paulus, W.; Kageyama, H., *Inorganic Chemistry* **2011,** 50, (9), 3988-3995.
120. Grenier, J.-C.; Ghodbane, S.; Demazeau, G.; Pouchard, M.; Hagenmuller, P., *Materials Research Bulletin* **1979,** 14, (6), 831-839.
121. Smura, C. F.; Parker, D. R.; Zbiri, M.; Johnson, M. R.; Gál, Z. A.; Clarke, S. J., *Journal of the American Chemical Society* **2011,** 133, (8), 2691-2705.
122. Knee, C. S.; Weller, M. T., *Journal of Solid State Chemistry* **2002,** 168, (1), 1-4.
123. Xiang, H. J.; Wei, S. H.; Whangbo, M. H., *Physical Review Letters* **2008,** 100, (16).
124. Kawakami, T.; Tsujimoto, Y.; Kageyama, H.; Chen, X.-Q.; Fu, C. L.; Tassel, C.; Kitada, A.; Suto, S.; Hirama, K.; Sekiya, Y.; Makino, Y.; Okada, T.; Yagi, T.; Hayashi, N.; Yoshimura, K.; Nasu, S.; Podloucky, R.; Takano, M., *Nature Chemistry* **2009,** 1, (5), 371-376.
125. Yamamoto, T.; Tassel, C. d.; Kobayashi, Y.; Kawakami, T.; Okada, T.; Yagi, T.; Yoshida, H.; Kamatani, T.; Watanabe, Y.; Kikegawa, T.; Takano, M.; Yoshimura, K.; Kageyama, H., *Journal of the American Chemical Society* **2011,** 133, (15), 6036-6043.
126. Whangbo, M.-H.; Kohler, J., *Nature Chemistry* **2009,** 1, (5), 351-352.